Forschungsbericht 2024-09

R-Mode: An Alternative to Global Navigation Satellite Systems for Terrestrial Navigation at Medium Frequencies

Lars Grundhöfer

Deutsches Zentrum für Luft- und Raumfahrt
Institut für Kommunikation und Navigation
Standort Neustrelitz

DLR
Deutsches Zentrum
für Luft- und Raumfahrt

Forschungsbericht 2024-09

R-Mode: An Alternative to Global Navigation Satellite Systems for Terrestrial Navigation at Medium Frequencies

Lars Grundhöfer

Deutsches Zentrum für Luft- und Raumfahrt
Institut für Kommunikation und Navigation
Standort Neustrelitz

175 Seiten
84 Bilder
8 Tabellen
120 Literaturstellen

DLR
Deutsches Zentrum
für Luft- und Raumfahrt

Herausgeber:

Deutsches Zentrum
für Luft- und Raumfahrt e. V.
Wissenschaftliche Information
Linder Höhe
D-51147 Köln

ISSN 1434-8454
ISRN DLR-FB-2024-09
Erscheinungsjahr 2024

DOI: 10.57676/dy71-6t71

R-Mode, GNSS, Navigation, Positionierung, PNT, CRB, Mittelwellen Empfänger

Lars Grundhöfer
DLR, Institut für Kommunikation und Navigation, Standort Neustrelitz

R-Mode: Eine Alternative zu globalen Satellitennavigationssystemen für die terrestrische Navigation bei mittleren Frequenzen

Technische Universität Ilmenau

Positions- und Zeitangaben sind für unser tägliches Leben in der heutigen Gesellschaft von grundlegender Bedeutung. Sie werden in vielen Anwendungen genutzt, z. B. in Telekommunikationsnetzen, Stromnetzen und natürlich in allgemeinen Navigationsanwendungen. Heutzutage werden diese wichtigen Informationen hauptsächlich von globalen Navigationssatellitensystem abgeleitet. Aufgrund der geringen Signalstärke sind diese Signale anfällig für Störungen und Spoofing. Als Gegenmaßnahme werden Backup-Systeme benötigt. R-Mode ist ein solches System, welche für den Einsatz im maritimen Bereich entwickelt wird. Bestehende Sendeinfrastrukturen werden genutzt, um ein modifiziertes Signal zu übertragen, welches eine Entfernungsmessung und bei ausreichender Anzahl von empfangenen Stationen zusätzlich eine Positionsbestimmung ermöglicht. Das Ziel dieser Arbeit ist es, den Prototyp eines Empfängers für die modifizierten Signale zu entwickeln, die auf der Mittelfrequenzen übertragen werden.

Um dieses Ziel zu erreichen erweitern wir im ersten Schritt die bestehenden Beschreibungen des Mittelfrequenz R-Mode-Systems, indem wir die verschiedenen Verzerrungen in der Sendekette und der Ausbreitung untersuchen. Dieses Wissen ist für die Entwicklung unseres R-Mode Empfängers von grundlegender Bedeutung, da der Empfänger diesen Einfluss abschwächen muss. In einem zweiten Schritt leiten wir die theoretischen unteren Leistungsgrenzen des Systems ab, die für die Vorhersage der Abdeckung für das R-Mode Baltic Testbed verwendet werden. Die abgeleiteten Grenzen werden außerdem verwendet, um die Leistung verschiedener Schätzer für das R-Mode-Signal zu testen.

Auf Grundlage der Schätzung entwickeln wir einen auf Software Defined Radio basierende Empfänger, der in der Lage ist, eine Echtzeitschätzung der Position durchzuführen. Verschiedene Hardwarekomponenten werden charakterisiert, um eine optimale Leistung und Integration in der entwickelte Empfängersoftware zu gewährleisten. Das Ergebnis sind Module, die frei kombiniert werden können, um den Empfänger für eine bestimmte Aufgabe anzupassen.

Für einen ersten Prototyp haben wir Messkampagnen durchgeführt, um reale dynamische und statische Positionierungsergebnisse zu erhalten. Während unserer Versuche konnten wir die erste Positionierungslösung im Fernfeld des R-Mode-Senders präsentieren

Im letzten Teil dieser Arbeit haben wir unsere Ergebnisse und Erfahrungen genutzt, um weitere Verbesserungen des Signals vorzuschlagen, die durch Simulationen verifiziert wurden.

R-Mode, GNSS, Navigation, Positioning, PNT, CRB, Medium Frequency Receiver

(Published in English)

Lars Grundhöfer
German Aerospace Center (DLR), Institute of Communications and Navigation, Location Neustrelitz

R-Mode: An Alternative to Global Navigation Satellite Systems for Terrestrial Navigation at Medium Frequencies

Technical University Ilmenau

Positioning and timing information is fundamental for our daily lives in today's society. Our society uses this information in many applications such as telecommunication networks, energy grids and general navigation applications. Today this crucial information is mainly derived from the global navigation satellite system. Due to the low signal strength, this signal is prone to jamming and spoofing. Therefore, we need backup systems as countermeasures. R-Mode is such a system under development for use in the maritime domain. We utilize existing transmitter infrastructure to transmit a modified signal that enables ranging, and, if a sufficient number of stations is received, positioning. Our goal in this thesis is to develop a prototype receiver for the modified signals transmitted at medium frequencies. In a first step, we extend the existing descriptions of the Medium Frequency R-Mode system by exploring the different biases introduced in the transmitter chain and propagation. The knowledge is fundamental for our development as any solution needs to mitigate this influence. In a second step, we derive the theoretical lower performance bound of the system, which we use for a coverage prediction for the R-Mode Baltic test-bed. We use the derived bounds further to test the performance of different estimation approaches on the R-Mode signal.

Around the estimation, we design a software-defined radio-based receiver that can perform real-time positioning estimation. We characterize different hardware components to ensure the best performance and integration in the developed receiver software. The results are modules that can be freely combined to fit the receiver for a given task. For a prototype, we conducted measurement campaigns to generate real dynamic and static positioning results. During our trials, we delivered the first positioning solution in the far field of the R-Mode transmitter. In the last part of this work, we used our results and experience to suggest further improvement on the signal verifying with simulations.

DISSERTATION

R-Mode: An Alternative to Global Navigation Satellite Systems for Terrestrial Navigation at Medium Frequencies

AUTOR: LARS GRUNDHÖFER

GUTACHTER: PROF. DR.-ING. GIOVANNI DEL GALDO
PROF. DR.-ING. THOMAS DALLMANN
PROF. DR. JORDI VILÀ-VALLS

Dissertation zur Erlangung des akademischen Grades Doktor-Ingenieur (Dr.-Ing)

Eingereicht am 18. Oktober 2022

Öffentlicher Teil der wissenschaftlichen Aussprache am 9. Juli 2024

Published and submitted content

Most contributions of this doctoral thesis have been published in journals and conferences. This section enumerates the involved publications and relates them to the main chapters and sections, specifying the way of inclusion.

JOURNAL ARTICLES

- (July, 2022) Grundhöfer, L.; Wirsing,M.; Gewies, S.; Galdo, G. D. "Phase Estimation of Single Tones Next to Modulated Signals in the medium frequency R-Mode system" Published in: *IEEE Access. IEEE* Ref. [1].
  DOI: 10.1109/ACCESS.2022.3190544
  Statement: the content from this publication is partially included in Chapter 4 and 6.

- (December, 2021) Grundhöfer, L.; Rizzi, F. G.; Gewies, S.; Hoppe, M.; Bäckstedt, J.; Dziewicki, M.,; Galdo, G. D. "Positioning with medium frequency R-Mode" Published in: *ION Navigation, 68, 829-841* Ref. [2].
  DOI: 10.3390/rs13152904
  Statement: the content from this publication is partially included in Chapter 4, 5 and 6 .

- (April, 2021) Grundhöfer, L.; Gewies, S.; Galdo, G. D. "Estimation Bounds of Beat Signal in the R-Mode Localization System." Published in: *IEEE Access. IEEE* Ref. [3].
  DOI: 10.1109/ACCESS.2021.3076845
  Statement: the content from this publication is partially included in Chapter 3, 4 and 7.

- (December, 2018) Grundhöfer, L.; Gewies, S. " R-Mode receiver development for medium frequency signals" Published in: . *Scientific Journals of the Maritime University of Szczecin. Maritime University of Szczecin* Ref. [4].
  DOI: 10.17402/314
  Statement: the content from this publication is partially included in Chapter 3.

CONFERENCE ARTICLES

- (2021, September) Grundhöfer, L.; Rizzi, F. G.; Gewies, S.; Del Galdo, G. "Improving medium frequency R-Mode ranging with GMSK modulation " Accepted in: *Proceedings of the 34th International Technical Meeting of the Satellite Division of the Institute of Navigation ION GNSS + 2021* . Ref. [5].
  Statement: the content from this publication is partially included in Chapter 7.

- (2021, September) Rizzi, F. G.; Grundhöfer, L.; Gewies, S. "Medium frequency R-Mode range estimation with phase locked loop approach " Accepted in: *Navigation 2021*. Ref. [6].
  Statement: the content from this publication is partially included in Chapter 4.

- (2020, November) Grundhöfer, L.; Gewies, S. “Equivalent Circuit for Phase Delay in a Medium Frequency Antenna“ Accepted in: *2020 European Navigation Conference (ENC)*. Ref. [7].
  Statement: the content from this publication is partially included in Chapter 2.
- (2020, March) Grundhöfer, L.; Gewies, S.; Hehenkamp, N.; Del Galdo, G. “Redesigned Waveforms in the Maritime Medium Frequency Bands“ Accepted in: *2020 IEEE/ION Position, Location and Navigation Symposium (PLANS)*. Ref. [8].
  Statement: the content from this publication is partially included in Chapter 7.
- (2019, October) Grundhöfer, L.; Gewies, S.; Hehenkamp, N.; Hoppe, M.; Walterfang, M. “Characterization of a transmitter in a medium frequency maritime terrestrial navigation system “ Accepted in: *2019 IEEE Intelligent Transportation Systems Conference (ITSC), IEEE.* . Ref. [9].
  Statement: the content from this publication is partially included in Chapter 2.

Note: The material contained in this work from these sources is not necessarily singled out with typographical means and references.

Other research merits

During my research work, I had the opportunity to learn more about the system view on R-Mode and to transfer my knowledge to other classes of problems. The resulting publications are out of scope for this thesis. For the sake of completeness, they are listed in this section, along with submitted patents and other related activities.

ADDITIONAL PUBLICATIONS

- (2022, September) Grundhöfer, L.; “Calculating Lower Bounds within the PyTorch Framework“ Accepted in: *Proceedings of the 35th International Technical Meeting of the Satellite Division of the Institute of Navigation ION GNSS + 2022*. Ref. [10].
  DOI: 10.1007/s00170-021-07591-5

- (2021, June) Meister, S.; Grundhöfer, L.; Stüve, J.; Groves, R. M. “Imaging sensor data modelling and evaluation based on optical composite characteristics.“ Published in: *International Journal of Advanced Manufacturing Technology, 2021,* . Ref. [11].
  DOI: 10.1007/s00170-021-07591-5

- (2020, September) Medina, D.; Grundhöfer, L.; Hehenkamp, N.“Evaluation of Estimators for Hybrid GNSS-Terrestrial Localization in Collaborative Networks.“ Accepted in: *2020 IEEE International Conference on Intelligent Transportation Systems, ITSC 2020. IEEE.* . Ref. [12].
  DOI: 10.1109/ITSC45102.2020.9294750

- (2020, July) Rieck, C.; Gewies, S.; Grundhöfer, L.; Hoppe, M. “Synchronization of R-Mode Base Stations “ Accepted in: *2020 Joint Conference of the IEEE International Frequency Control Symposium and International Symposium on Applications of Ferroelectrics (IFCS-ISAF), IEEE* . Ref. [13].
  DOI: 10.1109/IFCS-ISAF41089.2020.9234840

- (2020, March) Gewies, S.; Grundhöfer, L. ; Hehenkamp, N. “Availability of Maritime Radio Beacon Signals for R-Mode in the Southern Baltic Sea“ Published in: *TransNav : International Journal on Marine Navigation and Safety of Sea Transportation, Faculty of Navigation Gdynia Maritime University, 2020, 14, 173-178* . Ref. [14].
  DOI: 10.12716/1001.14.01.21

- (2019, September) Gewies, S.; Grundhöfer, L.; Wirsing, M.; Raulefs, R.; Bronk, K.; Koncicki, P.; Rafał, N.; Hoppe, M.; Bäckstedt, J.; Rieck, C. “R-Mode in the Baltic Sea region“ Accepted in: *IALA Workshop on Ranging-Mode, 9th - 12th September 2019, Saint-Germain-en-Laye, France* . Ref. [15].

- (2019, June) Grundhöfer, L.; Hehenkamp, N.; Heymann, F. “Concept For Selectable Composite Radar Screens “ Accepted in: *2019 20th International Radar Symposium (IRS), IEEE*. Ref. [16].
  DOI: 10.23919/IRS.2019.8768108

OTHER RESEARCH ACTIVITIES

- Student Chair for the German Chapter of the IEEE ITS Society (2021–Present).
- Best Paper Award for the paper “ R-Mode receiver development for medium frequency signals” for the MTE ISI 2018.

CONTENTS

1

INTRODUCTION

Position Navigation and Timing (PNT) is an important asset in today's society, often unnoticed by its users. Applications range from our daily communications over financial transactions to the supply of essential commodities. Failure affects both the economic and private sectors. Currently, information comes from satellite systems that differ in their global or regional coverage. The former are collectively known as Global Navigation Satellite System (GNSS) and include the American Global Positioning System (GPS) [17], the European Galileo [18], Russian Global Navigation Satellite System (GLONASS) and Chinese BeiDou Navigation Satellite System (BDS) [19]. Regional systems include Indian Navigation Indian Constellation (NavIC) [20] and the Japanese Quasi-Zenith Satellite System (QZSS) [21].

The United States of America (USA) Cybersecurity & Infrastructure Security Agency (CISA) lists as an example 10 critical infrastructure sectors and highlight especially communications, transportation and water and wastewater systems[22]. Moreover, they showcase what impact a not properly provided PNT information can have.

> "On April 6, 2019, a $500M radio system supporting New York City government operations crashed and remained offline for days due to improperly configured GPS receivers. On that same day, dozens of international flights were canceled due to the same configuration error."[22]
>
> (CISA)

But not only miss-configuration of the receiver can influence the availability and quality of PNT. Due to the low signal strength, today's satellite systems are prone to intended spoofing and jamming[23]. Even unintended natural interference can decrease the performance [24]. For some cases, an optimized GNSS receiver or antenna can mitigate the issue, but still, there is a risk. For the aerospace and maritime domain, Bhatti and Kerns showed successful spoofing attacks in the past [25, 26]. Widespread jamming in South Korea is also a well-known issue [27] and gets featured in the public press [28]. Moreover, the

United States Coast Guard Navigation Center (NavCen) collects reports of interference and publishes them regularly [29].

Because our daily lives rely so heavily on PNT, there is also a high level of political interest the USA passed executive order 13905 in 2020 to research alternative systems [30]. This thesis focuses on the work of such an alternative system called Ranging-Mode (R-Mode).

R-Mode is based on existing maritime infrastructures but is not limited to use in the near-water environment. It continues a long line of terrestrial navigation systems for shipping, on whose infrastructure it is still indirectly based. Other systems like Decca [31], and Loran-C [32] are not able to provide the needed information anymore in Europe, as the responsible operators shutted the transmitters down [33].

However, there is still a clear awareness in the maritime world of the need for reliable PNT information.

> "Golden rule
>
> Never trust a position gained by only one means. Good navigators are always looking for ways to validate their position. This does not change in the age of GNSS."[34]
>
> (The Nautical Institute)

Different organisations worldwide work actively on eLoran, a successor to Loran-C [35, 36]. Grant et al. showed that GNSS outage have a significant effect on maritime safety [37]. On the vessel's side, various systems are affected like DGPS receivers, the Automatic Identification System (AIS) transponder, the dynamic positioning system, gyro calibration system and digital selective calling system, autopilot [37, 25].

In the tradition of terrestrial navigation and the urgent need for reliable positioning, the idea of R-Mode was born [38]. Johnson and Swazek showed the feasibility of the system in the ACCSEAS project [39, 40, 41]. The original idea was to modify the marine radio beacons and AIS base stations operating in the Very High Frequency (VHF) and Medium Frequency (MF) band to transmit synchronized range signals and combine them with eLoran when required. Current research concentrated on VHF Data Exchange System (VDES) over AIS[42, 43].

The accuracy of the complete system is following International Association of Lighthouse Authorities (IALA) recommendation R-129 [44], specifying a minimum accuracy of 100 m for coastal navigation and 10 m for port approaches and navigation in restricted waters. The IALA derives these figures from the International Maritime Organisation (IMO) requirements for a future GNSS [45] and current global radio navigation systems for the same areas of application [46].

In this thesis, we concentrated on the Differential Global Navigation Satellite System (DGNSS) maritime radio beacon service, which was developed in the late 1980s and established in the early 1990s [47]. The original goal was to minimize the error introduced by Selective Availability (SA) in GPS, which limited GPS accuracy to 100 m for civil use cases [48]. Therefore, DGNSS messages, as defined in the Radio Technical Commission for Maritime Services (RTCM) standard [49], were broadcast on the infrastructure of the existing maritime direction finding service. The DGNSS service was designed not to interfere

Figure 1.1: Testbed R-Mode Baltic: MF station operated in February 2021.

with existing equipment using the same infrastructure [50]. However, the direction-finding beacon service is no longer available today.

With the increase in accuracy of GPS, the deactivation of SA [48], and the availability of more GNSS systems, the DGNSS service cannot improve accuracy as much as in the past and is now mainly used for integrity checking. This leads to a natural evolution of the system by adding the possibility of range estimation. The current change adds two Continuous Waves (CWs) that are time-synchronized across all stations so that we can derive ranges from the phase estimates on the receiver side, while maintaining the legacy use [39].

In the R-Mode Baltic project, a testbed for MF R-Mode consisting of eight stations in Sweden, Denmark, Poland, and Germany was established [51]. In Fig. 1.1 we see the operated stations as of February 2022. We want to highlight that not all transmitter were functional during our trials. Therefore, the used transmitters might change slightly.

R-Mode as a system under development has plenty of possibilities to contribute to increased the performance of the service, which we want to investigate in this thesis. At the beginning of our work, the potential performance was already well explained, and Hoppe conducted the first pseudo-range measurements. However, we identified a incomplete description for the wave propagation and transmitting error. Moreover, no MF R-Mode receiver was available to provide a positioning solution. The main contribution of this dissertation is the conception, design and practical verification of a Medium Frequency (MF) R-Mode receiver that can perform positioning in real-time.

Therefore, we must determine the error influences on the phase at the transmitter, at the receiver and during propagation. On the other hand, we focus on phase estimation and which disturbances we need to consider to get the best results. Due to the gained experience, we develop modifications on the signal level to further improve the performance. Based on our work, we were able to demonstrate the first R-Mode position solution under realistic conditions. Our first approach already meets the requirements for coastal navigation [2].

Following the idea of describing and defusing problems, starting from the transmitter to the receiver, we structure the work as follows:

We give an overview of the current MF R-Mode signal and what errors we need to consider in Chapter 2. We have adapted several general theoretical approaches to R-Mode to describe the behaviour of the whole system, which remained undescribed in other related works. To document this in reality, we have carried out measurements and described some characteristics of different transmitters in more detail. Based on this study, we provide descriptions of previously unknown transmitter offsets.

In Chapter 3, we derive the Cramer-Raó Bound (CRB), taking the complete R-Mode signal into account, to give an estimate of the performance that we can potentially archive. We show a first application example of the bound, in which we compare the results for a coverage estimate and show the expected position accuracy in the Baltic Sea region. With this result, the thesis contributes an important decision-making tool for the overall system design.

As a first step in developing the actual receiver, we describe the Maximum Likelihood (ML) estimator and its efficient computation as Fast Fourier Transform (FFT) for our problem in Chapter 4. Furthermore, we show how this estimator compares to the previously derived CRB. Based on these findings, we describe two different Least Square (LS) approaches and how they compare to the ML. Independently, we also describe the simple positioning algorithm we use to achieve the first results. The main challenge we solved in this chapter is to find an optimized estimator for the MF R-Mode signals.

Consequently, we describe the needed hardware for our development in Chapter 5. Here we first clarify which properties the various components require and characterise them with measurements. On this basis, we design three hardware configurations for different purposes and different price ranges. Afterwards, we describe the software, enabling users to provide real-time results. With this chapter, we showcase the feasibility of R-Mode even without laboratory-grade equipment.

In Chapter 6 we contribute, real-time positioning utilizing the ML for two maritime scenarios. Moreover, we study the long-term behaviour of the phase for static installations and show the advantage of a LS estimator over the initial approach.

Based on the gained experience, we suggest optimization of the current R-Mode design by adjusting the bit sequences, changing the modulation and a complete redesign of the band in Chapter 7. Therefore, the thesis contributes first ideas for further developments of MF R-Mode.

2

SYSTEM DESCRIPTION

To develop a R-Mode receiver and improve the overall performance of the system, a detailed description of the current state is essential. Since R-Mode is a new system, we have to develop an initial specification in this chapter. We aim to qualitatively motivate the various error influences to account for our subsequent developments of the R-Mode medium frequency receiver. We give quantitative values wherever it is possible for us through measurements.

In Section 2.1 we describe the current R-Mode signal first presented by Johnson and Swazek [52, 39]. We extend the existing work with a signal model and describe how we can obtain range measurements from the signal. In 2.2 we specify the influence of the propagation path on the system described in the measurements of Johnson [53]. Johnson [39, 53, 54] also presents how the R-Mode signal is generated at the station. But his description neglects the propagation delay within the station, which introduces a bias in the distance estimate. To address this problem, Section 2.3 introduces the different components of the transmitter chain and the necessary modifications to upgrade it to an R-Mode transmitter. Consequently we present initial characterisations and errors of the main components of this chain. We also present the variety of components that we are facing by retrofitting the system R-Mode into the existing infrastructure. Furthermore, in Section 2.4, we give recommendations on how these faults are considered in an operational system based on the descriptions.

2.1. CURRENT R-MODE SIGNAL

The current suggested R-Mode signal needs to fulfil the legacy use of transmitting RTCM messages [55]. The International Telecommunication Union (ITU) defines the broadcast of marine DGNSS radio beacons in Recommendation M.823-2 of the ITU [56]. According to this, the code-differential corrections for GNSS is modulated as a Minimum Shift Keyed (MSK) signal with a carrier frequency in the band from 283.5 kHz to 315 kHz and bandwidth of 500 Hz in Europe. For North America, a band between 285 kHz to 325 kHz is used with a bandwidth of 1000 Hz. The operator can choose the bit rate between 50, 100, 200 bits/s. In this work, we will concentrate on the 500 Hz bandwidth at 100 bit/s as this is currently implemented in the Baltic sea testbed.

The MSK signal at the carrier frequency f_c is placed at the centre of the R-Mode signal with an amplitude A_{MSK}. This component for a single bit duration can be described as

$$s_{\mathrm{MSK}}(t) = A_{\mathrm{MSK}} \sin(\omega_{\mathrm{c}}\, t + b_\tau \frac{\pi t}{2 T_{\mathrm{bit}}} + \varphi_{\mathrm{memory}}). \tag{2.1}$$

Here, b_τ describe the transmitted bit at time t, T_{bit} is the time duration of each bit, ω_{c} is the corresponding circular carrier frequency $\omega_{\mathrm{c}} = 2\pi f_c$ and $\varphi_{\mathrm{memory}}$ denotes the phase memory of the MSK to maintain the phase continues behaviour of the modulation [57].

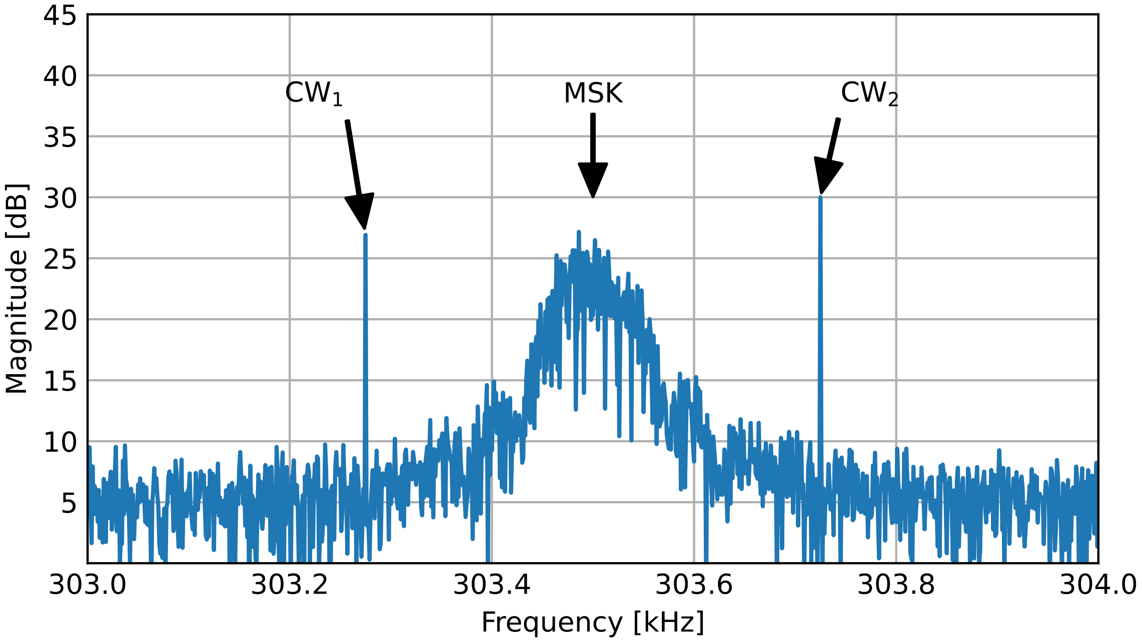

Figure 2.1: Spectra of the simulated R-Mode signal at 303.5 kHz for 1 s at sample rate of 1 MHz. CW1 and CW2 point to the upper and lower tone, with the MSK pointing to the signal due to modulation.

There were initial considerations to synchronize the bit transitions of the modulation between the different stations to enable distance measurements with the legacy signal. However, it became apparent that the estimation of these transitions on the receiver side did not meet the accuracy requirements [39].

Instead, it was proposed in [39] to place CWs as aiding carriers in the zero crossing of the power density spectrum of the MSK modulation. The phases at the full second of these additional signals, also called tones, are synchronized and enable a likewise synchronized receiver to obtain the distance by estimating the phase offsets φ_1 and φ_2 of the tones in each channel. In this work, we use the acronyms lower frequency Continuous Wave (CW1) and higher frequency Continuous Wave (CW2) to refer to the tone we are discussing. As CW1 and CW2 use a common time source for all stations, synchronization of the receiver can be done within the R-Mode system when multiple stations are received.

Mathematically, the CWs can be described with amplitudes A_1 and A_2 as

$$s_{\mathrm{CW1}}(t) = A_1 \sin(\omega_1 t + \varphi_1), \tag{2.2}$$

$$s_{\mathrm{CW2}}(t) = A_2 \sin(\omega_2 t + \varphi_2). \tag{2.3}$$

The frequency of the tones f_1, f_2 are expressed by the circular frequencies,

$$\omega_1 = 2\pi f_1, \tag{2.4}$$

$$\omega_2 = 2\pi f_2 \tag{2.5}$$

chosen to be placed in the fourth zero crossing on both side of the MSK power spectrum. For the case of 500 Hz bandwidth with a bit rate of 100 bit/s this leads to $f_1 = f_c - 225$ and$f_1 = f_c + 225$ [39]. The choice of this frequency compromises the frequency distance of both estimations limitedness of the channel. Combining (2.3) and (2.1) we obtain the signal model as

$$\begin{aligned} s_{\mathrm{complete}}(t) = & A_1 \sin(\omega_1 t + \varphi_1) \\ & + A_{\mathrm{MSK}} \sin(\omega_{\mathrm{c}} t + b_\tau \frac{\pi t}{2 T_{\mathrm{bit}}} + \varphi_{\mathrm{memory}}) \\ & + A_2 \sin(\omega_2 t + \varphi_2). \end{aligned} \tag{2.6}$$

Based on this model, we build a simulation environment in Python [58], which is used in the further course of this thesis. Fig 2.1 shows how the R-Mode signal should look like. The resulting spectra are an output of our simulation environment. We can identify the different signal components. However, since we add noise, the zero crossings described before cannot be seen.

2.1.1. DERIVING RANGES

For the system, it is essential to derive a range out of the phase estimation. Therefore, in the first step, we calculate the propagation time $t_{\mathrm{p},i}$ of the signal between the transmitter and the receiver, which is obtained for each tone i by

$$t_{\mathrm{p},i} = \frac{\varphi_i}{2\pi f_i}. \tag{2.7}$$

Considering the speed of light in vacuum c_0, we can calculate the pseudo range $r_{\mathrm{p},i}$ as

$$r_{\mathrm{p},i} = t_{\mathrm{p},i}\, c_0. \tag{2.8}$$

The above-presented calculations are valid for an ideal system.

However, due to the cyclic nature of the phase, the range estimate is ambiguous with the wavelength, meaning for R-Mode that we can only estimate the absolute range in around 1 km distance around the transmitter. To overcome this issue, Johnson suggested using the difference frequency of both tones, which has a larger wavelength [39]. So, we need to calculate the so-called beat frequency f_{beat}, which is the lower tone obtained from the multiplication between higher and lower CWs. We then use the phase of the resulting frequency to remove the ambiguities. For simplicity, the phase derives from the difference between the different estimates. In the specific case of the Additive White Gaussian Noise (AWGN), by mixing the signal the overall noise variance is doubled. Moreover, the range error scaled directly with wavelength which is strongly enlarged. Moreover, each error leads to an increased deviation due to the larger wavelength. Another possible approach is to start on an initial position and track the phase wrap to derive an offset.

This approach needs to address several biases, which we describe as accumulated phase offset φ_{bias} according to

$$\varphi_{\text{bias}} = \varphi_{\text{transmitter}} + \varphi_{\text{propagation}} + \varphi_{\text{receiver}}. \tag{2.9}$$

The first error source is the phase variety of transmitter chains, as each of them leads to an individual phase offset $\varphi_{\text{transmitter}}$ which we describe in more detail in Section 2.3. The next cause of the error is the propagation path phase bias $\varphi_{\text{propagation}}$ described in Section 2.2, which we either see as a change in speed of light or a phase offset. The last error is the receive phase offset $\varphi_{\text{receiver}}$, which we describe in Chapter 5. Our receiver needs to know all the biases to add them as a correction term to our estimate and provide an absolute distance determination. However, it was not possible to characterize all transmitters during this work. Therefore, a calibration measurement was conducted for the field tests as described in Chapter 6.

2.2. PROPAGATION

Electromagnetic waves can propagate in different ways. For the frequency range relevant in this work, two propagation modes dominate the transmission between the R-Mode transmitter and the receiver. As sketched in Fig. 2.2, the received signal is being affected by multipath effects. Not only does this influence the amplitude but also the phase of the received signal. Combined with the characteristics of the individual paths, the overall result is the phase offset $\varphi_{\text{propagation}}$. Consequently, this leads to reduced accuracy and needs to be mitigated.

2.2.1. GROUNDWAVE

The groundwave is the propagation path whose length we want to estimate to obtain a range. For this propagation mode the wave follows the curvature of the earth, which allows increased range compared to a line of sight propagation, but need to be considered in the positioning solving. The finite conductivity of the soil must be taken into account in wave propagation, as it affects the phase delay. Therefore, we qualitatively describe the propagation as introduced in [59].

The Cartesian coordinate system with x, y and z coordinates spans our space. A perfect conducting plane is specified in the x-y direction, as shown in blue in Fig. 2.3. A wave propagating in the x-direction produces an electric field (E-field) perpendicular to this plane. The corresponding magnetic field (H-field) component lies in the plane and induces a surface current density in the direction of propagation. If we now assume a finite conductivity for the surface, we must consider the penetration depth of the skin

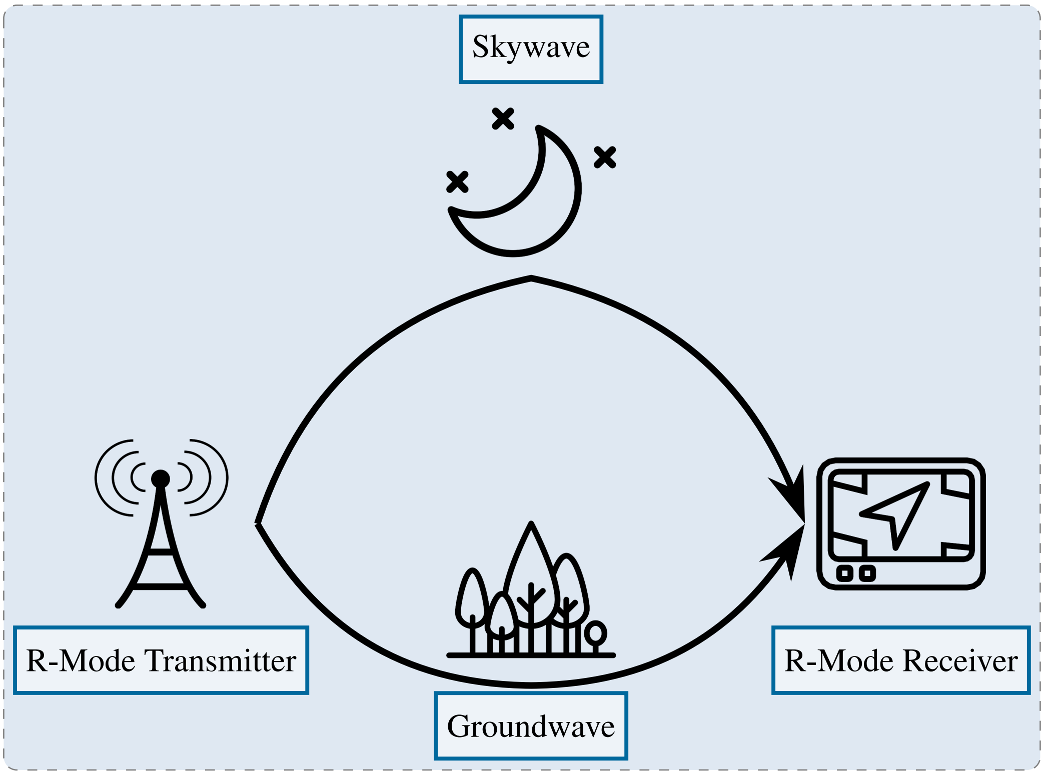

Figure 2.2: MF propagation paths.

$$\delta = \sqrt{\frac{2}{\omega \mu_0 \gamma}}. \tag{2.10}$$

Here, ω denotes the circular frequency, μ_0 the magnetic permeability and γ the electrical conductivity of the plane.

Due to this effect, the x-components of the E-field and the H-field are only partially in-phase and cause energy flow into the plane. As we see in Fig. 2.3, the initially vertically oriented electric field tilts in the direction of propagation, and the initially vertical phase fronts curve near the ground with a component of the active energy fluxes into the ground. Due to this ground absorption, the field strength and the radiation density decrease towards the surface. Thus, the vertical directional diagram of a transmitter antenna near the ground becomes more and more constricted with increasing distance from the transmitter.

The explained model is a qualitative description of the influence of soil conductivity on the phase front, which we need to consider in the distance estimation in R-Mode. However, the bias strongly depends on the propagation path of the signal.

Furthermore, we express how the phase offset is to be considered in the position solution to improve the accuracy. A widely used description introduces a propagation function $F(r)$ for the electric field. With this function, the E-field E_{0z} with distance r, is described as

$$E_{0z} = E_0 \, F(r), \tag{2.11}$$

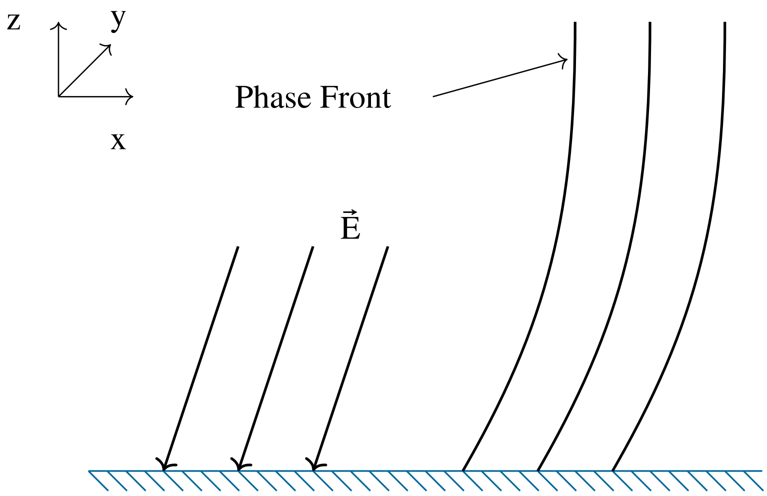

Figure 2.3: Field vector $\vec{E}$ and phase front over finite conductive plane.

with E_0 the field for free-space propagation of distance r. As we are interested what is the phase contribution $\Phi_{\text{propagation}}$ of the propagation distance we need to evaluate

$$\Phi_{\text{propagation}} = arg(F(r)) \tag{2.12}$$

Wait obtained the propagation method with different methods [60]. However, we have shown that for the R-Mode system, we gain good results when we use a combination of the so-called Sommerfeld approach for a short distance up to 15km and the residual approach for long distances. Furthermore, we have only shown propagation over a homogeneous surface, but in reality, the propagation path is composed of different parts with different conductivity. The Millington method combines the different segments [61], enabling a more precise calculation of the path offsets. We assume the effect to be constant over time, as the information of the ground conductivity doesn't change. However, in reality, the conductivity of the soil can vary due to weather conditions. During daytime, we only consider the groundwave propagation for the phase bias $\varphi_{\text{propagation}}$.

2.2.2. SKYWAVE

Skywave describes propagation paths that are not influenced by the absorption and curvature of the earth. In general, the wave propagates near the ground. For certain frequencies, f_i, the waves can be refracted or reflected towards the earth in the ionosphere, introducing additional propagation paths. Here, the plasma frequency f_p of the different ionospheric layers describe the overall effect. For $f_i < f_\text{p}$, the waves are also reflected back to earth at perpendicular incidence. For $f_i > f_\text{p}$ we need to consider the critical angle of total reflection. The ionosphere reflects the incident wave when the angle of incidence is smaller than the critical angle. However, if the angle is greater than the critical angle, the wave enters the plasma and is diffracted and attenuated accordingly [59]. We observe all these effects on the receiver side as an additional propagation path that overlaps with the groundwave path and affects the resulting accuracy of the estimate.

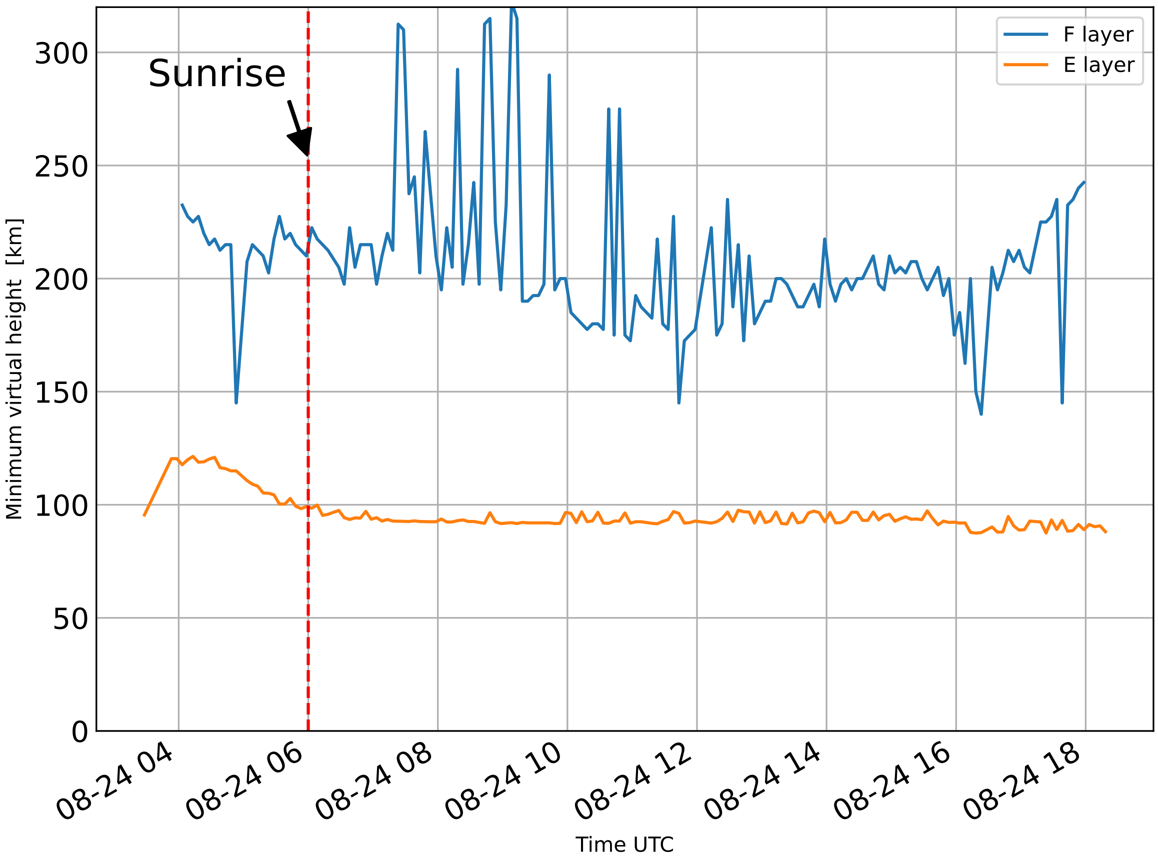

Figure 2.4: Minimum height of E and F layer between 4:00 and 18:00 of the 24th of August in Juliusruh

In the frequency band between 283.5 kHz and 315 kHz, we assume that the E or F layer reflected the wave at around 200 km height. The actuall reflection depends on the angle of the incident and the past solar activity. During daytime, the E and D layer has formed below the F layer due to solar activity. We observe this behaviour in Fig. 2.4, derived from the Global Ionospheric Radio Observatory (GIRO) database [62], for the E and F layer. The plot shows the derived virtual height of the E layer as orange and for the F layer as a blue line for the 24th of August 2020 from 4:00-18:00. The values are derived from the ionosonde station at Julisruhe, on the Baltic coast near the R-Mode testbed, which provides data only for this time frame and not for the D layer. As the sun has a hugh impact on the layer ot the ionosphere, we indicate the sunrise with a red vertical line.

We observe that the minimum height of the E layer is taller during nighttime and starts to decrease about one hour before sunrise. The D layer grows due to the sunlight, and the same applies to the D layer and dampens the reflection path considerably during daytime. This effect occurs before sunrise, as sunrise is defined as the time when the sun crosses the horizon. However, the energy of the sun is already remarkable before this point and influences the ionosphere [59, 14].

For the F layer, we can observe that the layer is present over the whole day but is less stable than the E layer. The minimum height is around 200km, with high volatility between 7:00-13:00. We can see if the skywave path is not damped and reflected at such a layer that the path also becomes unstable and will change accordingly with a phase offset φ_{sky_1} and φ_{sky_2}. The signal model of the CWs is extended to describe the multipath as

$$s_{\mathrm{CW1\ sky}}(t) = A_1 \sin(\omega_1\, t + \varphi_1) + d_{\mathrm{CW1}}\, A_1 \sin(\omega_1\, t + \varphi_1 + \varphi_{\mathrm{sky}_1}), \tag{2.13}$$

$$s_{\mathrm{CW2\ sky}}(t) = A_2 \sin(\omega_2\, t + \varphi_2) + d_{\mathrm{CW2}}\, A_2 \sin(\omega_2\, t + \varphi_2 + \varphi_{\mathrm{sky}_2}). \tag{2.14}$$

Here, d_{CW1} and d_{CW1} represents the damping factor for the multipath, with respect to the ground path. During daytime, the values are near or equal to zero so that the influence of the multipath is not recognizable. It is also important to notice that the skywave is only an issue if we receive the signal at distances larger than 80 km, due to the given geometry. However, to ensure high performance of the R-Mode system at all times, we must also take this effect into account.

2.3. TRANSMITTER CHAIN

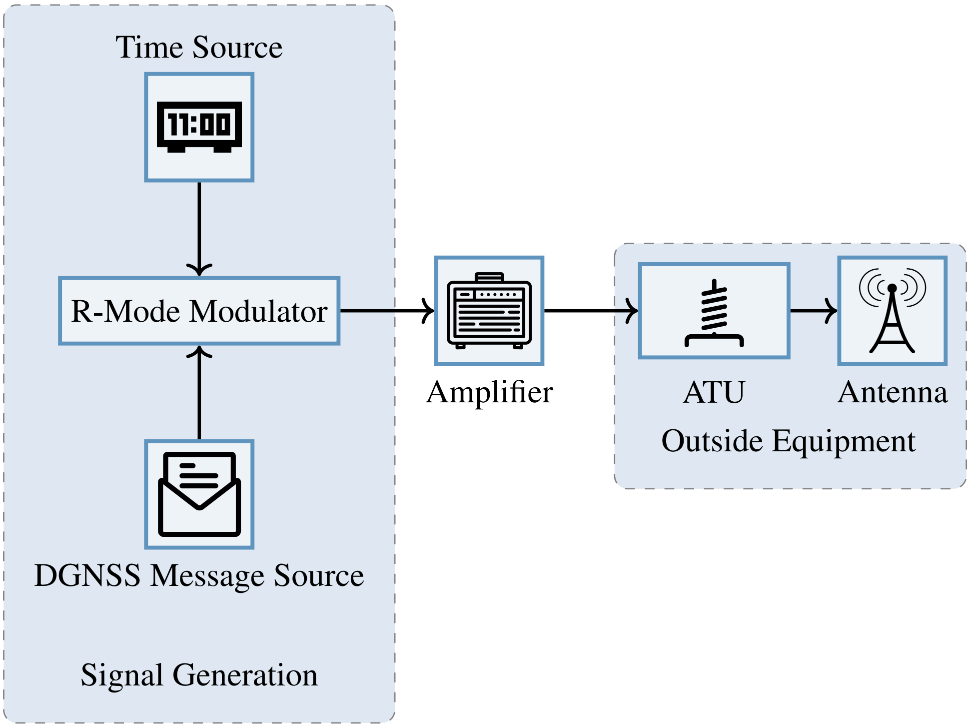

Figure 2.5: Block diagram of R-Mode Transmitter Chain.

The transmission chain is the infrastructure that makes positioning with R-Mode possible in the first place. One of the main features of MF R-Mode is the reuse of existing broadcast infrastructure. Therefore, each chain uses different components, which each influences the phase.

Fig. 2.5 describes the generalised transmitter chain of a station, starting with the signal generation, an amplifier stage to the external devices consisting of the antenna tuning unit (ATU) and the actual antenna. Since these components were not designed to provide synchronized signals for ranging within the system, we must consider each as a source of error for R-Mode, which accumulates to the phase offset $\varphi_{\text{transmitter}}$ according to

$$\varphi_{\text{transmitter}} = \varphi_{\text{signal}} + \varphi_{\text{amplifier}} + \varphi_{\text{antenna}} \tag{2.15}$$

Therefore, we would like to assess the phase offsets φ_{signal} from the signal generation, $\varphi_{\text{amplifier}}$ from the amplifier and φ_{antenna} from the ATU and antenna. Furthermore, we want to show which characteristics are required to achieve the best possible performance for R-Mode.

2.3.1. SIGNAL GENERATION

In this section, we describe how the transmitting station generate the R-Mode signal represented in Section 2.1 . The IALA recommendation describes two possible configurations for generating the R-Mode signals.

The first method retains the existing MSK modulator and adds an external signal generator to produce the added tones. We show in Fig. 2.6 the implementation sum of the modulated signals and the subcarrier to the output signal.

The continuous wave generator needs an external time source to synchronize different transmitters. This is the disadvantage of this method because only the subcarrier is synchronized, but the MSK modulation remains unsynchronized. Therefore, the receiver cannot use the modulated part later to obtain additional distance information. Moreover, the signal is synchronized at the output of the signal generator. Therefore the cable for interconnections and the combiner adds a delay which accumulates to the phase offset φ_{signal}.

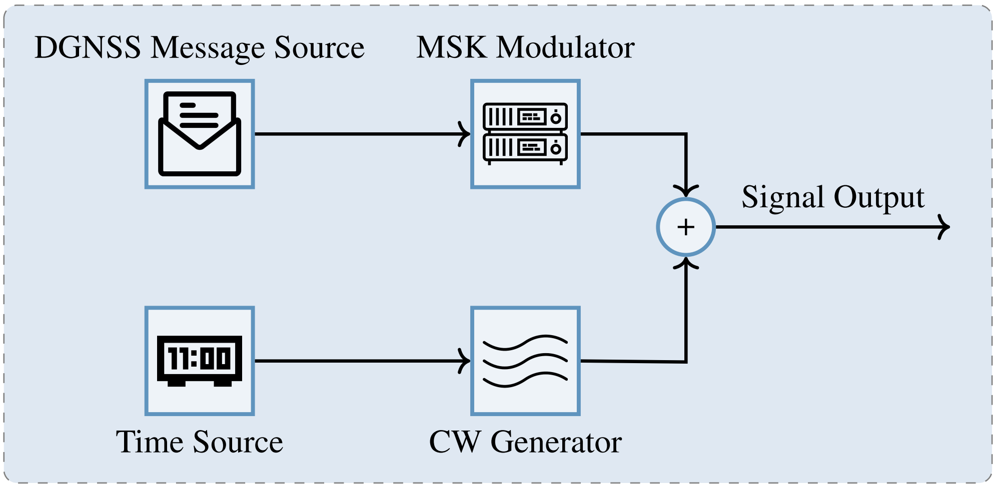

Figure 2.6: R-Mode signal generation with external tone generation.

The second method uses a special R-Mode signal generator that combines the MSK modulator and the generation of the subcarrier in one device. Such an R-Mode generator that produces the complete signal as output requires an external source for time and the DGNSS messages. We show the basic setup in Fig. 2.7. With this configuration, it is also possible to synchronize the MSK signal. Furthermore, this approach can significantly reduce the number of components, as can be seen by comparing the setup in Fig. 2.6 and Fig. 2.7. As a result, the generator saves maintenance fees, the cost of equipping new stations and the introduced phase bias φ_{signal}. However, a mismatch is still present due to connection to the amplifier and production fluctuation, which leads to a leftover φ_{signal}.

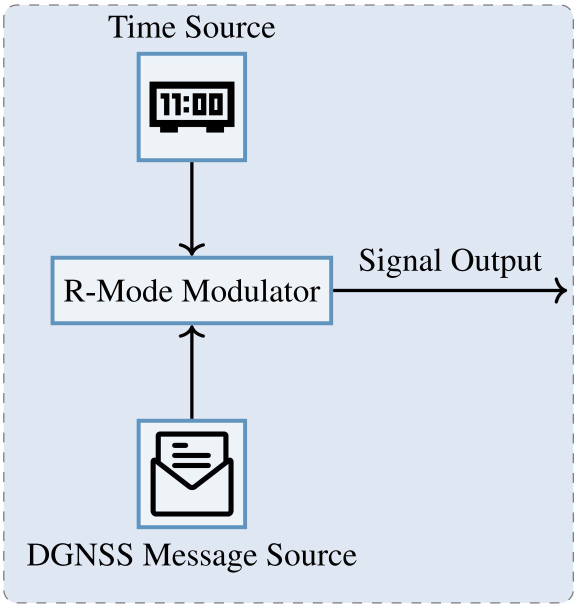

Figure 2.7: R-Mode signal generation with integrated signal generator.

2.3.2. TRANSMITTER

In the following section, we describe the amplifier of the DGNSS transmitting station. As a non-linear component, it influences the phase and thus the estimated propagation time, which we take into account as $\varphi_{\text{amplifier}}$. As with all parts of the transmit chain, many different amplifiers are used. Class A amplifiers are installed in older stations, while class D amplifiers often operate in modern stations. We show the influence of a Class A amplifier on the time delay of the R-Mode signal. Furthermore, we describe why using a Class D amplifier can be problematic.

AMPLIFIER DELAY

We had the opportunity to characterize the Class A amplifier in the transmitting station Koblenz. The specification was to use widely available measurement devices. Instead of using vectorial measurements, we compared the time series of different test signals before and after the amplifier, using only a signal generator and an oscilloscope for this characterization. We published the measurements and results first in [9].

The basic idea is to send a pulsed test signal through the amplifier as a DUT and a direct path to a two-channel oscilloscope. We store the measurement of both channels and correlate the inputs with each other. If we calculate the peak of the correlation in the time series, we get the value of the time delay in the amplifier.

Tab.2.1 summarises the results for different frequencies. The first column lists the frequency of the test signal, while the second column gives the corresponding absolute time delay when using a pulsed signal. The third column shows the time delay calculated according to (2.7) when we use a continuous wave signal. This change to a continuous signal

Table 2.1: Measurement results for different test cases evaluated with correlation

Frequency	Time Delay	Ambiguous	Range Error
302.5 kHz	4.42 µs	1.11 µs	333 m
325.0 kHz	4.40 µs	1.32 µs	396 m
283.5 kHz	4.40 µs	0.87 µs	261 m

introduces ambiguities, as we cannot distinguish between zero-crossings anymore. The last column shows the estimated range error with ambiguities. The time delay seems to remain constant over the frequency range. Due to the different wavelengths, we obtain a difference in the distance measurement considering the offset as $\varphi_{\text{amplifier}}$.

This first characterisation clearly shows how the time delay of the transmitter affects the absolute range measurement and thus also indicates the relevance in the overall system.

CLASS D AMPLIFIER

Most current R-Mode transmitters use a class A amplifier, as described above, which produces no intermodulation products but has low efficiency.

In comparison, modern DGNSS stations use a class D amplifier, also called a switching amplifier; it aims to increase the power efficiency of the amplifier. Class D works by reducing the leakage current in the output stage that occurs in other types of linear amplifiers. To this end, the transistors in class D output stages are always fully open or closed, with no drain current flow, when they are not fully driven.

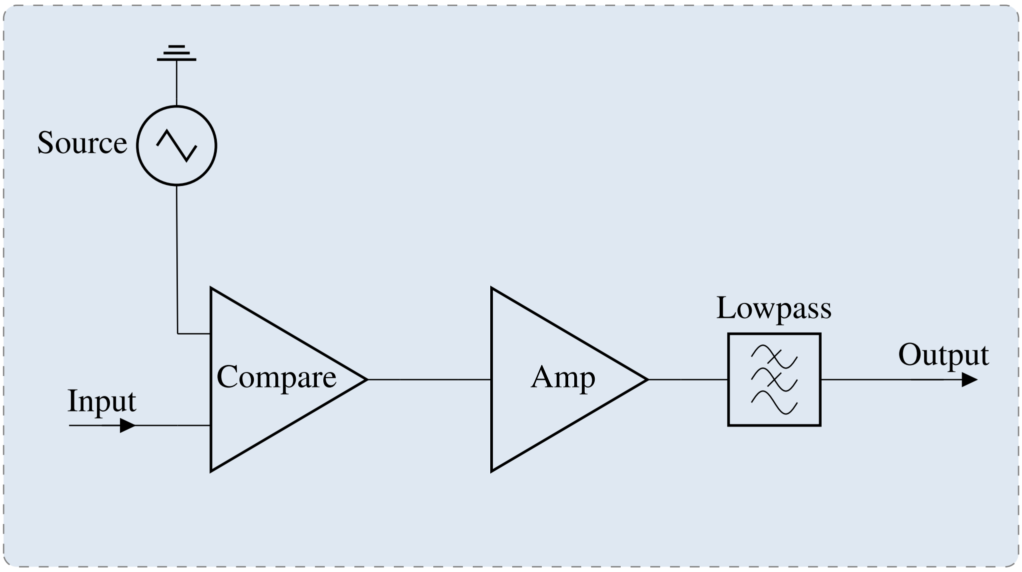

Figure 2.8: Circuit diagram of class D amplifier.

In Fig. 2.8 we present a block diagram of a class D amplifier. In the first step, the input signal compares with a triangular signal. After that, we get a square waved modulation called Pulse Width Modulation (PWM). The amplification stage is driven by this signal, turning the transistor on and off. In the last stage, a low-pass filter demodulates the amplified signal. Other modulation methods for the signal, such as. Pulse Density Modulation (PDM) instead of PWM, are also possible. All essential modulation methods produce a signal with only two states [63].

Because of the harmonics introduced into the modulation, electromagnetic interference is critical for this type of amplifier. In addition, Intermodulation Distortion (IMD) occurs due to non-linearities in the modulation.

We describe the IMD by multiplying two or more signals of different frequencies, resulting in frequencies that represent not only harmonics but also the sum and difference of the original frequencies and their multiples. Thus, if the frequencies of two input signals are given as f_u and f_z, we express the output frequency components $f_{\text{distortion}}$ as

$$f_{\text{distortion}} = m f_u \pm o f_z, \tag{2.16}$$

for m and o as integer values [64].

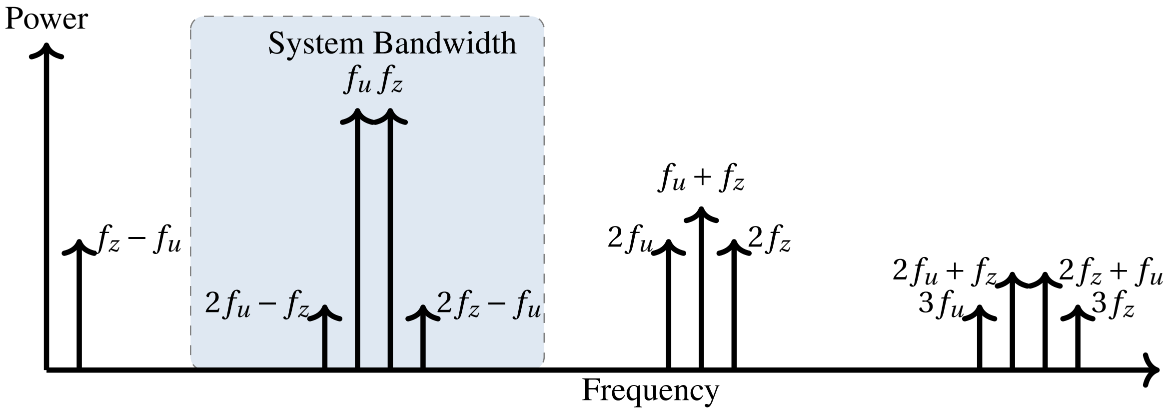

Figure 2.9: Intermodulation peaks class D amplifier.

In Fig. 2.9 we present the IMD products of the first three orders graphically. The different frequencies of the third order are close to the original signals when the frequency difference is small. The blue box shows the transmission bandwidth of the system, which includes the entire transmitter chain discussed in this chapter. This could cause problems with the R-Mode signals, which consist of three signal components because the third-order products are not in the zero-crossing of the modulation. For this case, the signal quality of the MSK signal is no longer guaranteed.

The influence of this intermodulation was tested during the R-Mode trail out in Rozewie. Afterwards, the transmitter was replaced by a class A amplifier for further operation. However, we tested other class D transmitters capable of transmitting the modified signal in the laboratory. Therefore, the selection and description of the transmitter is a crucial task in R-Mode systems, affecting not only the positioning accuracy but also the signal quality of the legacy signal.

2.3.3. ANTENNA

The MF R-Mode system wants to reuse the existing antennas of the DGNSS stations. Historically, the administrations adopted some antennas from older terrestrial navigation systems such as DECCA or marine radio beacons. Therefore, they use a variety of different antenna systems with varying characteristics. The impedance of these antennas leads to different phase offsets φ_{antenna} for the radiated R-Mode signals. We describe the crucial influence of these antennas on the system in this section, as they represent various sources of error. Moreover, they directly affect the radiated power and thus has an impact on the estimation at the receiver side, especially for the beat signal.

This section is structured as follows. First, we will shortly describe a generalized dipole with the equivalent circuit for discrete elements. We published these results first in [7]. Secondly, we will introduce different antennas used in the R-Mode Baltic test-bed.

EQUIVALENT CIRCUIT

All transmitter antennas in the testbed are electrical dipoles. Therefore, we described them as a series circuit of resistance R, inductance L and capacity C. The physical construction of the antenna defines the value of these parameters. We split the resistance into the ohmic loss of the antenna R_{l} and the radiation resistance R_{r}. Here, the index r indicates components that describe the power transmission of the antenna, where the index l marks losses.

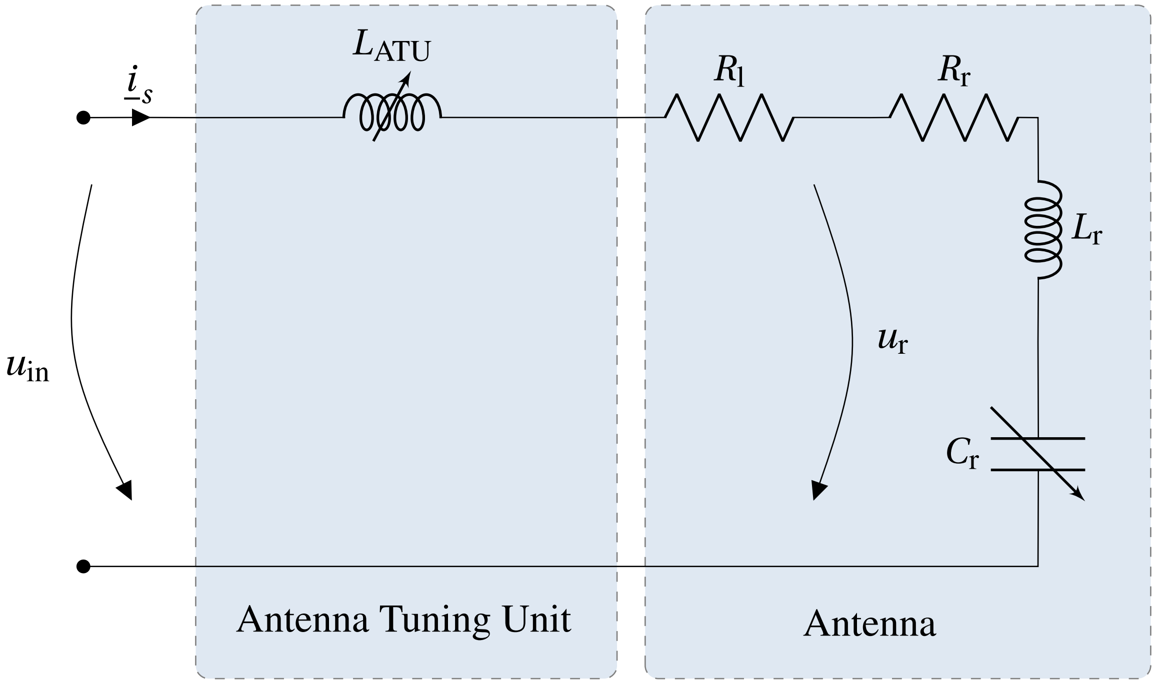

Figure 2.10: Equivalent circuit for dipole antenna .

It is well-known, that the antenna works most effectively when the radiation impedance is purely ohmic. As the impedance depends on the transmission frequency, the optimum case is found by

$$\omega_{\text{res}} = \frac{1}{\sqrt{LC}} \tag{2.17}$$

with ω_{res}, the so-called resonance frequency [65].

To operate the transmitter effectively, ω_{res} should be close to the transmitted frequencies ω_{c}. Our goal is reached by choosing the head capacity of the antenna accordingly and introducing inductance at the feed point.

However, due to environmental conditions, the capacity is changing over time, the inductance has to change accordingly, to maintain the operation point. The so-called ATU control the parameter to optimize the transmitted power. In Fig. 2.10, we show the lumped element equivalent circuit of the dipole antenna, considering the change of the inductance at the feed point L_{ATU} and the capacity C_{r}.

Thereby u_{r} is in phase to the transmitted signal. As we are interested in the phase relation between the input voltage u_{in} and the voltage u_{r} over the radiation parts R_{r}, C_{r} and L_{r}. We need to calculate the complex voltage divider, using the overall impedance Z_{all} as

$$\frac{u_{\text{r}}}{u_{\text{in}}} = \frac{Z_{\text{r}}}{Z_{\text{all}}} \tag{2.18}$$

with

$$Z_{\text{r}} = R_{\text{r}} + j(\omega L_{\text{r}} - \frac{1}{\omega C_{\text{r}}}) \tag{2.19}$$

$$Z_{\text{l}} = R_{\text{l}} + j\omega L_{\text{ATU}} \tag{2.20}$$

$$Z_{\text{all}} = Z_{\text{l}} + Z_{\text{r}}. \tag{2.21}$$

To calculate the phase delay of the antenna, we obtain the phase of the voltage divider. Given that this depends on C_{r} and L_{ATU}, it becomes clear that the system needs to consider the state of the ATU and the environmental influence on C_{r} as dynamic phase offset. Moreover, as we describe the antenna as a resonance circuit, the tuning will change the so-called quality factor Q, which is given by

$$Q = \frac{1}{R_{\text{l}} + R_{\text{r}}} \sqrt{\frac{L_{\text{ATU}} + L_{\text{r}}}{C_{\text{r}}}} \tag{2.22}$$

The factor describes a ratio between the stored and the lost energy [66]. In an antenna, the radiated field store the energy. Therefore, the tuning changes the radiated power of the transmitter and thus also the estimation accuracy, as we describe in more detail in Chapter 3.

For better understanding this effect, we evaluated the voltage divider given in (2.18) for values, that were obtained from real measurements at the antenna in Zeven, Germany. The system is described by the values $R_\mathrm{r} = 10\,\Omega$ $R_\mathrm{l} = 0.1\,\Omega$, and $L_\mathrm{r} = 1\,\mathrm{mH}$. The capacity and ATU are initialized with the values $C_\mathrm{r} = 240\,\mathrm{pF}$ and $L_\mathrm{ATU} = 0.172\,69\,\mathrm{mH}$. In the next step we detune the system by choosing $C_\mathrm{r} = 220\,\mathrm{pF}$, we then calculate change of inductance ΔL to restore the initial resonance frequency, for the ATU by

$$\Delta L = -\frac{\Delta C (L_\mathrm{ATU} + L_\mathrm{r})}{C_\mathrm{r}} \tag{2.23}$$

with the capacity change ΔC [65].

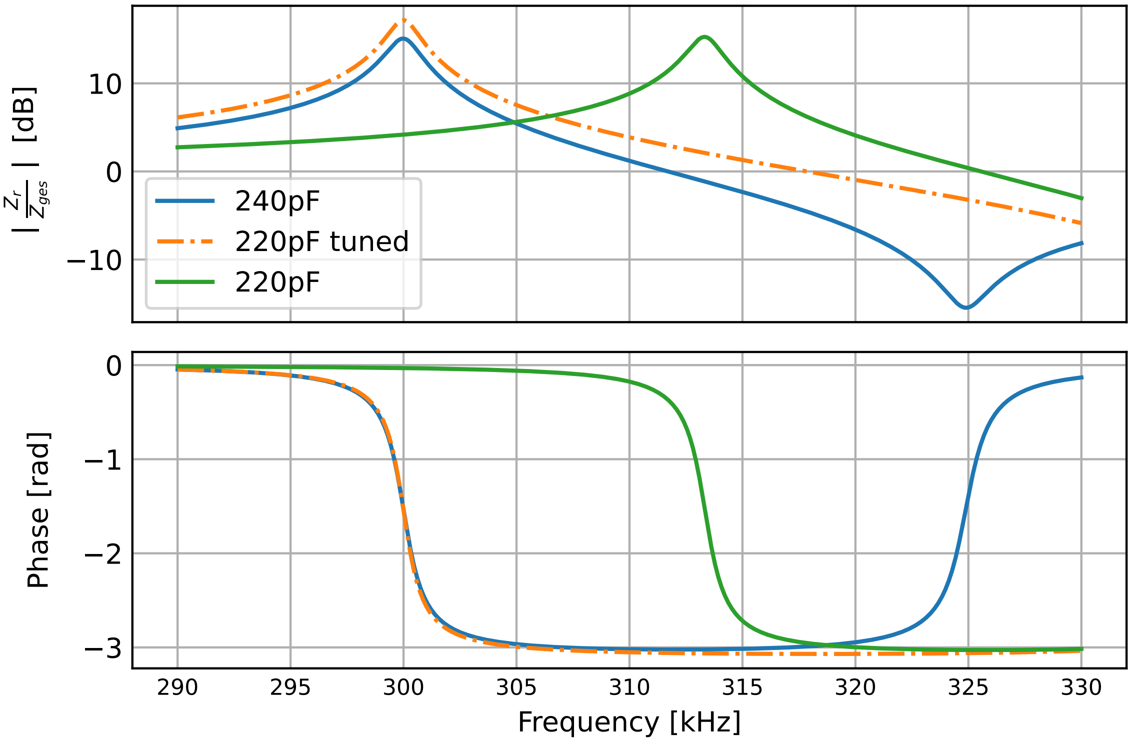

Figure 2.11: Frequency response locus.

In Fig. 2.11 we have calculated the frequency response curve with (2.18) for the previously given values. The upper graphs show the amplitudes, whereas the lower plot presents the phase offset between the voltages. The initial values result in the continuous blue line. It is clear that we have the resonance frequency at 300 kHz with the amplitude maximum around 15 dB for a Q-factor of 218.8 and a 3 dB bandwidth of 2.4 kHz. Around the resonance frequency, we see a rapid change of the phase. At 300 kHz the phase dropped by $\pi/2$. The overall phase shift is symmetric to this point up to a value of π. At about 320 kHz the phase starts to change back to zero. Accordingly, the function gets to its minima at 325 kHz.

If we modify the capacitance to 220 pF the new resonant frequency is 313.341 kHz. The phase change remains the same at the new resonant frequency, although the amplitude changes slightly to 15.2 dB as the Q-factor increases to 228.6. The resulting bandwidth also changes slightly to 2.37 kHz.

In the next step we use (2.23) to get the new value $L_{\mathrm{ATU}} = 0.2791\,\mathrm{mH}$. In Fig. 2.11 the frequency response is shown by the orange dashed line. It can be clearly seen, that we obtain the resonance frequency of 300 kHz again. The phase shows only slight differences near the resonance frequency. Due to the changed value, the minima of this response are not visible in the graph, so the phase after the resonance frequency in blue begins to differ from the original phase representation. Due to the higher Q-factor of 238.8, we have an increased amplitude of 17.2 dB, leading to a smaller 3 dB bandwidth of 1545.9 Hz. The reactance of the antenna describes this effect. Increasing the head capacitance is also called electrical extension in the literature. Since the antenna now behaves like a longer dipole, it has a higher efficiency [59].

With this equivalent circuit, we could describe the tuning process for the antenna with the ATU, and observe that the offset φ_{antenna} is different for the continuous waves but symmetrical for $\pi/2$. With a dynamic capacitance change, the phase response shows only minor differences as soon as we reach the resonance frequency again, neglecting the transient width. However, the ATU does not always hit the perfect resonant frequency. Therefore, we expect different phase shifts for each continuous wave, which change with time. Also, the amplitude of the tones will not be equal if we have a slight detuning of the system. These effects are dependent on the antenna design, as the bandwidth of the antennas used has a wide range.

STATION ANTENNA

We have previously shown theoretically that the electrical properties of the antenna have a strong influence on the R-Mode phase estimation. Decisive for the description is the size of the head capacity, as we have already shown. We had the opportunity to visit several transmitters for this work. In this part, we would like to give an overview of the main antenna types used in the R-Mode Baltic testbed, to motivate that an individual correction factor φ_{antenna} is necessary for each installation.

The so-called whip antenna is one of the most common antenna types. This type consists of a flexible fibreglass mast that can move in the wind. The wire led to the top end, essentially determining the inductance L_{r} of the equivalent circuit in Fig. 2.10. At the top of the mast is the head capacitance C_{r} [67]. Fig. 2.12a and Fig. 2.12b show two different whip antennas. The main difference is the head capacity, as we point out in the figures. While the antenna in Fig. 2.12b has only a small round cage made of four wires, the antenna in Fig. 2.12a has enlarged this to a square cage with several wires.

Other antennas use different designs to achieve larger capacities and consequently a wider bandwidth and higher efficiency. The old DECCA system used the so-called T-antennas. With this type of antenna, wires are stretched horizontally between two masts that form the head capacity. The actual antenna is a wire that runs between the masts to the ground, where the amplifier feeds the antenna. This kind of antenna uses a large area to build up capacity, which increases the bandwidth and efficiency [59]. Fig. 2.13a shows the T-shaped antenna in Holmsjö, Sweden, which now transmit MF R-Mode signals.

A third type uses a support mast as the antenna, insulated from the earth. The mast forms the antenna, while insulated guy wires form the capacitance. Again, compared to the

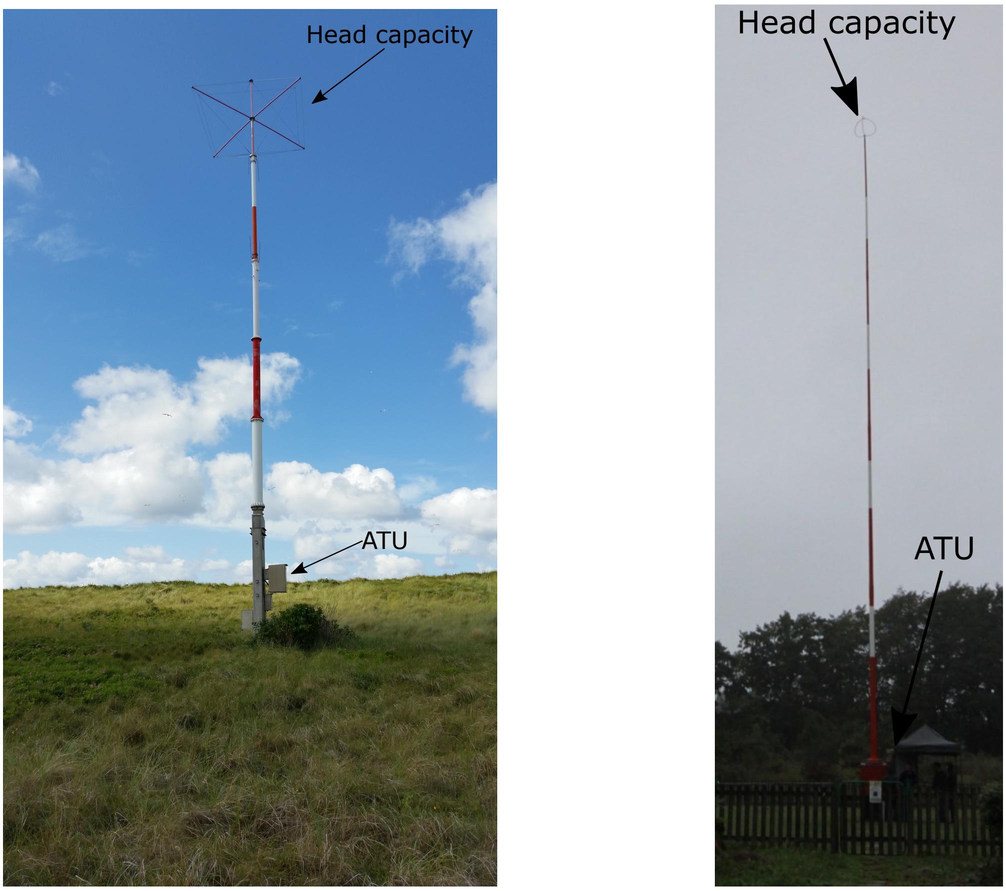

(a) (b)

Figure 2.12: Whipe type antennas (a)DGNSS antenna on Heligoland, Germany, (b) DGNSS antenna in Rozewie, Poland.

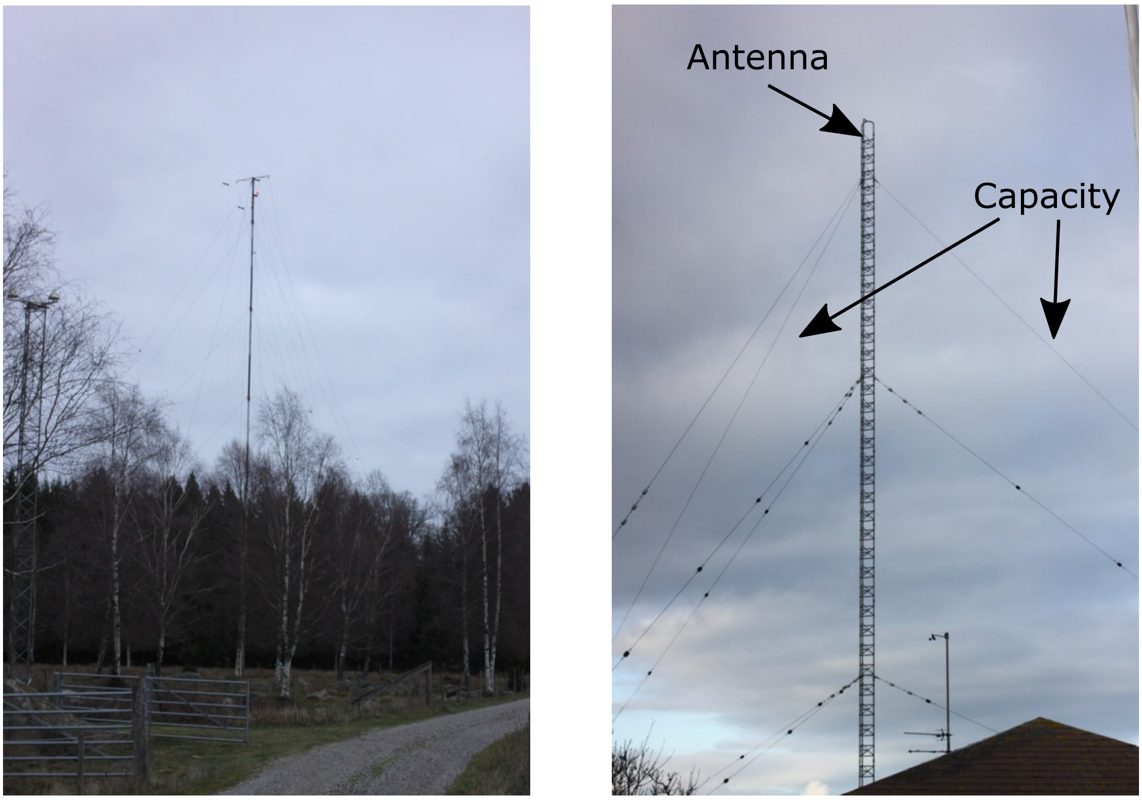

(a) (b)

Figure 2.13: Mast and T-shaped antennas (a) DGNSS antenna in Holmsjö, Sweden, (b) DGNSS antenna in Hammerodde, Denmark.

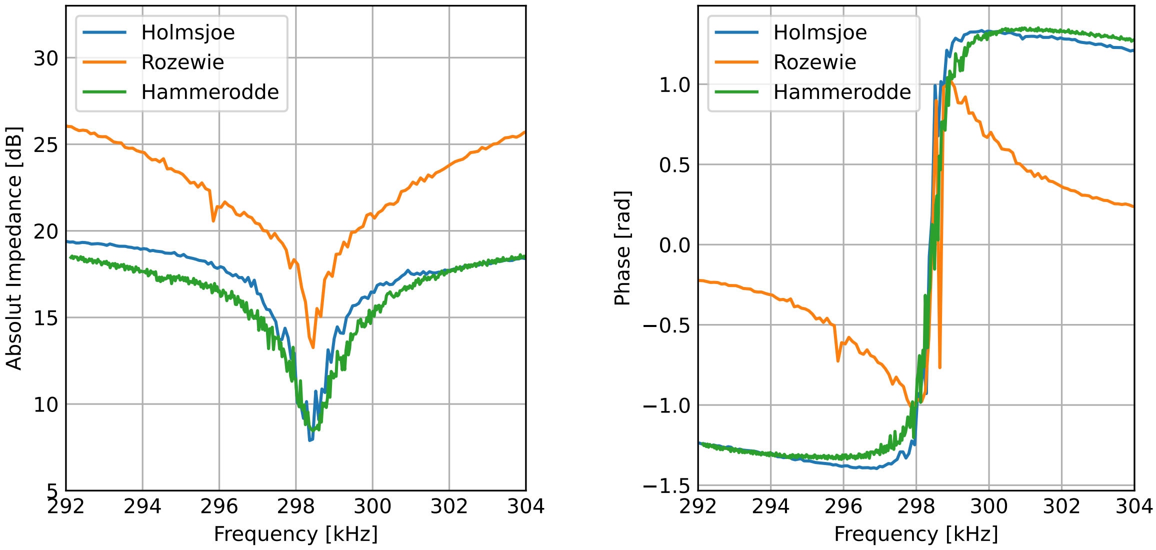

(a) Impedance response of different antennas.

(b) Phase response of different antennas.

Figure 2.14: Results of LRC measurement at the antenna at Holmsjö, Rozewie and Hammerodde.

whip antenna, higher bandwidth and effectiveness is achieved. Fig 2.13b show the antenna at Hammerodde at the island Bornholm at the centre of the testbed.

During the inspection of the different antenna sides, the Federal Water and Shipping Administration (WSV) performed measurements at the feed point of the antenna with an LRC meter. It is possible to calculate the impedance concerning frequency based on the method we presented in Section 2.3.3. Fig 2.14 illustrate the results for the stations Holmsjö, Rozewie and Hammerodde. To compare the different results, we have shifted the measurements to the carrier frequency of Rozewie at 298.5 kHz. The resulting graphic draw the absolute value of impedance in the sub-figure 2.14a, where we see that the whip antenna at Rozewie has a high overall impedance with a relatively small 3 dB bandwidth, at Holmsjö and Hammerodde, the impedance is lower. The lattice mast antenna at Hammerodde is slightly wider than the T-shaped antenna at Holmsjö. A plot describes the phase results of the antennas in sub-figure 2.14b. Here, we observe that from the lower CW all phases start to fall off before rising steeply around the carrier frequency. After the measurement settles down, the value begins to fall off slowly. The slope at Rozewie is comparatively steeper before and after the carrier frequency than at the other stations. We also observed a small phase jump at the carrier frequency for the whip antenna. These results are in line with our theoretical considerations, so we have to take into account the different behaviour of the antenna to allow positioning and ranging, as the phase response is different for all three antennas at the supporting CWs, leading to different phase bias φ_{antenna}. The receiver considers this effect only as a constant offset φ_{antenna} for each antenna in a first approximation.

2.4. ERROR MITIGATION

The operational medium-frequency R-Mode system need to take all the sources of error above into account for optimum performance. We divide the sources of error into four groups to derive mitigation techniques. The categories describe whether the error is constant or fluctuates over time and where the error occurs, at the transmitter or in the propagation path.

The mentioned errors sorted in Tab. 2.2 into the different categories. In the last part of this chapter, we want to present our ideas on how a complete system can mitigate the different groups of errors.

Table 2.2: Error Matrix of the MF R-Mode system

	Time varying	Time constant
Propagation	skywave, weather	groundwave
Transmitter	antenna matching	amplifier delay, cable delay

The most difficult errors to describe came from the time-varying sources. To compensate, we propose a monitor network from which the receiver obtain corrections. The MSK modulator insert a navigation message for R-Mode into the RTCM data-stream to provide the information.

For the transmitter chain, we need near-field observation to measure the error of the antenna, as the monitor neglected the propagation effect in the near field. In addition, the near-field receiver receives other stations to enable time synchronization in the system. The challenge here is to develop a device that can handle the strong input signal from the local station and the weak signals.

Since we are developing a MF R-Mode receiver in the further course of this thesis, we would like to keep in mind not only its use as a mobile receiver for the end-user but also near field and area monitoring. Therefore, we consider both dynamic measurements and static measurements in the development and real-world results in Chapter 6.

3

LOWER BOUND OF THE R-MODE SYSTEM

In this chapter, we will develop several lower CRBs for different use cases of the R-Mode system. In general, the bound describes the best performance for an unbiased maximum likelihood estimator, but it can also be used as a general tight performance bound. In the case of a single tone, the bound is well described by Rife [68, 69] and Kay [70]. Swazek applied the single CW bound to the MF R-Mode system [39], not considering the complete signal. We will extend this work to the beat estimation problem and the influence of the MSK signal. Moreover, we will consider a dynamic scenario and introduce various parameter transformations used in this work. The CRBs form the basis for estimating the expected performance of the system. We use the results in Chapter 4 to evaluate the performance of the proposed estimators and in Chapter 7 to propose modifications to the signal. In addition, the limits give an overview of the coverage of the MF R-Mode system, which we describe in the last section of this chapter.

3.1. LOWER BOUND FOR PHASE ESTIMATION

Here we present, in abbreviated form, the calculation of the lower bound for the phase estimate of the beat frequency from a sample set, which we first presented in [3]. For this purpose, the derivatives of the unknown parameters constructed the Fisher Information Matrix (FIM), where the diagonal elements of the inverse matrix equal the bounds of the parameters [68, 70]. We describe the individual calculation steps in detail in the appendix 8. We are mainly interested in whether the estimates of the two individual tones are statistically independent; in this case, the sum of the bounds for the single phases forms the lower bound of the beat frequency. We will show that this is not always the case due to MSK modulation with a finite observation time. Furthermore, as a by-product, we provide the lower bound of the estimate of a single-tone phase, which we use to compare the obtained results with the literature. We presented the described work first in our paper "Estimation Bounds of Beat Signal in the R-Mode Localization System" [3].

3.1.1. LOWER BOUND FOR BEAT SIGNAL

As a first step in obtaining the CRB, we need a signal model concerning a discrete-time step t_n. Here the index n is in the range of $0 \leq n < N$, where N is the total number of samples and the time difference between each step is given by Δt. Two added tones form the model as

$$\begin{aligned} s_{\text{add}}(t_n, \boldsymbol{\theta}) = & A_1 \sin(\omega_1 t_n + \varphi_1) \\ & + A_2 \sin(\omega_2 t_n + \varphi_1 + \varphi_{\text{beat}}). \end{aligned} \tag{3.1}$$

The individual tones are described by the discrete angular frequencies ω_1, ω_2 and the independent amplitudes A_1 and A_2. The first tone has a phase shift φ_1. However, for the beat phase φ_{beat} we are interested in the phase difference of the two tones, so the phase for the second tone is expressed as $\varphi_1 + \varphi_{\text{beat}}$. We obtain the parameter vector

$$\boldsymbol{\theta} = [\varphi_1, A_1, A_2, \varphi_{\text{beat}}]^\top. \tag{3.2}$$

We choose the order within the vector for a convenient representation in the inverse FIM. The entries of the FIM are calculated, for any signal model $s(t_n, \boldsymbol{\theta})$ according to

$$\boldsymbol{J}(\boldsymbol{\theta})_{ij} = \frac{1}{\sigma^2} \sum_{n=0}^{N-1} \frac{\partial s(t_n, \boldsymbol{\theta})}{\partial \boldsymbol{\theta}_i} \frac{\partial s(t_n, \boldsymbol{\theta})}{\partial \boldsymbol{\theta}_j}. \tag{3.3}$$

Here, the index i denotes the column of the matrix to which an entry in the parameter vector $\boldsymbol{\theta}$ corresponds. One can thus denote the parameter for which obtains the derivative of the signal model with $\boldsymbol{\theta}_i$. However, it would also be possible to express the parameter by the index j, which represents the row of the matrix. Moreover, we also need to consider the Additive White Gaussian Noise (AWGN) power σ^2. The necessary derivatives for the formation of the FIM are given by

$$\begin{aligned} \frac{\partial s_{\text{add}}(t_n, \boldsymbol{\theta})}{\partial \varphi_1} = & A_1 \cos(\omega_1 t_n + \varphi_1) \qquad (3.4) \\ & + A_2 \cos(\omega_2 t_n + \varphi_1 + \varphi_{\text{beat}}), \\ \frac{\partial s_{\text{add}}(t_n, \boldsymbol{\theta})}{\partial \varphi_{\text{beat}}} = & A_2 \cos(\omega_2 t_n + \varphi_1 + \varphi_{\text{beat}}), \qquad (3.5) \\ \frac{\partial s_{\text{add}}(t_n, \boldsymbol{\theta})}{\partial A_1} = & \sin(\omega_1 t_n + \varphi_1), \qquad (3.6) \\ \frac{\partial s_{\text{add}}(t_n, \boldsymbol{\theta})}{\partial A_2} = & \sin(\omega_2 t_n + \varphi_1 + \varphi_{\text{beat}}). \qquad (3.7) \end{aligned}$$

The appendix 8 present the calculation of the entries of the FIM in more detail. In the computation, we have to sum over the trigonometric functions. To do so, we assume that the sampling set must always sample an integer number of wavelengths. For the case of two tones and an arbitrary phase offset ϕ, this results in

$$\frac{1}{N} \sum_{n=0}^{N-1} \cos(\omega_i t_n + \phi) = 0, \tag{3.8}$$

$$\frac{1}{N}\sum_{n=0}^{N-1}\sin(\omega_i\, t_n+\phi)=0. \tag{3.9}$$

Take the results from (3.8) and (3.9), we yield the FIM as

$$\boldsymbol{J}_{\text{add}}(\boldsymbol{\theta})=\frac{N}{2\sigma^2}\begin{pmatrix} A_1^2+A_2^2 & 0 & 0 & A_2^2\\ 0 & 1 & 0 & 0\\ 0 & 0 & 1 & 0\\ A_2^2 & 0 & 0 & A_2^2 \end{pmatrix} \tag{3.10}$$

and the corresponding inverse

$$\boldsymbol{J}_{\text{add}}^{-1}(\boldsymbol{\theta})=\frac{2\sigma^2}{N}\begin{pmatrix} \frac{1}{A_1^2} & 0 & 0 & -\frac{1}{A_1^2}\\ 0 & 1 & 0 & 0\\ 0 & 0 & 1 & 0\\ -\frac{1}{A_1^2} & 0 & 0 & \frac{1}{A_1^2}+\frac{1}{A_2^2} \end{pmatrix}. \tag{3.11}$$

Evaluating the diagonal, with respect to the corresponding parameter, we get the lower bounds as

$$\operatorname{var}(\varphi_1)\geq\frac{2\sigma^2}{NA_1^2}, \tag{3.12}$$

$$\operatorname{var}(\varphi_{\text{beat}})\geq\frac{2\sigma^2}{N}\left(\frac{1}{A_1^2}+\frac{1}{A_2^2}\right), \tag{3.13}$$

$$\operatorname{var}(A_1)\geq\frac{2\sigma^2}{N}, \tag{3.14}$$

$$\operatorname{var}(A_2)\geq\frac{2\sigma^2}{N}. \tag{3.15}$$

(3.12) provide the lower bound for the phase of the single tone, which corresponds to the values given in the literature if a real-valued model is assumed. For a complex-valued model, the result deviates by a factor of 1/2 [69].

The result for the beat phase, given in (3.13), clearly shows that the estimation of the two tones is statistically independent since (3.13) is formed from the sum of two variances determined by (3.12) for different amplitudes.

Based on these results, we can modify the bound to express it by different parameters. The formulation helps us to improve the transmitted signal and the algorithm used later in this work. In the first step, we express the total number of samples as $N = T_{\text{obs}}\, f_{\text{sample}}$, where f_{sample} is the sampling rate and T_{obs} is the observation time. Moreover, according to [70] , the Signal-to-Noise Ratio (SNR) with respect to any amplitude A is defined as $\text{SNR}_A=\frac{A}{\sigma^2}$. Therefore, we can rewrite the bounds for the phase as

$$\mathrm{var}(\varphi_1) \geq \frac{2}{T_{\mathrm{obs}}\, f_{\mathrm{sample}}\, \mathrm{SNR}_{A_1}}, \tag{3.16}$$

$$\mathrm{var}(\varphi_{\mathrm{beat}}) \geq \frac{2}{T_{\mathrm{obs}}\, f_{\mathrm{sample}}} \left(\frac{1}{\mathrm{SNR}_{A_1}} + \frac{1}{\mathrm{SNR}_{A_2}} \right). \tag{3.17}$$

We moreover replace the sampling rate by the bandwidth b, according to the Nyquist theorem $b = \frac{f_{\mathrm{sample}}}{2}$. Therefore, we obtain the bounds with respect to the bandwidth

$$\mathrm{var}(\varphi_1) \geq \frac{1}{T_{\mathrm{obs}}\, b\, \mathrm{SNR}_{A_1}}, \tag{3.18}$$

$$\mathrm{var}(\varphi_{\mathrm{beat}}) \geq \frac{1}{T_{\mathrm{obs}}\, b} \left(\frac{1}{\mathrm{SNR}_{A_1}} + \frac{1}{\mathrm{SNR}_{A_2}} \right). \tag{3.19}$$

So far, we have only considered the variance of the estimated phase. However, for the R-Mode system, we are interested in the pseudo range $r_{\mathrm{p},i}$. The derivation of the pseudo ranges is shown in Chapter 2 and here given as $g(\varphi_i)$, combining (2.7) and (2.8). To apply this to the variance, we use the following transformation [70]

$$var\{r_{\mathrm{p},i}\} = var\{\varphi_i\} * \left(\frac{\delta g(\varphi_i)}{\delta \varphi_i} \right)^2 \tag{3.20}$$

Applying the transform, we get the variance

$$var\{r_{\mathrm{p},i}\} \geq \frac{c_0^2}{\mathrm{SNR}_{A_1}\, {\omega_i}^2\, T_{\mathrm{obs}}\, b} \tag{3.21}$$

The result describes the estimation bound of a single tone. Since we only use the beat frequency to resolve ambiguities, the single CW bound corresponds to the overall performance of the system. However, the range estimate r_{beat} from the beat frequency ω_{beat} is also of interest to check in which range the R-Mode system is fully functional. We use 3.20 again and obtain the bound.

$$\mathrm{var}(r_{\mathrm{beat}}) \geq \frac{c_0^2}{{\omega_{\mathrm{beat}}}^2\, T_{\mathrm{obs}}\, b} \left(\frac{1}{\mathrm{SNR}_{A_1}} + \frac{1}{\mathrm{SNR}_{A_2}} \right). \tag{3.22}$$

We can characterise the whole system on different levels with the described bounds, assuming the estimation of the continuous waves is statistically independent.

3.1.2. PHASE DIFFERENCE IN A DYNAMIC SCENARIO

So far, we have considered the lower bound for the case where the phase offset remains constant, which is correct for static transmitters and receivers, corresponding to a first approximation for slow objects. Now we want to extend the model (3.1) for a dynamic case, with a constant unknown radial velocity v, normalised to the speed of light c_0. We define the time-dependent phase shift as

$$\varphi_{\text{velocity}} = \omega_i \, t_n \, \frac{v}{c_0}. \tag{3.23}$$

This results in the signal model

$$\begin{aligned} s_{\text{dynamic}}(n, \boldsymbol{\theta}) = & A_1 \sin(\omega_1 \, t_n + \omega_1 \, t_n \, \frac{v}{c_0} + \varphi_1) \\ & + A_2 \sin(\omega_2 \, t_n + \omega_2 \, t_n \, \frac{v}{c_0} + \varphi_1 + \varphi_{\text{beat}}). \end{aligned} \tag{3.24}$$

We must note that the phase shifts φ_1 and φ_{beat} represent the phase shift at the beginning of the observation time. The change in phase shift is represented by the terms $\omega_1 \, t_n \, \frac{v}{c_0}$ and $\omega_2 \, t_n \, \frac{v}{c_0}$. We define the resulting parameter vector as

$$\boldsymbol{\theta} = [\varphi_1, \varphi_{\text{beat}}, v, A_1, A_2,]^{\top}. \tag{3.25}$$

The partial derivatives result

$$\begin{aligned} \frac{\partial s_{\text{dynamic}}(t_n, \boldsymbol{\theta})}{\partial \varphi_1} &= A_1 \cos\left(t_n \, \omega_1 \, (\frac{v}{c_0} + 1) + \varphi_1 \right) \\ & \quad + A_2 \cos\left(t_n \, \omega_2 \, (\frac{v}{c_0} + 1) + \varphi_1 + \varphi_{\text{beat}} \right), \end{aligned} \tag{3.26}$$

$$\frac{\partial s_{\text{dynamic}}(t_n, \boldsymbol{\theta})}{\partial \varphi_{\text{beat}}} = A_2 \cos\left(t_n \, (\omega_1 \, \frac{v}{c_0} + \omega_2 \, \frac{v}{c_0} + \omega_2) + \varphi_1 + \varphi_{\text{beat}} \right), \tag{3.27}$$

$$\begin{aligned} \frac{\partial s_{\text{dynamic}}(t_n, \boldsymbol{\theta})}{\partial v} &= A_1 \, \frac{\omega_1 \, t_n}{c_0} \cos\left(t_n \, \omega_1 \, (\frac{v}{c_0} + 1) + \varphi_1 \right) \\ & \quad + A_2 \, \frac{\omega_2 \, t_n}{c_0} \cos\left(t_n \, \omega_2 \, (\frac{v}{c_0} + 1) + \varphi_1 + \varphi_{\text{beat}} \right), \end{aligned} \tag{3.28}$$

$$\frac{\partial s_{\text{dynamic}}(t_n, \boldsymbol{\theta})}{\partial A_1} = \sin\left(t_n \, \omega_1 \, (\frac{v}{c_0} + 1) + \varphi_1 \right), \tag{3.29}$$

$$\frac{\partial s_{\text{dynamic}}(t_n, \boldsymbol{\theta})}{\partial A_2} = \sin\left(t_n \, \omega_2 \, (\frac{v}{c_0} + 1) + \varphi_1 + \varphi_{\text{beat}} \right). \tag{3.30}$$

We are again interested in the sum over the tones with angular frequency ω, taking $\frac{\omega \, v}{c_0}$ as Doppler frequency and the simplified case that $\frac{\omega \, v}{c_0}$ is an integer we can assume

$$\sum_{\text{n=0}}^{\text{N}-1} n \, \Delta t \cos(t_n \, \omega \, (\frac{v}{c_0} + 1) + \varphi_i) \approx 0. \tag{3.31}$$

Since we suppose that the shifted frequency is an integer frequency, (3.31) is a sum over a full wavelength. We are aware that in practice, the assumption of the sum can only hold at an unrealistic speed. The FIM simplified in this way is given as

$$\boldsymbol{J}_{\text{dynamic}}(\boldsymbol{\theta}) = \frac{N}{2 \, \sigma^2} \begin{pmatrix} \boldsymbol{J}_{3\times 3} & \boldsymbol{0}_{3\times 2} \\ \boldsymbol{0}_{2\times 3} & \boldsymbol{I}_{2\times 2} \end{pmatrix}. \tag{3.32}$$

To simplify, $\mathbf{0}_{2\times3}$ and $\mathbf{0}_{3\times2}$ represent 2×3 and 3×2 null matrices respectively, while $\boldsymbol{I}_{2\times2}$ is the 2×2 unit matrix. Since the lower bounds now depend on more correlated parameters, the calculation of the inverse FIM is beyond the scope of this thesis and yields little insight. The complete inverse is given in Appendix 8. For our investigation, it is important that if we consider v as known, we can delete the third row and the third column of the FIM (3.32). As a result, we get a FIM equal to (3.11), and thus the same resulting bounds as in (3.12) to (3.15). Therefore, if our estimation can compensate for the motion, the receiver possibly achieves the same accuracy.

$$\boldsymbol{J}_{3\times3} = \begin{bmatrix} A_1^2 + A_2^2 & A_2^2 & \frac{(N-1)\left(A_1^2\omega_1 + A_2^2\omega_2\right)\Delta t}{2} \\ A_2^2 & A_2^2 & \frac{A_2^2\omega_2(N-1)\Delta t}{2} \\ \frac{(N-1)\left(A_1^2\omega_1 + A_2^2\omega_2\right)\Delta t}{2} & \frac{A_2^2\omega_2(N-1)\Delta t}{2} & \frac{(N-1)(2N-1)\left(A_1^2\omega_1 + A_2^2\omega_2\right)\Delta t^2}{6} \end{bmatrix} \tag{3.33}$$

3.1.3. LOWER BOUND FOR PHASE ESTIMATION NEXT TO MSK MODULATED SIGNAL

In the previous sections, the signal model only includes two independent tones. In the R-Mode system, however, we must estimate the phase of these two tones next to the MSK-modulated legacy signal. To adequately describe the beat frequencies, we need to represent (2.6) in discrete time. To do this, we extend (3.1) and define the discrete-time modulation as

$$s_{\mathrm{MSK}}(t_n) = A_{\mathrm{MSK}} \sin(\omega_c t_n + b_\tau[n]\frac{\pi t_n}{2T_{\mathrm{bit}}} + \bar{\varphi}_\tau[n]), \tag{3.34}$$

where ω_c is the angular frequency of the modulated signal, T_{bit} is the bit duration and $\bar{\varphi}_\tau[n]$ is the memory of the discrete MSK combined with the phase offset from the modulated part. $b_\tau[n]$ is a vector containing the bit sequence as a sampled square wave signal. We sample the bit sequence concerning the time step t_n and discretise the vector $\bar{\varphi}_\tau[n]$ in a similar way to sum all components.

We include the MSK component $s_{\mathrm{MSK}}(t_n)$ in our signal model as

$$\begin{aligned} s_{\mathrm{signal}}(t_n,\boldsymbol{\theta}) =& A_1 \sin(\omega_1 t_n + \varphi_1) \\ &+ A_{\mathrm{MSK}} \sin(\omega_c t_n + b_\tau[n]\frac{\pi t_n}{2T_{\mathrm{bit}}} + \varphi_1 + \bar{\varphi}_\tau[n]) \\ &+ A_2 \sin(\omega_2 t_n + \varphi_1 + \varphi_{\mathrm{beat}}), \end{aligned} \tag{3.35}$$

where A_{MSK} is the amplitude of the modulated signal part. Moreover, the phase difference between signals with frequency ω_1 and ω_c can be described as part of $\bar{\varphi}_\tau[n]$. In this case, we extend the parameter vector to

$$s_{\mathrm{signal}}(t_n,\boldsymbol{\theta}) \text{ with } \boldsymbol{\theta} = [\varphi_1, \bar{\varphi}_\tau[n], \varphi_{\mathrm{beat}}, b_\tau[n], A_1, A_{\mathrm{MSK}}, A_2]^\top. \tag{3.36}$$

Again we need to calculate the partial derivatives

$$\begin{aligned}\frac{\partial s_{\text{signal}}(t_n,\boldsymbol{\theta})}{\partial \varphi_1} &= A_1 \cos(\omega_1\, t_n + \varphi_1) \\ &\quad + A_{\text{MSK}} \cos(\omega_{\text{c}}\, t_n + b_\tau[n]\frac{\pi\, t_n}{2\, T_{\text{bit}}} + \varphi_1 + \bar{\varphi}_\tau[n]) \\ &\quad + A_2 \cos(\omega_2\, t_n + \varphi_1 + \varphi_{\text{beat}}),\end{aligned} \tag{3.37}$$

$$\frac{\partial s_{\text{signal}}(t_n,\boldsymbol{\theta})}{\partial \bar{\varphi}_\tau[n]} = A_{\text{MSK}} \cos(\omega_{\text{c}}\, t_n + b_\tau[n]\frac{\pi\, t_n}{2\, T_{\text{bit}}} + \varphi_1 + \bar{\varphi}_\tau[n]), \tag{3.38}$$

$$\frac{\partial s_{\text{signal}}(t_n,\boldsymbol{\theta})}{\partial \varphi_{\text{beat}}} = A_2 \cos(\omega_2\, t_n + \varphi_1 + \varphi_{\text{beat}}), \tag{3.39}$$

$$\frac{\partial s_{\text{signal}}(t_n,\boldsymbol{\theta})}{\partial b_\tau[n]} = A_{\text{MSK}} \frac{\pi\, t_n}{2\, T_{\text{bit}}} \cos(\omega_{\text{c}}\, t_n + b_\tau[n]\frac{\pi\, t_n}{2\, T_{\text{bit}}} + \varphi_1 + \bar{\varphi}_\tau[n]), \tag{3.40}$$

$$\frac{\partial s_{\text{signal}(t_n,\boldsymbol{\theta})}}{\partial A_1} = \sin(\omega_1\, t_n + \varphi_1), \tag{3.41}$$

$$\frac{\partial s_{\text{signal}}(t_n,\boldsymbol{\theta})}{\partial A_{\text{MSK}}} = \sin(\omega_{\text{c}}\, t_n + b_\tau[n]\frac{\pi\, t_n}{2\, T_{\text{bit}}} + \varphi_1 + \bar{\varphi}_\tau[n]), \tag{3.42}$$

$$\frac{\partial s_{\text{signal}}(t_n,\boldsymbol{\theta})}{\partial A_2} = \sin(\omega_2\, t_n + \varphi_1 + \varphi_{\text{beat}}). \tag{3.43}$$

For calculating the FIM we resort to the assumption (3.8) and extend it for the modulated signal for the three cases

$$S_{\text{sum}} = \frac{1}{N}\sum_{n=0}^{N-1} \cos(\omega\, t_n + b_\tau[n]\frac{\pi\, t_n}{2\, T_{\text{bit}}} + \varphi_1 + \bar{\varphi}_\tau[n]) \approx 0, \tag{3.44}$$

$$S_{\text{linear}} = \frac{1}{N}\sum_{n=0}^{N-1} \left(\frac{\pi\, t_n}{4\, T_{\text{bit}}}\right) \cos(\omega\, t_n + b_\tau[n]\frac{\pi\, t_n}{2\, T_{\text{bit}}} + \bar{\varphi}_\tau[n] - \varphi_{beat}) \approx 0, \tag{3.45}$$

$$S_{\text{squared}} = \frac{1}{N}\sum_{n=0}^{N-1} \left(\frac{\pi\, t_n}{2\, T_{\text{bit}}}\right)^2 \cos(\omega\, t_n + b_\tau[n]\frac{\pi\, t_n}{2\, T_{\text{bit}}} + \varphi_1 + \bar{\varphi}_\tau[n]) \approx 0. \tag{3.46}$$

This assumption only holds for specific bit patterns, provided that the memory of the MSK is zero at each second, and we sum up an integer number of wavelengths of ω_{c}. Moreover, we need to translate T_{bit} to N_{bit} the bit duration in the number of samples. Under this assumption, we calculate the matrix entries in the appendix 8 and obtain the FIM

$$\boldsymbol{J}_{\text{signal}}(\boldsymbol{\theta}) = \frac{N}{2\,\sigma^2}\begin{pmatrix} \boldsymbol{J}_{4\times 4} & \boldsymbol{0}_{4\times 3} \\ \boldsymbol{0}_{3\times 4} & \boldsymbol{I}_{3\times 3}\end{pmatrix}, \tag{3.47}$$

with

$$
\boldsymbol{J}_{4\times 4} = \begin{pmatrix} A_1^2 + A_{\text{MSK}}^2 + A_2^2 & A_{\text{MSK}}^2 & A_2^2 & \frac{\pi\, A_{\text{MSK}}^2 (N-1)}{4\, N_{\text{bit}}} \\ A_{\text{MSK}}^2 & A_{\text{MSK}}^2 & 0 & \frac{\pi\, A_{\text{MSK}}^2 (N-1)}{4\, N_{\text{bit}}} \\ A_2^2 & 0 & A_2^2 & 0 \\ \frac{\pi\, A_{\text{MSK}}^2 (N-1)}{4\, N_{\text{bit}}} & \frac{\pi\, A_{\text{MSK}}^2 (N-1)}{4\, N_{\text{bit}}} & 0 & \frac{\pi^2\, A_{\text{MSK}}^2\, (N-1)(2\,N-1)}{24\, N_{\text{bit}}^2} \end{pmatrix} \tag{3.48}
$$

and $\mathbf{0}_{3\times 4}$, $\mathbf{0}_{4\times 3}$ represent 3×4 and 4×3 null matrices, while $\boldsymbol{I}_{3\times 3}$ is the 3×3 unit matrix. Accordingly, the inverse FIM is computed to

$$
\boldsymbol{J}_{\text{signal}}^{-1}(\boldsymbol{\theta}) = \frac{2\,\sigma^2}{N} \begin{pmatrix} \boldsymbol{J}_{4\times 4}^{-1} & \mathbf{0}_{4\times 3} \\ \mathbf{0}_{3\times 4} & \boldsymbol{I}_{3\times 3} \end{pmatrix}, \tag{3.49}
$$

with

$$
\boldsymbol{J}_{4\times 4}^{-1} = \begin{pmatrix} \frac{1}{A_1^2} & -\frac{1}{A_1^2} & -\frac{1}{A_1^2} & 0 \\ -\frac{1}{A_1^2} & \frac{4\,A_1^2\,N + A_{\text{MSK}}^2\,N - 2\,A_1^2 + A_{\text{MSK}}^2}{A_1^2\,A_{\text{MSK}}^2\,N + A_1^2\,A_{\text{MSK}}^2} & \frac{1}{A_1^2} & -\frac{12\,N_{\text{bit}}^2}{\pi\,A_{\text{MSK}}^2\,N + \pi\,A_{\text{MSK}}^2} \\ -\frac{1}{A_1^2} & \frac{1}{A_1^2} & \frac{A_1^2 + A_2^2}{A_1^2\,A_2^2} & 0 \\ 0 & -\frac{12\,N_{\text{bit}}^2}{\pi\,A_{\text{MSK}}^2\,N + \pi\,A_{\text{MSK}}^2} & 0 & \frac{48\,N_{\text{bit}}^2}{\pi^2\,A_{\text{MSK}}^2\,N^2 - \pi^2\,A_{\text{MSK}}^2} \end{pmatrix} \tag{3.50}
$$

Finally, we get the lower bound for the signal model including MSK modulation as

$$
\operatorname{var}(\varphi_1) \geq \frac{2\sigma^2}{N\,A_1^2}, \tag{3.51}
$$

$$
\operatorname{var}(\bar{\varphi}_\tau[n]) \geq \frac{2\,\sigma^2 (4\,A_1^2\,N + A_{\text{MSK}}^2\,N - 2\,A_1^2 + A_{\text{MSK}}^2)}{N\,(A_1^2\,A_{\text{MSK}}^2\,N + A_1^2\,A_{\text{MSK}}^2)}, \tag{3.52}
$$

$$
\operatorname{var}(\varphi_{\text{beat}}) \geq \frac{2\sigma^2}{N}\left(\frac{1}{A_1^2} + \frac{1}{A_2^2}\right), \tag{3.53}
$$

$$
\operatorname{var}(b_\tau[n]) \geq \frac{2\sigma^2\,48\,N_{\text{bit}}^2}{N\,A_{\text{MSK}}^2 \pi^2 (N^2 - 1)}, \tag{3.54}
$$

$$
\operatorname{var}(A_1) \geq \frac{2\sigma^2}{N}, \tag{3.55}
$$

$$
\operatorname{var}(A_{\text{MSK}}) \geq \frac{2\sigma^2}{N}, \tag{3.56}
$$

$$
\operatorname{var}(A_2) \geq \frac{2\sigma^2}{N}. \tag{3.57}
$$

The variances of the phases φ_1, φ_{beat} and the amplitudes A_1, A_2 are the same as for the signal model s_{add} in (3.1). We can observe this in (3.48) as there is no correlation between the modulation and the individual tones. For this case, the variance of the phase estimates remains the same whether the bit sequence b_τ is known or not. All the transformations introduced in the previous section can also be applied and lead to the same result. We want to point out that our result is not valid in every case for a finite observation time.

This is because the equations (3.44), (3.45) and (3.46) are only satisfied for certain bit patterns, that allow to sum over closed waveforms. Therefore, some of the non-diagonal entries in the FIM can become non-zero so that the individual estimates are no longer statistically independent but correlated with each other via the MSK signal. The influence of the MSK means that the estimator cannot reach the ideal limit presented, but it still represents a lower limit and serves us as a guide for the further course of the work. Furthermore, in the following chapters, we will apply various techniques to minimise the influence of the modulated component, using (3.44), (3.45) and (3.46) as design targets for our developments of improved messages.

3.1.4. VALIDITY OF THE BOUND NEXT TO MSK MODULATED SIGNALS

In the previous sections, we described a lower bound for the phase estimator for the R-Mode system. There we show that the variance scales with one over the bandwidth and one over the observation time when we take the Gaussian noise energy into account. However, depending on this value, a larger bandwidth increases the influence of the MSK signal component on the phase estimate. In this section, we want to show that for long observation times, the influence of the MSK signal is potentially reduced.

We assume that the noise power can be divided into a part σ^2, representing the power AWGN, and another part corresponding to the remaining power of the MSK signal in the band of interest P_{MSK}. We obtain the modified bound for A_i, the amplitude of any tone as

$$\operatorname{var}(\varphi_i) > \frac{\sigma^2 + P_{\mathrm{MSK}}}{T_{\mathrm{obs}}\, b\, A_i^2}. \tag{3.58}$$

This can be split again into

$$\operatorname{var}(\varphi_i) > \frac{\sigma^2}{T_{\mathrm{obs}}\, b\, A_i^2} + \frac{P_{\mathrm{MSK}}}{T_{\mathrm{obs}}\, b\, A_i^2}. \tag{3.59}$$

To obtain P_{MSK}, we use the Power Spectrum Density (PSD) $\frac{G(f_{\mathrm{base}})}{T_{\mathrm{bit}}}$ in baseband

$$\frac{G(f_{\mathrm{base}})}{T_{\mathrm{bit}}} = \frac{16}{\pi^2}\left(\frac{\cos\left(2\pi\, f_{\mathrm{base}}\, T_{\mathrm{bit}}\right)}{1-16\, f_{\mathrm{base}}^2\, T_{\mathrm{bit}}^2}\right)^2 \tag{3.60}$$

with T_{bit} time duration of a bit, and f_{base} the frequency in baseband.

If we assume all our signal components repeat cyclically we can calculate P_{MSK} by integrating $\frac{G(f_{\mathrm{base}})}{T_{\mathrm{bit}}}$ over the bandwidth b with the centre frequency of the baseband tone f_{cw} we are interested in as

$$P_{\mathrm{MSK}}(f_{\mathrm{cw}}, b) = \frac{16\, A_{\mathrm{MSK}}^2}{\pi^2} \int_{f_{\mathrm{cw}}-\frac{b}{2}}^{f_{\mathrm{cw}}+\frac{b}{2}} \left(\frac{\cos\left(2\pi\, f_{\mathrm{base}}\, T_{\mathrm{bit}}\right)}{1-16\, f_{\mathrm{base}}^2\, T_{\mathrm{bit}}^2}\right)^2 \delta f_{\mathrm{base}}. \tag{3.61}$$

We also want to consider the Gaussian noise. For a given sample rate, the noise power within a bandwidth b should scale with the linear factor K_{PSD}, according to

$$\sigma^2 = b\,K_{\mathrm{PSD}}. \tag{3.62}$$

In the next step, we combine the bound with the expression for the noise energy components:

$$\operatorname{var}(\varphi_i) > \frac{b\,K_{\mathrm{PSD}}}{T_{\mathrm{obs}}\,b\,A_i^2} + \frac{16\,A_{\mathrm{MSK}}^2}{T_{\mathrm{obs}}\,A_i^2\,\pi^2\,b}\int_{f_{\mathrm{cw}}-\frac{b}{2}}^{f_{\mathrm{cw}}+\frac{b}{2}}\left(\frac{\cos\left(2\pi\,f_{\mathrm{base}}\,T_{\mathrm{bit}}\right)}{1-16\,f_{\mathrm{base}}^2\,T_{\mathrm{bit}}^2}\right)^2\delta f_{\mathrm{base}}. \tag{3.63}$$

The bandwidth vanished in the first part of the equation

$$\operatorname{var}(\varphi_i) > \frac{K_{\mathrm{PSD}}}{T_{\mathrm{obs}}\,A_i^2} + \frac{16\,A_{\mathrm{MSK}}^2}{T_{\mathrm{obs}}\,A_i^2\,\pi^2\,b}\int_{f_{\mathrm{cw}}-\frac{b}{2}}^{f_{\mathrm{cw}}+\frac{b}{2}}\left(\frac{\cos\left(2\pi\,f_{\mathrm{base}}\,T_{\mathrm{bit}}\right)}{1-16\,f_{\mathrm{base}}^2\,T_{\mathrm{bit}}^2}\right)^2\delta f_{\mathrm{base}}. \tag{3.64}$$

We can summarize that for a short observation time, the estimator becomes biased when the MSK signal is present. Considering that f_{cw} is in the zero crossing of (3.60), one can expect that the achievable accuracy with MSK approaches that without MSK for long observation times. Therefore, we expect that an efficient estimator for the problem of estimating single phases is also an efficient estimator for estimating phases on the R-Mode signal and can achieve the lower bound presented. In Section 4.1.3 we confirm this result with Monte Carlo simulations.

3.2. POSITIONING ACCURACY PREDICTION

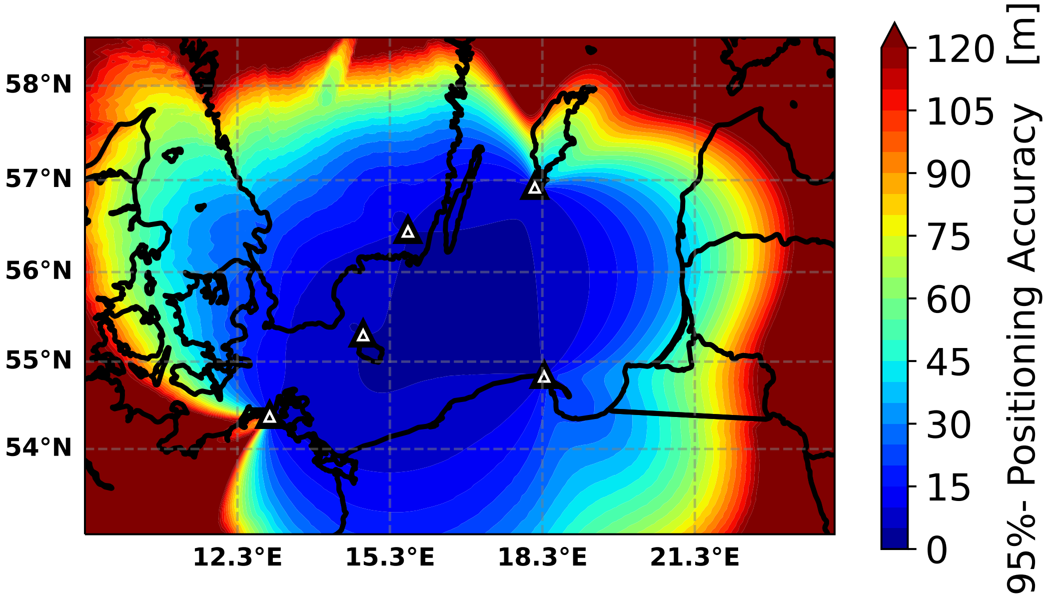

Figure 3.1: Position accuracy prediction using phase estimation of single CW, with Δ indicating the position of the transmitters.

In preparation for the R-Mode Baltic testbed, the General Lighthouse Authority (GLA) performed a positioning accuracy prediction. The position accuracy estimation performed is based on the CRB for the phase estimate of a single tone in AWGN, the variance of the clock and a maximum likelihood positioning.

To derive the CRB, the GLA calculates a Carrier-to-Noise Ratio (CN_0) for daytime and nighttime. Since this data was provided to us by the GLA, we used the CRBs derived in this chapter to generate the positioning accuracy predictions for our single tone. In addition, we have also considered the beat frequency to show that we can resolve the ambiguities of the R-Mode single tones, which have wavelengths of about 1 km.

In Fig. 3.1 we show the estimated 95% position accuracy that MF R-Mode can achieve for the western Baltic Sea in case the stations Rozewie, Holmsjö, Hoburg, Groß Mohrdorf and Hammerodde are transmitting R-Mode signals. We only consider the estimation of the single tone phase the resolution of ambiguities is not yet considered. We predict the accuracy of less than 30 m for most of the area shown. Based on this result, the R-Mode Baltic testbed selected the transmitting stations to upgrade. Within this area, our first trials took place, which we present in Chapter 6.

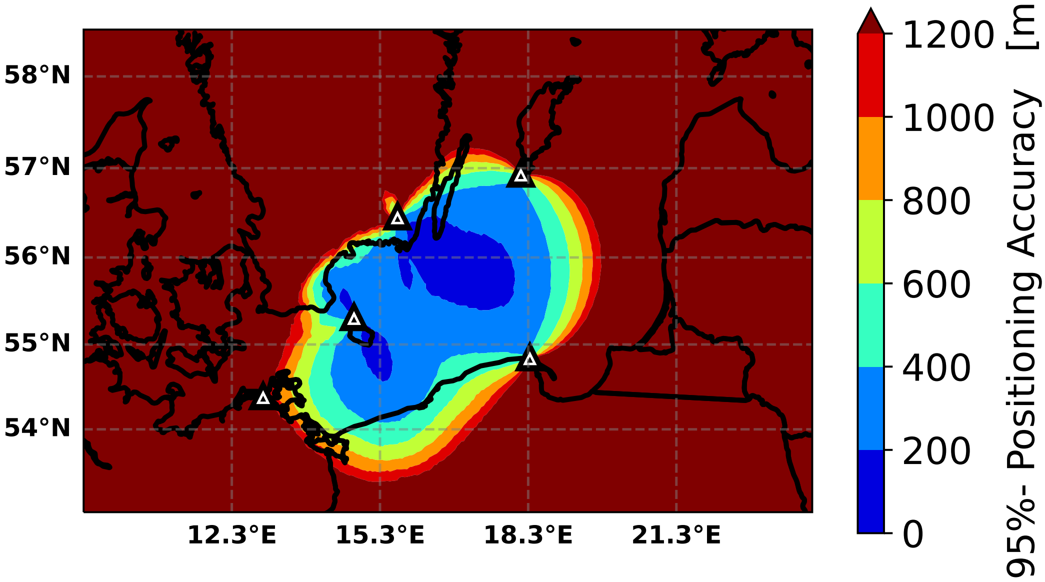

Figure 3.2: Position accuracy prediction using estimation of the beat signal, with Δ indicating the position of the transmitters.

To account for the ambiguities, we applied the CRB as described in (3.15) for the beat frequency, assuming a signal spacing of 450 Hz, to the CN_0 values. Furthermore, when we compute the difference between the phase estimates, the clock drift is cancelled out. We yield the positioning accuracy prediction in Fig 3.2, again we plot the 95% positioning accuracy. This plot was chosen instead of predicting the estimate of a single station, as we had already shown that this approach is not accurate enough [4].

As expected, the accuracy decreases drastically, but in the middle of the testbed, we predict the accuracy of less than 400 m, which would be sufficient to eliminate the ambiguities.

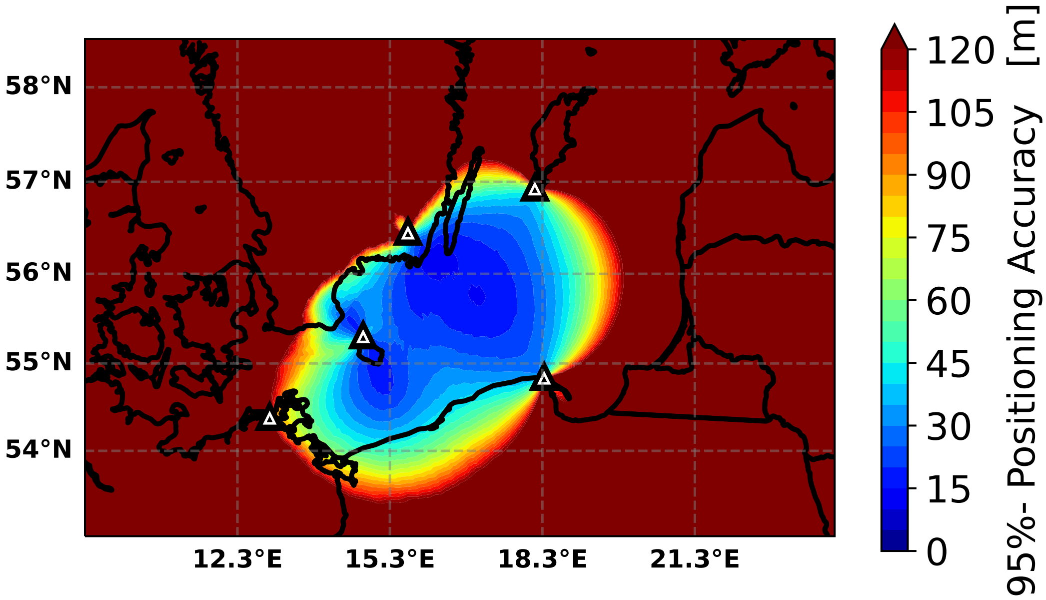

Figure 3.3: Position accuracy prediction using phase estimation of single CW taking the skywave into account, with Δ indicating the position of the transmitters, with Δ indicating the position of the transmitters.

For the system, however, the nighttime performance is also crucial, since here the skywave described in Chapter 2 reduces the achievable accuracy. The GLA dataset includes data for various models that describe this influence. We plot the resulting positioning accuracy for the case where the skywave is considered as additional noise and no ambiguities are resolved in Fig. 3.3. It can be clearly seen that the area in which we achieve high accuracy below 30 m decreases drastically, so that position solution is only possible in the middle between stations. With a few stations we can no longer cover large areas, but with a sufficiently high station density, positioning at nighttime also seems possible.

If, as we have described, the accuracy decreases for the case without ambiguities, it is also true for the ambiguity resolution with the beat frequency. We keep the model of describing the skywave as an additional noise component and can use the CRB for the beat frequency from (3.13) analogously to Fig 3.2. Fig 3.4 represents the resulting positioning accuracy, in which we barely achieve accuracies of 12 km in the centre of the testbed, which is not sufficient to resolve ambiguities.

Therefore, we can assume that the MF R-Mode system can provide a fully independent positioning solution during the daytime by using the beat frequency to resolve the ambiguities. For nighttimes, the estimation of the beat frequency cannot resolve the ambiguity problems anymore. Here, a grid search approaches as proposed in [53] or continuous phase tracking, which we use for our experiments in Chapter 6, could solve the problem.

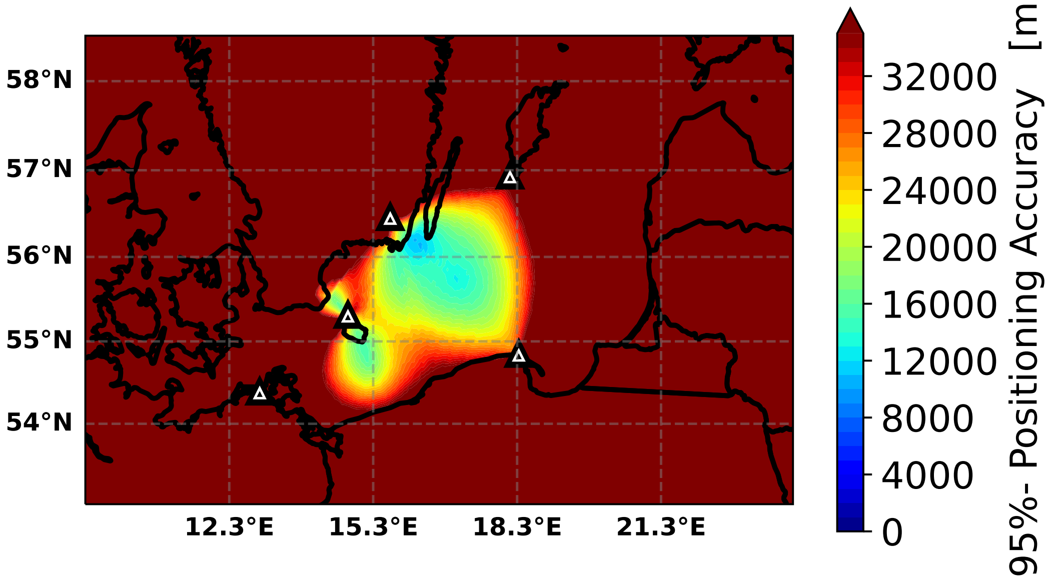

Figure 3.4: Position accuracy prediction using phase estimation of the beat signal taking the skywave into account, with Δ indicating the position of the transmitters.

4

ALGORITHM

For the development of the R-Mode receiver, we need firstly an algorithm that provides a phase estimate for each station, and secondly, an algorithm that determines the current position based on the pseudo range derived from the phase estimates. We focus on obtaining the best performance in phase estimation. Therefore, we introduce the different phase estimation approaches and their properties, followed by a description of a single point position algorithm we use in the later experiments.

The system is based on the parameter estimation of harmonics, which has been a fundamental research area in the field of signal processing. Estimating, for instance, the directions of arrival, frequencies, Doppler shifts, phase and more is required in a wide range of applications including radar [71], sonar [72], channel sounding [73], wireless communications [74] and power electronics [75]. Therefore, different methods can be used to estimate the harmonics parameter such as the Discrete Fourier Transform (DFT) [68, 69], Phase Lock Loop (PLL) [70] and more recent techniques such as Estimation of Signal Parameters via Rotational Invariance Techniques (ESPRIT) [76] and MUltiple SIgnal Classification (MUSIC) [77].

In this chapter, we first describe a ML estimator for a single tone and show the application for the R-Mode signal in Section 4.1. Swaszek and Johnsen [52, 54] also use the well-known estimator to obtain phase estimates. However, since each estimator can only track one signal, their implementation in [54] is limited to up to three stations, which is not suitable for productive use. We overcome this limitation and present a way to efficiently estimate all channels of the R-Mode system at once by exploiting the correspondence between the ML estimator of the phase and the DFT. Furthermore, we show that our approach is an effective estimator for the R-Mode signal phase estimation problem.

Moreover, we have shown in Section 3 that ML estimation is not optimal for our signal model, so we extend our work to LS estimators in Section 4.2. In doing so, we maintain the computationally effective DFT, we investigate windowing for our estimator and show the performance improvements for short observation times. Furthermore, we aim to minimise the integration time of our estimator by using a PLL. In Section 5.2.5 we then compare all three approaches.

Finally, we present shortly the well-known least square approaches to estimate the position from the ranges derived before, taking into account the curvature of the earth, in Section 4.4.

4.1. MAXIMUM LIKELIHOOD PHASE ESTIMATION

A ML estimator for different tones i with amplitude A_i and phase offset φ_i in samples is given in [69], based on the likelihood function

$$\mathscr{L} = \sum_{i=1}^{k} \{2A_i \operatorname{Re}[e^{j\varphi_i}\Lambda(\omega_i)] - A_i^2\},$$

with (4.1)

$$\Lambda(\omega_i) = \frac{1}{N}\sum_{n=0}^{N-1}(X_n - jY_n)e^{-jn\omega_i\Delta t}.$$

Here $\boldsymbol{X}$ is defined as the vector of samples with the n-th sample X_n and $\boldsymbol{Y}$ as the corresponding Hilbert transform vector and single sample Y_n, with length N for the two vectors. Further, k is the number of tones to be estimated, define each tone according to our signal model (2.6). To maximize the Likelihood function $\mathscr{L}$, we need parameters that maximize $\Lambda(\omega_i)$. Therefore, we obtain our estimates at the beginning of the observation time at t_0 by

$$\hat{A}_i = |\Lambda(\omega_i)| \tag{4.2}$$

and

$$\hat{\varphi}_i = \arg[e^{-j\omega_i t_0}\Lambda(\omega_i)]. \tag{4.3}$$

We assume a known frequency ω_i of the tone. Under this assumption, we get the estimates $\hat{\varphi}_i$ for the phase and $\hat{A}_i$ for the amplitude. Our interest is in the estimations of the different tones to calculate the position. In this case, the presented approach does not scale and leads to a high computational cost.

4.1.1. REALIZATION AS FOURIER TRANSFORM

As shown in the previous part, the estimation of phase for many stations can be very computationally intensive. To simplify the problem, we exploit the fact that parametric estimation can equal a DFT [68].

To do this, we describe $\Lambda(\omega_i)$ from (4.1) assuming

$$\omega_i = 2\pi\frac{K_i}{N\Delta t}, \tag{4.4}$$

we yield the DFT basis function as

$$e^{-j2\pi\frac{K_i}{N}n}, \tag{4.5}$$

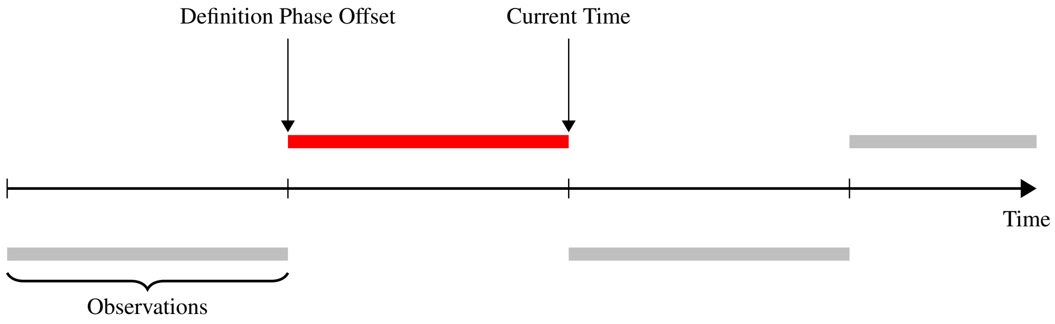

Figure 4.1: Overview about the different points in time that are crucial for the ML estimation.

where K_i describe the point in the DFT spectrum. We obtain the matrix representation

$$\Lambda(\omega_i) = \frac{1}{N}(\boldsymbol{X} - j\boldsymbol{Y})^{\mathsf{T}} \begin{pmatrix} e^{-j0\omega_i \Delta t} \\ e^{-j1\omega_i \Delta t} \\ \dots \\ \dots \\ e^{-jN\omega_i \Delta t} \end{pmatrix}, \tag{4.6}$$

which is one column of the transformation matrix of the DFT. With the FFT a computationally efficient method is known to obtain the DFT, and thus to estimate K bins at once. It is important to note that we must satisfy the equation (4.4), which means that the centre frequencies of the DFT bins must match the frequencies of the Continuous Waves to be estimated. Here is the main difference to Maximum Likelihood estimation, where we only compute one bin, and the choice of the centre frequency is arbitrary. In DFT, the K-bins are evenly distributed over the frequency band and increasing the observation time leads to higher frequency resolution. We calculate the DFT-bin for the i-th signal as

$$f_i = \frac{K_i}{N\Delta t} = \frac{K_i}{T_{\text{obs}}}, \tag{4.7}$$

for a complex DFT, for a real DFT K_i need to change accordingly, due to the negative symmetric spectra. Consequently, if the frequency of a tone f_i is not on the centre frequency of a bin, K_i is not an integer, leading to performance losses and lowering the accuracy of the results. Both estimation methods yield complex numbers, where the phase represents the required phase information at the beginning of the observed time interval of length T_{obs}.

4.1.2. OBSERVATION POINT IN TIME

To obtain precise position information from the R-Mode system, to know at what point in time our phase estimation is most accurate is crucial. Fig. 4.1 describe a timeline where the grey and red rectangles represent different observation intervals. The red box is the time slot currently evaluated in the ML approach. We first need to collect samples over the observation time T_{obs} before we can start the calculation. According to our signal model (2.6), we got an estimation in (4.3), that represents the phase offset at the beginning of the time interval. Therefore, the phase estimates represent the position with a delay which equals roughly observation interval, neglecting the calculation time.

Another problem occurs when the receiver is in movement. Here the phase offset will change continuously during the observation time, as described in Section 3.1.2 which leads to a modified signal model for two single tones

$$s_{\text{dynamic}}(n,\boldsymbol{\theta}) = A_1 \sin(\omega_1\, t_n + \omega_1\, t_n \frac{v}{c_0} + \varphi_1). \qquad (4.8)$$
$$+ A_2 \sin(\omega_2\, t_n + \omega_2\, t_n \frac{v}{c_0} + \varphi_1 + \varphi_{\text{beat}}).$$

We describe the dynamic part of the phase offset in 3.23 as

$$\varphi_{\text{velocity}} = \omega_i\, t_n \frac{v}{c_0}. \qquad (4.9)$$

For the phase estimation we can assume from (4.3) and (4.1), that we calculate an average over $\varphi_{\text{velocity}}$. That can be considered an additional error or mitigated by assuming that the receiver's movement is known. In Section 3.1.2 we show that for a known velocity v, the CRB is equal to the bound presented in Section 3.1.1. Assuming knowledge about the movement is valid for real scenarios when we use PNT fusion approaches, including inertial measurements. The overall influence of the described effects becomes crucial for higher velocity. Our first trials, described in Chapter 6, neglects this influence, as most vessels move relatively slow. However, we have shown here that MF further improves R-Mode when integrated into a complete PNT solution.

4.1.3. FFT AN EFFICIENT ESTIMATOR TO THE PROBLEM

We now want to investigate how the FFT behaves as an estimator for the phase estimation of the R-Mode signal. It is well known that the Maximum Likelihood estimator meets the Cramer-Raó Bound. The same applies to the FFT due to the correspondence if we choose the frequency bins appropriately as described in Section 4.1.1.

However, in Section 3.1.1, we neglect that we correlate with the different signal components when we introduce the MSK signal into our problem. As a result, there is an expected deviation between the estimate and the calculated limit. Since the ML estimator derives under the assumption of AWGN from our likelihood function (4.1), the estimator we use is not optimal but computationally efficient and is therefore examined in more detail in this thesis. In Section 3.1.4 we investigate how the bandwidth of the ML estimator affects this deviation when we model the MSK signal as a noise influence. As a result, since the bandwidth of the FFT bins decreases for longer observation times, the FFT does not match the derived bound for short observations but converges to it as the observation time increases.

To check this assumption, we performed a Monte Carlo simulation within our simulation environment, based on the signal model described in Section 2.1. We conducted 100 runs with noise variance $1.22\,10^{-5}$ for observation times T_{obs} varied by integer seconds at a sample rate of 1 Ms/s. Here, the FFT served as the estimator and the amplitudes were chosen with reference to our signal model (2.6) as $A_1 = 0.001$ $A_2 = 0.002$ and $A_{\text{MSK}} = 0.004$. We choose all parameters to correspond to realistic observations, which we describe in more detail in Chapter 6. We present the results of this simulation in Fig. 4.2. Here, the variance of the estimated phase is plotted as a blue bar for each observation time interval in seconds, while the CRB is a red line. We see that we deviate from the bound in the first 5s for longer observation time we see a good agreement between the estimate and the bound. Our estimator seems to perform better than the bound due to the time-limited simulation of the noise and finite number of simulations runs.

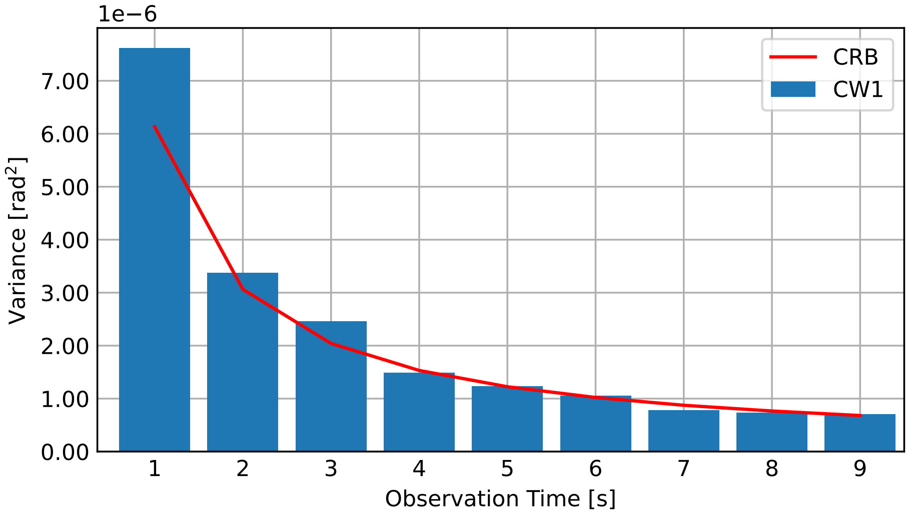

Figure 4.2: CRB and simulation result for CW1.

Moreover, in 3.1.1 we emphasized that our estimator should be statistically independent. Therefore Fig. 4.3 shows the variance of the phase estimate of CW1, CW2 and the beat signal. Here a blue bar shows the variance of CW1, an orange bar indicates the variance of CW2 above it. Next to the CWs, a green bar represents the variance of the beat signal. Furthermore, a red line draws the CRB of the beat signal. We see a divergence between the estimate of the beat phase and the corresponding bound in the beginning. The bar plot converges to the bound for the longer observation times. We can graphically evaluate the sum of the variance of CW1 and CW2. If this is equal to the variance of the beat signal, our estimate is statistically independent, and we obtain the expected result from Section 3.1.3. We see that the differences between the sum of the variance of the CWs and the variance of the beat signal become smaller for longer observation times as the influence of the MSK signal decreases.

As we have shown, simulation and the theoretical assumptions from Section 3.1.4 match. Both estimates become statistically independent, and we met the lower bound for long observation times. Therefore, the FFT can be called an efficient estimator for the phase estimation of the R-Mode signal for CW1 and CW2 as well as for the beat signal.

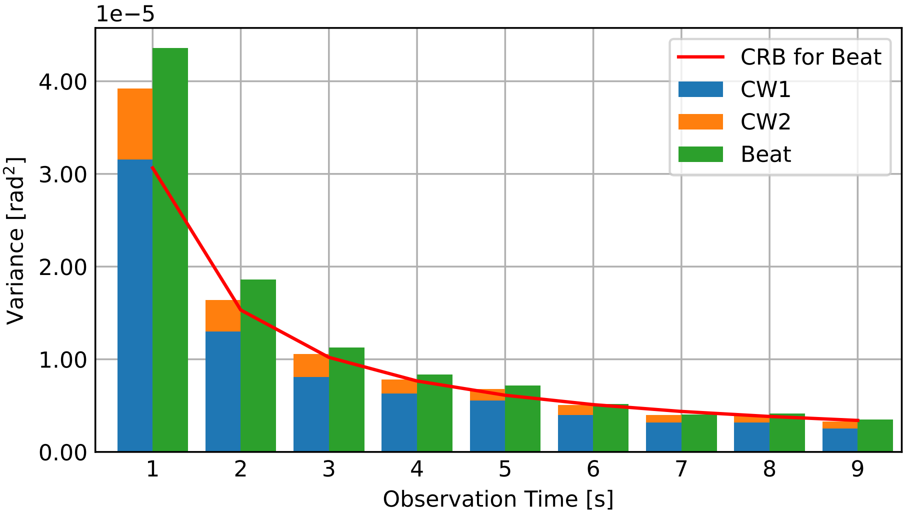

Figure 4.3: CRB of beat signal and simulation result combined for CW1, CW2 and beat signal.

4.2. LEAST SQUARE PHASE ESTIMATION

The ML estimation requires a specific observation time, and the estimates are averaged over this time, leading to reduced performance in a dynamic scenario as described in Section 4.1.2. Moreover, we have shown in 4.1.3 that we met the lower bound only for longer observation times. We investigate in this section the least square estimation as an alternative method that can overcome these issues. In this section, we investigate the use of a windowing function to the FFT and the PLL.

4.2.1. WINDOWING ON FFT

From the non-diagonal elements in the FIM, shown in Section 3, we became aware that the modulated MSK signal interfere with the aiding carrier below and above. In a very simplified model, this can be seen as power leakage when we apply the FFT, which motivates the use of a windowing approach, as we first suggest in our Paper "Phase Estimation of Single Tones Next to Modulated Signals in the medium frequency R-Mode system" [1]. Schuster proved that we do not reach the CRB anymore [78] when we apply a window. So, this approach potentially increases the performance only for short observation times.

To find an optimal window to our problem, we first need to analytical describe how a window $w(t)$ influence the noise floor in the bin we want to consider for our phase estimation. We assume the Fourier transform of any time-limited signal model $s(t)$ as

$$S_{\text{obs}}(f) = \int_{-\frac{T_{\text{obs}}}{2}}^{\frac{T_{\text{obs}}}{2}} s(t) e^{2\pi jft} \, \mathrm{d}t, \tag{4.10}$$

If we consider the time limited window $w(t)$, this leads to

$$S_{\text{obs}}(f) = \int_{-\infty}^{\infty} s(t) w(t) \cdot e^{2\pi jft} \, \mathrm{d}t. \tag{4.11}$$

For our estimation problem, we are interested in $S(f_i)$, which is the value of the Fourier transform at the specific frequency f_i where the CW carrier is located. Considering the continuous frequency domain transform $S(f)$ and $W(f)$ for $s(t)$ and $w(t)$, we can use Parseval's theorem [79] and rewrite (4.11) as

$$S_{\text{obs}}(f_i) = \int_{-\infty}^{\infty} S(f)W(f-f_i)\,\mathrm{d}f. \tag{4.12}$$

These are the evaluation of a single point in the convolution operation.

When we want to estimate CW1, from signal model $s_{\text{complete}}(t)$ in (2.6), $s(t)$ can be divided into three different components, which results in

$$s(t) = s_{\text{CW1}}(t) + s_{\text{MSK+CW2}}(t) + n(t), \tag{4.13}$$

here $s_{\text{CW1}}(t)$ is the signal model of CW1, the tone to estimate, $s_{\text{MSK+CW2}}(t)$ combines the signal of MSK and CW2 and $n(t)$ describes the AWGN noise term. Therefore, we express S_{obs} with $\mathcal{N}(f)$ as Fourier transform of a noise term as

$$\begin{aligned} S_{\text{obs}}(f_i) &= \int_{-\infty}^{\infty} (S_{\text{CW1}}(f) + S_{\text{MSK+CW2}}(f) + \mathcal{N}(f))W(f-f_i)\mathrm{d}f & (4.14)\\ &= \int_{-\infty}^{\infty} S_{\text{CW1}}(f)W(f-f_i)\,df & (4.15)\\ &+ \int_{-\infty}^{\infty} (S_{\text{MSK+CW2}}(f) + \mathcal{N}(f))W(f-f_i)\,\mathrm{d}f, & (4.16) \end{aligned}$$

where (4.15) denotes the required part of (4.14) and (4.16) represents the undesired parts $\mathcal{N}(f)$ caused by noise and $S_{\text{MSK+CW2}}(f)$ the interfering MSK signal.

Our aim is to maximise the contribution of (4.15) and minimise the contribution of (4.16). We, therefore, consider the quotient of the energy contributions of the individual components:

$$\text{SNR} = \frac{\left(\int_{-\infty}^{\infty} S_{\text{CW1}}(f)W(f-f_i)\mathrm{d}f\right)^2}{\left(\int_{-\infty}^{\infty}(S_{\text{MSK+CW2}}(f) + \mathcal{N}(f)))W(f-f_i)\,\mathrm{d}f\right)^2} \tag{4.17}$$

In the same way, we could compute the SNR for CW2. As we also attenuate the signal power with windowing, we need to find an offset between the parameter process gain, peak side-lobe level and equivalent noise bandwidth of the parametrized window.

The process gain describes how much the power of our signal reduces when a window is applied. The peak-side-lobe level represents the highest sidelobe and indicates how well the window suppresses the modulation. The equivalent noise bandwidth corresponds to the width of a rectangular window, with the same peak power gain that would result in the same noise power in the bin. However, only Gaussian noise is considered [80].

The optimal window heavily depends on the received signal strength, the strength of the modulation and the general noise floor. As we influence the noise and signal power in the bin by applying a window, the SNR is a good figure of merit to estimate the performance of a window. However, this has to be calculated for each noise scenario separately.

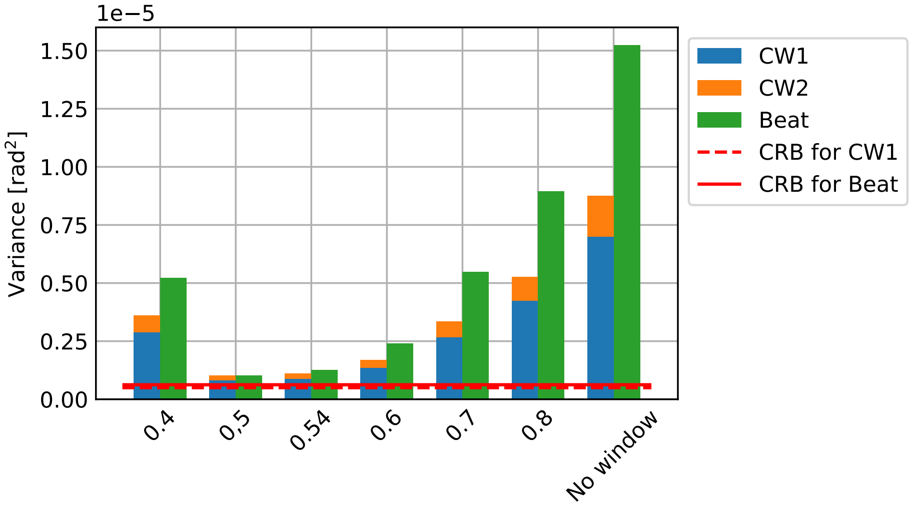

Figure 4.4: Variance difference for different windows in low noise environments for phase estimates of CW1, CW2 and Beat. With indication of the corresponding CRB for CW1 and Beat signal.

In order to be able to adjust adaptive the window for a given noise scenario, we want to use a window with length N, that can be changed with a parameter a_0, here we choose the modified Hann window [80]

$$w_{\text{hann}}(t) = \left[a_0 - (1-a_0)\cos\left(\frac{2\pi t}{N}\right)\right]\text{rect}\left(\frac{t}{T_{\text{obs}}}\right). \tag{4.18}$$

In the specific case of $a_0 = 0.54$, the window is called the Hamming window and has the highest suppression of the first side lobe [80].

To show the general improvement of this approach, we conduct a Monte Carlo simulation of 5000 runs each, for $a_0 = [0.4, 0.5, 0.54, 0.6, 0.7, 0.8]$ in three different noise conditions within our environment, only considering a single station. We use the same model parameter as in Section 4.1.3 with amplitude values $A_1 = 0.001$ $A_2 = 0.002$, $A_{\text{MSK}} = 0.004$. Moreover, we choose a sample rate of 1 Ms/s and a fixed observation time of 1 s. The noise levels are referred to as low noise for a noise variance of 2.50×10^{-7}, medium noise for variance of 1.22×10^{-5} and high noise with variance 8.09×10^{-5}. These values are obtained by linearly scaling the amplitude of the simulated noise.

We plot the result for the low noise scenario in Fig. 4.4 as a bar graph of the resulting variance of our estimated phase. Again, the blue bar shows the results for CW1, the orange bar for CW2 and the green bar for beat frequency. For ease of comparison, the red-solid line shows the theoretical CRB for the beat variance and the dashed line indicate the lower limit of CW1 for the simulated noise level as derived in Chapter 3.

We show that the estimate without a window is far from the lower bound, and we approach it when we change the parameter a_0. Our performance increases with smaller parameter values until we almost reach the lower limit at $a_0 = 0.5$. For smaller values, the variance starts to grow again. We also see that the maximum suppression of the first side lobe at $a_0 = 0.54$ does not lead to the best result. Because our modulated signal is further away than the first side lobe. At the minimum, the sum of CW1 and CW2 variance describe the beat estimate variance. Indeed, this is what we expect as we attenuate the signal

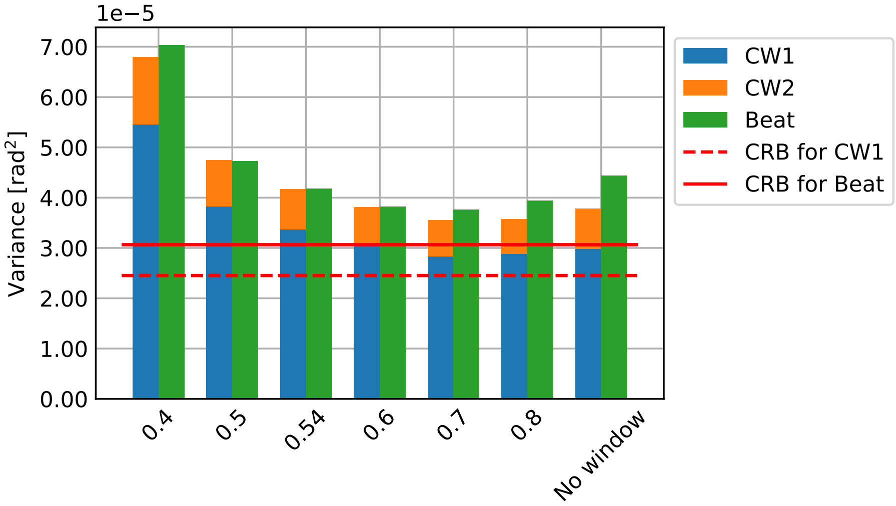

Figure 4.5: Variance difference for different windows in medium noise environments for phase estimates of CW1, CW2 and Beat. With indication of the corresponding CRB for CW1 and Beat signal.

correlating the tones, and thus the diagonal entries of the Fisher Information Matrix from Chapter 3 become smaller.

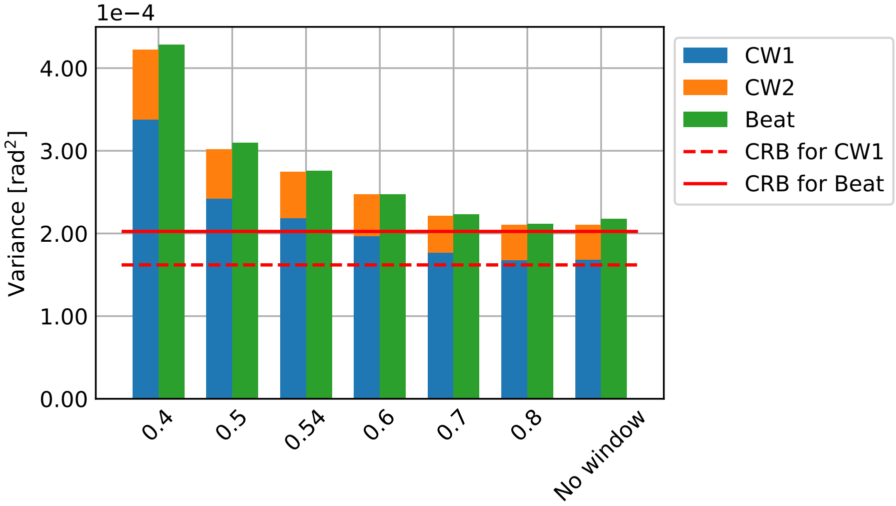

Figure 4.6: Variance difference for different windows in high noise environments for phase estimates of CW1, CW2 and Beat. With indication of the corresponding CRB for CW1 and Beat signal.

In Fig. 4.5 we present the results for the medium noise scenario in the same way as in Fig. 4.4 for low noise. We see that the variance minimization parameter is now $a_0 = 0.8$, as the broadened main slope contributes more noise than before, which changes the SNR. However, the non-windowed case is again slightly outperformed and in general, the performances are close. The statistic-independent estimation condition still applies to the lower values of the parameter since we are still suppressing the modulated signal at the cost of a wide main lobe that introduces more general noise.

Table 4.1: Window comparison results for CW1 phase estimation.

Noise level	Parameter	SNR	var(CW1)
Low	$a_0 = 0.4$	483.19	2.89×10^{-6}
	$a_0 = 0.5$	949.55	8.12×10^{-7}
	$a_0 = 0.54$	921.00	8.94×10^{-7}
	$a_0 = 0.6$	720.06	1.35×10^{-6}
	$a_0 = 0.7$	514.15	2.67×10^{-6}
	$a_0 = 0.8$	417.56	4.24×10^{-6}
	no Window	328.32	6.99×10^{-6}
Medium	$a_0 = 0.4$	106.60	5.45×10^{-5}
	$a_0 = 0.5$	132.43	3.83×10^{-5}
	$a_0 = 0.54$	139.71	3.37×10^{-5}
	$a_0 = 0.6$	147.59	3.07×10^{-5}
	$a_0 = 0.7$	153.91	2.83×10^{-5}
	$a_0 = 0.8$	154.41	2.88×10^{-5}
	no Window	148.61	2.98×10^{-5}
High	$a_0 = 0.4$	42.21	3.38×10^{-4}
	$a_0 = 0.5$	50.36	2.42×10^{-4}
	$a_0 = 0.54$	52.87	2.18×10^{-4}
	$a_0 = 0.6$	55.86	1.97×10^{-4}
	$a_0 = 0.7$	58.99	1.77×10^{-4}
	$a_0 = 0.8$	60.41	1.67×10^{-4}
	no Window	60.73	1.68×10^{-4}

The trend in variance with medium noise continues in the high noise scenario, the results of which we show in Fig. 4.6 in the same way as before. Because of the different scaling, the variance now appears to match the CRB, but in absolute terms, the difference is about the same. The window for $a_0 = 0.8$ slightly outperforms the non-windowed case, and as a_0 decreases, the performance decreases. Nevertheless, for smaller values, we can observe that we have suppressed the influence of the modulation, which in the best case leads to uncorrelated measurements.

From the theory, we suggested the SNR as a figure of merit to the different windows. To verify this approach, we calculated the noise contribution for each window by generating a signal without the carrier of interest and evaluating the amplitude of the bin to estimate after a FFT, so we derived a measure of the noise. As the window also influence the signal energies, we repeat this with a carrier only to get a metric of the signal, obtaining a SNR value that closely describes the influence for each window. A script computes the SNR for us, which can act as a design tool to optimize the estimator in a given noise scenario.

In Table 4.1, we compare the resulting SNR values with the achieved variance of CW1 phase estimation in our Monte Carlo simulation for all three noise scenarios. We obtain that the choice of the parameter a_0 affects the SNR and in most cases, we get a lower variance for higher values. Furthermore, this corresponds to the expected behaviour of the CRB in Chapter 3, which decreases at higher SNR values. The fact that the SNR at high noise is slightly higher for the non-windowed estimate than for the more powerful window $a_0 = 0.8$ is a simulation problem due to the limited simulation time and is within the expected accuracy of this configuration.

4.2.2. PHASE LOCK LOOP

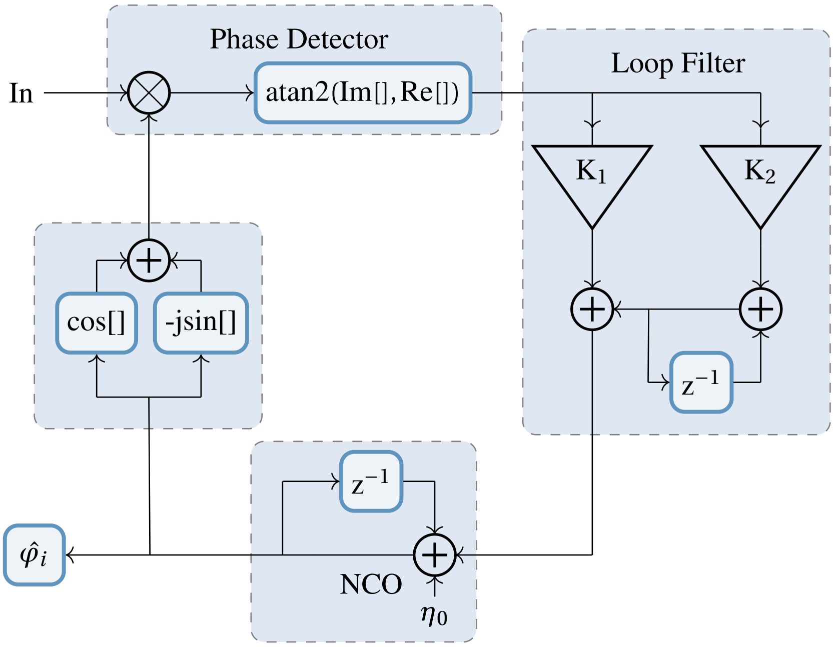

Figure 4.7: Block diagram of PLL.

The ML approach obtain phase estimation with a certain delay, as shown in 4.1.2. The same problem occurs when we apply windowing to the FFT. To overcome this delay, we review PLLs as the possibility to provide instantaneous phase estimation in this section because the PLL is a LS estimator for frequency and phase [81]. We presented the initial result in [6].

The PLL architecture used in this work is a second-order discrete-time PLL which we easily implemented in software. The discrete-time PLL derives from a well-known analogue model to have similar behaviour. Fig. 4.7 depicts the block diagram of the discrete-time PLL and three main blocks are visible, the Phase Detector (PD), Loop Filter (LF) and Numerically Controlled Oscillator (NCO). The PD is composed of a complex multiplier and a four-quadrant arctangent operator, which extracts the phase difference among the incoming complex samples $s(n)$ and the samples generated by the complex conjugate operator. The PD output is a phase error signal which the LF is subsequently filtering. The LF has a fundamental role in filtering out the noise and the higher frequency components. Afterwards, the filtered signal coming from the LF go to the NCO, which steers its frequency and generates the new phase estimate.

The loop filter is a Proportional Plus Integrator (PI) filter chosen because it provides better tracking performance concerning other first-order filters. Indeed, without noise, the steady-state phase error is zero in the case of phase and frequency offset, which is a typical condition for the dynamic case. The behaviour of a second-order PLL depends on two main parameters, the loop noise equivalent bandwidth B_n and the damping factor ζ.

The convergence to steady-state strongly depends on B_n, where smaller loop bandwidth values correspond to longer transient and higher phase estimate accuracy. On the opposite, the ability to follow the dynamic signal variation increases with the increase of B_n. Therefore, a trade-off is required in the design of the PLL to guarantee fast locking time and good accuracy.

The discrete-time PLL behaviour can be set by using three parameters, the PI filter coefficients K_1, K_2 and the quiescent frequency of the NCO η_0. They are fixed as follows:

$$\eta_0 = 2\pi f_0 \Delta t, \tag{4.19}$$

$$\mathrm{K}_1 = \frac{4\zeta\left(\dfrac{\mathrm{B}_n \Delta t}{\zeta + \dfrac{1}{4\zeta}}\right)}{1 + 2\zeta\left(\dfrac{\mathrm{B}_n \Delta t}{\zeta + \dfrac{1}{4\zeta}}\right) + \left(\dfrac{\mathrm{B}_n \Delta t}{\zeta + \dfrac{1}{4\zeta}}\right)^2}, \tag{4.20}$$

$$\mathrm{K}_2 = \frac{4\left(\dfrac{\mathrm{B}_n \Delta t}{\zeta + \dfrac{1}{4\zeta}}\right)^2}{1 + 2\zeta\left(\dfrac{\mathrm{B}_n \Delta t}{\zeta + \dfrac{1}{4\zeta}}\right) + \left(\dfrac{\mathrm{B}_n \Delta t}{\zeta + \dfrac{1}{4\zeta}}\right)^2}, \tag{4.21}$$

where Δt is the time step between two samples, ζ is the so called damping factor and f_0 is the NCO frequency which must be equal to f_i the CW frequency to track.

To improve the performance of the PLL, we apply the processing technique shown in Fig. 4.8 to the signal before entering the loop. The approach uses a Notch filter, and it allows to isolate the CW, reducing the noise and the interference terms. Subsequently, the constraint on the loop noise equivalent bandwidth can be slightly relaxed without performance loss and improving the convergence time. We do this by splitting the signal into two paths. The first path is delayed by z^{-1}, and on the second path, a Notch filter filters out the signal of interest. In the last step, we subtract both paths and obtain a small bandpass filter.

The notch filter that matches the tone of interest has the response function [82]

$$H(z) = \frac{1 - z_0 z^{-1}}{1 - \kappa z_0 z^{-1}} \text{ with } 0 \le \kappa < 1 \tag{4.22}$$

Here z_0 is the complex zero point, which is the frequency f_i to be suppressed and can be calculated over this frequency according to

$$z_0 = e^{j 2\pi f_i \Delta t}. \tag{4.23}$$

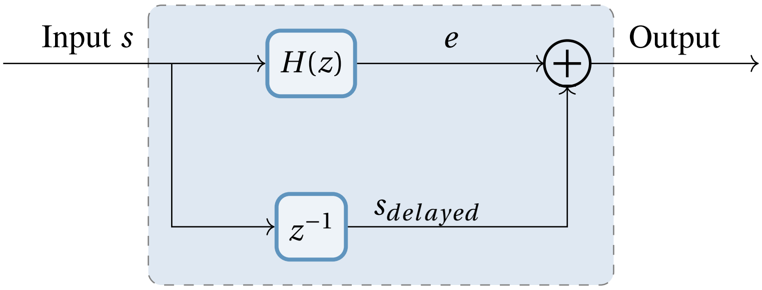

Figure 4.8: Block diagram of notch filter.

The pole position depends on κ, the so-called contraction factor, which makes the bandwidth of the filter [83].

We implemented the PLL and the notch filter in Python, as described above, to simulate and test them first. In general, a PLL is real-time capable when implemented close to the hardware, but our simulation requires considerably more computing power and is therefore not suitable for real-time testing. The advantage of our implementation is that it fits easily into the existing simulation environment and allows for easy changes.

EQUIVALENT OBSERVATION TIME

Up to now, it was clear that the only samples taken into account are within our defined observation time. That does not apply to the PLL anymore, because here we compare the phase sample by sample. However, the different filter steps also considered measurements acquired in the past. To compare the performance of our different approaches, we want to calculate the amount of sample that we would need at least in a Maximum Likelihood estimator to achieve the same performance as a converged PLL.

We assume that the ML estimation reach the CRB [70] as defined in (3.15). When we know the amplitude A of the aiding carrier and the variance of the phase estimate $\mathrm{var}(\varphi_1)$ and noise σ^2, we can transform the CRB to

$$N \geq \frac{2\sigma^2}{\mathrm{var}(\varphi_1)\, A^2}, \tag{4.24}$$

to give an indication how many samples a ML estimation would need at least to have similar performance, we taking in to account the sample rate. Consequently, we calculate an equivalent observation time T_{eq}. To get knowledge of the needed parameter, we utilize again a Monte Carlo simulation with 1000 runs. The parameters are chosen to a frequency of 303.275 kHz and an amplitude $A = 0.001$ for a sample rate of 1 Ms/s. As noise variance we again use σ^2 =2.50×10^{-7} as low, σ^2 =1.22×10^{-5} as medium and σ^2 =8.09×10^{-5} as high noise variance.

The phase of the simulated samples is then estimated with the Python implementation of the PLL with different values of B_n and $\zeta = 1/\sqrt{2}$, utilizing a notch filter with $\kappa = 0.9999$. From the estimates, we can calculate the variance after convergence of the result and obtain a sample equivalent.

In Tab. 4.2 we see the obtained estimation variance, the equivalent sample number and observation time T_{eq} for the three defined noise levels as a result of our simulation. As the

Table 4.2: Calculated equivalent observation times for three noise levels.

Noise level	B_n	$\mathrm{var}(\varphi_1)$	N	T_{eq}
Low	0.4	3.15×10^{-6}	158620	0.16 s
	0.2	7.03×10^{-7}	710320	0.71 s
	0.1	1.43×10^{-7}	3486793	3.49 s
Medium	0.4	3.74×10^{-6}	6411107	6.41 s
	0.2	7.3×10^{-7}	32860064	32.86 s
	0.1	1.64×10^{-7}	145570595	145.50 s
High	0.4	3.67×10^{-6}	44007063	44.00 s
	0.2	7.13×10^{-7}	226468066	226.46 s
	0.1	1.61×10^{-7}	1000784842	1000.78 s

PLL includes a filter, we observe that the performance depends on the noise level, where the PLL can increase the performance compared to the ML estimation for higher noise levels as T_{eq} increase. By changing the parameter B_n and ζ to maximise the equivalent observation time, the performance is further adjusted.

4.3. COMPARISON OF PHASE ESTIMATION ALGORITHMS

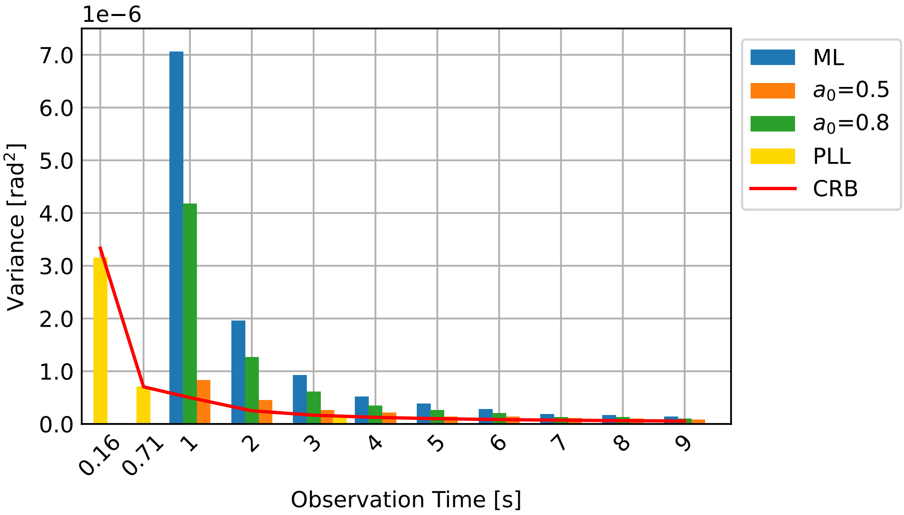

Figure 4.9: Estimation variance and CRB of CW1 for different observation times in low noise conditions.

In this chapter, we have described three different approaches to estimating the phase in a MF R-Mode signal. First, we evaluated the properties of ML estimation, which we extended to LS estimation by applying windows to improve performance for short observation times. As a second LS approach, we described a PLL to obtain continuous phase estimates and improve performance at high dynamics.

So far, we have already compared these approaches with the ML estimator for three different noise scenarios. In this section, we want to compare all three estimators in a static scenario and extend the comparison to the observation time for a complete R-Mode signal. As before, we simulate the three noise levels low, medium and high with the corresponding variance $\sigma^2 = 2.50 \times 10^{-7}$, $\sigma^2 = 1.22 \times 10^{-5}$ and $\sigma^2 = 8.09 \times 10^{-5}$.

For each scenario, we estimate the phase for the lower continuous wave at 303.275 kHz derived from the FFT, two window approaches and the PLL. We simulate the FFT and the windows with parameter $a_0 = 0.5$ and $a_0 = 0.8$ for the observation time from 1 s to 9 s in 1 s steps. To compare these results with the PLL, we use T_{eq} from Tab. 4.2 as the observation time for the PLL. Therefore, we need to use the same simulation as before, with a notch filter with $\kappa = 0.9999$ and the PLL with $\text{B}_n = [0.4, 0.2, 0.1]$ and $\zeta = 1/\sqrt{2}$.

In Fig. 4.9 we plot the results of CW1 for the low-noise scenario as a bar graph, where the blue bar represents the FFT, the orange one the window with $a_0 = 0.5$, the green one the window with $a_0 = 0.8$ and the yellow one the PLL results. In addition, we show the CRB as a red line to indicate the expected best performance.

For the lower noise scenario, the PLL only achieves low observation times up to 3.49 s However, as described in Section 4.1.3, the result approaches the lower limit at a longer observation time. As expected, the windowing approaches are most beneficial for short observation times, with the window $a_0 = 0.5$ performing best, which is consistent with the results in Section 4.2.1. This sequence continues until 9 s of observation time, while the difference between the approaches decreases.

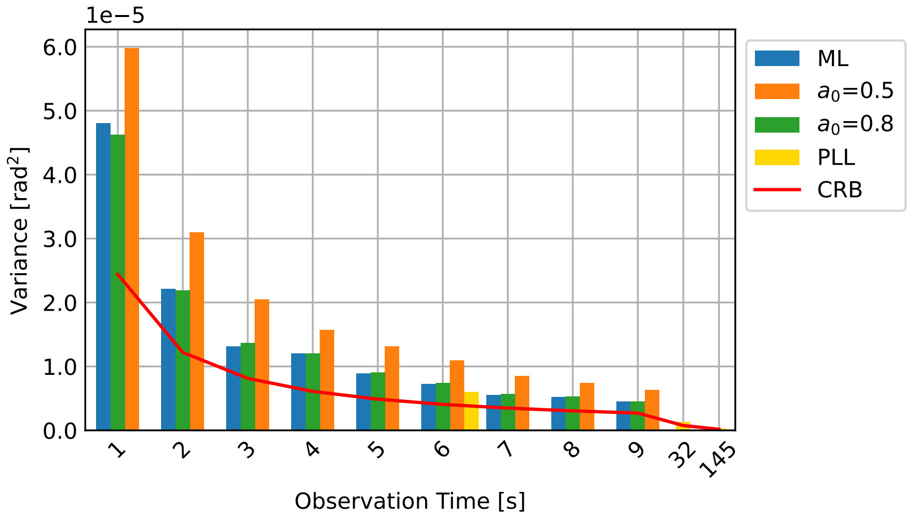

Figure 4.10: Estimation variance and CRB of CW1 for different observation times in medium noise conditions.

Fig. 4.10 present the result for the medium noise scenario. We keep the colour coding from Fig. 4.4. In general, we see that all diverge towards the limit for longer observations. As the noise increases, we observe that the performance of the window with $a_0 = 0.5$ is now the worst, while the window with $a_0 = 0.8$ and the FFT have similar performance as we have already observed in Section 4.2.1. It is clear that the PLL is very good at suppressing noise and outperforms the other results at 6 s observation time. The smaller bandwidth of the PLL also shows a fit to the lower limit.

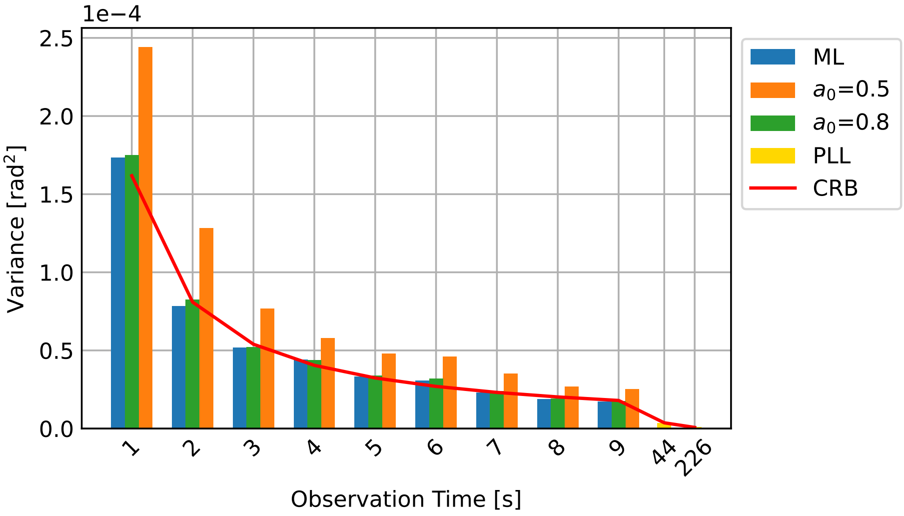

Figure 4.11: Estimation variance and CRB of CW1 for different observation times in high noise conditions.

The last scenario for high noise levels is drawn with the same colour scheme as before in Fig. 4.11. Now the noise influence becomes the leading influence, and the MSK contribution get negligible. Therefore, the FFT outperformed the window approaches, and we come very near the lower bound. Again, it is clear that the PLL suppresses large parts of the broadband noise and gives results with longer equivalent observation times.

All three noise levels are consistent with the general assumptions we described in the theoretical introduction of our estimator in Section 4.1 and Section 4.2. In this section, we have clearly shown that a carefully designed LS estimator can outperform the ML estimator. In low noise enviroments, the windowing approach performs best as the power leakage can not be neglected. For higher noise levels, the noise suppression of the PLL becomes the best performing approach. Therefore, a suitable estimator must be chosen for each application. In Section 6.3.1, we compare different window functions with real measurements to verify our approach. The comparison was not possible for the PLL because our current software implementation uses too many computing resources, but an improved implementation will fix the issue in the future.

4.4. INITIAL POSITION ESTIMATION

In the previous sections of this chapter, we have described various phase estimation methods. However, to show that the MF R-Mode is suitable for position estimation, we need a position solver. Our initial approach to this problem is discussed in this section. For this work, we focus on the use of a Least Square solver. Nevertheless, other position solvers are conceivable, such as a Kalman filter.

For our approach, we have to consider that the signal propagates as a groundwave, as described in Chapter 2. Consequently, we cannot derive the geometric distance between transmitter and receiver by a line of sight given by the classical Euclidean distance formula. Instead, we have to obtain the range by the so-called "geodesic curve" or simplified "geodesic" [84], which describes the minimum distance between two points on the Earth, which is assumed to be a perfect ellipsoid. The reference system WGS84 is used to locate ships at sea. Due to the non-linearity of the problem, the LS approach is suitable to estimate the position of the receiver and the clock error, as described in [85].

The system of equations we want to solve contains three unknowns, the geodetic latitude ϕ_u, the geodetic longitude λ_u and the receiver clock error δt. Concerning the R-Mode system time. The pseudo range $r_{\mathrm{p},i}$, which we calculate from the phase estimate according to Chapter 2, also takes into account the calibration error, can be modelled as follows

$$r_{\mathrm{p},i} = \rho_i + c_0 \delta t + \epsilon_i. \tag{4.25}$$

Here i indicates the station index, while ρ represents the geometric distance and ϵ a noise term. Using the iterative Vincenty approach, [86], we can calculate the geodetic ρ from our estimate. Through this approach, we also obtain estimates for the forward and backward angles we use to directly define the geometry matrix.

For an overdetermined system with m observations, we can generally compute the LS solution as [85, 87]

$$\mathbf{x}_l = \mathbf{x}_{l-1} + \mathbf{M}(\mathbf{H}^{\mathrm{T}}\mathbf{W}\mathbf{H})^{-1}\mathbf{H}^{\mathrm{T}}\mathbf{W}\mathbf{y}_{l-1}, \tag{4.26}$$

where l is the recursion index of the algorithm. With $\mathbf{x}_l$ we represent the updated estimate $(\phi_{u_l}, \lambda_{u_l}, \delta t_l)^{\mathrm{T}}$, while $\mathbf{x}_{l-1}$ is the previous estimate $(\phi_{u_{l-1}}, \lambda_{u_{l-1}}, \delta t_{l-1})^{\mathrm{T}}$ of the unknowns. $\mathbf{H}$ describes the geometry matrix and $\mathbf{W}$ denotes a weight matrix, while $\mathbf{M} \in \mathbb{R}^{m\times 3}$ is a transformation matrix, which we can obtain as [85]

$$\mathbf{M} = \begin{pmatrix} 1/R_M(\phi_{u_{l-1}}) & 0 & 0 \\ 0 & 1/[R_E(\phi_{u_{l-1}})\cos\phi'_{l-1}] & 0 \\ 0 & 0 & 1 \end{pmatrix}. \tag{4.27}$$

Here we refer to $R_M(\phi)$ as the north-south radius of curvature, $R_E(\phi)$ as the east-west radius of curvature and ϕ' as the angle taken by an east-west great circle changing by one unit of length. These values depend on the latitude of the user, and we calculate them according to [85]

$$R_M(\phi) = \frac{a(1-e^2)}{(1-e^2\sin^2\phi)^{3/2}} \tag{4.28}$$

$$R_E(\phi) = \frac{a}{(1-e^2\sin^2\phi)^{1/2}} \tag{4.29}$$

$$\cos\left(\phi'\right) = \sqrt{1 - \frac{R_M^2(\phi)}{R_E^2(\phi)}\left(1-\cos^2\left(\phi\right)\right)}. \tag{4.30}$$

Where a and e are the semi-major axis and eccentricity of the WGS84 ellipsoid.

We calculate the geometry matrix $\mathbf{H} \in \mathbb{R}^{m\times 3}$, which contains the unitary components of the line of sight vector in the navigation frame, using the bearing angle α obtained by

Vincenty's formula, as follows [88]

$$\mathbf{H} = \begin{pmatrix} \cos\alpha_1 & \sin\alpha_1 & 1 \\ \cos\alpha_2 & \sin\alpha_2 & 1 \\ \vdots & \vdots & \vdots \\ \cos(\alpha_m) & \sin(\alpha_m) & 1 \end{pmatrix} \tag{4.31}$$

The weighting matrix $\mathbf{W} \in \mathbb{R}^{m \times m}$ should account for the differences in data quality [87]. Since we derive the characterisation of the errors only from the first measurements, we assume that the weighting matrix is a diagonal matrix in which all stations are treated equally, i.e. we choose all values on the diagonal to be 1. Finally, we define $\mathbf{y}_{l-1}$ as pre-fit residuals, which are determined as follows

$$\mathbf{y}_{l-1} = \begin{pmatrix} r_{\mathrm{p},1} - \hat{\rho}_{1_{l-1}} \\ r_{\mathrm{p},2} - \hat{\rho}_{2_{l-1}} \\ \vdots \\ r_{\mathrm{p},m} - \hat{\rho}_{m_{l-1}} \end{pmatrix}. \tag{4.32}$$

Where $\hat{\rho}_{i_{l-1}}$ represents the geodesic for the previous estimated point to i-th station.

The algorithm presented here was implemented in and integrated into the processing, which we described in more detail in Section 5.3.

5

RESEARCH RECEIVER

So far, this thesis has covered the theoretical background of how we can determine the range and position from the MF R-Mode signals. However, to make this approach a reality, we need well-described hardware to build a receiver. We decided to use Software Defined Radio (SDR) with an analogue front end to test the described algorithms. Johnson [53] and Swazek [39] describe a similar approach. Compared to our work, they use digital acquisition cards for a Personal Computer (PC) and a single defined front end whose phase influence is not well described. In contrast, we have tested different hardware components in terms of phase influence to build a modular research receiver that can use different components and thus give the best possible results for use as a static or dynamic receiver.

Each receiver included four main components: the antenna, a gain stage, filtering and digitisation. We used several commercially available and home-built parts that we need to characterised to indicate how well they are suited to our application. In Section 5.1, we describe the antenna, the amplifier and the filter. The antennas, in this case, pose a particular problem, as conventional antenna measuring devices do not support this frequency range due to the long wavelength. In 5.2, we examine three different devices for digitisation in various price ranges. We use the components described above to find a frontend that fits the price class of the unit. In the last step, we design an MF R-Mode simulator to test the previously described designs.

5.1. FRONTEND COMPONENTS

Similar to the transmitter chain described in Section 2.3, each component of the receiver introduces some delay. However, we have easier access to the receiver because of the smaller size of the parts. Therefore, we can characterize each device separately with S-parameter measurements. These measurements can be linked together in a linear simulation, for example, QucsStudio [89] or scikit-rf [90] can be used for this. On this basis, we have a flexible simulation of the phase delay in the receiver, and we can describe the influence of new components in advance.

5.1.1. RECEIVING ANTENNA

The receiving antenna of our system must meet specific requirements. Besides a good antenna gain, we also need knowledge about the phase shift of the received signal. We have shown in Section 2.3.3 that transmitting dipole E-field antennas can be described with equivalent circuits of lumped elements. The same applies to E-field dipoles and single loop antennas on the receiving side. Commercially available radio beacon antennas usually use a grid of H-field antennas to compensate for the blind spot of a single loop. They are optimised to receive signals from all directions, resulting in a phase offset depending on the direction of arrival. For conventional radio beacon service, this is irrelevant but crucial for MF R-Mode, as we need to ensure that by the phase of the received signal, to estimate the propagation delay.

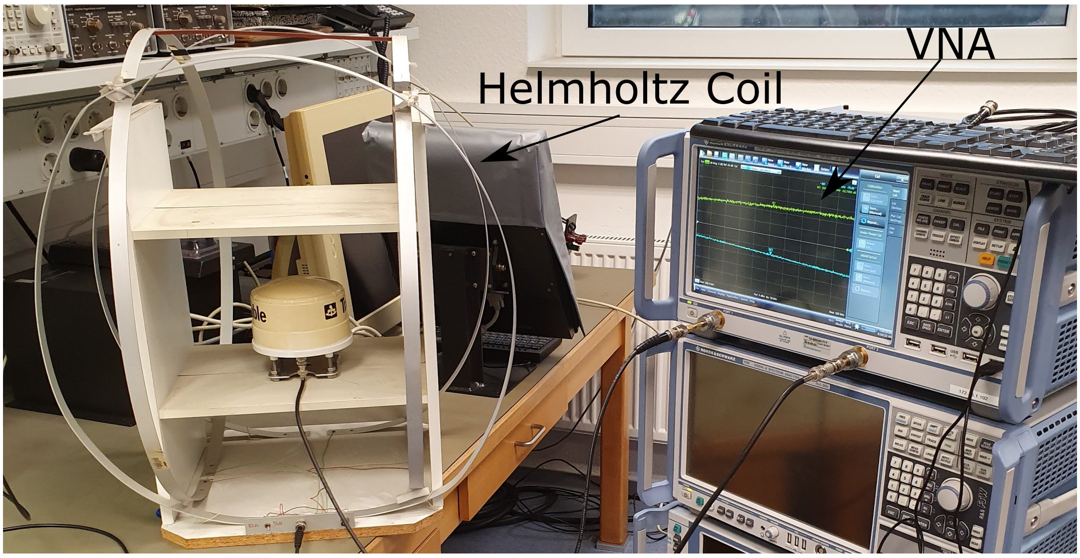

Figure 5.1: Measurement setup with Helmholtz coil and VNA.

We verified this effect with laboratory measurements. The antenna cannot be measured as two-port as easy as the other components. However, on the receiver side, the size of the antenna decreases compared to the transmitter side. Thus, we can install the antenna in a Helmholtz coil, which provides a far-field condition in a small space [91]. For our measurement, the coils work as transmission antenna, and the antenna under test receives the signal. This measurement can be conducted by a Vector Network Analyser (VNA). Fig. 5.1 at the WSV shows the overall setup in the laboratory in Koblenz.

We show the result of the above measurement for a commercial CSI H-field antenna in Fig. 5.2. The orientation was changed manually in interval steps of 90° so that we show four measurements named according to their orientation angle. It is clear that the measured phase depends on the direction of arrival, so this type of antenna is not suitable for use in a dynamic MF R-Mode receiver, as the measured distance to the transmitter would depend on the unknown orientation of the antenna.

ALTERNATIVE ANTENNAS

As an alternative to the described commercial DGNSS antennas, we propose the use antennas with simple patterns and known phase shift of the signal not depending on the angle

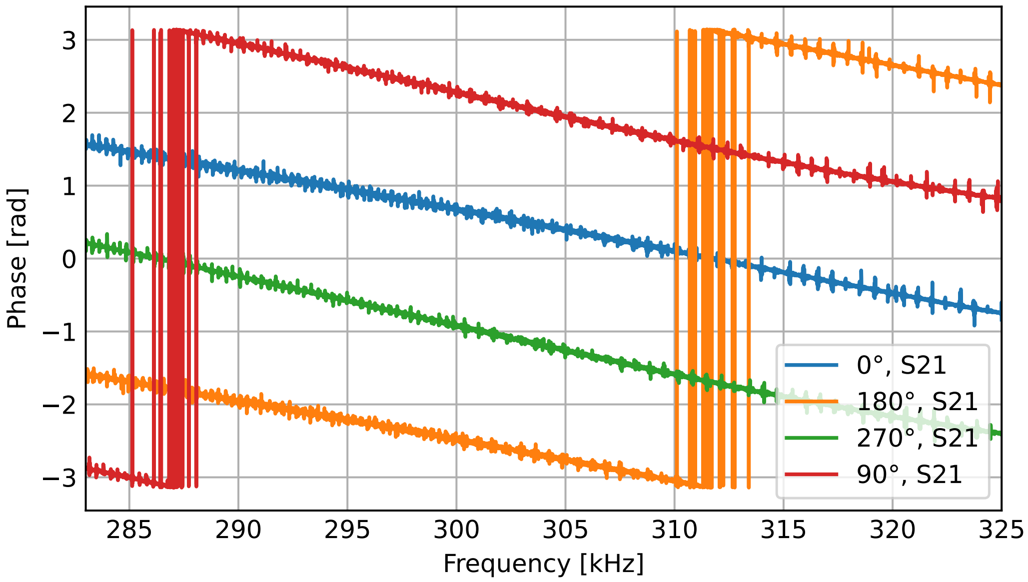

Figure 5.2: Phase shift for different angle of arrival measured in the Helmholtz coil for the MF R-Mode band.

of arrival. In this work we have tested two types of antennas, an H-field loop antenna and an E-field dipole antenna. The assumption that the phase is independent of the direction of incidence is not given for the H-field antenna, the sign is changed depending on the passage direction, but this can be easily corrected.

A single loop antenna has two minima in the directional diagram, geometrically located on each side of the surface that spans the loop. At each of the minima the phase changes by π in the pattern, after which the phase stayed constant until the next minimum. This directional pattern can be used to mask out nearby disturbances in a static scenario.

For the dipole, the description is even simpler, since the antenna has a circular pattern in the plane along the earth's surface, and thus the phase shift is the same in all directions.

The general assumption is that an E-field antenna is more susceptible to interference than an H-field antenna. To verify this, we tested the antenna amplifier MegaLoop FX [92] connected to a loop of 80 cm diameter and a BoniWhipe [93] dipole E-field antenna in the field. The measurement was made at a distance of about 40 km from the radio beacon Zeven. A Rohde & Schwarz (R&S) FPC1000 spectrum analyser [94] was used to measure the spectrum with 30 Hz bandwidth. Fig. 5.3 shows the recorded spectra of the E-field antenna in orange and the MegaLoop in blue.

The total noise levels in Fig. 5.3. are similar for both antennas. However, it is clear that the E-field antenna is more susceptible to distortion than the H-field loop. In particular, the peak at 301 kHz and the high noise floor between 305 kHz and 310 kHz are not to be expected. It has been our experience that the noise was greatly reduced after earthing the cable's shielding. In addition, a suitable power supply must be set up to achieve good results.

From these simple initial tests, we conclude that for the MF R-Mode system, a properly set up H-field loop antenna such as the MegaLoop is the first choice for monitoring stations in defined locations, as the change of the sign is neglectable. The E-field antenna is more

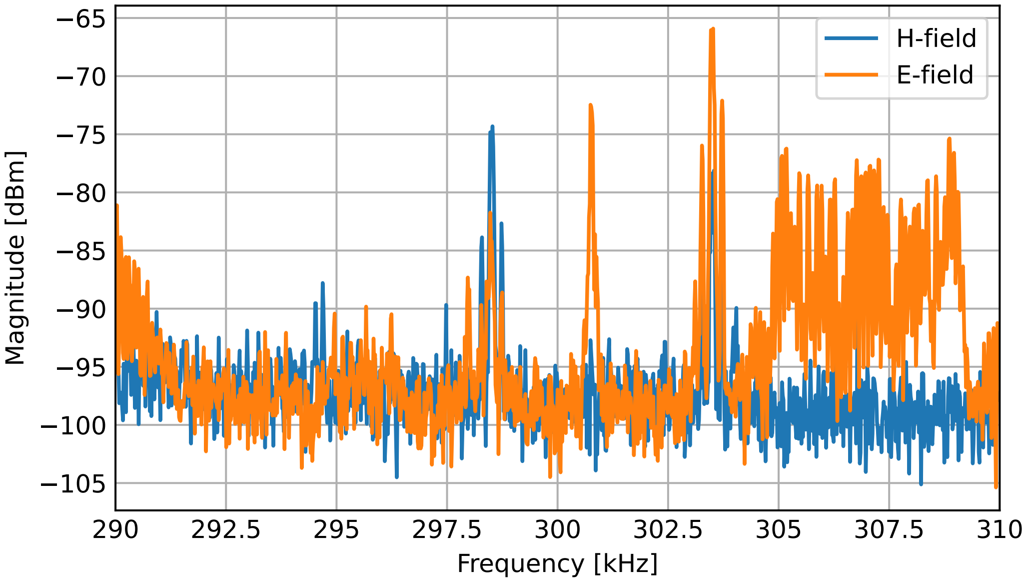

Figure 5.3: Comparison of received spectra from E-field and H-field antenna.

suitable for mobile users due to its omnidirectional antenna pattern in phase. We will follow this idea in the further course of this work.

5.1.2. TWO PORT CHARACTERIZATION

Compared to the previously characterized antenna, which only has an input port and transmits a signal, filter and amplifier are two-port components. That simplifies the measurement technique considerably, as we can use a VNA for measurements. For our test of the two-port parts, we used an R&S ZNL [95] which is calibrated with a ZN-Z235 CalKit [96]. Doing so allows measurements with a phase uncertainty of less than 0.5°. Utilizing the S-parameter measurement results, we can cascade the different components to describe the different configurations in the future.

AMPLIFIER

We need an amplifier in the receiver to detect weak transmitters and allow stable estimations on the signals. So far, we have tested two different types, the Low Noise Amplifier (LNA) MiniCircuit ZFL-500Ln+ [97] and the Hewlett Packard MSA-0335 [98] power amplifier. Both units are in a metal housing that also contains a bias network. We present the resulting amplitude measurements transmission S21 in Fig 5.4a. Here, we observe that both amplifier work with a gain of around 11 dB for the MSA-0335 and a gain of 31 dB for the ZFL-500Ln+. Also, of interest is the phase change over frequency, which we show in Fig. 5.4b. The overall phase change between 100 kHz - 900 kHz is quite huge with around 0.5 rad for the LNA and for the power amplifier. For both amplifiers, the most significant change happened in the lower band up to 400 kHz. Unfortunately, this includes the frequencies where MF R-Mode is operating. A closer examination shows that the ZFL-500Ln+ changes phase by 1.6° and the MSA-0335 by 2° for the MF band of interest. Another problem with S-parameter measurements is that we cannot resolve the ambiguity that occurs within the

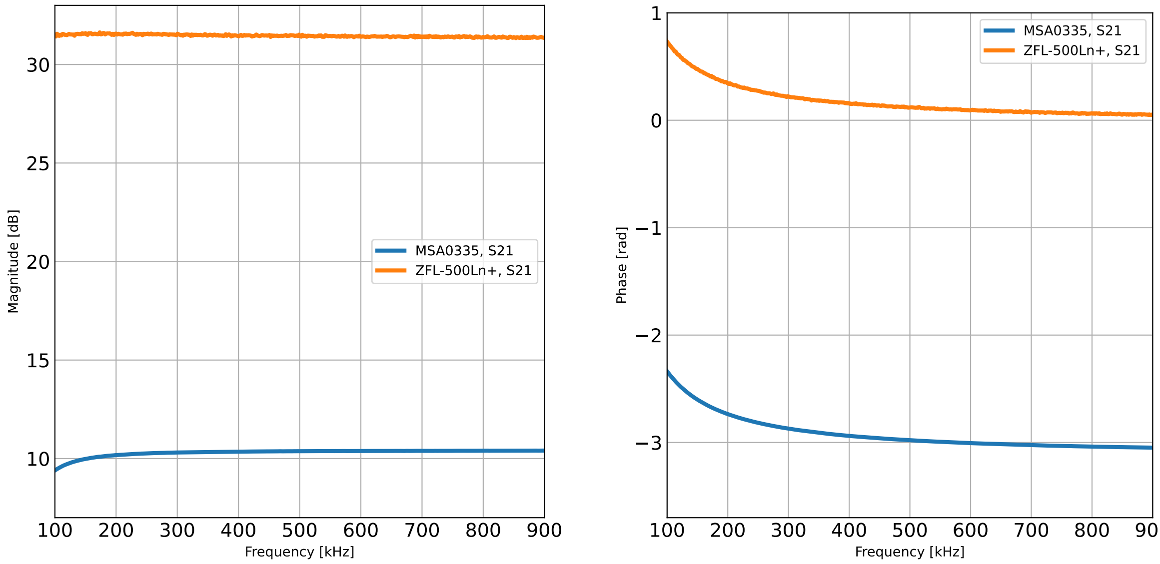

(a) (b)

Figure 5.4: Comparison of S12 between two amplifiers for (a) magnitude and (b) phase.

Device Under Test (DUT). One possible solution would be to apply time gating, which deliver a propagation delay.

FILTER

The last component we describe is the bandpass filter, which mitigates out-of-band distortion and noise energy. So far, we have measured three different filters. The Krohn-Hite Model FMB3002 is an active filter [99] with passband 285 kHz to 325 kHz. Furthermore, we tested a passive approach by combining the low-pass LPF-BOR35+ [100] with cut-off frequency at 350 kHz and the high-pass ZFHP-0R23-S+ starting at 230 kHz [101] from Mini-Circuits and our design from discrete components on the stripboard with the designed passband from 250 kHz to 375 kHz. How we select these components and design the discrete filter is described in more detail in the Appendix A.

In Fig. 5.5a we show the magnitude of the S-parameter S21 for the three different components. The Krohn-Hite filter has a high insertion loss and a very flat slope for the higher bands. Furthermore, the insertion loss seems to be huge. Here it is important to note that we set the gain to zero. The homemade component is the narrowest of the filters, with a steeper slope than the Krohn-Hite and the same insertion loss. The combination of low-pass and high-pass is wider-banded but has distinct band edges where the slopes decrease quickly and a low insertion loss.

Of great interest for the R-Mode system is the phase of such a filter, which we show in Fig. 5.5b for the S-parameter S21. All filters have multiple circular shifts within the band from 100 kHz to 500 kHz. In addition, the phase shift is not linear, which makes correction difficult. We can see that we need a separate correction term for each CW we want to estimate in our receiver since the phase shift depends strongly on the frequency. The filters have different advantages and disadvantages. The active filter can provide additional amplification if required. The passive low-pass and high-pass combination brings only

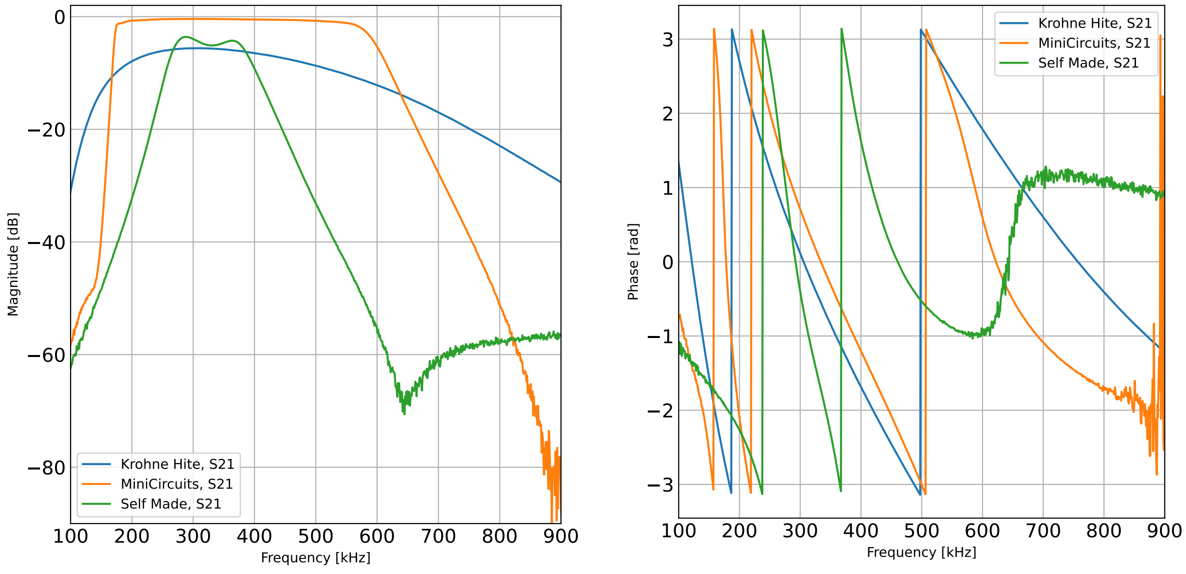

(a) (b)

Figure 5.5: Comparison of S12 between the three different filter for (a) magnitude and (b) phase.

minimal insertion loss, and the self-built filter offers good suppression of interference in the close range. So the choice depends on the receiver's application.

5.2. RECEIVER DESIGNS

We combined the previously introduced components with a different acquisition device in different price ranges. As the overall design is modular, each component could potentially be replaced by the other to increase performance or reduce the size of the setup. Therefore, the introduced designs are only an example of designs in different price ranges and suited for different problems. First we introduce the German Aerospace Center (DLR) research receiver in 5.2.1, used for the field test presented in Chapter 6. We then present a design that overcomes the issue of internal delay in the acquisition step, based around an oscilloscope in 5.2.2. With the latest design, based around the RTL-SDR in 5.2.3, we took the first step to a more widely used receiver, showcasing that no laboratory-grade equipment is needed to gain good performance, and therefore a commercial application is possible. In order to verify the ideas, we build an MF R-Mode simulation environment in 5.2.4 , which is used in the end for a comparison in 5.2.5.

5.2.1. DLR RESEARCH RECEIVER

The hardware of the research receiver of the DLR was first used for initial field tests and has been continuously developed since then. The components have changed only slightly. The receiver typically uses off-the-shelf components, which allows for faster development, easy installation of modifications and easy replicability. It has therefore been possible for the German and Swedish administrations responsible for DGNSS to use our receiver as a monitoring station.

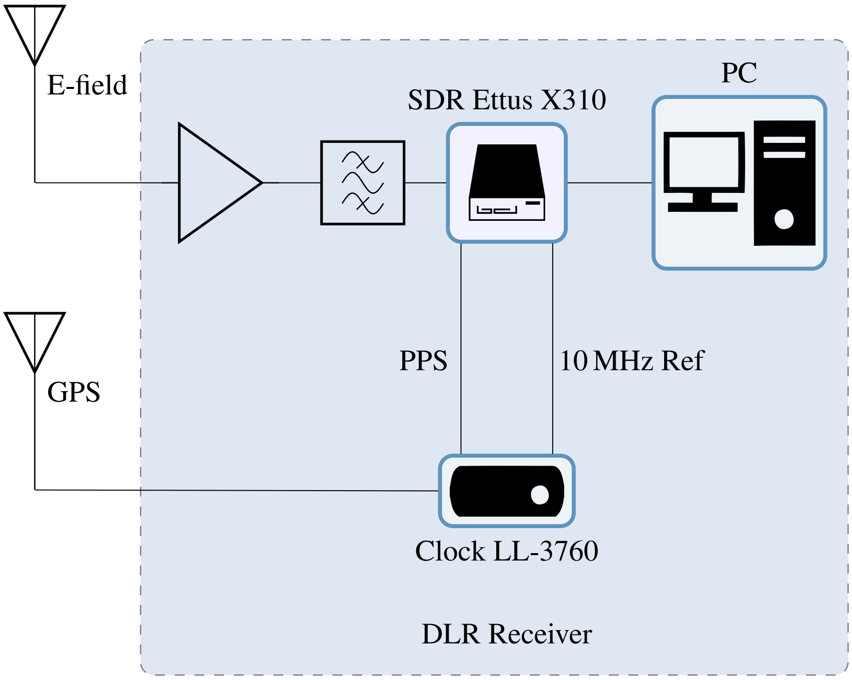

Figure 5.6: Block diagram of MF R-Mode receiver.

Fig.5.6 shows the chosen SDR-based approach for our receiver. We used an active bandpass filter as the front end for the SDR. For this purpose, we currently use the Krohn-Hite FBM3004 with a passband of 285 kHz to 325 kHz and an adjustable gain of up to 30 dB. Alternatively, the external Mini Circuits ZFL-500LN+ LNA provide fixed amplification of 24 dB, and we choose the filter gain to zero.

In one version of this receiver, the Ettus N210 [102] with two channels is used as the SDR, which offers the same interface as the alternatively used Ettus X310 [103] with four channels. Due to the increased number of channels, MF and VDES R-Mode can use the same SDR for reception, but VDES R-Mode is outside the scope of this work. In addition, the X310 offers the possibility of implementing advanced Digital Signal Processing (DSP) functions with RFnoc [104] on the SDR, so the SDR process more tasks in the future. However, we were not able to characterise the propagation delay between the input port and the internal Analog Digital Converter (ADC), which introduces a slight offset when we only want to estimate the distance to a single station.

The SDR provide the samples of the digitized signal to the PC. We currently use a computer with Intel i7 CPU, 16 GB RAM, two 1 Gbit Ethernet interfaces, one Solid State Disk (SSD) and 5 TB HDD. This configuration is intended to provide more computational power for research activities; in general, our approach can run with fewer resources. The various processing steps that occur within a Linux operating system are discussed in Section 5.3.

In addition, a GNSS-stabilized rubidium clock Lange Electronics LL-3760 provides an accurate time and frequency reference, which we connect to the SDR as a Pulse Per Second (PPS) and 10 MHz signal. This external reference was necessary during the first field tests because not enough stations were able to send MF R-Mode signals, and thus no synchronization within the system was possible. So, we used the clock as an additional station. Also, a stable reference is needed to use our receiver as a monitor station because we want to evaluate the quality of the individual station, not the complete system.

5.2.2. OSCILLOSCOPE RECEIVER

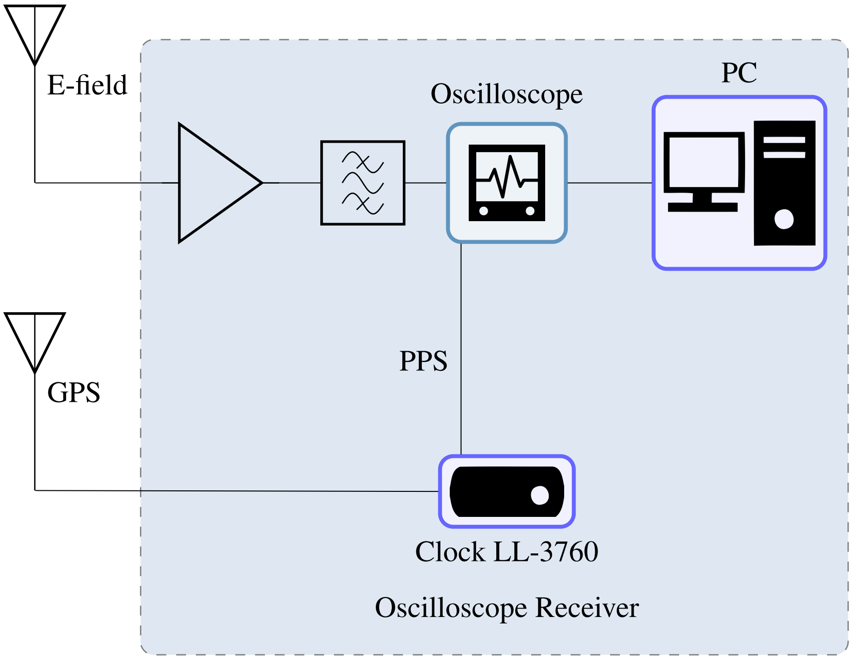

Figure 5.7: Block diagram of MF R-Mode receiver based around an oscilloscope.

The SDR-based receiver presented in 5.2 has a problem due to the unknown input delay, which is not optimal for use as a monitor station. We overcome the problem with modern digital oscilloscopes that we use as limited SDR [105], which is the basis for the alternative design presented here. The filter and oscilloscope used are cheaper than the components used in Section 5.2.1, but we expect lower performance due to the lack of synchronization capability. The general idea is to use the trigger functionality of the oscilloscope with the PPS signal of a clock to generate chunks of samples, where the full second starts the first sample. After the acquisition, the data are transmitted to a PC, where we can apply the phase estimation and consequently the positioning in the end. However, as we first need to transfer the data before a new acquisition is triggered, we must either reduce the observation time to less than 1s or only obtain data with a dead time in between, where we have no samples. We decided to accept lower update times, as we want to use this kind of design in a static scenario.

Fig. 5.7. present the general block diagram of this approach. Similar to the description in 5.2, we use an E-field antenna followed by an LNA and a bandpass filter. The oscilloscope triggered by the PPS signal performs then the digitization. In this approach, the recording device neglects the input delay since we use the trigger function of the oscilloscope, which has a known time relationship with the input signal. This is an advantage when we do not want to estimate the position but the distance to a station, which makes this approach practical for monitoring sites where the receiver observes the quality of the transmitted signals. Unfortunately, most oscilloscopes do not have a 10 MHz reference input that

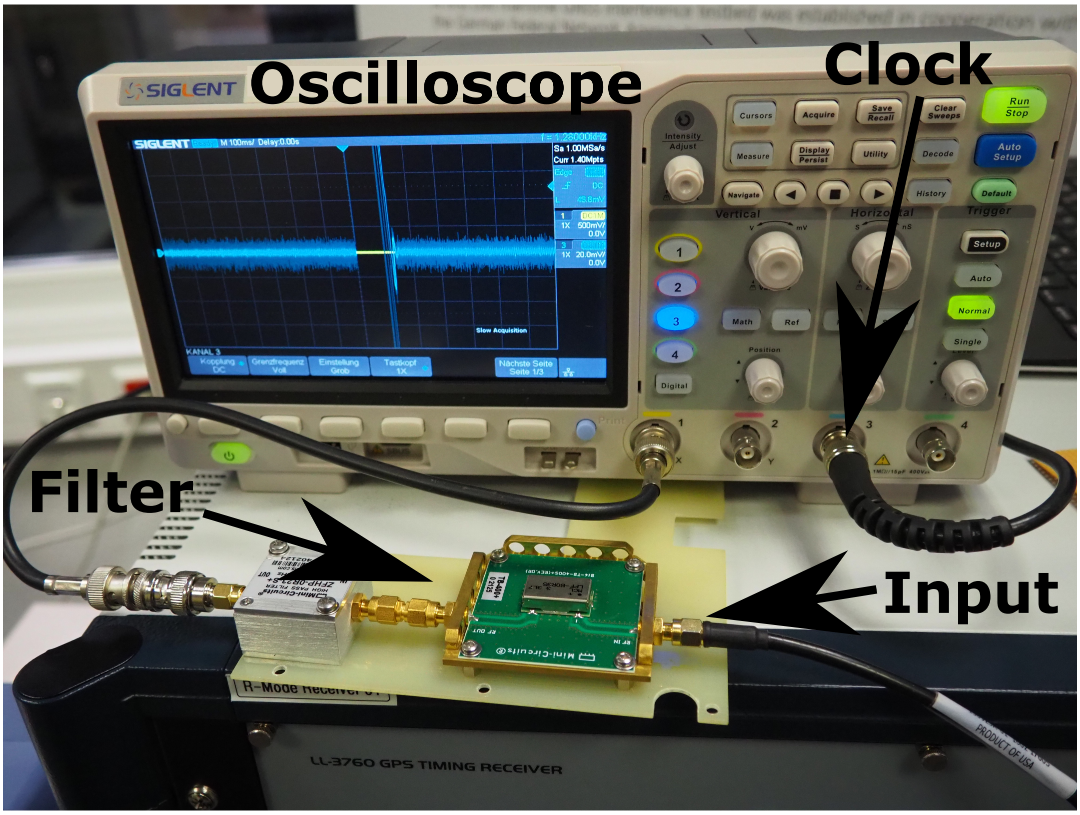

Figure 5.8: MF R-Mode receiver based utilizing an Oscilloscope.

allows synchronization with an external frequency reference, which reduces the accuracy of estimating the phase.

In Fig. 5.8 we show an example configuration for this approach that we tested in our lab. Since we are using a generated R-Mode signal, the LNA stage is not required, so the signal is fed directly to the bandpass filter. The filter consists of Mini Circuits TB-LPF-B0R35+ low-pass filter and ZFHP-0R23-S+ high-pass filter, forming a bandpass between 230 kHz and 350 kHz as described in Section 5.1. The oscilloscope we use is a Siglent SDS 1104X-E [106], which offers up to 1 GHz sample rate and a memory depth of 10 Mpoints. The bandpass filter link to channel one, and the PPS trigger connects to channel three. With this distribution between the channels, we achieve the maximum performance, as the sampling rate would otherwise be limited.

On the screen in Fig. 5.8 we see the display of the PPS signal in blue and the R-Mode test signal in yellow the blue edge rises in the middle of the screen, which corresponds to time zero, therefore triggering occurs correctly. In various tests, we have found that a visual check is beneficial to avoid misconfigurations.

5.2.3. RTL-SDR BASED RECEIVER

The previously presented receiver designs utilize external synchronization for high performance. However, it is not suitable for stand-alone use on a ship outside the initial tests. Discarding external allows us of much cheaper components. Therefore, we tried to design a receiver as affordable as possible.

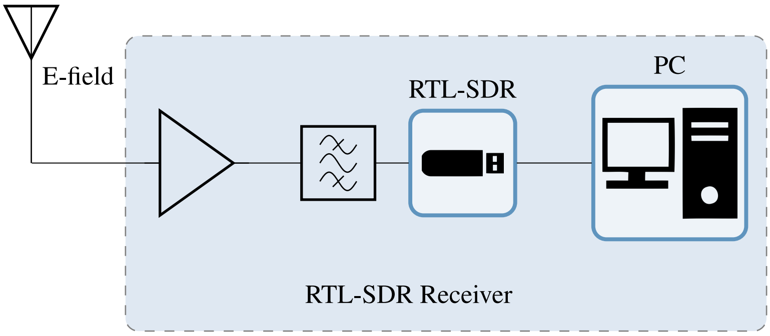

Figure 5.9: Block diagram of MF R-Mode receiver based on RTL-SDR.

Probably the cheapest SDR is the RTL SDR [107], which comes in various forms and price ranges. What they all have in common is that they use the RTL2832U [108] chipset in combination with a front-end chip originally developed for terrestrial television reception. However, the SDR can also deliver raw data to a host computer. For our experiment, we use the RTL-SDR V3, as this version has a built-in Temperature Compensated Oscillator (TCXO) with 1 ppm [109], which is crucial for estimation accuracy. However, without modification, the lower frequency band is around 500 kHz. Therefore, the built-in bias inductor had to be removed, after which the RTL-SDR MF R-Mode can receive signals. Further modifications are possible to bypass the internal TCXO and provide an external 10 MHz signal [110]. Also synchronization with a PPS signal is possible [111]. However, this would again require an external clock which is not the goal of this design.

In Fig. 5.9 draw a block diagram to present the different components. As previously, the front end consists of an E-field antenna, LNA and bandpass filter, followed by the RTL-SDR as a recording device, which has no external synchronization.

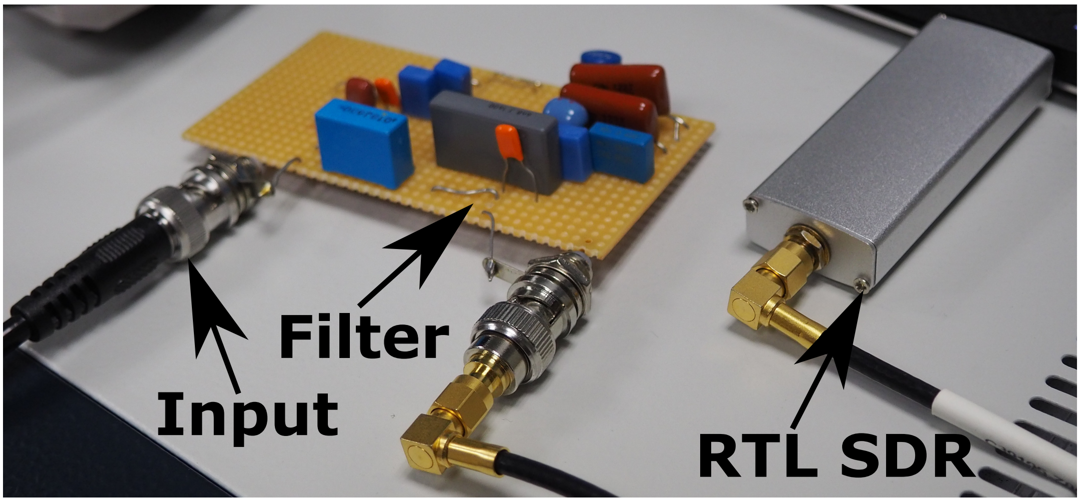

Figure 5.10: Low Cost MF R-Mode receiver based on RTL-SDR .

We tested the constructed design in the lab, which can be seen in Fig. 5.10, neglecting the LNA in the first stage. As a filter, we designed a discrete component filter with a passband of 250 kHz - 375 kHz, soldered on stripe board for fast inertial tests. Appendix A describe this filter in more detail.

5.2.4. HARDWARE IN THE LOOP SIMULATION FOR R-MODE SIGNALS

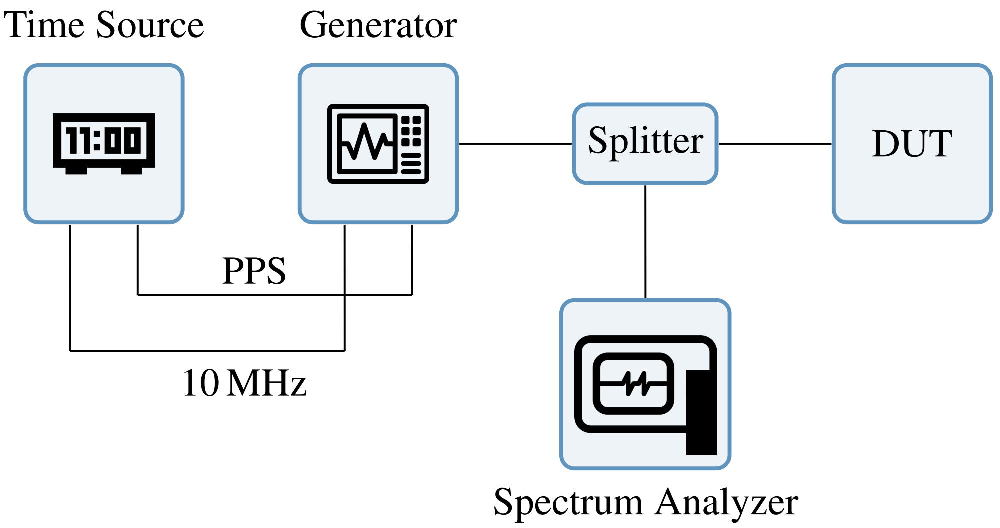

Figure 5.11: Block diagram of MF R-Mode simulation measurements.

To test our receivers in the laboratory, before we bring them to the field, we have developed an R-Mode hardware simulator based on an arbitrary function generator and shown as a block diagram in Fig. 5.11. In this case, we use a Tektronix AFG 31022 [112] replaying Comma Separated Values (CSV) files generated with our Python environment as described Section 2. This approach allows us to simulate an independent station on each channel for the marine beacon band and modify each component separately as in the software simulation. For precise timing, an external time source synchronizes the generator, in our case a GPS-stabilised rubidium clock. For initial measurements, the generated signal distributes to various DUTs, for example, the MF R-Mode receivers of DLR [3]. In addition, we fed one portion of the signal to a spectrum analyser, which monitors the generated signal. The setup is presented in Fig. 5.12. In our setup, we use the R&S FPC1000. For future field tests, it would be possible to use the signal generator on the transmitter side for initial tests by replacing the DUT with the transmitter of the station.

5.2.5. COMPARISON

To compare the three designs presented in 5.2, we set our signal simulator described in 5.2.4 to provide a test signal for three DUTs at once. The signal distribution allowed us to test all receivers simultaneously for 20 minutes after a warm-up period of the same length. To mitigate short-term effects, we compare the beat frequency of each receiver for a station centred around 303.5 kHz.

We do not synchronize the RTL-SDR to either a common PPS or a 10 MHz signal. Therefore, we expect our phase estimate to drift since we have not synchronized our local time frame to the modulator. Fig. 5.13 describe the initial result for the RTL-SDR. As expected, the phase estimate drifts linearly with the observed time. If we consider multiple stations for positioning, this constant drift will be reflected in the clock distortion, as explained in Section 4.4. Since we only want to compare the performance of a single station

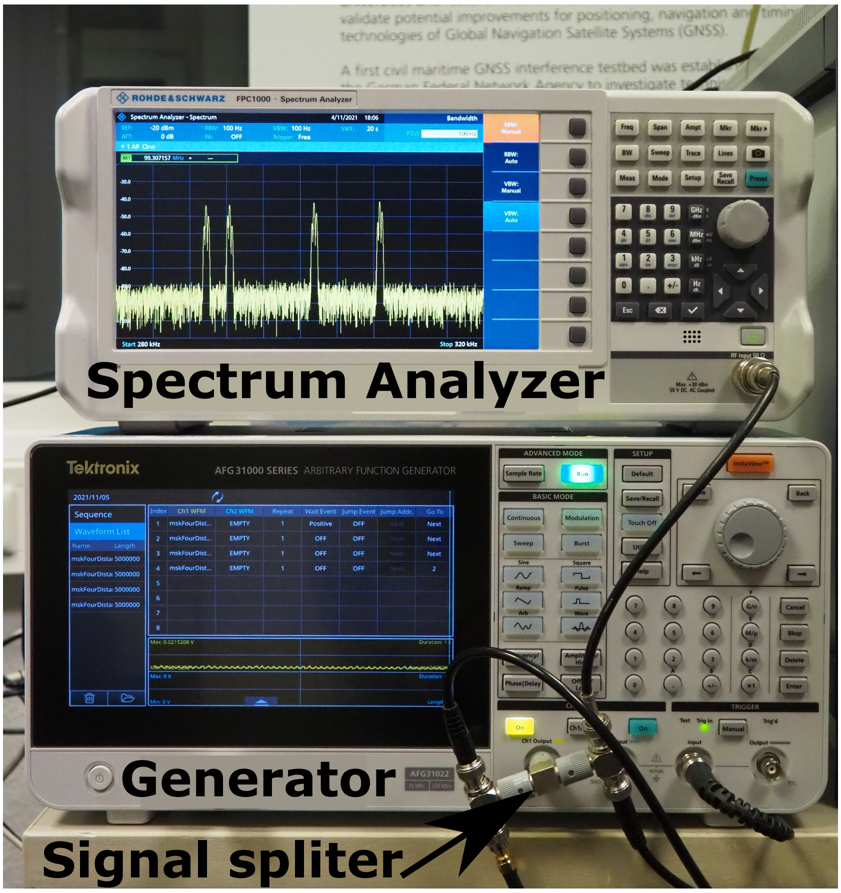

Figure 5.12: MF R-Mode signal simulator.

here, to reflect the use case of a monitoring receiver, we approximate the drift by a linear fitting, with a gradient of -0.86×10^{-3} rad/s, and correct our estimate accordingly.

The Ettus SDR based design used in this experiment utilise the N210 SDR synchronized with a 10 MHz reference and a 1PPS signal. It is important to note that we use two separate clocks for the signal generation and the receiver. However, we assume good synchronization between the different clocks because the external antennas are close together. We use the results of the DLR receiver as a reference to compare the designs that are not so closely synchronized.

We present the mean free results between the corrected RTL-SDR and the Ettus based receiver for 20 minutes in Fig. 5.14. For the first half, the estimation has a similar performance. Afterwards, the RTL-SDR result start to drift slightly until the end of the measurement to an offset of 0.5×10^{-3}. For the observed timespan we obtain a variance of 1.131×10^{-7} for the RTL-SDR and 6.153×10^{-8} for the Ettus SDR.

As a third design, we used the setup around the Siglent SDS 1104X-E, which triggers a measurement on our 1PPS signal. Thus, our estimation is periodically synchronized, and a constant drift is not expected. Since the data transmission end always after the acquisition, we can only take measurements every two seconds. In Fig. 5.15 we see the mean free error of the oscilloscope compared to those of the Ettus-based receiver. The oscilloscope has a peak-to-peak error that is two orders of magnitude higher, resulting in a variance of

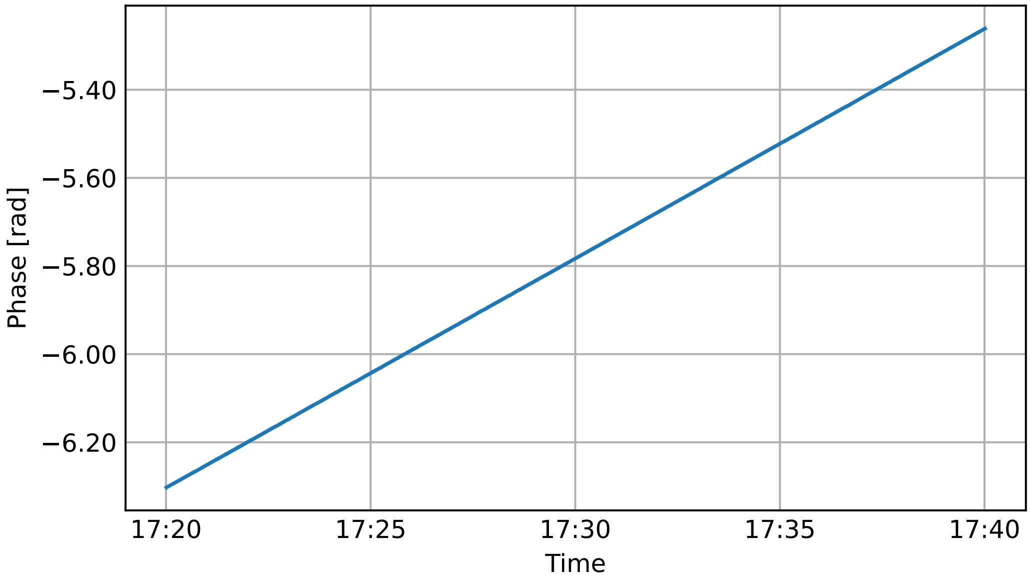

Figure 5.13: Phase drift of RTL-SDR.

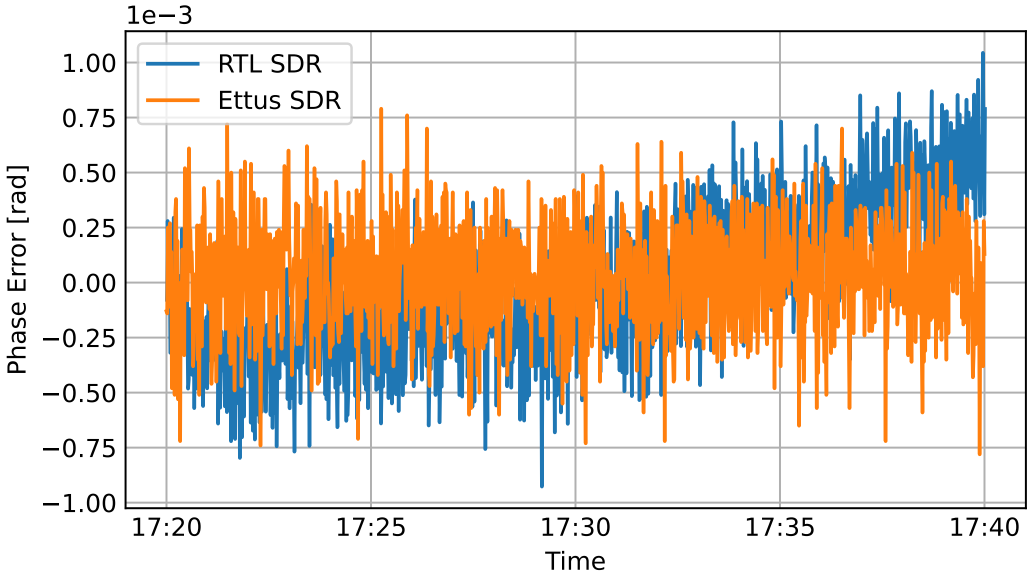

Figure 5.14: Comparison of phase error RTL SDR and Ettus SDR.

7.65×10^{-5}. This relatively poor performance may be due to a comparatively inferior local oscillator on the oscilloscope, but we could not find any indication of this in the datasheet [106]. Other oscilloscopes that use a higher quality internal or external reference potential improve the results.

Overall, we have shown that all three approaches are capable of tracking the aiding carrier of the R-Mode signal and that we achieve good performance with low-cost components. As we move forward, we will combine the different parts more freely as we continuously work towards higher intergeneration of the components to prove the feasibility of our designs and non-research products.

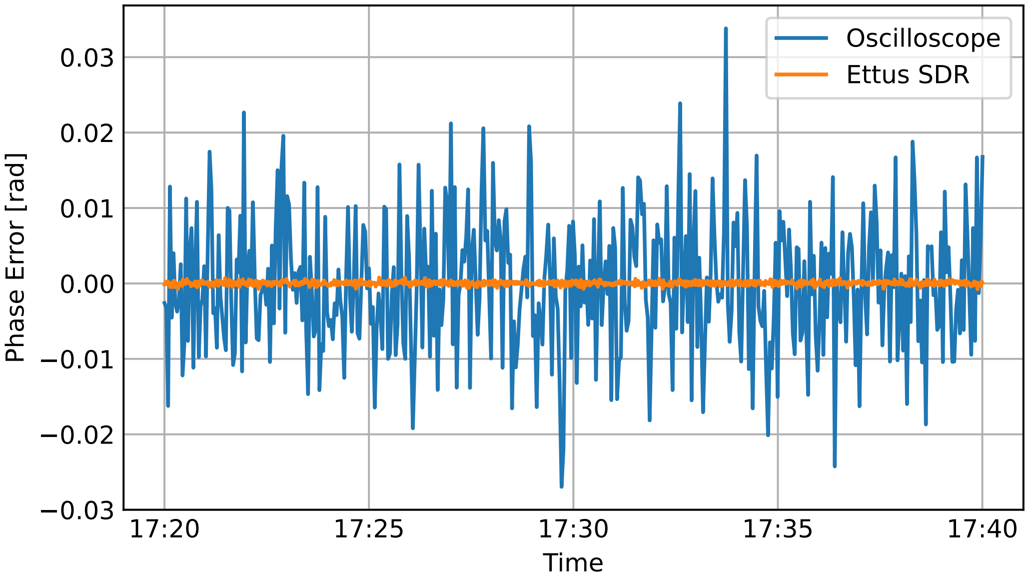

Figure 5.15: Comparison of phase error Oscilloscope and Ettus SDR.

5.3. SOFTWARE DESIGN

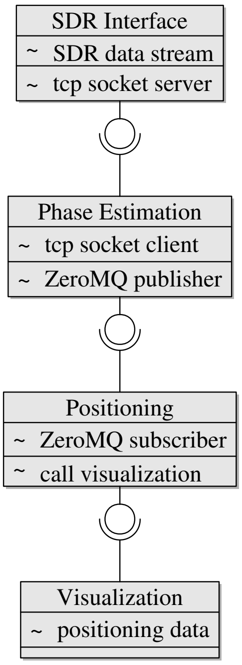

Figure 5.16: Block diagram of signal processing chain.

In the previous section, we described the various designs tested for setting up an MF R-Mode receiver. All concepts have in common that we digitize the received signal, which the PC then processed. To do this, we have developed software mainly in Python [58], that is capable of processing faster than the observation time of our system. To achieve this goal, we need to run several processes simultaneously. We decided on four main tasks: SDR coupling, phase estimation, positioning and visualization, which use Transmission Control Protocol (TCP) sockets and ZeroMQ [113] to interact with each other. Fig. 5.16 shows an overview of how each task interacts with the following by defining input and an output interface. It is possible to split the processing chain at every point and establishes parallel processing. In this way, we can compare different approaches in real-time. In the following paragraphs, we describe the function of each task in more detail.

SDR INTERFACE

The routine "SDR Interface" controls the communication with the hardware and is closely linked to the hardware in its functionality and must be adapted accordingly. Here, we select all settings regarding time source and antennas, desired channel and sampling rate. The interface transfers the samples to the phase estimator. For simplicity, this routine generates packages for the selected observation period. The required observation time in the receiver determines the size of each chunk. For now, we use a sample rate of 1 MHz in most of the experiments.

During our development, we have used different approaches to implement this task. Initially, we use a GNURadio [114] graph that handles the interface for different SDRs with drop-in replacement and delivers chunks of samples to a ZeroMQ TCP socket. Fig. 5.17 show an example flow graph, where we use a simulated sine signal for testing purposes.

Furthermore, we have extended the RTFramework recorder of the DLR to interact with the Ettus SDR. Besides providing the chunks on a TCP socket, the data is also stored in an SQLite database here. So, we can later replay the samples in real-time to test our processing chain and reprocess the data. Also, in this approach, each sample chunk is given a timestamp for the first sample, which facilitates analysis. The measurement campaigns presented in Chapter 6 utilize this implementation.

To use the oscilloscope, we need to provide a data packet for each trigger event to a TCP socket with a small Python script.

Signal Source
Sample Rate: 1M
Waveform: Cosine
Frequency: 298.275k
Amplitude: 1
Offset: 0
Initial Phase (Radians): 0

Throttle
Sample Rate: 1M

Complex To Real

Stream to Vector

ZMQ PUB Sink
Vec Length: 1M
Address: tcp://127.0.0.1:5555
Timeout (msec): 100
Pass Tags: No

Figure 5.17: Flowgraph in GNU radio for the SDR interface.

PHASE ESTIMATION

In this task, the phase for the incoming sample chunks is determined and then corrected. To provide a near-real-time phase estimate, the execution time of each estimation is crucial.

Therefore, we decided to implement the FFT as a default phase estimator. According to Section 4.1, this corresponds to a Maximum Likelihood estimator with a bandwidth of 1 Hz for 1 s observation time and is an efficient estimator for our problem.

To overcome the ambiguity solution in a first attempt, we implemented a phase tracking algorithm that compensates for phase jumps. The tracking adds a multiple of 2π to the phase estimate so that the resulting phase never changes more than π from one epoch to the next. The tracked phase thus starts between 0 and 2π, but can reach very high values for long continuous signal tracking.

We need to correct the tracked phase for any bias described in Section 2. For the case that the bias is unknown in advance, we implement a routine that estimates the offset depending on the difference of the expected phase, which is calculated based on the known own position from GNSS and the measured phase. This step is necessary because not all transmitters have a known delay. Johnson[53] proposed a similar approach for R-Mode measurement on land.

We use the speed of light for propagation over seawater to calculate a range, and the following processing routine receives the information. Here we use a publisher-subscriber pattern from ZeroMQ [113], as up to this point, execution time is crucial to prevent memory overflow, and the ranges drastically reduce memory consumption. The pattern works as a buffer and enables the distribution of the ranges to different positioning algorithms in the future.

POSITIONING

The positioning routine implements the LS algorithm presented in Section 4.4. To improve the estimation accuracy, we would like to mitigate the influence of the propagation path effect, which is the subject of several research projects within the DLR. We described this influence already in Section 2.2. Since this correction factor depends on the position, we proposed to apply the correction model iteratively using a correction map. To do this, we need to mitigate the impact as soon as the model and the map are available. The general investigation of how this problem is solved is beyond the scope of this thesis.

We store the obtained position and clock error with a timestamp in a CSV file. In addition, the positioning and pseudo ranges are passed to the visualisation, again using ZeroMQ.

VISUALIZATION

Visualization is a crucial point to present the data and how well the R-Mode can work. We deliver initial results in a measurement campaign using the streamed data sets. To realize a program to fulfil this task, we wrote a Python-based user interface utilizing Tkinter. You can see the resulting user interface plotting the estimated phase over time in Fig. 5.18. The operator can choose between different stations at the bottom of the program window and obtain the current amplitude and range error.

For easy access to the stored data, we recommend Grafana, which enables us to design dashboards according to the user's needs. We show an example of such a dashboard in Fig. 5.19, where the user can choose the most recent data or a specific period in the past. In addition, we can display other data to the user, such as temperature.

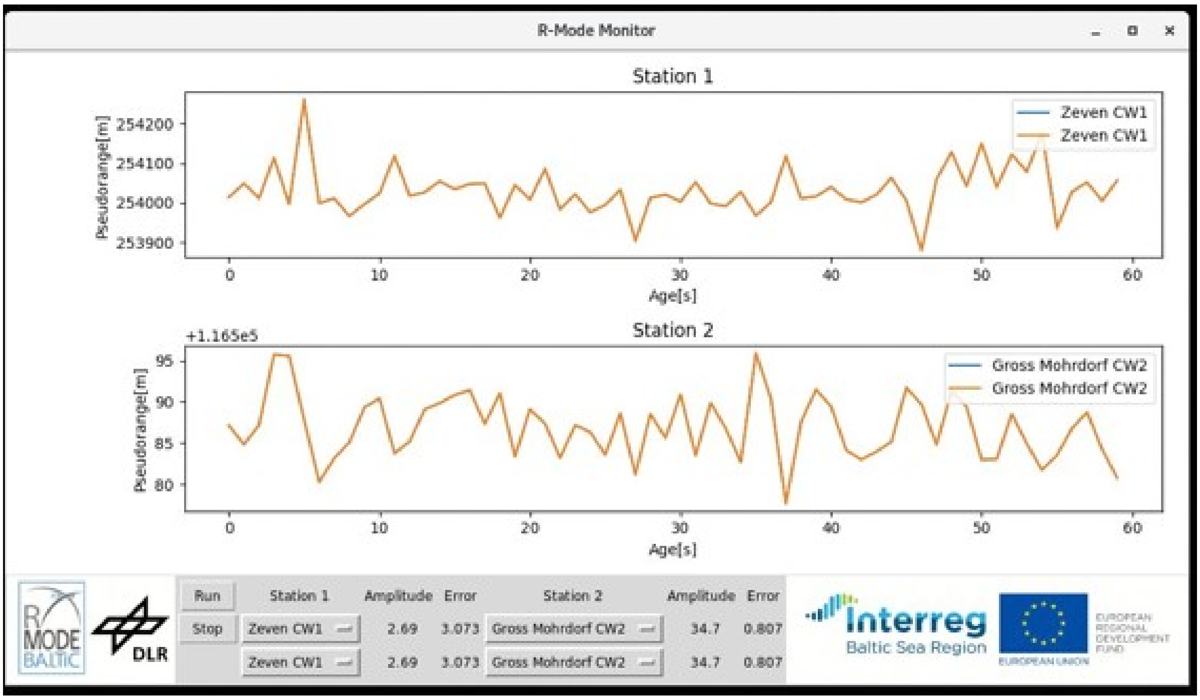

Station 1	Amplitude	Error	Station 2	Amplitude	Error
Zeven CW1	2.69	3.073	Gross Mohrdorf CW2	34.7	0.807
Zeven CW1	2.69	3.073	Gross Mohrdorf CW2	34.7	0.807

Figure 5.18: User interface based on Tkinter.

Temperatur Neustrelitz: 7.20

Temperatur Groß Mohrdorf: 7.90

Figure 5.19: User interface based on Grafana.

6

REAL WORLD RESULTS

In the course of this dissertation, we have introduced the medium frequency R-Mode and have described all necessary parts to build a receiver for the system. In this chapter, we want to present the first results utilizing our work. Swazek conducted the first practical test during the first R-Mode trials. Here only the range were derived due to a lack of available stations. Johnson [53] presented the first positioning solving for nearby stations, where only near field signals were received. With the measurement campaign on the Fyrbyggaren, which we describe in Section 6.1, we were able to obtain a real-time positioning in the far-field and the maritime domain for the first time [2], utilizing the FFT only. Moreover, we conducted a second measurement campaign in a worse case scenario on the vessel Deneb, where we present the results in Section 6.2. In the end, we also conducted static long-term measurements to test our different estimation approaches and verify the simulation results in Section 6.3, to have comparable conditions.

6.1. MEASUREMENTS ON THE FYRBYGGAREN

We had the opportunity to conduct a measurement campaign in the R-Mode Baltic Testbed with the Fyrbrygarren, a buoy tender provided by Swedish Maritime Administration (SMA). The measurement took place in August 2020 near the geometric connection line of the Holmsjö and Rozewie stations. With previous work by Johnson [53] already showing that near-field positioning is possible, we were able to demonstrate a real-time positioning solution with R-Mode in the far-field for the first time. We present results in our article "Positioning with medium frequency R-Mode" [2].

For these measurements, we deployed the DLR research receiver described in 5.2 on the ship using the E-field antenna, utilizing 1 MHz sample rate. In addition, we used a Saab R5 GNSS Real Time Kinematic (RTK) [115] receiver, which provided the RTK position for initial offset calibration in the field and as ground truth. The received R-Mode signal is then processed and recorded in the software described in Section 5.3. To mitigate further the effect of the groundwave, we assume a propagation speed over sea water for our signals of 299 616 913 m/s [2], which only holds as long as the land-path does not change too much.

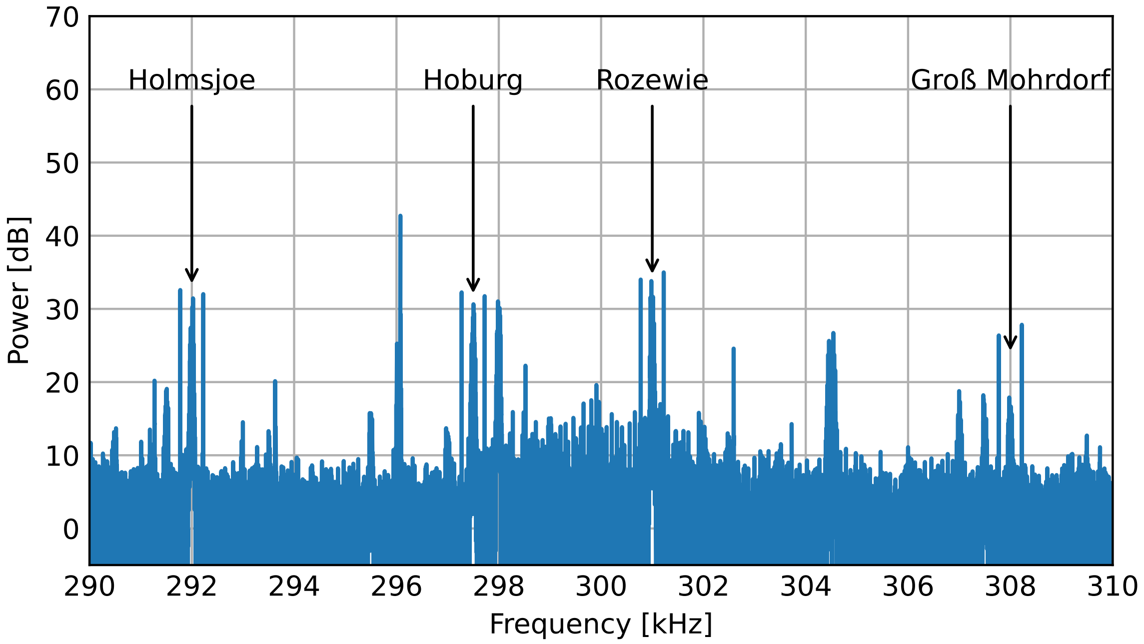

Figure 6.1: Overview of measured frequency spectrum in the Fyrbyggaren.

Furthermore, we utilized phase tracking to overcome the ambiguities, as the performance of the beat signal was not accurate enough. We performed the positioning with six tracked signals from the three closest R-Mode transmitters. Our receiver was able to output and store a position in real-time.

Fig. 6.1 shows an overview of the received signals during daytime in the centre of the testbed. We can see Holmsjö, Hoburg, Rozewie and Groß Mohrdorf with the corresponding CWs. The observation is in line with our expectation of receivable R-Mode capable transmitters at this time.

The results will be explained in the following sections, for which we have chosen two scenarios. In the first part, our measurement consists of quasi-static and dynamic data. At the beginning of the data set, we assume that the ship is in a static state. However, low wind speed and small sea waves cause some movements. For this reason, we refer to this scenario as quasi-static. We performed the second part of the measurements at a speed of 5 kn, a scenario we will refer to as low velocity, while we performed the last part at 10 kn referred to as high speed condition. For the second set of data, we chose a purely dynamic test, where the ship was sailing at a velocity of 10 kn and in adverse weather conditions with strong sea waves.

6.1.1. POSITIONING WITH LEAST SQUARE ALGORITHM

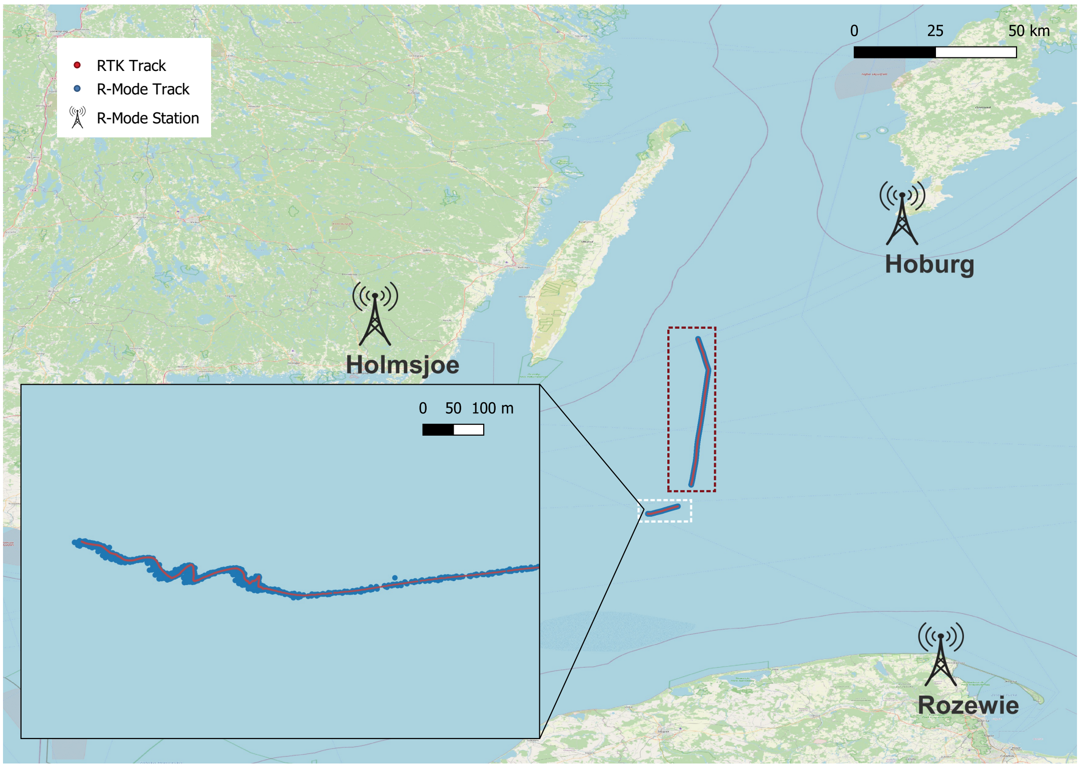

Figure 6.2: Track comparison between R-Mode and RTK for measurements on the Fybrygarren.

To give an overview of the positioning results in the two scenarios, we compare in Fig. 6.2 the positioning obtained by our R-Mode receiver after 30 s initialization time with the RTK position. We describe the process in more detail in Chapter 5. An antenna symbol indicates the location of the received transmitter. In the white box within Fig. 6.2, we present the first data set, recorded for about 90 minutes in the morning, about 1.5 hours after sunrise. In the inset of Fig. 6.2, we can clearly see that the R-Mode position matches the RTK position, with some systematic scatter towards the south.

The second data set, shown in the red box, was recorded on the same day for slightly less than five hours and yields similar behaviour. The figure also shows that the propagation path of the Hoburg and Rozewie signals is over the sea most of the time, while for the Holmsjö signal, the length of the land-path component changes. Consequently, we expected a changed signal delay for Holmsjö, which does not correspond to our correction.

In Fig. 6.3 we plot the horizontal error of the R-Mode receiver against time over the entire first data set. As we expect, it coincides with the R-Mode and RTK track of Fig. 6.2, where both are very close to each other. It appears that most of the epochs are characterised by an error significantly less than 10 m, but the presence of repeated peaks exceeding this value is noted. We see some outliers with more than 20 m. We like to emphasise that outliers occur every minute, which we take as an indicator of a systematic error. The 95 % limit for the positioning error (ϵ_{95}) we obtained is very similar for the three phases of quasi-static, low and high speed with 10.3 m, 7.5 m and 7.6 m respectively. If we evaluate the entire data set, the 95 % limit for the positioning error ϵ_{95} is 8.4 m. Thus, we already achieve the requirement for supporting navigation in the harbour approach. The maximum error ϵ_M

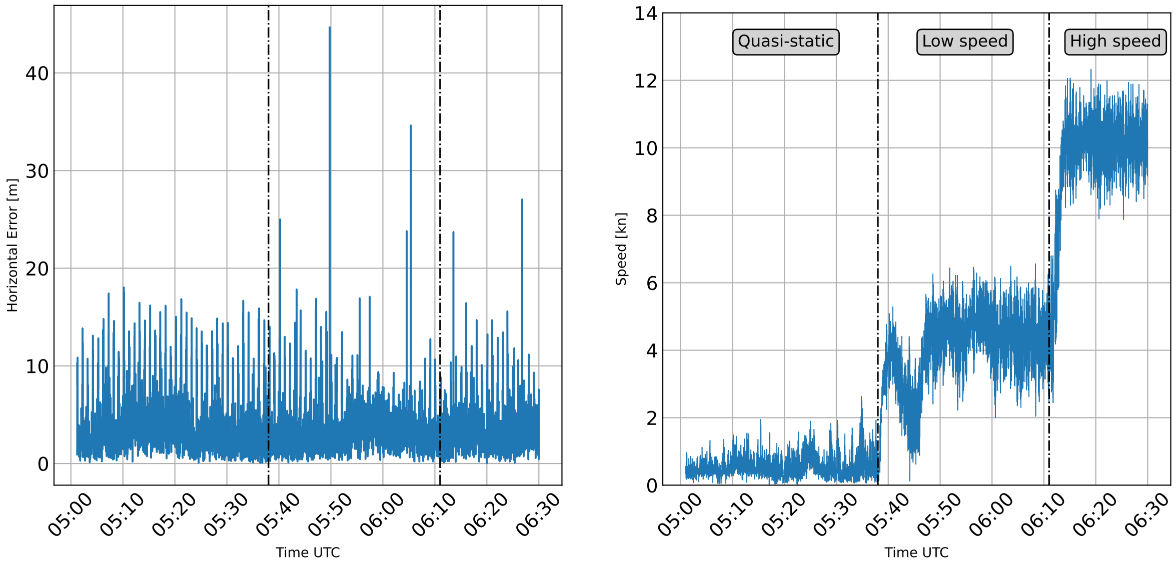

(a) (b)

Figure 6.3: Horizontal position error (a) and RTK based speed of the ship (b) over the time for the first data set.

reflects the outliers in R-Mode positioning. It is 18.1 m for the quasi-static, 44.7 m for the slow and 27.1 m for the high speed phase of the experiment. To investigate the reasons for these outliers, we will examine the individual stations in more detail later in this thesis.

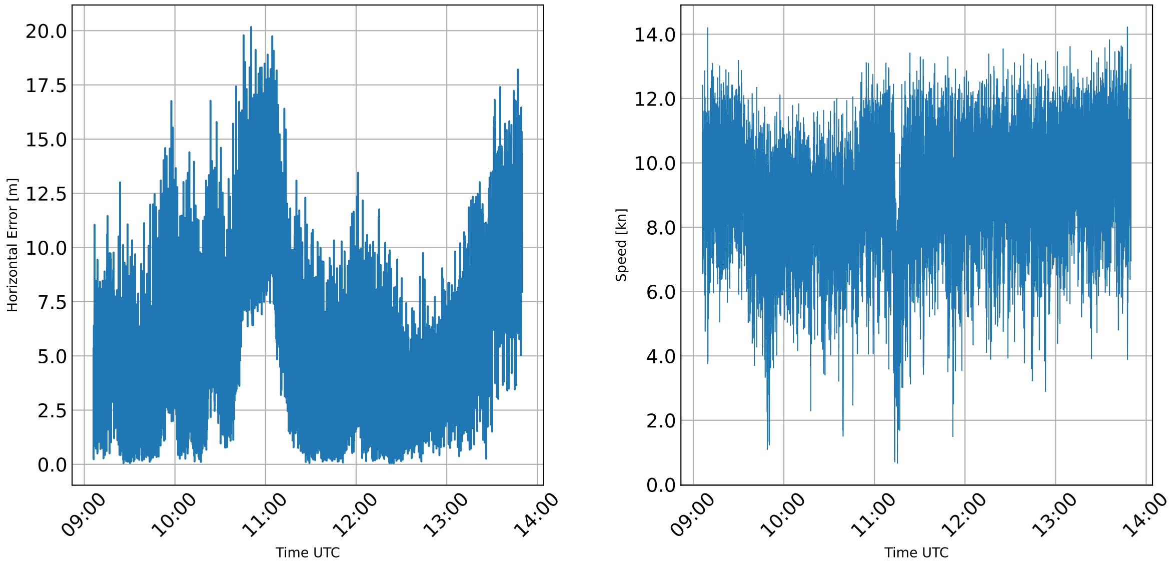

(a) (b)

Figure 6.4: Horizontal position error (a) and RTK based speed of the ship (b) over the time for the second data set.

For the second set of data, the ship is travelling at a higher speed, which we demonstrate in Fig. 6.4b where the speed of the vessel, measured by the GNSS receiver, is plotted against time. Fig. 6.4a shows the horizontal position error in R-Mode. An error of less than 20 m characterises most epochs, and the presence of the repeating peaks is also visible in this case. Compared to 6.3a, a time-varying distortion can be seen, especially clearly from 10:20 to 11:15 and from 13:00 to the end of the experiment. In this experiment, ϵ_{95} is 12.0 m, which is slightly higher than the value of the first data set. We assume that this result is due to the larger variations of the ship's position during the 5 h period and the uncompensated effects of the changes in the ground conductivity. The maximum horizontal error ϵ_M calculated by us, which may represent outliers, was found to be 20.2 m. Here we no longer meet the requirements for the port approach but are still within the 100 m limit for coastal navigation [44].

6.1.2. PSEUDO RANGES WITH REAL MEASUREMENTS

To clarify the reason for the outlier in the positioning, we want to evaluate the pseudo range error resulting from the subcarriers per station in more detail. To do this, we calculate the difference between an RTK base distance and the distances derived from the R-Mode, for the stations used, Holmsjö, Hoburg and Rozewie. We plot the result for the first data set in Fig. 6.5 against time.

Rapid fluctuations can be observed at the three stations, which represent the noise of the pseudo range. In most cases, this is much smaller than 10 m. In addition to the noise, a slight temporal deviation is observed at all stations, caused by the changes in the signal propagation path over land, as we described in Chapter 2. We also see that this influence varies from station to station, as the signals are transmitted along different paths and therefore influenced by various effects. We have not taken this influence into account in our receiver so far.

The pseudo range error for Holmsjö in Fig. 6.5a explains the spikes we observed in the position error in Fig. 6.3a since we see the same pattern. Every minute the pseudodistance error of both CWs increases by 10 m to 15 m for 7 s. In approximately 12 % of the epochs, this causes a significant error independent of the velocity. In 2023, we found that the Station was still transmitting non-directional beacon signals due to a misconfiguration, which caused the phase jumps.

We repeat the evaluation of the stations for the second data set in Fig. 6.6. Hoburg (see 6.6b) shows a slight negative deviation of about 5 m towards the end of the expiration but is otherwise very stable over the measured period. Rozewie (see Fig. 6.6c) behaves similarly but shows a higher noise level compared to Hoburg. The high reception power of the Hoburg station is explained by the fact that the transmitter has the highest transmission power. Therefore, we receive a stronger signal, which leads to a better estimate, as shown in Chapter 3. The stability of the Hoburg and Rozewie stations results from the fact that most of the signal was transmitted over the sea. At Holmsjö (Fig. 6.6a), on the other hand, the overland component fluctuated strongly, and we observe an increase in the offset from 9:00 to 11:00 UTC and a decrease from 11:00 to 13:30 UTC. Furthermore, by eliminating these systematic errors, the achievable accuracy can be further increased in the future.

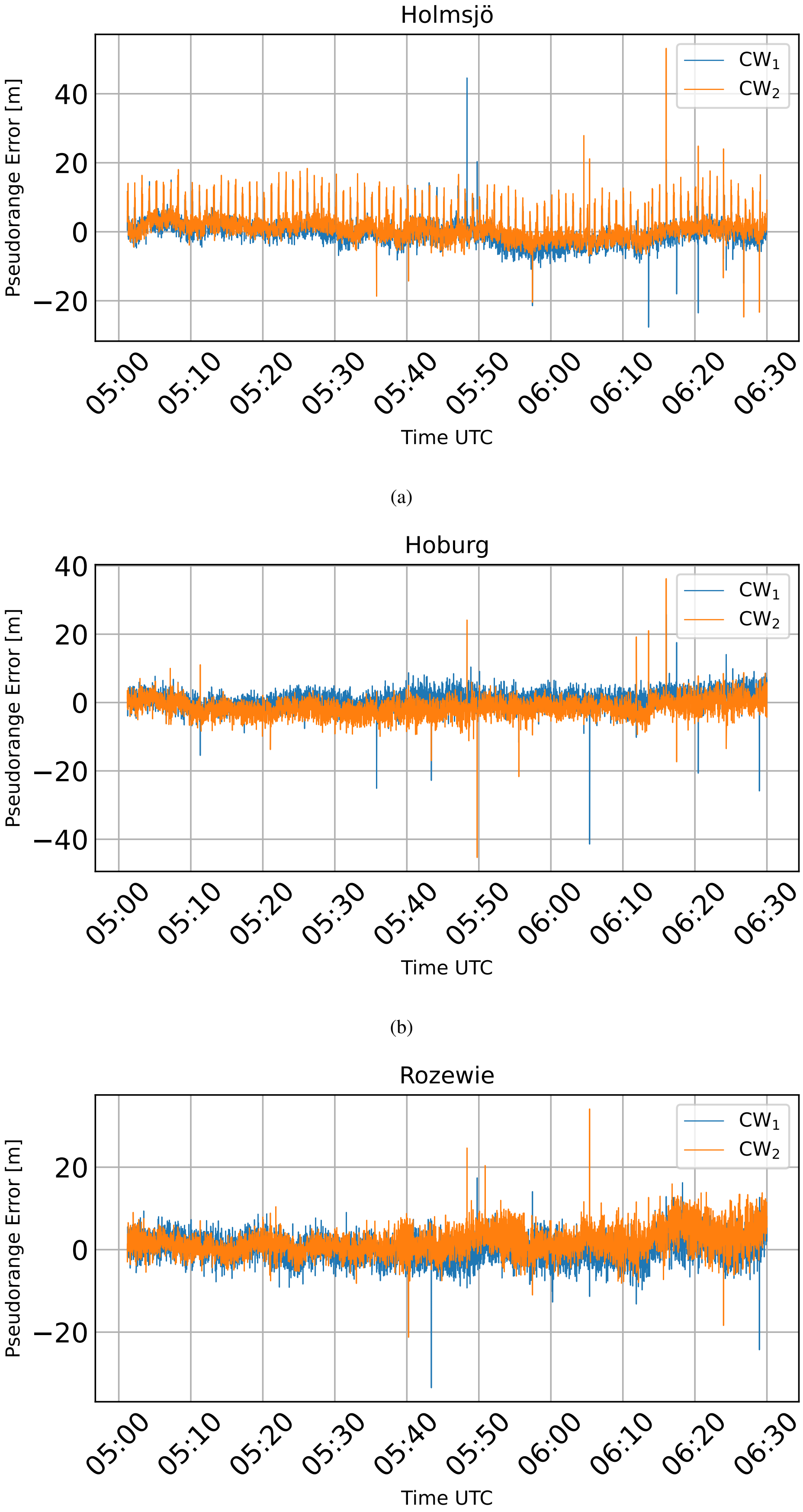

(a)

(b)

(c)

Figure 6.5: Pseudo range residuals of the first data set for Holmsjö (a), Hoburg (b), and Rozewie (c).

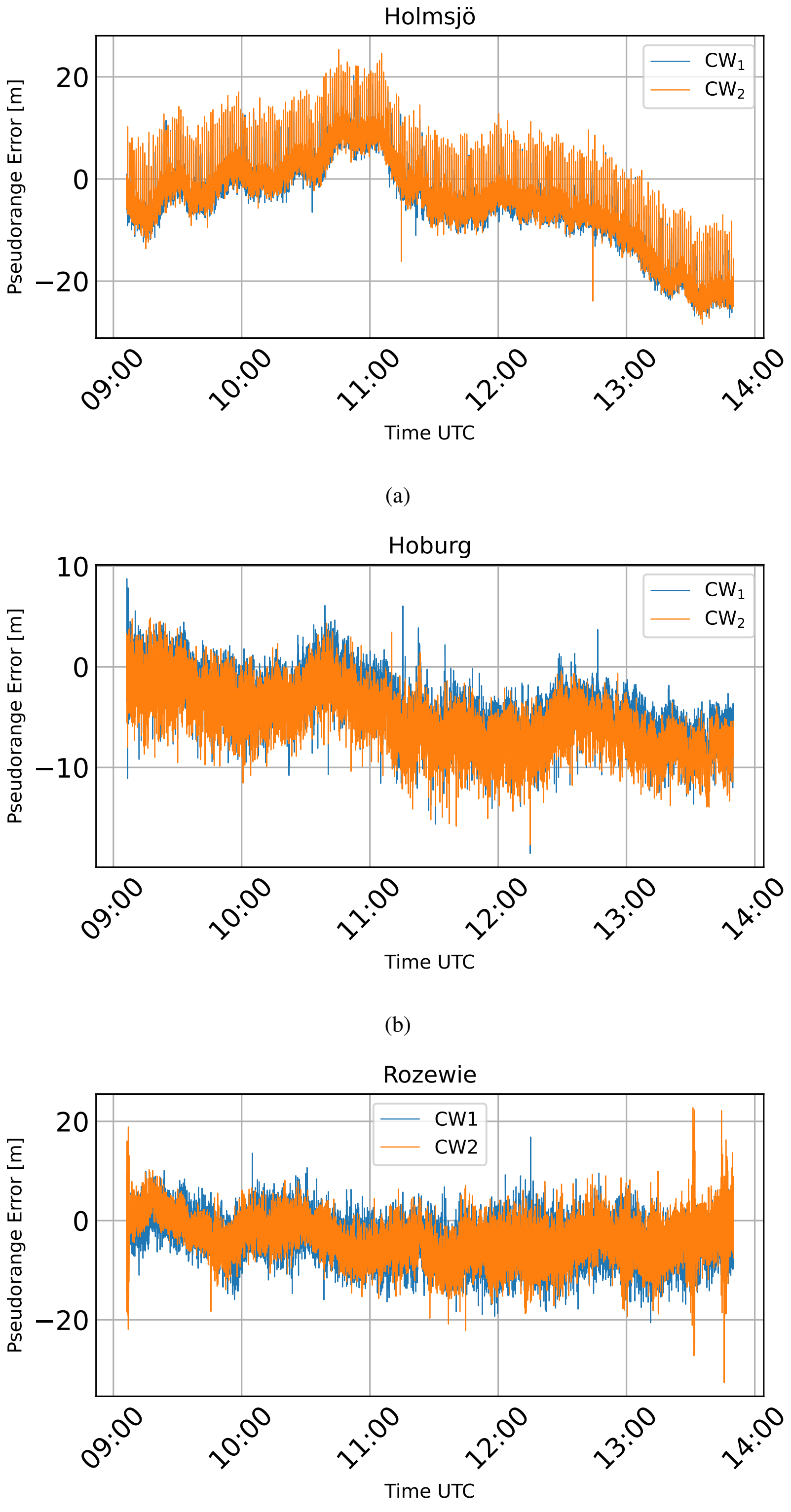

(a)

(b)

(c)

Figure 6.6: Pseudo range residuals of the second data set for Holmsjö (a), Hoburg (b), and Rozewie (c).

6.2. MEASUREMENTS ON THE DENEB

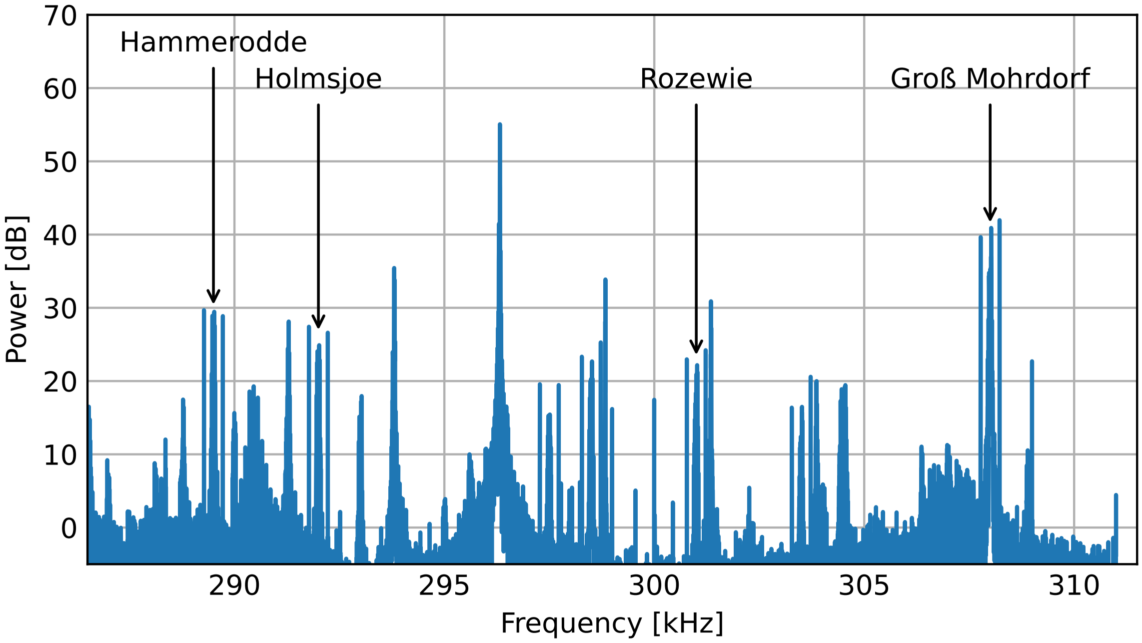

Figure 6.7: Overview of measured frequency spectrum at 11:00 UTC.

A second measurement campaign was carried out off the island of Rügen in February 2021, on the Federal Maritime and Hydrographic Agency of Germany (BSH) ship Deneb. This campaign aimed to verify the results of the first tests with the Fyrbyggaren described in Section 6.1 and to collect meaningful data on the influence of the propagation path theoretically described in Section 2.2. Therefore, we choose a scenario where the ship manoeuvres in coastal waters near the coast of Rügen, in a daytime scenario between 10:15 and 12:40 UTC. We start the initialization of the receiver roughly an hour before the start of this measurement. The change in propagation path in the selected areas is larger than in the earlier results, resulting in lower accuracy without further corrections. Therefore, these measurements are essential to provide a data foundation to correct this error in the future.

We used again the DLR research receiver described in 5.2 on the ship, together with a Saab R5 [115] GNSS RTK receiver, which provided the necessary ground truth. We do not change the sample rate of 1 MHz to ensure compatibility between different measurements. We also added two additional development receivers to the setup, but they could not provide real-time estimates at this stage.

For the test, the receiver derived the position from estimates of the four stations Hammerodde, Groß Mohrdorf, Holmsjö and Rozewie. We give the received spectrum plot in Fig. 6.7. As a single antenna provides a signal to three receivers, we significantly reduce the signal strength, which leads to a decreased accuracy of the ranges and positioning in our analysis. We first present the results of the positioning with Least Square algorithm to show that our approach works also in a different scenario, and we identified potential areas of interest. Secondly, we have a closer look at each station to describe the various influences on the propagation paths.

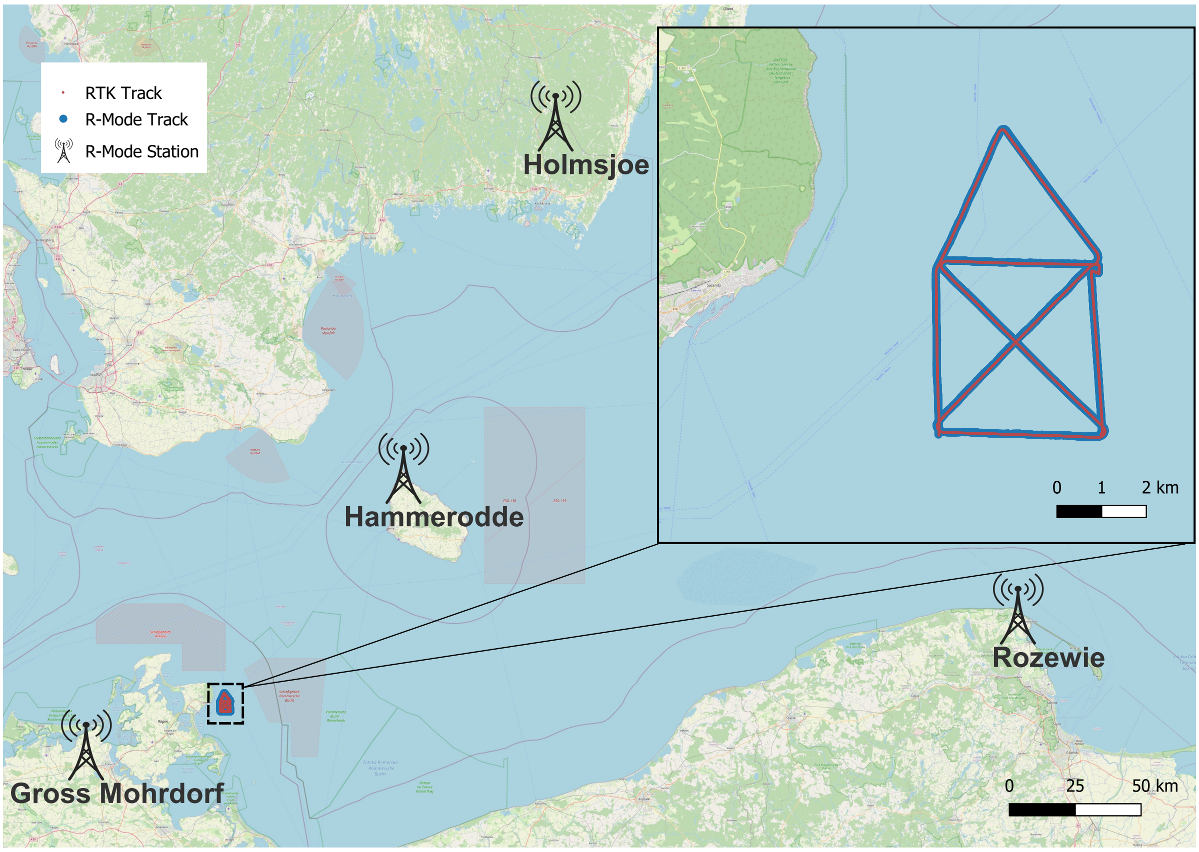

Figure 6.8: Track comparison between R-Mode and RTK for measurements on the Deneb.

6.2.1. POSITIONING WITH LEAST SQUARE ALGORITHM

We show the completed track in Fig. 6.8, where we compare the reference trajectory of the RTK solution with the result of our medium frequency solution in the inlay. Here, an antenna symbol marks the location of the received transmitting stations. We observe that we have a good matching between the reference and the R-Mode track. However, the terrestrial solution seems to be biased to the east.

In Fig. 6.9 the horizontal error in metres for the R-Mode position with respect to GNSS is shown. The maximum error is 40.3 m, which occurs at 10:40 UTC. We like to highlight the non-uniformly distribution of the error. Moreover, we see a changing bias over time. We assume that this error is due to the relatively large changes in the propagation paths, which seem to be particularly evident between 10:30 and 11:00 UTC.

To compare these results with the previous errors in 6.1, we calculate the 95 % limit for the position error ϵ_{95} to be 28.7 m. This value is about three times higher than in the previous campaign, which we explained by the lower reception power and the challenging environment.

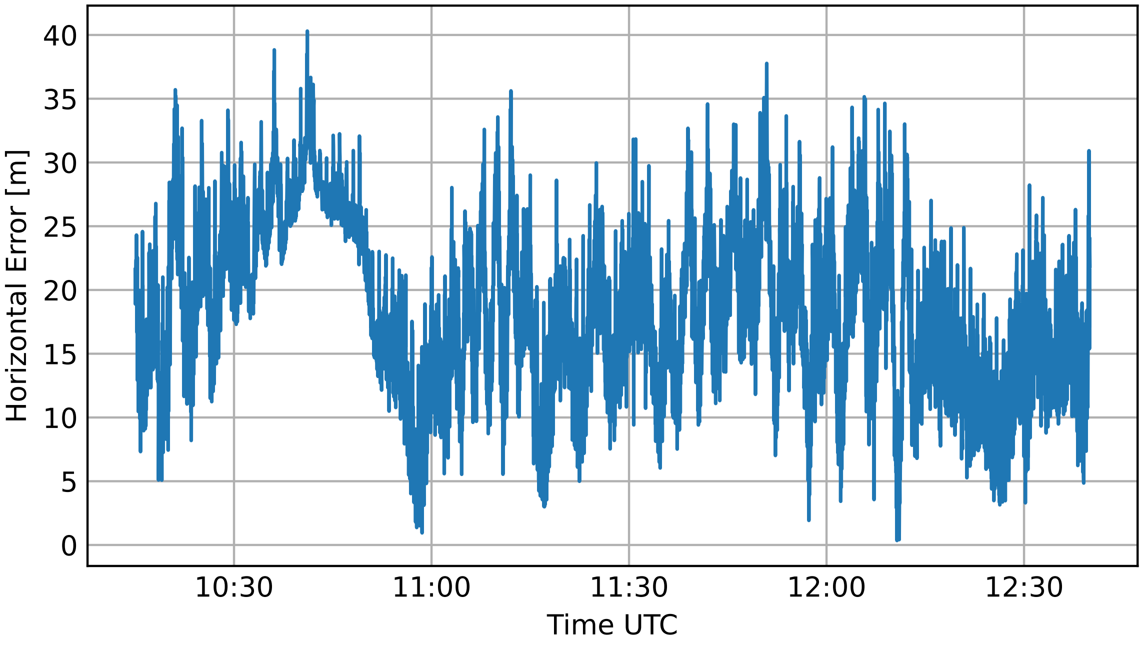

Figure 6.9: Horizontal position error over the time.

6.2.2. PSEUDO RANGES WITH REAL MEASUREMENTS

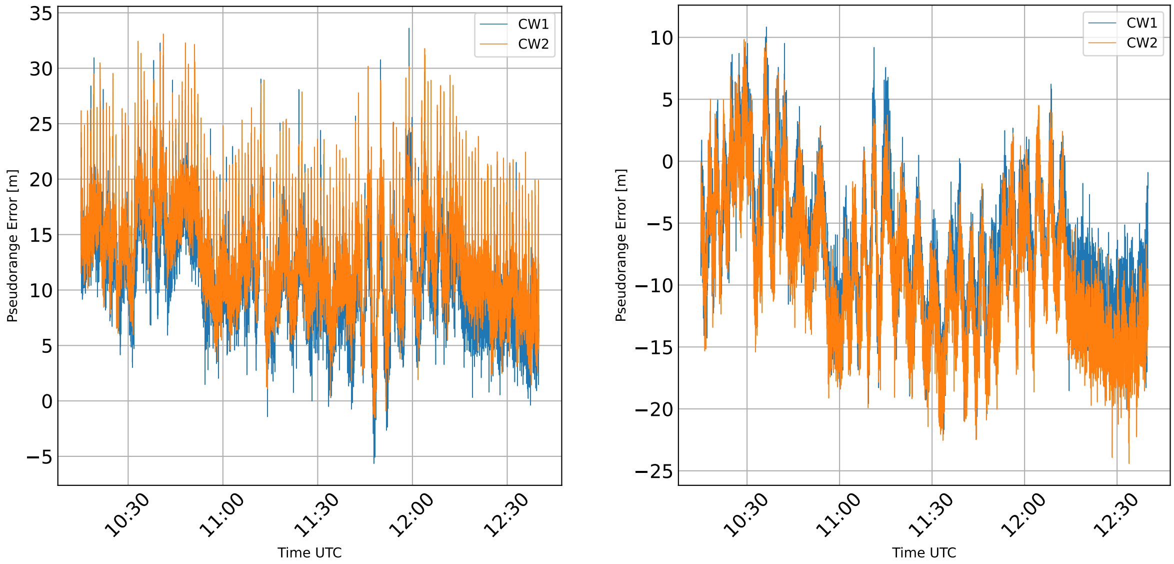

(a) (b)

Figure 6.10: Pseudo range residuals of the second data set for Holmsjö (a) and Hammerodde (b).

To understand the positioning error, we again evaluate the pseudorange error for each station concerning the RTK positioning. For the station at Holmsjö in Fig. 6.10a, we observe an increase in the pseudo range error of both CWs by 10 m for 7 s every minute, similar to the result in Section 6.1. The results show an offset between the initialisation of the receiver and the start of the measurements due to the influence of the land path. Fig. 6.10b shows the range error for the station at Hammerodde on the island of Bornholm. The error is in the range between 10 m and −22 m, mainly due to peaks occurring at random time intervals and ending at about 12:15 UTC. Unfortunately, the reason for these spikes is unclear to us, as the land-sea path should not change so much and so quickly. Furthermore, the result is again not the mean zero, as we did not initialise our receiver at the beginning of the measurement.

We continue with the description of the results for the station in Rozewie in Fig. 6.11a. Here the error, with a range from 12 m to −34 m, is slightly higher than at Hammerodde, which is due to the greater distance. However, we see time intervals with huge errors unevenly distributed, which hold for the whole measurement.

In Fig. 6.11b we plot the error for the nearest station Groß Mohrdorf. Since we had chosen the route of the ship to maximise the influence of the propagation path, we identified a high peak-to-peak error from 15 m to −50 m, which is mainly due to a drift of the estimate between 10:20 and 11:00 UTC at the northern part of the route. Since the Groß Mohrdorf station is the closest, we expect the best SNR, resulting in a slight variation between individual phase estimates, as shown in Fig. 6.11b clearly. The result supports the assumption that the observed drifts are due to the changing propagation path. Therefore, future approaches to propagation path suppression can use the dataset.

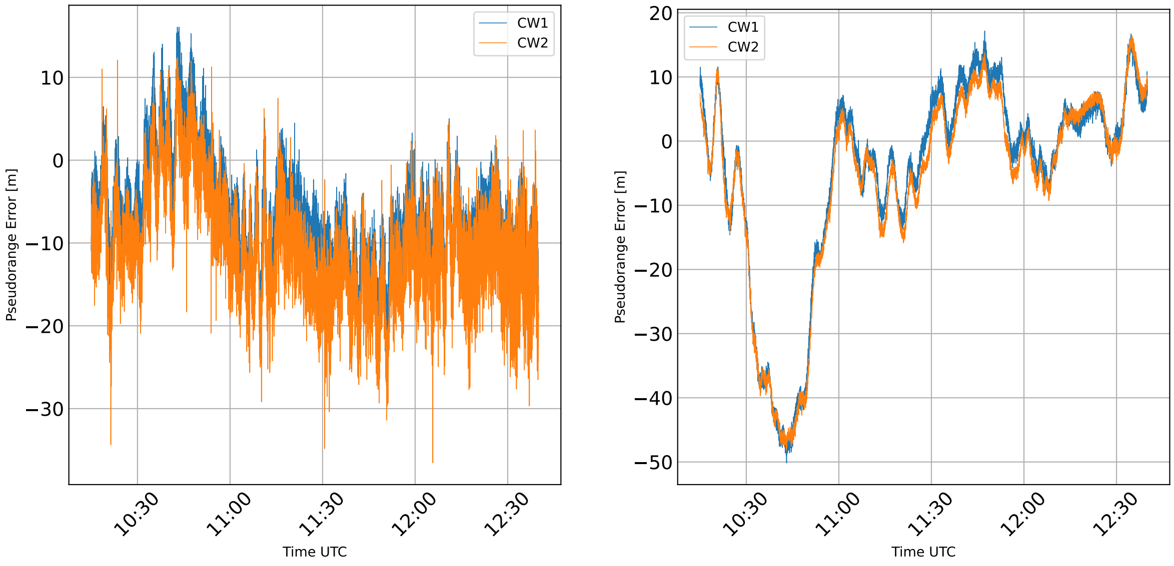

(a) (b)

Figure 6.11: Pseudo range residuals of the second data set for Rozewie (a) and Groß Mohrdorf (b).

6.3. LONG-TERM STABILITY OF THE PHASE

We had the opportunity to use our receiver as a near-field and far-field monitor to investigate how such a monitoring system might work in the future. Swazek [52] and Hoppe[55] conducted experiments with far-field monitors already in the past, focusing on testing the feasibility of the R-Mode system, especially in the presence of a skywave. These were mainly concerned with investigations on time series [54, 55]. We also consider near-field monitoring and extend this work by evaluating the histograms for several days to describe the error statistically, obtaining a more appropriate estimator and simulations for our problem in the future. With this approach, we hope to improve the overall performance of the MF R-Mode system. Since we want to apply the correction to the estimated phases, we are interested in the phase rather than range values. With these assumptions, we show the result for near-field observation in the Subsection 6.3.1 as a histogram and compare the performance for different window functions when we use a sample rate f_{sample} of 1 MHz. In Subsection 6.3.2 we evaluate histograms obtained with an area monitor.

6.3.1. NEAR FIELD MONITOR

In August 2020, a near-field monitor was set up at the Zeven transmitting station to demonstrate the functionality of a near-field monitor and the feasibility of synchronization in the system.

The MF R-Mode receiver of the DLR, as described in Chapter 5, was modified to use the station's local time receiver. The approach mitigates errors in time synchronization between receiver and transmitter. We took the measurements evaluated here between the 2nd and 13th of August 2020. In addition, at 9th the receiving antenna was changed from an E-field to an H-field antenna to check the different characteristics described in Section 5.1.

HISTOGRAM EVALUATION

First, we evaluate the local transmitter Zeven and the distant transmitter Heligoland as normalised histograms when we apply the FFT without windowing. We also fitted the Normal and Laplace distribution to see if we can describe the results in future simulations with a stochastic process. Here we only look at the lower CW to give a good overview. We have summarised the missing evaluations of the second carrier in the Appendix B.

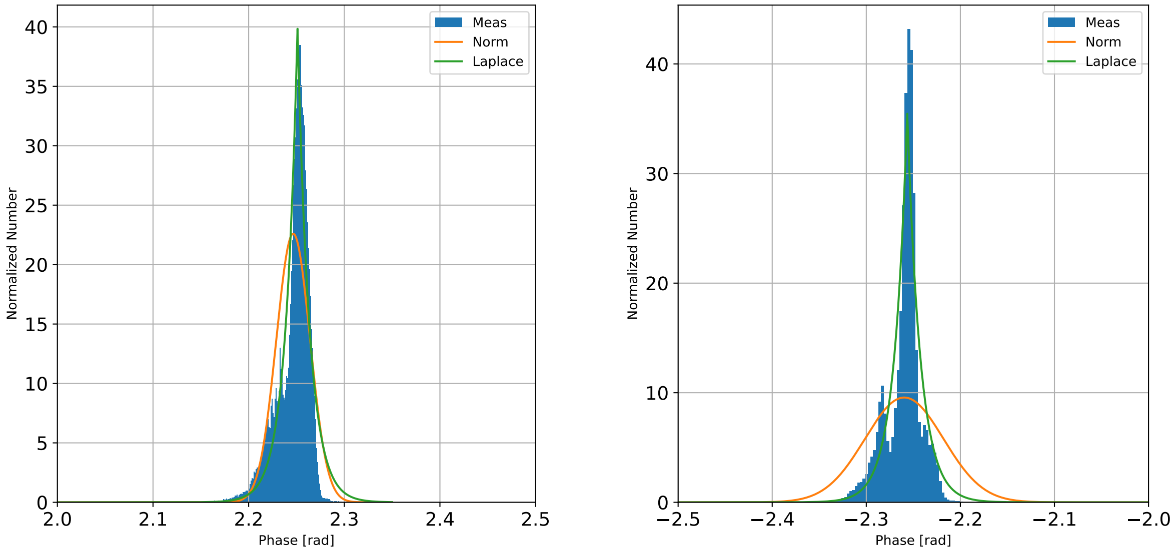

(a) (b)

Figure 6.12: Histograms of received station Zeven and distribution fit during daytime for near field with (a) E-field antenna, (b) H-field antenna.

In Fig. 6.12 we evaluate the normalised histogram during daytime in the near field. For the E-field antenna in sub-figure (a), we find that we do not closely follow any of the distributions used, as we have a side lobe at the lower phase values, giving us a variance of 3.12×10^{-4} rad^2. After switching to the H-field antenna, the main lobe hides large parts of the side lobe due to the high variance of 1.741×10^{-3} rad^2.

With the Normal distribution, a large discrepancy can be seen in the histogram. The Laplace distribution thus seems to hit the mean better but cannot describe the side lobes in the results.

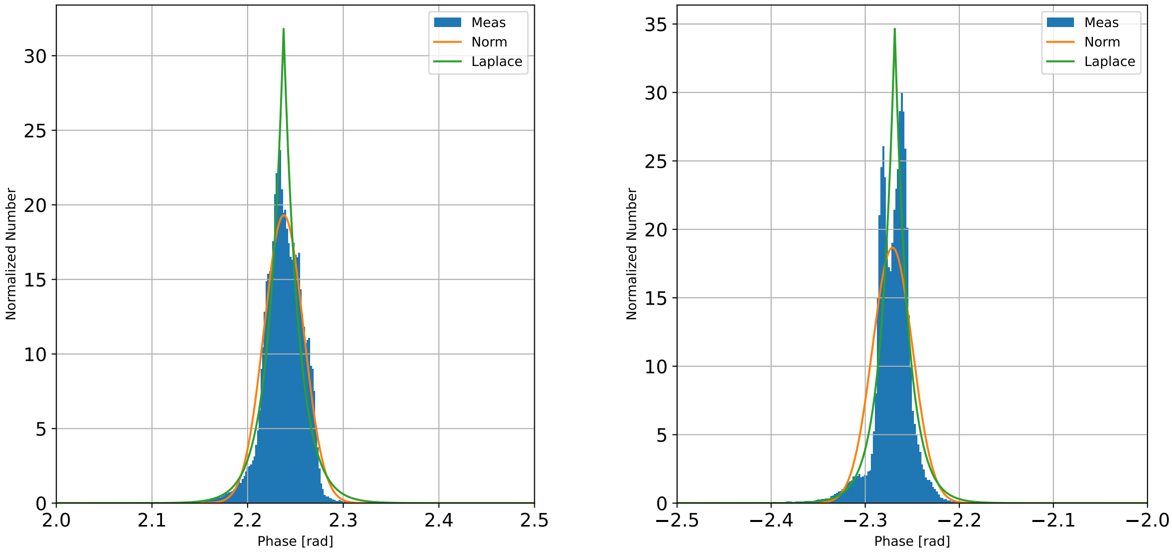

(a)

(b)

Figure 6.13: Histograms of received station Zeven and distribution fit during nighttime for near field with (a) E-field antenna, (b) H-field antenna.

Fig. 6.13 show the behaviour of the near-field station during nighttime. We do not expect a large deviation from the daytime results, as no skywave is visible from the near-field station. We observe a slightly increased variance of 4.27×10^{-4} rad^2 for the E-field and H-field antenna. For Fig. 6.13a, both fit roughly follow the shape of the histogram. Fig. 6.13b describe two peaks side by side for the H-field antenna results, which could be due to the influence of the MSK signal [3] or any other distortion. These two overlapping cases are difficult to describe with a standard distribution, so we cannot find a good fit with the Laplace or the Normal distribution.

For the far-field, Fig. 6.14 show the daytime results, where we see the resulting histogram of the E-field antenna in subframe (a). Here we now see side lobes on either side of the main lobe, which together gives a variance of 0.064 rad^2. Again, neither distribution can follow the side lobes. In subplot (b), the sidelobes are less prominent, so the variance drops to 0.020 rad^2. The result is consistent with the expectation of a lower variance in the far-field when using an H-field antenna compared to an E-field antenna, as described in Section 5.1.1. Furthermore, the Laplace fit seems to describe our error better than the Normal distribution, especially for the main lobe.

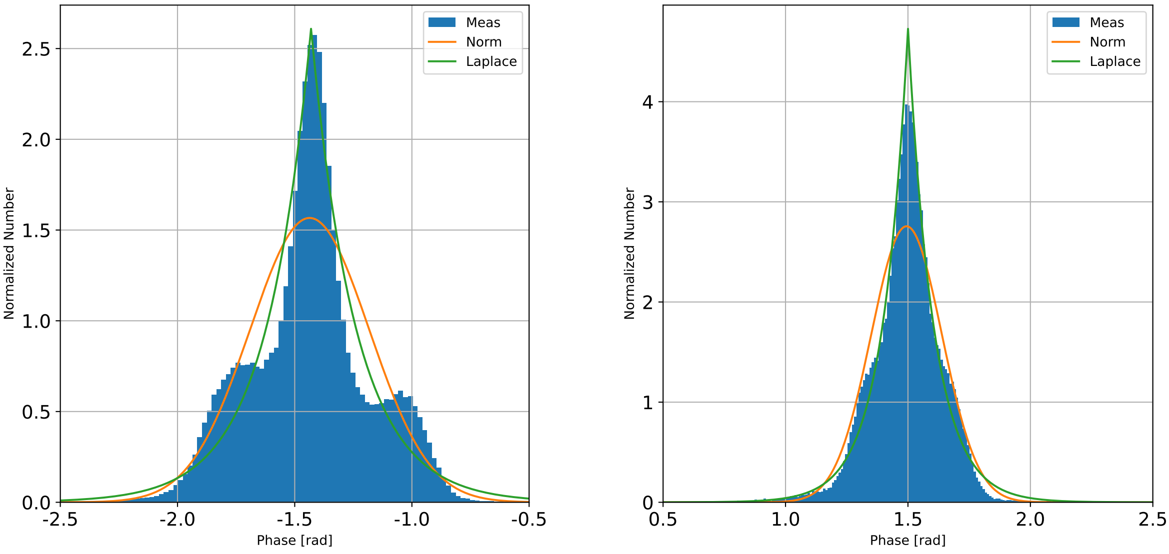

(a) (b)

Figure 6.14: Histograms of received station Heligoland and distribution fit during daytime for far field with (a) E-field antenna, (b) H-field antenna.

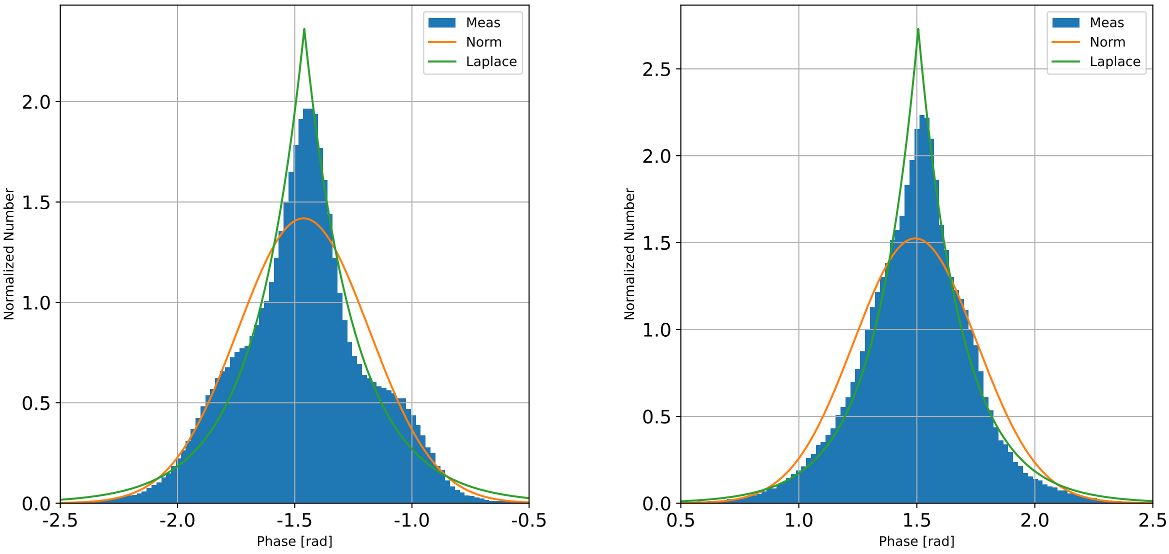

(a) (b)

Figure 6.15: Histograms of received station Heligoland and distribution fit during nighttime for Far field with (a) E-field antenna, (b) H-field antenna.

The nighttime result in the far-field for the E-field in Fig. 6.15a, shows an even higher variance of 0.079 rad^2 due to the skywave effect. The sidelobes are still visible but become part of the main lobe. We note that the Laplace fit seems to fit the main lobe but cannot describe the remnants of the side lobes. In Fig. 6.15b we show the result of the histogram of the H-field antenna, as before the variance of 0.068 rad^2 is reduced compared to the measurements of an E-field antenna. Furthermore, we cannot observe any side lobes and obtain a good agreement between the fitted Laplace distribution and the histogram of the measured values.

The measurements show that each lobe is best described by a Laplace distribution. However, the side lobes occur for an unknown reason, indicating that the results have different biases. This trend seems valid during the nighttime when the side lobes overlap more due to increased variance. In general, we need to account for disturbances within our measurements in future developments. Therefore, in the following subsection, we want to clarify the temporal correlations and investigate whether we can suppress them by windowing, as presented in Section 4.2.1. Furthermore, in Section 6.3.2 we present the result of another long-term observation to verify the results obtained here.

INTERFERENCE MITIGATION

In the previous part, we described the histogram of our phase estimates in the near and far-field next to the Zeven transmitter.

We found unexpected side lobes that could be the result of a time dependent bias in the near field. We are also interested in how the variance is disturbed over time for further investigations. Therefore, we look at the first five minutes of each hour and calculate the variance for CW1 of both stations. Appendix A provides the results for CW2. This time we only consider the E-field antenna results from the 2nd to the 9th of August 2020 to reduce the computation time. Moreover, we extend the existing processing chain by applying windows as described in Section 4.2 as this approach potentially reduce the power of disturbances.

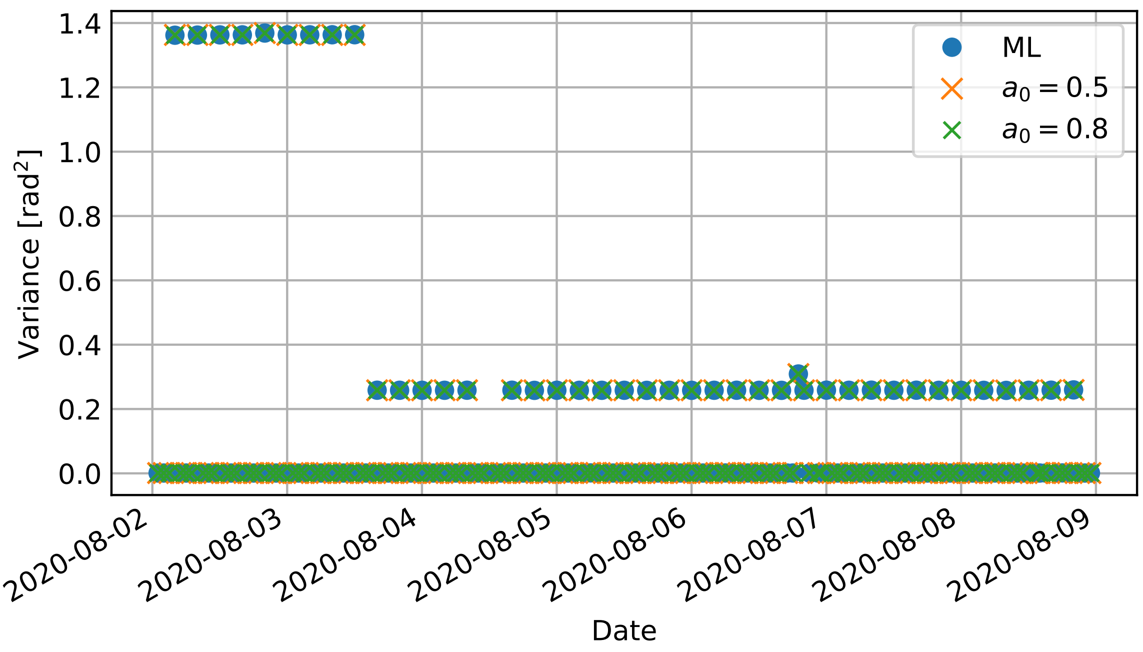

Figure 6.16: Variance for CW1 from transmitter Zeven the first 5min of each hour for different window functions.

For the result derived from the received near-field signal from Zeven station, shown in Fig.6.16, we see an increased variance every four hours, with two exceptions, first around noon of 4th and in the morning of 7th. Moreover, we observe a higher level of perturbed values of about 1.35 rad^2 during the first two days, which decreases to 0.25 rad^2 thereafter. However, as expected, the majority of the variance values obtained are close to zero.

The behaviour we observe in Fig.6.16 appears to be the same for the ML case, i.e. the un-windowed FFT, and the result for applying an increased cosine window of 0.5 and 0.8. The impression is only due to the large scale of the y-axis, as the difference between the estimators is of the order of 10^{-5}. Evaluation of the mean-variance of all three approaches shows that the window with $a_0 = 0.5$ performs best, followed by the window $a_0 = 0.8$. The measurement is consistent with the results obtained in our simulation for high signal-to-noise ratios in Section 4.2.1.

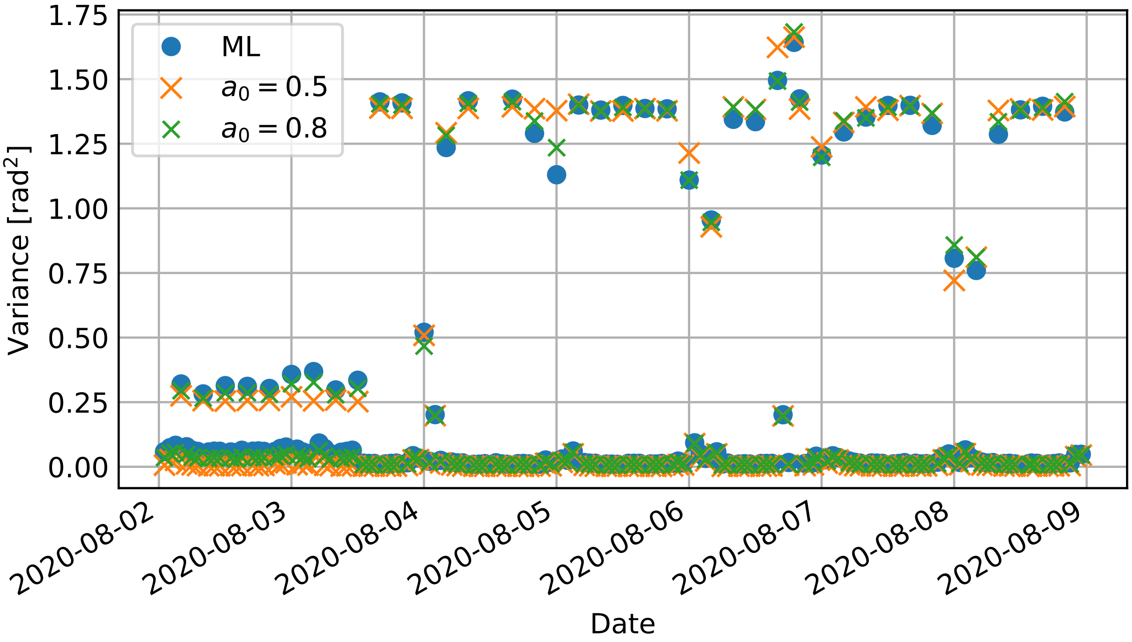

Figure 6.17: Variance for CW1 from transmitter Heligoland the first 5min of each hour for different window functions.

Consequently, we also examine the far-field result for CW1 from the Heligoland transmitter in Fig. 6.17. Similar to before, we see an increase in variance for several time slots, grouped in two stages, where we have a decreased variance for the first two days and a larger one afterwards, so the influence seems to be frequency-dependent, which is consistent with the result for CW2 in the Appendix. It is also important to note that we do not observe a higher variance every four hours now. Instead, we have additional time windows in between and where before we only had exceptions to the levels in the near field, we now observe an increased variety in the results obtained. Also, most of the variance is slightly higher in the first two days and then decreases. This effect is possibly the result of environmental changes along the dispersion path.

Concerning the different estimators, we can see that windowing reduces the variance in the first two days, with the window with $a_0 = 0.5$ outperforming the other approaches. After that, the windows still improve the lower variance values. However, in the case of outliers, the window approach increases the variance values. We explain this by considering a higher noise floor in the time window with reduced power. So, we may change the scenario to lower SNR values as simulated in Section 4.2.1.

Table 6.1: Comparison results for real-world phase-estimation variance in rad^2 of Zeven Station.

Parameter	var(CW1)	var(CW2)	var(Beat)
$a_0 = 0.5$	1.30×10^{-6}	2.24×10^{-6}	1.20×10^{-6}
$a_0 = 0.8$	6.55×10^{-6}	3.64×10^{-6}	1.29×10^{-5}
No window	0.0059	0.0440	0.0177

To compare our window approach with our simulation, we evaluated further measurements from June 2020 in the near field of the Zeven transmitter. Since this was only a preliminary test, the measurement data is limited to one hour in which we detect no disturbances. Due to the strong signal in the near field of the transmitter, we expect the inter-channel interference to be the main contributor, leading to a high SNR. The preconditioning of our signal significantly improves the variance of our estimate of the near station, such that a graphical comparison is no longer possible. Instead, we present the results in Tab. 6.1, where we present the results for the window parameters $a_0 = 0.5$ $a_0 = 0.8$ and the estimate without preconditioning. We can see that the window cases outperform the other test cases by two orders of magnitude. The windowed case $a_0 = 0.5$ shows the best performance, which we expected from our simulation in Section 4.2.1. Since the beat variance is smaller than the sum of the carrier estimates, this indicates that there is another general disturbance that the windows can suppress.

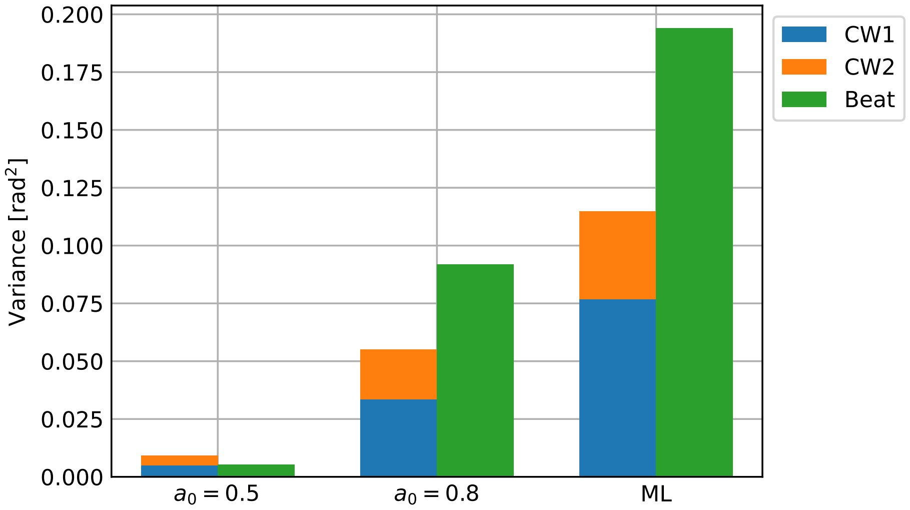

Figure 6.18: Comparison of windows with $a_0 = 0.5$,$a_0 = 0.8$, notch filter and ML estimator for the Heligoland signal received in Zeven.

Furthermore, with such a strong signal, all close channels benefit from the near-band suppression. Therefore, we evaluate the signal from the Helgoland station with a bandgap of 5 kHz and a distance of 134 km from the local station, which we can potentially use for synchronisation. We evaluate the recorded signal for the signal of the Helgoland station and present the results in Fig. 6.18. Here, we show the resulting variance for CW1 in blue, for CW2 in orange and for the beat signal again in green. Since we now have coloured noise, we do not show the CRB in this plot. Similar to the local signal the preconditioned signal performs better than the non-window filter. Again, the windowed approach, where $a_0 = 0.5$, outperforms all tested approaches by almost an order of magnitude.

Summarising the results of this subsection, we concluded that an unknown disturbance at specific points in time influenced the observation. However, windowing improves performance in time without distortion, even in a real scenario. This effect is even more powerful when the modulated signal is strong. The approach is therefore suitable for use in a monitor station. Moreover, we can even suppress the observed interference to a certain extent.

6.3.2. AREA MONITOR

In the previous section we noted unknown disturbances to our long-term observation. To verify whether this is a problem of this particular setup and the medium-frequency R-Mode has no general problem with this influence, we now present the results of another long-term measurement.

This time, we placed the MF R-Mode receiver of the DLR at a WSV facility in Großkönigsförde on the Kiel Canal. Here we were able to receive the three R-Mode stations Zeven, Helgoland and Groß Mohrdorf over 21 days between 9th and 24th August 2021.

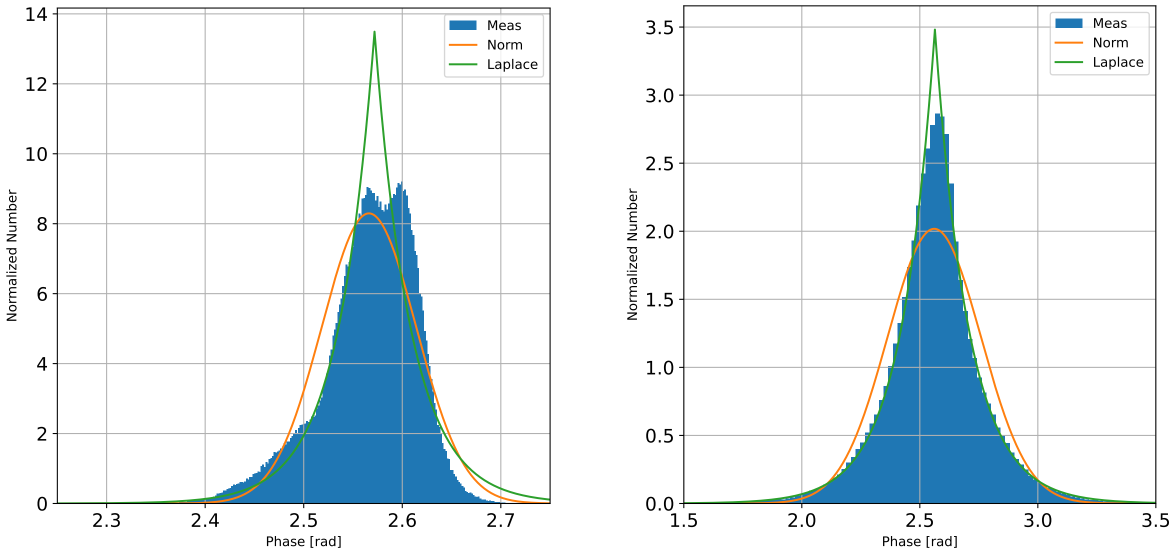

(a) (b)

Figure 6.19: Histograms of received station Heligoland with distribution fit during (a) daytime, (b) nighttime.

To compare the results with the near-field observation in Section 6.3.1, the histograms of the estimated phase are again plotted separately for daytime and nighttime. A Normal and a Laplace distribution then fitted to the results. As before, we present only CW1 in this paper; Appendix B list the corresponding results of CW2.

The signal from the Heligoland station travels about 130 km over a mixed land-sea path before the signal is received in Großkönigsförde. Fig. 6.19a shows the histogram during daytime where we can see two peaks near the mean, resulting in a variance of 0.0023 rad^2.

The right slope of the histogram seems to follow a Laplace distribution to the higher phase values. The left slope shows a different behaviour with a reduced decrease, similar to our observation in the near field. Due to the different peak values, neither the Laplace nor the Normal distribution shows a good matching with the measurement. This changes with the results during nighttime, which Fig. 6.19b show. Here we observe an enlarged variance of 0.039 rad^2 due to the skywave, with a single peak. The slope agrees with the fitted Laplace distribution, which diverges only at the top of the histogram, which we cannot reproduce by the Normal distribution.

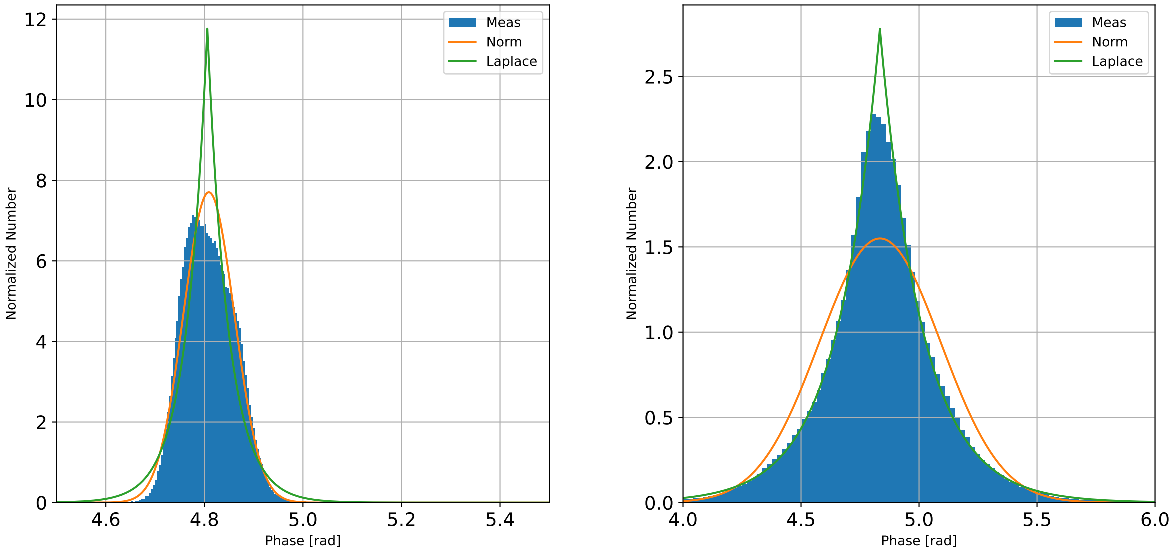

(a) (b)

Figure 6.20: Histograms of received station Zeven with distribution fit during (a) daytime, (b) nighttime.

Zeven station emits a second signal to be received, which propagates over 126 km pure land. Fig. 6.20a plotted the histogram for the received daily results, with a variance of 0.0026 rad^2. Here the Normal distribution seems to best describe the slope of the results, while the Laplace distribution shows only weak agreement. However, the Normal distribution does not follow the peak, as the maximum value tends towards the lower phase values. Possibly two different distributions overlap here due to interference.

Fig.6.20b show the results for nighttime. We get a variance of 0.0662 rad^2, which we expect due to the skywave. Furthermore, we again see a better fit of the Laplace compared to the Normal curve, as the former only shows a divergence at the peak.

Groß Mohrdorf broadcast the third station considered here, which is about 197 km from our receiver. It is the weakest and most influenced station in our test as the signal has to travel a land-sea-land path. Moreover, the variance increases to 0.1106 rad^2, and we get the histogram in Fig. 6.21a. Here we see a large discrepancy between the two distributions due to a small second peak of height 0.1 around 2 rad, which we can not recognized in the plot. Therefore neither distribution can be used to describe the result.

For the results during nighttime, shown in Fig.6.21b, we get good agreement between the Laplace distribution and the measurements. However, where the slope in Fig. 6.19b and Fig. 6.20b coincide, we see a divergence for the received signal from Groß Mohrdorf at the

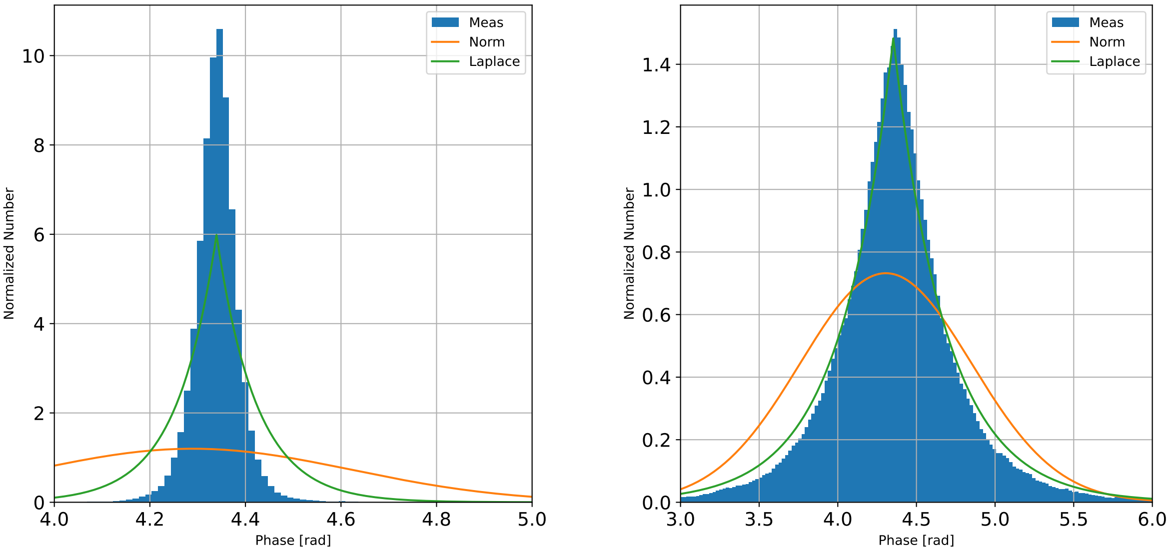

(a) (b)

Figure 6.21: Histograms of received station Groß Mohrdorf with distribution fit during (a) daytime, (b) nighttime

location. In contrast, fig. 6.21b shows a better fit to the peak values for the Laplace fitted results.

In summary, the far-field measurements presented here show reduced side lobes that completely disappeared due to overlap at nighttime, which is consistent with our results from the near-field monitor. However, during the daytime, we observed the histogram in Fig. 6.19a, which shows fewer side-lobes compared to our first measurement in Section 6.3.1. Further investigations are needed in the future to find the possibly cause for the phase distortion.

Furthermore, we show that the results during nighttime can be fitted with a Laplace distribution. In our future work, based on this knowledge, we can tune our simulation of the skywave and account for the distribution in our positioning algorithm.

7

POSSIBLE OPTIMIZATION TO THE R-MODE SIGNAL

In Chapter 2 we gave an overview about different crucial points within the R-Mode positioning system to mitigate the different influences. Up to now, we tried to optimize an estimator for the given MF R-Mode signal, which we introduced in Section 2.1. Now we investigate three changes to the signal. First, we investigate the benefit of an optimised bit sequence. Secondly, we propose the change of modulation, and at last, we discuss a complete reallocation of the band.

7.1. OPTIMIZED BIT SEQUENCE

To achieve best performance, the phase estimates of the tones, described in Section 2.1, should be statistically independent. However, it was shown in Section 3.1.3 and 4.1.3, that the MSK signal influence our results for limited observation times. This concept was first presented by us in [2]. To improve the system performance, we want to introduce a bit pattern that fulfil the equations

$$S_{\text{sum}} = \frac{1}{N}\sum_{n=0}^{N-1} \cos\left(\omega\, t_n + b_\tau[n]\frac{\pi\, t_n}{2\, T_{\text{bit}}} + \varphi_1 + \bar{\varphi}_\tau[n]\right) \approx 0 \tag{7.1}$$

$$S_{\text{linear}} = \frac{1}{N}\sum_{n=0}^{N-1} \left(\frac{\pi\, t_n}{4\, T_{\text{bit}}}\right) \cos\left(\omega\, t_n + b_\tau[n]\frac{\pi\, t_n}{2\, T_{\text{bit}}} + \bar{\varphi}_\tau[n] - \varphi_{beat}\right) \approx 0, \tag{7.2}$$

$$S_{\text{squared}} = \frac{1}{N}\sum_{n=0}^{N-1} \left(\frac{\pi\, t_n}{2\, T_{\text{bit}}}\right)^2 \cos\left(\omega\, t_n + b_\tau[n]\frac{\pi\, t_n}{2\, T_{\text{bit}}} + \varphi_1 + \bar{\varphi}_\tau[n]\right) \approx 0, \tag{7.3}$$

given in Section 3.1.3.

As the analytical solution is rather complex to this problem, we want to give a qualitative description of the optimization of the bit pattern. When we assume an unequal amount of 1 and -1 bits during the MSK modulation, we observe a phase shift. In that case, the sum is not performed over an integer wave number, and the associated phase error could be large.

However, when the observation considers an equal number of 1 and -1, the phase estimate would result unbiased. In this case, another source of error becomes recognizable. Since a bit change leads to a mismatch in the sum and results in a small error. We conduct a simulation within our Python simulation environment for an observation time of 1 s and 100 bits/s. We apply the ML for the CWs next to the modulated signal for four-bit pattern b_1, b_2, b_3, b_4, for comparison we used the same amplitude values as in Section 5.2.5. Here, b_1 repeats the sequences [-1,1] , b_2 alternates [-1,-1,1,1] and b_3 alternates the sequence [-1,-1,-1,-1,1,1,1,1,1]. For comparison to the current bit pattern, the sequence b_4 is generated based on a uniformly distributed random sequence, with an uneven number of -1, 1 bit.

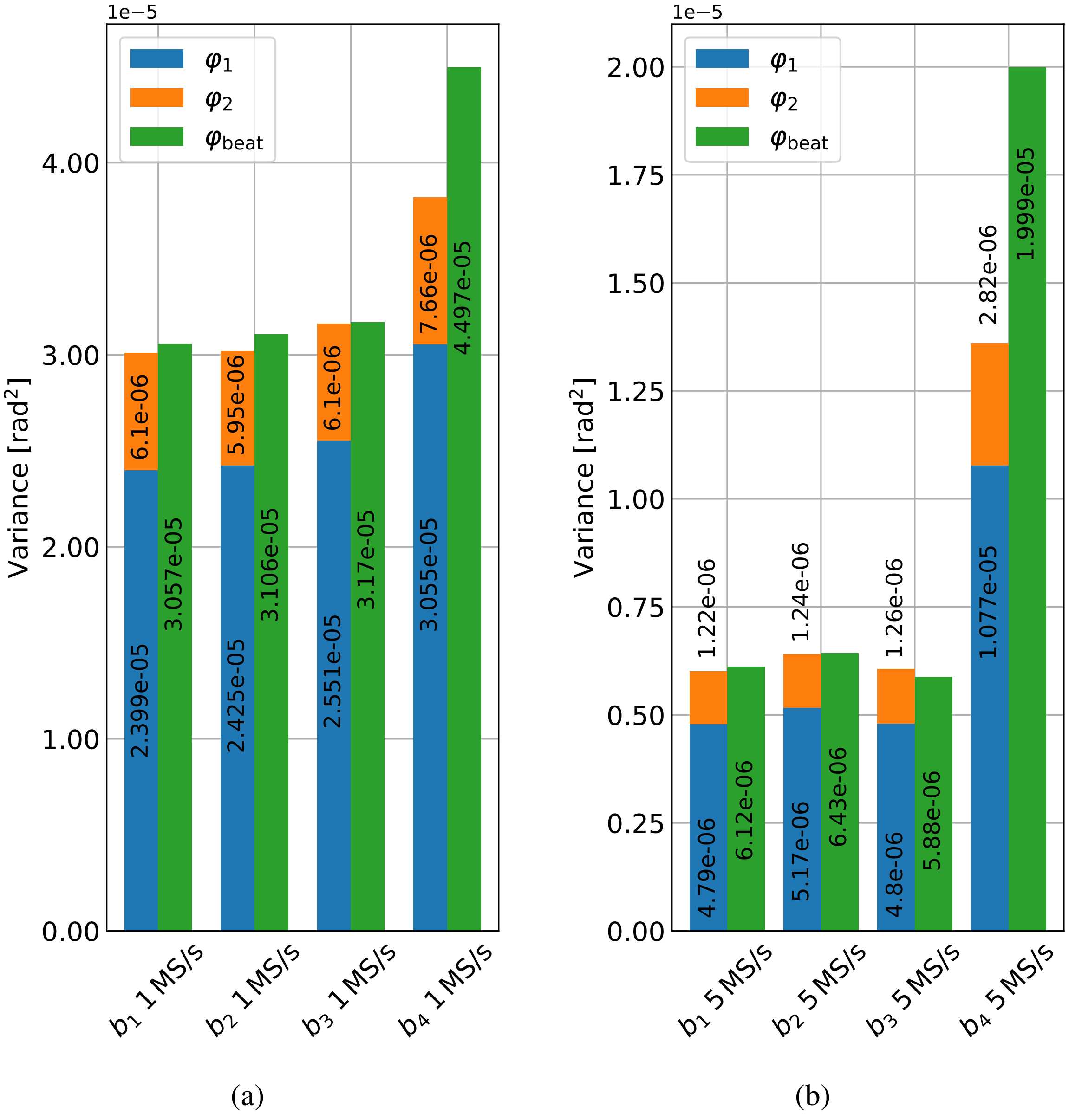

(a) (b)

Figure 7.1: Bar plot of simulation results for the signal model with MSK for 1 MS/s (a) and 5 MS/s (b). The optimized bit sequence b_1, b_2 and b_3, show that the estimates of the continuous wave are statistically independent. This is not the case for the random bit sequence b_4.

The bar chart in Fig. 7.1(a) shows the variance in rad^2 of the phase estimations next to the different bit sequences b_1, b_2, b_3, b_4 for 1 MS/s sampling rate. The blue bar represents the variance for the estimated phase φ_1 of CW1; the orange bar, above the first result, marks the variance for φ_2 of CW2. Since the results of the individual continuous waves are superimposed, we compare the result with the green bar, which represents the variance of the difference, i.e. the beat signal. The representation allows us to evaluate visually whether the results are statistically independent, which we use as a figure of merit, as described in Chapter 3. Fig. 7.1(b) shows the results for 5 MS/s sampling rate in the same way.

We see, in Fig. 7.1, that the variance obtained with the bit sequences b_1 , b_2 and b_3 scales by a factor of 5 with the sampling rate due to the increased energy of the signal. Furthermore, the variance of the beat frequencies is approximately equal to the sum of the variance for the two estimated different tones. We also see that the differences in the resulting mismatch do not have a significant effect when summed over the MSK signal. For the random distribution, where we need to account for the MSK energy, the variance scales by $\sqrt{5}$, as we expected from calculating the SNR from the PSD MSK and signal energy. Furthermore, the estimates of the sinusoids are no longer statistically independent, as the sum of the variance now differs from the variance of the beat frequencies. Furthermore, we observe that the resulting variance has grown significantly compared to the bit sequences with the same number of bits.

We have demonstrated that recoding the data signal so that the same number of bits are always present contributes to reduced inter-canal interference. The effect leads to a reduced variance of the estimation for the ML estimators used in this work, which we presented in Chapter 4, and can thus increase the overall performance of the R-Mode system in case LS estimators are not suitable.

7.2. IMPROVED PHASE ESTIMATION WITH GMSK

We have shown that we can improve the estimation of the phase near the modulated signal by optimizing the bit sequences in Section 7.1. Similarly, we can find better modulation that improves the spectral efficiencies and thus reduces the additional power within the evaluated bandwidth. With Gaussian Minimum Shift Keying (GMSK), as used in the Global System for Mobile Communications (GSM) standard, there is a known modulation that fulfils this condition. We showed the result first in our paper "Improving medium frequency R-Mode ranging with GMSK modulation" [5].

Like MSK, GMSK is a Continuous Phase Modulation (CPM) which also depends on the parameters of the circular center frequency ω_c, the bit duration T_bit, the signal amplitude A_GMSK. In general, the CPM can be described, depending on the modulation index h, as follows [116]

$$s_\mathrm{GMSK}(t) = A_\mathrm{GMSK} \sin\left(\omega_\mathrm{c}\, t + \sum_{\tau=0}^{p} b_\tau\, h\, q(t-\tau\, T_\mathrm{bit})\right), \quad p\, T_\mathrm{bit} < t < (p+1)\, T_\mathrm{bit}. \tag{7.4}$$

The memory of the modulation φ_memory is described by considering all the previous bits $p-1$ in the sum. To obtain the GMSK modulation, the integral $g(t)$ of the phase response $q(t)$ is chosen a to a Gaussian shape. [117]. Furthermore, the function$g(t)$ depends on the parameter BT, which describes the bandwidth of the response for an infinite time duration as

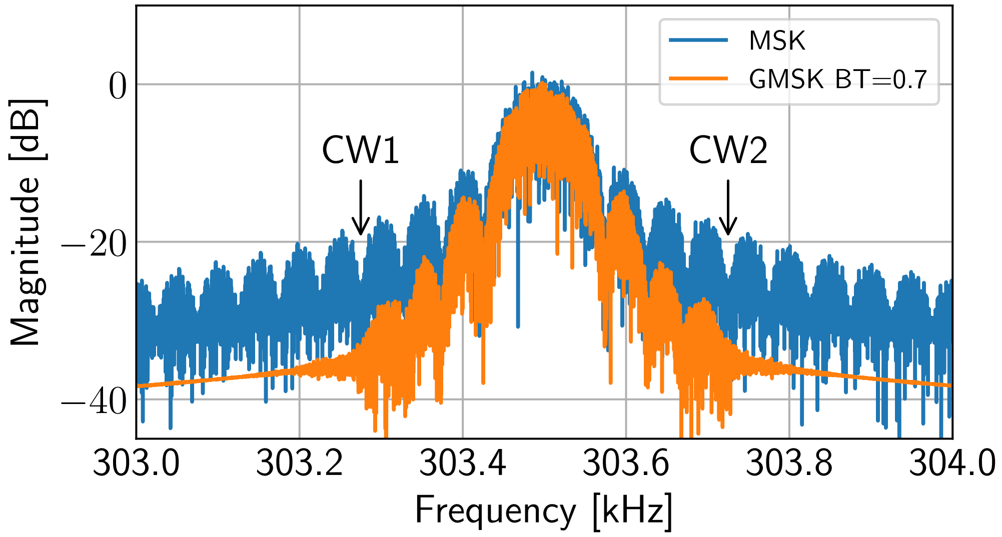

Figure 7.2: Comparison between the simulated spectra of an MSK and GMSK modulation with $BT = 0.7$ at a centre frequency of 303.5 kHz and a bit rate of 100 bit/s.

$$g(t) = \frac{1}{2\,T_{\text{bit}}}\left\{Q\left[2\pi BT\frac{t-\frac{T_{\text{bit}}}{2}}{(\ln 2)^{1/2}}\right] - Q\left[2\pi BT\frac{t+\frac{T_{\text{bit}}}{2}}{(\ln 2)^{1/2}}\right]\right\} \tag{7.5}$$

with

$$Q(t) = \int_t^\infty \frac{1}{\sqrt{2\pi}} \mathrm{e}^{-\Pi^2/2}\, d\Pi \tag{7.6}$$

This description leads to a truncation effect if we consider only a limited time. For the simulation, the modulation index h is set to 0.5 to allow the use of legacy receivers. For GMSK, there is no analytical solution for the PSD. However, Anderson [116] approximated the case by calculating an averaged PSD.

Moreover, changing the modulation to GMSK would fulfil the requirements of legacy use. As GMSK was already under discussion during the development of the maritime radio beacons [117]. Murato [118] has shown that there is no significant increase in the bit error rate when the modulation is changed accordingly. Furthermore, due to the similarity of both modulation schemes, the existing DGNSS receiver on the transmitting side would not need to be adapted to the changed modulation from MSK to GMSK [117].

In Fig. 7.2 we compare the simulated spectra of a GMSK with $BT = 0.7$ and an MSK modulation. The figure shows a power drop of 15 dB between the modulations, at the frequency where the potential continuous waves for the R-Mode are located. For the simulation, we use our simulation environment based on the model for MSK presented in Section 2.1. However, since the Gaussian shape must be unbounded in time [116], our simulation approach is not sufficient for GMSK, since we usually generate single data stacks. For the same reason, we can define the signal model for MSK with a single bit in (3.35), but we must consider all the previously sent bits for GMSK in (7.4).

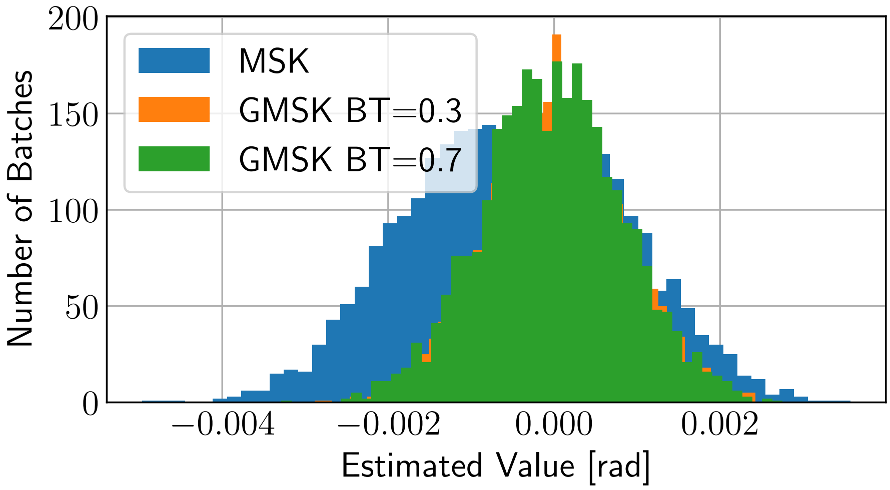

Figure 7.3: Historgam of phase estimation for CW1 next to MSK, GMSK $BT = 0.3$ and $BT = 0.7$ modulation.

To overcome this issue, we simulate 1 s batches with GNURadio [114], including GMSK modulated bits, which are then read into our legacy Python environment. We also expect a truncation effect for the 1 s evaluation, which is shown in Fig. 7.2, as the GMSK curve no longer shows any modulation at the edges.

We verify our assumption that higher spectral efficiency potentially increases the accuracy of the estimation. For this purpose, we simulate three signal combinations: the phase estimation of a tone at the fourth zero-crossing of an MSK and for the modified modulation on GMSK with $BT = 0.7$ and $BT = 0.3$. Again, we use our environment with external GMSK modulation as in the generation of Fig. 7.2 . Each estimation runs 3000 times. In accordance with the simulation in Chapter 4, we choose the amplitude values $A_1 = 0.001$ $A_2 = 0.002$, $A_{\mathrm{GMSK}} = 0.004$. Moreover, we choose a sample rate of 1 Ms/s. bitrate of 100 bits/s and a fixed observation time of 1 s.

Fig. 7.3 shows the histogram of the simulated phase estimate for the lower frequency (CW1) of an R-Mode signal at 303.5 kHz. The simulator produces a phase zero at the beginning of every full second and a random bit sequence. We can see that using GMSK modulation below improves the accuracy of the estimates. All three histograms seem to be Gaußian distributed, with two peaks. This is similar to the results obtained in Section 6.3.2. The results are again summarised numerically in the column "Std [rad] Software" of Tab.7.1. For this purpose, the different Standard Deviations (Std) of our software simulations are compared. In accordance with Fig. 7.3, we find that the estimation accuracy has improved by a factor of 1.5. However, the value of BT seems to have only a small influence on the result.

7.2.1. HARDWARE IN THE LOOP TESTS

To verify the simulated software results, we repeat the experiment of the three signal combinations with a hardware-in-the-loop test. Therefore, we utilize our R-Mode hardware simulator introduced in Section 5.2.4. We choose the sampling rate of the signal generator to be 10 MS/s, which is much larger compared to 1 MS/s for used the receiver. The higher

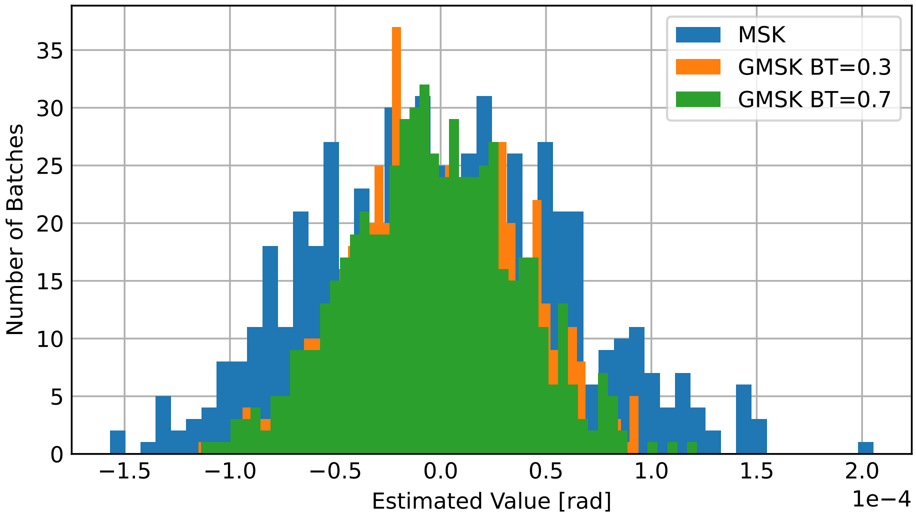

Figure 7.4: Resulting histogram for the Hardware in the loop simulation for an R-Mode signal with MSK or GMSK modulation at a centre frequency of 303.5 kHz and a bit rate of 100 bit/s.

sampling rate also results in a larger SNR, so we expect better performance, including hardware, as we choose the same values in the environment.

Fig. 7.4 shows the results for the lower frequency (CW1). This time in case we insert the hardware in the loop simulation. However, we present mean-free results because we have an unknown offset due to the cable length between the different components. Therefore, the performance improvement is not as evident as in Fig. 7.3. However, in general, the distribution of MSK modulations is broader than those of the GMSK modulations. In Tab.7.1 we give the Std of the estimate in the third column "Std [rad] Hardware", as before we see an improvement by a factor of 1.5 when we change the modulation to GMSK. Furthermore, the BT values in our simulation again do not seem to have any significant influence.

Table 7.1: Standard deviation of phase estimation for different signals, for software and hardware in the loop simulation.

Signal	Std [rad] Software	Std [rad] Hardware
GMSK $BT = 0.7$ + CW	0.0017	3.9004×10^{-5}
GMSK $BT = 0.3$ + CW	0.0016	3.9000×10^{-5}
MSK+ CW	0.0026	6.0000×10^{-5}

7.3. INCREASED BANDWIDTH OF MF R-MODE SIGNAL

With a channel width of 500 Hz, there is room for up to 63 channels in the maritime frequency band in Europe between 283.5 kHz to 315.5 kHz. Initial field tests have shown that up to 19 stations can be received simultaneously [14] in the Baltic Sea. Therefore, we have plenty of room to spread the signal in the frequency range to provide better service. We first presented these results in our publication [8].

We focus on optimization in the spectral domain and analyses the potential benefits of R-Mode ranging performance and skywave error mitigation in case the R-Mode signal uses more bandwidth of the maritime frequency band. Therefore, we maintain the MSK modulation schemes with the two added tones and suggest two different modifications. First, we want to add a second channel to each station. Secondly, we utilize the whole band per station. Here, we want to solve the problem of ambiguity solving and the skywave mitigation described in Section 2.1.

In Fig. 7.5 we simulated different spectra for the modified waveforms. In subplot (b) the centre peak (blue) is at 305 kHz. The spectra show a simulated MSK modulated RTCM2 message with a data rate of 100 bit/s, as it is widespread in Europe.

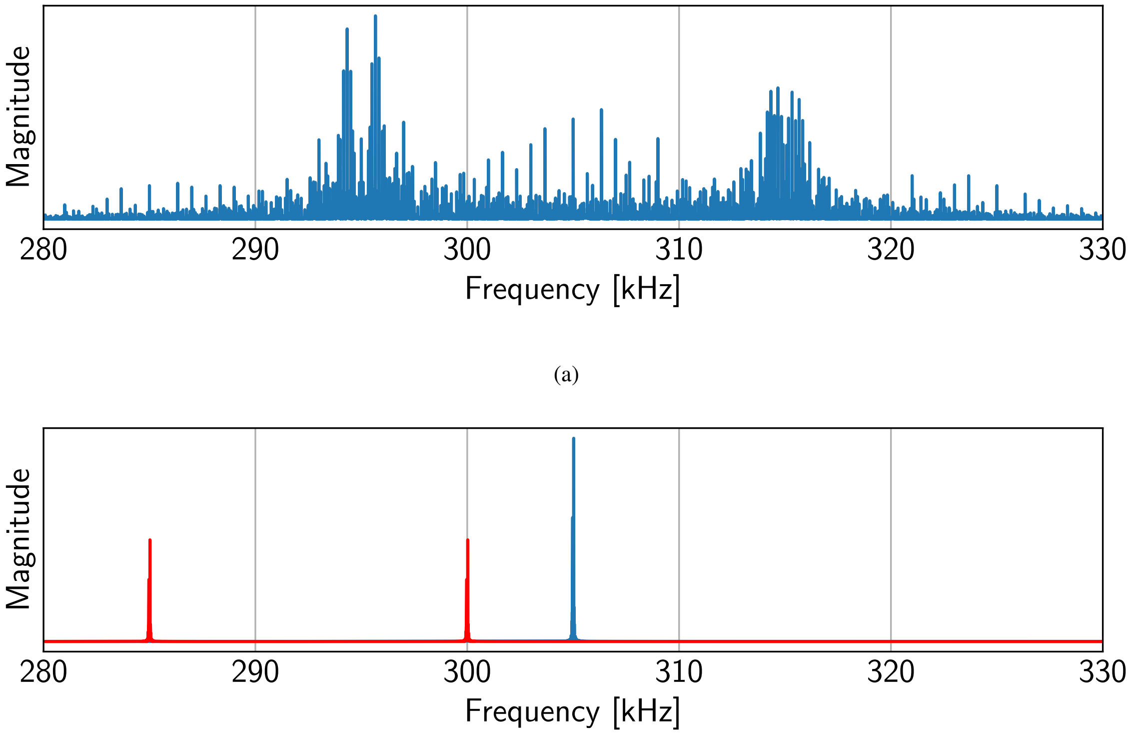

(a)

(b)

Figure 7.5: (a) Simulated MSK modulated RTCM2 messages with 40 kbit/s at center frequency 305 kHz in linear scale. (b) Simulated MSK modulated RTCM2 messages with 100 bit/s at center frequency 305 kHz (blue) and with two times 100 bit/s at 285.5 kHz and 300 kHz (red) in linear scale.

To maintain compatibility with the legacy signal, we can assign a second channel at the edge of the band. The channel doubles the total data rate and at the same time increases the spectral spacing of the potentially added CWs. We bisect the amplitudes of the signals to maintain the output power with this approach, which affects the coverage range of the signal. The two assigned channels are shown as peaks (red) at 300 kHz and 285.5 kHz in Fig. 7.5(b). In the past, each transmitter had two dedicated channels, which make this approach practicable for field trials.

Since the band still has enough space for 32 more stations, another option is to use the entire band with one station without supporting the legacy service. Here we considering the complete maritime frequency band from 285 kHz to 325 kHz utilizing 40 kHz of bandwidth [56]. Fig. 7.5a shows the simulated spectra for MSK-modulated RTCM2 messages at 40 kbit/s at centre frequency 305 kHz. The power spreads over the entire band, causing the amplitude to decrease.

The use of frequency division multiplexing access (FDMA), as in the previously described signals, is no longer possible when using the entire band. The broadcast use either Time Division Multiplexing Access (TDMA) or Code Division Multiplexing Access (CDMA) to distinguish the different stations. Here, we show the advantages of the proposed signals.

7.3.1. AMBIGUITY SOLVING

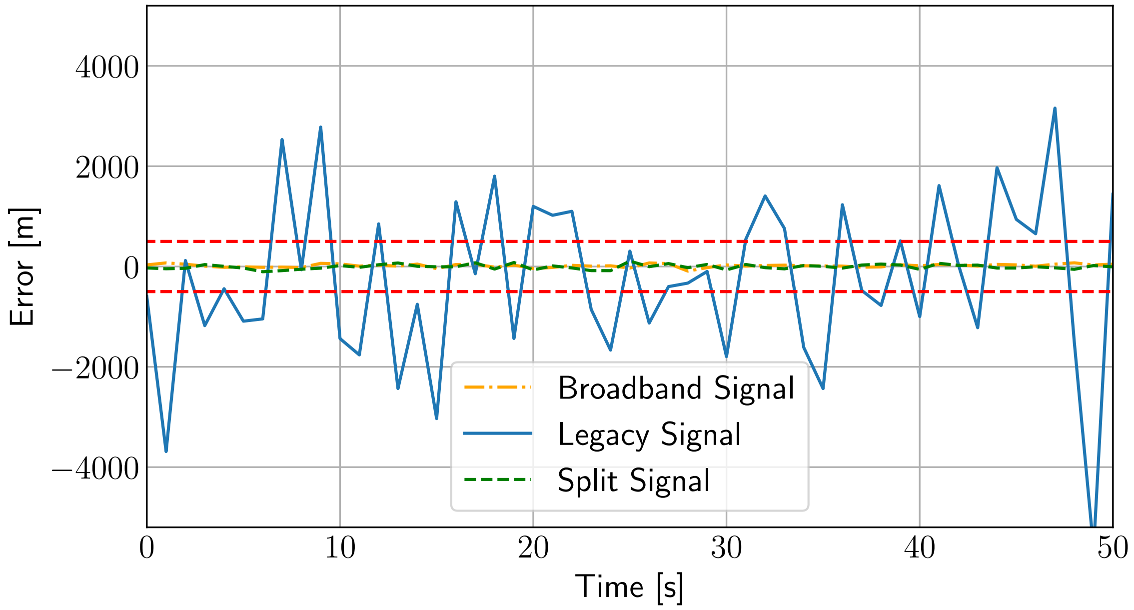

Figure 7.6: Estimation results of the beat signal phase for a simulated broadband channel in comparison to a simulated split channel. The dotted red line indicates the need error margin to resolve the ambiguities.

In Chapter 6, we had to use a phase tracker as the accuracy was not good enough to resolve the ambiguities. Here, a larger signal spacing between the continuous waves is beneficial for the ambiguity resolution as we described in Chapter 2 that the calculation of the propagation time depends on the frequency. Consequently, the uncertainty in the propagation time and thus the pseudo-range scales with the utilized frequencies f_i according to (2.7).

For the R-Mode approach described so far with two CWs in the channel, the frequency offset is chosen to be ±225 Hz, resulting in a beat signal of 450 Hz. For the two-channel split, we accordingly choose 225 Hz for the upper channel and −225 Hz for the lower channel to get a beat signal of 14 950 Hz, if we assume one channel at the lower end of the band at 285.5 kHz and another in the middle of the band at 300 kHz. With this offset we place the signals in a zero point of the MSK spectrum for a 100 bit/s signal. With this beat frequency, we now get ambiguities of 20 km, which can then be resolved by a lower beat frequency, with less accuracy. We use a third CW in one of the channels to achieve this.

For the second approach, we use the entire band for data transmission. The signal design shifted the zero crossings in the frequency range. Thus, for our aiding carrier, we select the second zero crossing of the wideband signal at ±20 kHz and obtain a wideband beat frequency of 40 kHz. The beat frequency now leads to an ambiguity of 7 km, which is resolved by an appropriately chosen third CW, with a lower accuracy requirement.

We have simulated all waveforms with constant amplitudes over the band to illustrate the advantages of the shifting approaches. For this, we estimate the pseudo ranges with an observation time of one second at 12 dB SNR. It is important to note that the CWs of each station must be distinguished using an FDMA or TDMA approach, not CDMA as proposed for the data channel.

Fig. 7.6 shows the range error of the beat signals as a result of the comparative simulation. The error of the original R-Mode signal is shown as a solid blue line, the split channel as a green dashed line and the high bandwidth signal as an orange solid/dashed line. The red dashed lines mark the error range between −500 m and 500 m, the distance in which a single CW resolve the ambiguity. The standard deviation of the estimate is 1726 m for the legacy signal, 50.3 m for the split signal and 37.6 m for the broadband signal.

Thus, we have shown that the modified waveforms can resolve the ambiguity of about one kilometre with an observation time of one second in a noisy environment. Changing the waveform can therefore make it possible to solve the ambiguities of the system with shorter observation times.

7.3.2. SKYWAVE MITIGATION

We described the mitigation of the distance estimation error caused by the skywave in Chapter 2. Here we now investigate the use of the matching-pursuit algorithm [119] to mitigate the influence. Lei [120] has already developed a similar approach for the Loran C system using the Split Augmented Lagrangian Shrinkage Algorithm (SALSA). To apply our design in the time domain, we need to send a known message with the samples $\boldsymbol{s}_{\text{tx}}(n)$ with n the discrete time index . The sampled received signal $\boldsymbol{s}_{\text{rx}}(n)$ can be written as

$$\boldsymbol{s}_{\text{rx}} = \boldsymbol{B} \times \boldsymbol{s} + \boldsymbol{w}. \tag{7.7}$$

$\boldsymbol{B}$ is a matrix in which each row i is a shifted sampled representation of $\boldsymbol{s}_{\text{tx}}(n - N_i)$, called an atom. Each atom is moved by a specific number of samples N_i. $\boldsymbol{s}$ is a vector specifying the combination of lines to solve for $\boldsymbol{s}_{\text{rx}}(n)$, and $\boldsymbol{w}$ is the additive measurement noise. The step size of N_i is the minimum time resolution we can achieve. To estimate the propagation time delay, we need to recreate the vector $\boldsymbol{s}$ from $\boldsymbol{s}_{\text{rx}}$. Here we use the matching-pursuit algorithm [119], which consists of two main steps. We compute

$$\boldsymbol{c} = \boldsymbol{B}^{\text{H}} \times \boldsymbol{s}_{\text{rx}}(n). \tag{7.8}$$

The vector $\boldsymbol{c}$ contains, after computation, the correlation of all rows of $\boldsymbol{B}$ with the incoming signal. We search for the item with the maximum correlation c_i and map it to s_i.

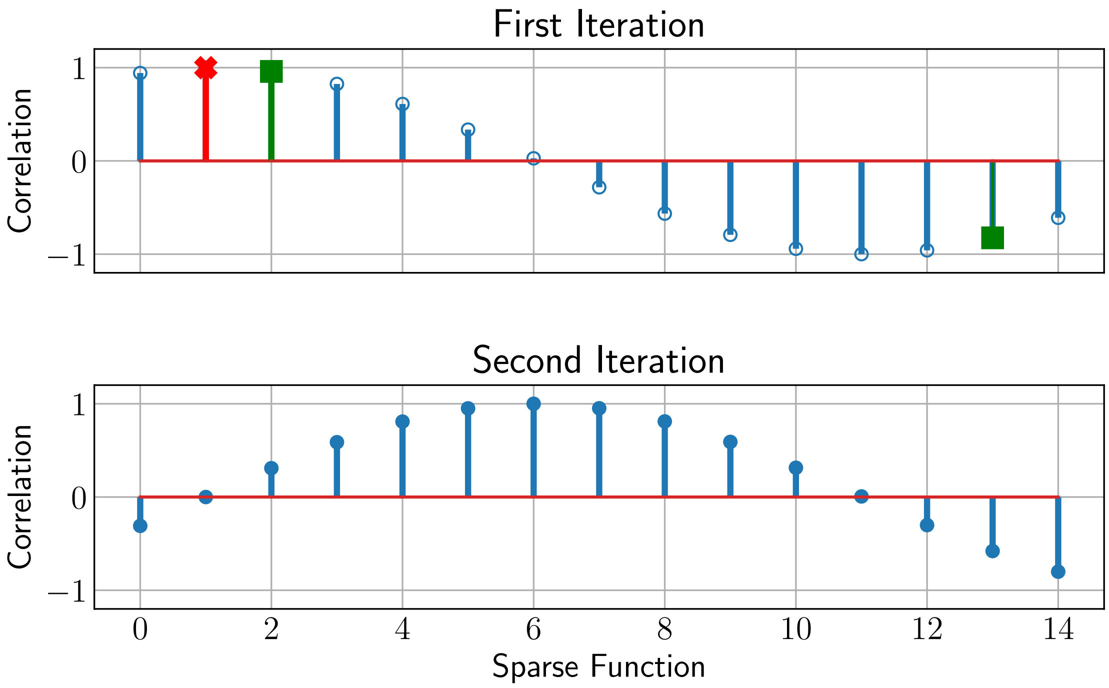

Figure 7.7: Normalized correlation peaks for first and second iterations in the matching pursuit algorithm for the legacy signal.

Next, we use the $\boldsymbol{B}_i$ row of $\boldsymbol{B}$ with the maximum correlation c_i to construct a new signal $\boldsymbol{s}_{\mathrm{rx}}(n)$ for the next run, which is described as

$$\boldsymbol{s}_{\mathrm{rx}}(n) = \boldsymbol{s}_{\mathrm{rx}}(n) - c_i \boldsymbol{B}_i. \tag{7.9}$$

These steps will be repeated until a threshold of energy is reached. We use the vector $\boldsymbol{s}$ to determine what delays have occurred compared to the known signal. Here, we expect two correlations peak, the first representing the groundwave, the second the skywave.

To show the practicability of our approach, we simulated the already described waveforms for signal snippets of 20 000 samples with a time resolution of 10 samples between the atoms and 1 MHz sampling rate. The received signal is described by

$$\boldsymbol{s}_{\mathrm{rx}}(n) = \boldsymbol{s}_{\mathrm{complete}}(n-20) + 0.5\, \boldsymbol{s}_{\mathrm{complete}}(n-130). \tag{7.10}$$

with $\boldsymbol{s}_{\mathrm{complete}}(n)$ a vector containing the sampled signal according to our signal model presented in Chapter 2.

We simulate a groundwave component that shows a delay of 20 samples and a skywave component that delays by 130 samples and is damped by half. Therefore, we expect the first correlation maximum to be at the third position in $\boldsymbol{c}$ in the first iteration and the 13th position in the second. The 110 samples of delay correspond to 110 µs, which is a realistic scenario for a distance of 550 km.

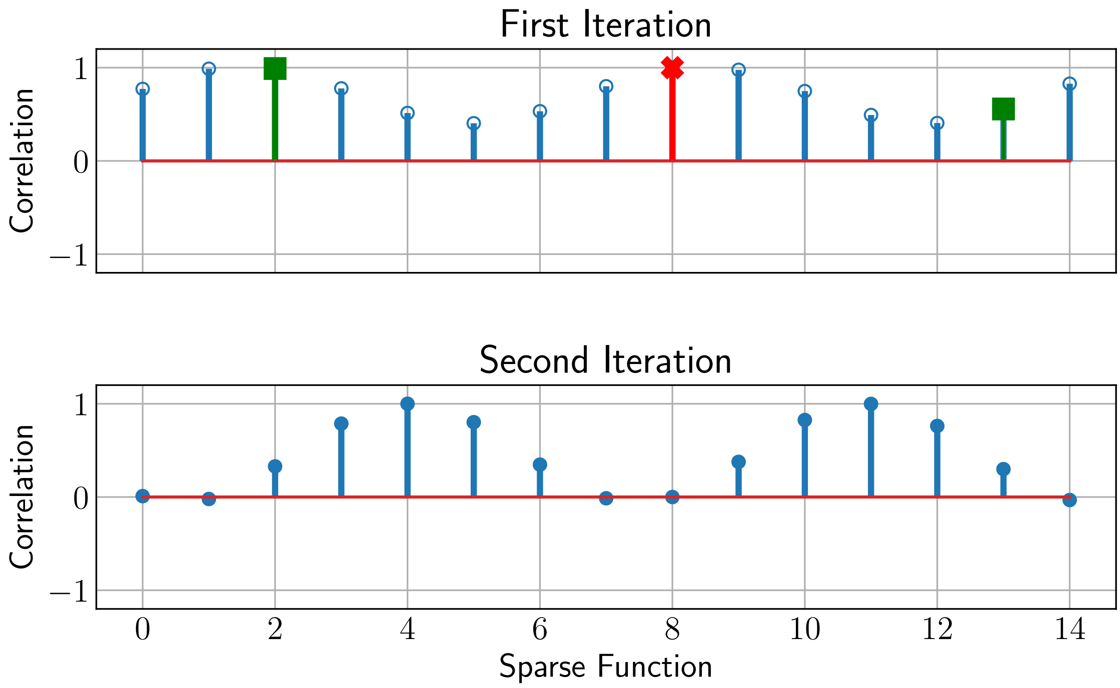

Figure 7.8: Normalized correlation peaks for first and second iterations in the matching pursuit algorithm for the split signal.

In the figures 7.7, 7.8 and 7.9 we present the results of the simulation. For this, we have plotted the vector $\boldsymbol{c}$ for the first and second iterations. We plot on the x-axes labelled sparse function the location in the vector and the corresponding atom in $\boldsymbol{B}$, while the y-value is the correlation value of $\boldsymbol{c}$ normalised to the maximum.

Fig. 7.7 shows the result for the legacy signal. We mark the highest marker as a red cross, the expected one as a green square and all others as a blue circle. We can see that the first correlation peak appears at the first position and is thus closer to the signal with higher amplitude but deviates from the expected value. In the second iteration, the correlation maximum shifts to the sides of the observed time window. The energy of the expected value has also disappeared, indicating that the atoms are too similar. With the given observation length, we cannot distinguish between the two signal components, and attenuation of the skywaves is not possible.

The result for the split signal in Fig. 7.8 behaves similarly to Fig. 7.7. We used the same colour coding as before. The main difference between the old and the split signal is that the first maximum now appears at the 8$^{\text{th}}$ position. We have also noticed that in the second iteration, the correlation peak is smaller compared to the legacy plot in Fig. 7.7 seems to fit. So, the performance of the overall signal seems to start to distinguish between the signal, but due to the limited bandwidth it is still not possible.

Finally, we present the results for the broadband signal in Fig. 7.9 We have again marked the correlation peaks as green squares. As expected, the first iteration shows a correlation peak at the second position. For the second iteration, the power in the left half of the graph has disappeared, as expected, and we can see the maximum at the 13th position. In this sce-

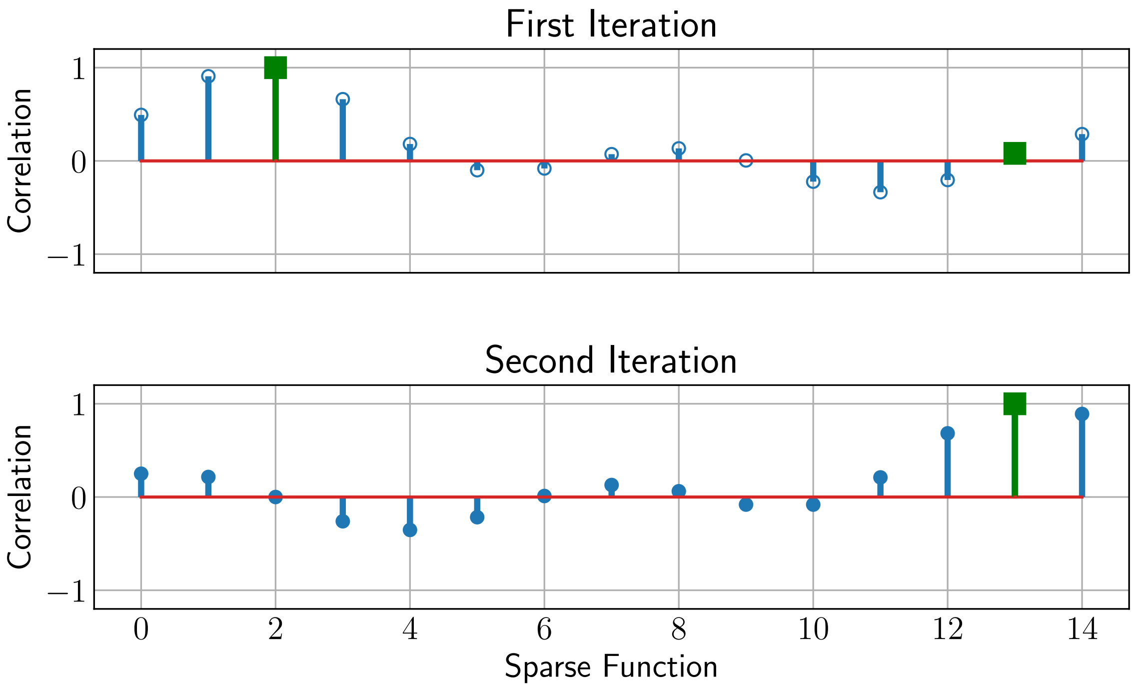

Figure 7.9: Normalized correlation peaks for first and second iterations in the matching pursuit algorithm for the broadband signal

nario, we can distinguish between the two signal components in the simulation. Therefore, we could separate the different paths in simulation and thus mitigate the skywaves.

8

CONCLUSION

The dissertation presented the first far-field R-Mode positioning and our approach to obtain these results. The results have proved that MF R-Mode is capable to provide PNT information in GNSS denied environment. Therefore, administrations could consider the system in future infrastructure planning and standardization not limited to the maritime domain.

Our work covered a wide variety of topics needed to design the navigation system. We started with the general ideas of using phase estimation to derive ranges and consequently a position.

During our research, we became aware that the existing description of the system is not sufficient to provide the best performance. We develop measurement procedures to describe the stations. So, we contribute to a better understanding of the influence on the phase at the transmitter side.

We utilized our gained knowledge to develop simulation software used in the further course of the work. However, there is still a leak of information for the propagation and the character of some stations in use as we were not able to visit all stations of the R-Mode Baltic testbed due to the Corvid-19 pandemic.

We continued on a more general level by extending the lower bound for the phase estimate next to a modulated signal. We calculated the bound for different cases, especially for the beat-phase, which is needed to resolve the ambiguities. Based on this, we showed the theoretical performance of the system using a coverage prediction, wrapping our contribution to the current system design.

In the next step, this work allowed us to improve the phase estimation and the entire system, both in accuracy and the required computing power. To do this, we described various algorithms and compared them to the lower bound. We have shown how to calculate all channels simultaneously with the help of FFT. In addition, we have further improved the influence of adaptive windowing. This dissertation provides an optimized estimator for MF R-Mode in different noise conditions.

Another area we had to work on to achieve our goal is the hardware side of the receiver. For this, we created three different designs for different purposes. We showed not only solutions for further development but also system monitoring. With the third low-cost design, we have presented that a receiver needs no laboratory-grade devices, even in the current state of development. Therefore, a commercial product is comparatively easy to implement. To compare the receivers, we have developed a test environment based only on a standard laboratory device, which we hope will enable more organisations to test their MF R-Mode developments. We present in this dissertation the possibility of reducing the cost of used hardware to broaden the applicability of the developed system.

All our work resulted in software development and testing in several measurement campaigns. We have repeatedly shown that it is possible to position ourselves in the far-field of the stations. We have thus achieved the primary goal, which was the conception, design and practical verification of a MF R-Mode receiver that can perform positioning in real-time. SMA and the WSV operate already the receiver presented here in the testbed. With this dissertation, we contributed a verification of the MF R-Mode in different dynamic and static scenarios.

However, this is not the end of the development of the MF R-Mode. Based on our work, we have made suggestions what future iterations at the signal level possibly could reach.We provided ideas of further developments of the MF R-Mode. Furthermore, we should consider R-Mode as part of a complete PNT solution in the future. We have already shown that the estimators presented here would benefit from information fusion. Positioning based on deep learning would also be conceivable. Canada and Korea developed further R-Mode testbeds. We are particularly pleased that in Canada, among others, our receivers are under test. The deployment allows new insights, as the Canadian administration uses a channel width of 1 kHz. Other applications outside of timing and positioning within the MF R-Mode are also being investigated, such as the observation of soil moisture and thus climatic development.

ACKNOWLEDGEMENTS

Writing this thesis was a unique experience, and it was always unclear to me if I could manage it to an end. Luckily, I have been surrounded by extraordinary people whose support and encouragement pushed me over the top. I will try to name at least a few of them.

First and foremost, I am very grateful to my PhD supervisor, Prof. Giovanni Del Galdo, for his invaluable advice, continuous support and patience while I worked on my thesis. Without his willingness to engage with the topic of R-Mode, this work would not have been possible. I am also very grateful for the teaching opportunity he gave me.

I would also like to express my sincere gratitude to my supervisor at DLR, Dr Stefan Gewies, for his continuous support of my PhD studies and related research and for the time spent discussing even small details to make our results even more valuable.

I am also very grateful for the support of our colleagues at the various project partners in the R-Mode Baltic project, especially the administrations. Without them, the testbed would not have been possible. Special thanks go to Michael Hoppe, who developed the idea of R-Mode in the first place. Without his support, the tests on the transmitter sides wouldn't be possible.

Moreover, I need to thank my other Colleges in our research group. Filippo for the coffee, the idea exchange, the help with the positioning solver and the work on the PLL. Niklas for the fruitful discussions on all R-Mode and non-R-Mode related topics.

Despite the R-Mode topic, I need to thank all the other colleagues and friends within DLR who supported me in finding my way through the jungle of DLR: Astrid, Shradah, Daniel, Christoph, Nis, Pawel, Uwe, Markus, Carsten, Ralf, Thoralf and last but not least Frank for keeping up the barbecue, the advice, spelling corrections and motivation. You all widened my mind to other topics and kept my back.

I also need to thank some people outside of my Neustrelitz department:

Sebastian, who started as my dive buddy and became a close friend. You always made sure that I stayed hydrated. It was good to have somebody who faced the same problems and struggled as much as I did.

Ines and Frank, for hosting me several times during my writecations.

My parents, Peter and Karin, for their numerous support over the years,

and last but not least, I would like to thank my beloved Girlfriend Birte, who probably suffered the most from my mood when I didn't succeed in something. Numerous times she had to cheer me up to finish this work.

APPENDIX: CRAMER RAÓ BOUND CALCULATION

A.1 CRAMER RAÓ BOUND FOR SIGNAL MODEL

In this appendix, we show the detailed calculation of the three different lower bounds. In the first step, we assume the signal model as

$$s(t_n, \boldsymbol{\theta}) \text{ with } \boldsymbol{\theta} = [\varphi_1, \varphi_{\text{beat}}]. \tag{1}$$

Where $\boldsymbol{\theta}$ is the parameter vector. The likelihood function for the signal model is

$$\mathscr{L}(t_n, \boldsymbol{\theta}) = \left(\frac{1}{\sigma^2 2\pi}\right)^N \exp\left[-\frac{1}{2\sigma^2}\sum_{n=0}^{N-1}\left(\boldsymbol{X}_{t_n} - s(t_n, \boldsymbol{\theta})\right)^2\right] \tag{2}$$

For a multi-parameter model, we can calculate the bound as

$$var\{\boldsymbol{\theta}_i\} \geq J^{-1}(\boldsymbol{\theta})_{ii} \tag{3}$$

with $\boldsymbol{J}_{ii}$ is the i-th diagonal element of $\boldsymbol{J}^{-1}$. $\boldsymbol{J}$ can be derived by

$$\boldsymbol{J}(\boldsymbol{\theta})_{ij} = -E\left[\frac{\delta^2 \ln(\mathscr{L}(t_n, \boldsymbol{\theta}))}{\delta\boldsymbol{\theta}_i \delta\boldsymbol{\theta}_j}\right] \tag{4}$$

with

$$\ln(\mathscr{L}(t_n, \boldsymbol{\theta})) = -\frac{N}{2}\ln(2\pi) - \frac{N}{2}\ln(\sigma^2) - \frac{1}{2\sigma^2}\sum_{n=0}^{N-1}\left(\boldsymbol{X}_{t_n} - s(t_n, \boldsymbol{\theta})\right)^2 \tag{5}$$

The step-wise derivation results in

$$\frac{\delta \ln(\mathscr{L}(t_n,\boldsymbol{\theta}))}{\delta\varphi_1} = \frac{1}{\sigma^2}\sum_{n=0}^{N-1}\left(\boldsymbol{X}_{t_n} - s(t_n,\boldsymbol{\theta})\right)\frac{\delta\, s(t_n,\boldsymbol{\theta})}{\delta\varphi_1}, \tag{6}$$

$$\frac{\delta \ln(\mathscr{L}(t_n,\boldsymbol{\theta}))}{\delta\varphi_{\text{beat}}} = \frac{1}{\sigma^2}\sum_{n=0}^{N-1}\left(\boldsymbol{X}_{t_n} - s(t_n,\boldsymbol{\theta})\right)\frac{\delta\, s(t_n,\boldsymbol{\theta})}{\delta\varphi_{\text{beat}}}, \tag{7}$$

$$\begin{aligned}\frac{\delta^2 \ln(\mathscr{L}(t_n,\boldsymbol{\theta}))}{(\delta\varphi_1)^2} &= \frac{1}{\sigma^2}\sum_{n=0}^{N-1}\left(\boldsymbol{X}_{t_n} - s(t_n,\boldsymbol{\theta})\right)\frac{\delta^2 s(t_n,\boldsymbol{\theta})}{(\delta\varphi_1)^2} \\ &\quad - \frac{1}{\sigma^2}\sum_{n=0}^{N-1}\frac{\delta\, s(t_n,\boldsymbol{\theta})}{\delta\varphi_1}\frac{\delta\, s(t_n,\boldsymbol{\theta})}{\delta\varphi_1},\end{aligned} \tag{8}$$

$$\begin{aligned}\frac{\delta^2 \ln(\mathscr{L}(t_n,\boldsymbol{\theta}))}{(\delta\varphi_{\text{beat}})^2} &= \frac{1}{\sigma^2}\sum_{n=0}^{N-1}\left(\boldsymbol{X}_{t_n} - s(t_n,\boldsymbol{\theta})\right)\frac{\delta^2 s(t_n,\boldsymbol{\theta})}{(\delta\varphi_{\text{beat}})^2} \\ &\quad - \frac{1}{\sigma^2}\sum_{n=0}^{N-1}\frac{\delta\, s(t_n,\boldsymbol{\theta})}{\delta\varphi_{\text{beat}}}\frac{\delta\, s(t_n,\boldsymbol{\theta})}{\delta\varphi_{\text{beat}}},\end{aligned} \tag{9}$$

$$\begin{aligned}\frac{\delta^2 \ln(\mathscr{L}(t_n,\boldsymbol{\theta}))}{\delta\varphi_1\delta\varphi_{\text{beat}}} &= \frac{1}{\sigma^2}\sum_{n=0}^{N-1}\left(\boldsymbol{X}_{t_n} - s(t_n,\boldsymbol{\theta})\right)\frac{\delta^2 s(t_n,\boldsymbol{\theta})}{\delta\varphi_1\delta\varphi_{\text{beat}}} \\ &\quad - \frac{1}{\sigma^2}\sum_{n=0}^{N-1}\frac{\delta\, s(t_n,\boldsymbol{\theta})}{\delta\varphi_1}\frac{\delta\, s(t_n,\boldsymbol{\theta})}{\delta\varphi_{\text{beat}}}.\end{aligned} \tag{10}$$

Assuming estimation with

$$\mathrm{E}(\boldsymbol{X}_{t_n} - s(t_n,\boldsymbol{\theta})) \approx 0, \tag{11}$$

we only need to solve

$$-\mathrm{E}\left(\frac{\delta^2 \ln(\mathscr{L}(t_n,\boldsymbol{\theta}))}{(\delta\varphi_1)^2}\right) = \frac{1}{\sigma^2}\sum_{n=0}^{N-1}\frac{\delta\, s(t_n,\boldsymbol{\theta})}{\delta\varphi_1}\frac{\delta\, s(t_n,\boldsymbol{\theta})}{\delta\varphi_1}, \tag{12}$$

$$-\mathrm{E}\left(\frac{\delta^2 \ln(\mathscr{L}(t_n,\boldsymbol{\theta}))}{(\delta\varphi_{\text{beat}})^2}\right) = \frac{1}{\sigma^2}\sum_{n=0}^{N-1}\frac{\delta\, s(t_n,\boldsymbol{\theta})}{\delta\varphi_{\text{beat}}}\frac{\delta\, s(t_n,\boldsymbol{\theta})}{\delta\varphi_{\text{beat}}}, \tag{13}$$

$$-\mathrm{E}\left(\frac{\delta^2 \ln(\mathscr{L}(t_n,\boldsymbol{\theta}))}{\delta\varphi_1\delta\varphi_{\text{beat}}}\right) = -\mathrm{E}\left(\frac{\delta^2 \ln(\mathscr{L}(t_n,\boldsymbol{\theta}))}{\delta\varphi_{\text{beat}}\delta\varphi_1}\right) = \frac{1}{\sigma^2}\sum_{n=0}^{N-1}\frac{\delta\, s(t_n,\boldsymbol{\theta})}{\delta\varphi_1}\frac{\delta\, s(t_n,\boldsymbol{\theta})}{\delta\varphi_{\text{beat}}}. \tag{14}$$

So, we can calculate $\boldsymbol{J}$ as

$$\boldsymbol{J}_{ij} = \frac{1}{\sigma^2}\sum_{n=0}^{N-1}\frac{\delta\, s(t_n,\boldsymbol{\theta})}{\delta\boldsymbol{\theta}_i}\frac{\delta\, s(t_n,\boldsymbol{\theta})}{\delta\boldsymbol{\theta}_j}, \tag{15}$$

which is the real part of the calculation in [57]. The representation in (15) simplified the derivation for the bound and is used in the following sections.

A.2 CRAMER RAÓ BOUND FOR TWO CONTINUOUS WAVES

Until now, we considered the amplitude of the signal component as known. However, in a realistic scenario this is not true, there for we extend the parameter vector $\boldsymbol{\theta}$ with two more parameters A_1 and A_2

$$s(t_n,\boldsymbol{\theta}) \text{ with } \boldsymbol{\theta} = [\varphi_1, A_1, A_2, \varphi_{\text{beat}}]. \tag{16}$$

Chose the signal model to

$$s_{\text{add}}(t_n,\boldsymbol{\theta}) = A_1 \sin(\omega_1\, t_n + \varphi_1) + A_2 \sin(\omega_1\, t_n + \omega_2\, t_n + \varphi_1 + \varphi_{\text{beat}}). \tag{17}$$

We need four derivates, namely

$$\frac{\delta s_{\text{add}}(t_n,\boldsymbol{\theta})}{\delta \varphi_1} = A_1 \cos(\omega_1\, t_n + \varphi_1) + A_2 \cos(\omega_1\, t_n + \omega_2\, t_n + \varphi_1 + \varphi_{\text{beat}}) \tag{18}$$

$$\frac{\delta s_{\text{add}}(t_n,\boldsymbol{\theta})}{\delta A_1} = \sin(\omega_1\, t_n + \varphi_1), \tag{19}$$

$$\frac{\delta s_{\text{add}}(t_n,\boldsymbol{\theta})}{\delta A_2} = \sin(\omega_1\, t_n + \omega_2\, t_n + \varphi_1 + \varphi_{\text{beat}}) \tag{20}$$

$$\frac{\delta s_{\text{add}}(t_n,\boldsymbol{\theta})}{\delta \varphi_{\text{beat}}} = A_2 \cos(\omega_1\, t_n + \omega_2\, t_n + \varphi_1 + \varphi_{\text{beat}}). \tag{21}$$

We obtain $\boldsymbol{J}_{\text{add}_{11}}$ by calculating

$$\begin{aligned}
\boldsymbol{J}_{\text{add}_{11}} &= \frac{1}{\sigma^2} \sum_{n=0}^{N-1} \left(A_1 \cos(\omega_1\, t_n + \varphi_1) + A_2 \cos(\omega_1\, t_n + \omega_2\, t_n + \varphi_1 + \varphi_{\text{beat}})\right)^2 \\
&= \frac{1}{\sigma^2} \sum_{n=0}^{N-1} A_1^2 \cos^2(\omega_1\, t_n + \varphi_1) + A_1 A_2 \cos(2\omega_1\, t_n + 2\varphi_1 + \omega_2\, t_n + \varphi_{\text{beat}}) \\
&\quad + A_1 A_2 \cos((\omega_2\, t_n + \varphi_{\text{beat}}) + A_2^2 \cos^2(\omega_1\, t_n + \omega_2\, t_n + \varphi_1 + \varphi_{\text{beat}}).
\end{aligned} \tag{22}$$

In the next step, we simplify the formula under the assumption of

$$\cos^2(v) = \frac{1}{2}(1 - \cos(2v)), \tag{23}$$

for any a, to

$$\begin{aligned}
\boldsymbol{J}_{\text{add}_{11}} &= \frac{1}{\sigma^2} \sum_{n=0}^{N-1} \frac{A_1^2}{2}(1 + \cos(2\omega_1\, t_n + 2\varphi_1)) \\
&\quad + A_1 A_2 \cos(2\omega_1\, t_n + 2\varphi_1 + \omega_2\, t_n + \varphi_{\text{beat}}) + A_1 A_2 \cos(\omega_2\, t_n + \varphi_{\text{beat}}) \\
&\quad + \frac{A_2^2}{2}(1 + \cos(2\omega_1\, t_n + 2\omega_2\, t_n + 2\varphi_1 + 2\varphi_{\text{beat}})).
\end{aligned} \tag{24}$$

Since,

$$\frac{1}{N} \sum_{n=0}^{N-1} \cos(2\omega\, t_n + \phi) \approx 0 \tag{25}$$

with ω is equal to ω_1 or ω_2 and ϕ any phase offset, we derive

$$\begin{aligned} \boldsymbol{J}_{\text{add}_{11}} =& \frac{1}{\sigma^2} \sum_{n=0}^{N-1} \frac{A_1^2}{2} + \frac{A_2^2}{2} \qquad (26) \\ =& \frac{N(A_1^2 + A_2^2)}{2\sigma^2}. \end{aligned}$$

With the steps and assumptions presented here, the remaining coefficients can be calculated as follows

$$\begin{aligned} \boldsymbol{J}_{\text{add}_{12}} =& \frac{1}{\sigma^2} \sum_{n=0}^{N-1} (A_1 \cos(\omega_1 t_n + \varphi_1) \qquad (27) \\ & + A_2 \cos(\omega_1 t_n + \omega_2 t_n + \varphi_1 + \varphi_{\text{beat}})) \sin(\omega_1 t_n + \varphi_1) \\ =& \frac{1}{\sigma^2} \sum_{n=0}^{N-1} \frac{A_1}{2} (\sin(2\omega_1 t_n + 2\varphi_1) - \sin(0)) \qquad (28) \\ & + \frac{A_2}{2} (\sin(2\omega_1 t_n + 2\varphi_1 + \omega_2 t_n + \varphi_{\text{beat}}) - \sin(\omega_2 t_n + \varphi_{\text{beat}})) \\ =& 0 \qquad (29) \end{aligned}$$

$$\begin{aligned} \boldsymbol{J}_{\text{add}_{13}} =& \frac{1}{\sigma^2} \sum_{n=0}^{N-1} (A_1 \cos(\omega_1 t_n + \varphi_1) \qquad (30) \\ & + A_2 \cos(\omega_1 t_n + \omega_2 t_n + \varphi_1 + \varphi_{\text{beat}})) \sin(\omega_1 t_n + \varphi_1 + \omega_2 t_n + \varphi_{\text{beat}}) \\ =& \frac{1}{\sigma^2} \sum_{n=0}^{N-1} \frac{A_1}{2} (\sin(2\omega_1 t_n + 2\varphi_1 + \omega_2 t_n + \varphi_{\text{beat}}) + \sin(\omega_2 t_n \varphi_{\text{beat}})) \qquad (31) \\ & + \frac{A_2}{2} (\sin(2\omega_1 t_n + 2\varphi_1 + 2\omega_2 t_n + 2\varphi_{\text{beat}}) - \sin(0)) \\ =& 0 \qquad (32) \end{aligned}$$

$$\begin{aligned}\boldsymbol{J}_{\text{add}_{14}} =& \frac{1}{\sigma^2}\sum_{n=0}^{N-1}\big(A_1\cos(\omega_1\, t_n+\varphi_1)+A_2\cos(\omega_1\, t_n+\omega_2\, t_n+\varphi_1+\varphi_{\text{beat}})\big) & (33)\\ & A_2\cos(\omega_1\, t_n+\omega_2\, t_n+\varphi_1+\varphi_{\text{beat}}) & \\ =& \frac{1}{\sigma^2}\sum_{n=0}^{N-1}\frac{A_1A_2}{2}\cos(2\omega_1\, t_n+\omega_2\, t_n+2\varphi_1+\varphi_{\text{beat}})+\frac{A_1A_2}{2}\cos(\omega_2\, t_n+\varphi_{\text{beat}}) & \\ & +A_2^2\cos^2(\omega_1\, t_n+\omega_2\, t_n+\varphi_1+\varphi_{\text{beat}}) & (34)\\ =& \frac{1}{\sigma^2}\sum_{n=0}^{N-1}A_1A_2\cos(\omega_1\, t_n+\omega_2\, t_n+\varphi_1+\varphi_{\text{beat}})+A_1A_2\cos(\omega_2\, t_n\varphi_{\text{beat}}) & (35)\\ & +\frac{A_2^2}{2}(1+\cos(\omega_1\, t_n+\omega_2\, t_n+\varphi_1+\varphi_{\text{beat}})) & \\ =& \frac{NA_2^2}{2\sigma^2} & (36)\end{aligned}$$

$$\begin{aligned}\boldsymbol{J}_{\text{add}_{22}} =& \frac{1}{\sigma^2}\sum_{n=0}^{N-1}\sin^2(\omega_1\, t_n+\varphi_1) & (37)\\ =& \frac{1}{\sigma^2}\sum_{n=0}^{N-1}\frac{1}{2}(1-\cos(2\omega_1\, t_n+2\varphi_1)) & (38)\\ =& \frac{N}{2\sigma^2} & (39)\end{aligned}$$

$$\begin{aligned}\boldsymbol{J}_{\text{add}_{23}} =& \frac{1}{\sigma^2}\sum_{n=0}^{N-1}\sin(\omega_1\, t_n+\omega_2\, t_n+\varphi_1+\varphi_{\text{beat}})\sin(\omega_1\, t_n+\varphi_1) & (40)\\ =& \frac{1}{\sigma^2}\sum_{n=0}^{N-1}\frac{1}{2}(\cos(\omega_2\, t_n+\varphi_{\text{beat}})-\cos(2\omega_1\, t_n+2\varphi_1+\omega_2\, t_n+\varphi_{\text{beat}})) & (41)\\ =& 0 & (42)\end{aligned}$$

$$\begin{aligned}\boldsymbol{J}_{\text{add}_{24}} =& \frac{1}{\sigma^2}\sum_{n=0}^{N-1}A_2\cos(\omega_1\, t_n+\omega_2\, t_n+\varphi_1+\varphi_{\text{beat}})\sin(\omega_1\, t_n+\varphi_1) & (43)\\ =& \frac{1}{\sigma^2}\sum_{n=0}^{N-1}\frac{A_2}{2}(\sin(2\omega_1\, t_n+2\varphi_1+\omega_2\, t_n+\varphi_{\text{beat}})-\sin(\omega_2\, t_n+\varphi_{\text{beat}})) & (44)\\ =& 0 & (45)\end{aligned}$$

$$
\begin{aligned}
\boldsymbol{J}_{\mathrm{add}_{33}} &= \frac{1}{\sigma^2}\sum_{n=0}^{N-1} \sin^2(\omega_1\, t_n + \omega_2\, t_n + \varphi_1 + \varphi_{\mathrm{beat}}) && (46)\\
&= \frac{1}{\sigma^2}\sum_{n=0}^{N-1} \frac{1}{2}(1 - \cos(2\omega_1\, t_n + 2\omega_2\, t_n + 2\varphi_1 + 2\varphi_{\mathrm{beat}})) && (47)\\
&= \frac{N}{2\sigma^2} && (48)
\end{aligned}
$$

$$
\begin{aligned}
\boldsymbol{J}_{\mathrm{add}_{34}} &= \frac{1}{\sigma^2}\sum_{n=0}^{N-1} A_2 \cos(\omega_1\, t_n + \omega_2\, t_n + \varphi_1 + \varphi_{\mathrm{beat}}) \sin(\omega_1\, t_n + \varphi_1 + \omega_2\, t_n + \varphi_{\mathrm{beat}}) && (49)\\
&= \frac{1}{\sigma^2}\sum_{n=0}^{N-1} \frac{A_2}{2}(\sin(2\omega_1\, t_n + 2\varphi_1 + 2\omega_2\, t_n + 2\varphi_{\mathrm{beat}}) - \sin(0)) && (50)\\
&= 0 && (51)
\end{aligned}
$$

$$
\begin{aligned}
\boldsymbol{J}_{\mathrm{add}_{44}} &= \frac{1}{\sigma^2}\sum_{n=0}^{N-1} \left(A_2 \cos(\omega_1\, t_n + \omega_2\, t_n + \varphi_1 + \varphi_{\mathrm{beat}})\right)^2 && (52)\\
&= \frac{1}{\sigma^2}\sum_{n=0}^{N-1} A_2^2 \cos^2(\omega_1\, t_n + \omega_2\, t_n + \varphi_1 + \varphi_{\mathrm{beat}}) && (53)\\
&= \frac{1}{\sigma^2}\sum_{n=0}^{N-1} \frac{A_2^2}{2}(1 + \cos(2\omega_1\, t_n + 2\omega_2\, t_n + 2\varphi_1 + 2\varphi_{\mathrm{beat}})) && (54)\\
&= \frac{N A_2^2}{2\sigma^2} && (55)
\end{aligned}
$$

We use that $\boldsymbol{J}_{ij} = \boldsymbol{J}_{ji}$ and we obtain the Fisher Information Matrix and their inverse as

$$
\boldsymbol{J}_{\mathrm{add}} = \frac{N}{2\sigma^2}\begin{pmatrix} A_1^2 + A_2^2 & 0 & 0 & A_2^2 \\ 0 & 1 & 0 & 0 \\ 0 & 0 & 1 & 0 \\ A_2^2 & 0 & 0 & A_2^2 \end{pmatrix}, \tag{56}
$$

$$
\boldsymbol{J}_{\mathrm{add}}^{-1} = \frac{2\sigma^2}{N}\begin{pmatrix} \frac{1}{A_1^2} & 0 & 0 & -\frac{1}{A_1^2} \\ 0 & 1 & 0 & 0 \\ 0 & 0 & 1 & 0 \\ -\frac{1}{A_1^2} & 0 & 0 & \frac{1}{A_1^2} + \frac{1}{A_2^2} \end{pmatrix}. \tag{57}
$$

Evaluating the diagonal entry of the inverse matrix, we obtain

$$var(\varphi_1) \geq \frac{2\sigma^2}{NA_1^2}, \tag{58}$$

$$var(\varphi_{\text{beat}}) \geq \frac{2\sigma^2(A_1^2 + A_2^2)}{NA_1^2 A_2^2}, \tag{59}$$

$$var(A_1) \geq \frac{2\sigma^2}{N}, \tag{60}$$

$$var(A_2) \geq \frac{2\sigma^2}{N}. \tag{61}$$

A.3 CRAMER RAÓ BOUND FOR A DYNAMIC CASE

In this section, we assume a constant radial velocity v, with the time-dependent phase shift determined as

$$\boldsymbol{\theta}_{\text{velocity}} = \omega_i \, v \, t_n. \tag{62}$$

We use the signal model

$$\begin{aligned} s_{\text{dynamic}}(t_n, \boldsymbol{\theta}) = & A_1 \sin(\omega_1 \, t_n + \omega_1 \, v \, t_n + \varphi_1) \\ & + A_2 \sin(\omega_1 \, t_n + \omega_2 \, t_n + \omega_{beat} \, v \, t_n + \varphi_1 + \varphi_{\text{beat}}) \end{aligned} \tag{63}$$

with

$$\omega_{beat} = \omega_1 - \omega_2. \tag{64}$$

We obtain the derivates

$$\begin{aligned} \frac{\delta s_{\text{dynamic}}(t_n, \boldsymbol{\theta})}{\delta \varphi_1} = & A_1 \cos\left(\omega_1 \, t_n \, v + \omega_1 \, t_n + \varphi_1\right) \\ & + A_2 \cos\left(\omega_{\text{beat}} \, t_n \, v + \omega_2 \, t_n + \varphi_1 + \varphi_{\text{beat}}\right), \end{aligned} \tag{65}$$

$$\frac{\delta s_{\text{dynamic}}(t_n, \boldsymbol{\theta})}{\delta \varphi_{\text{beat}}} = A_2 \cos\left(\omega_{\text{beat}} \, t_n \, v + \omega_2 \, t_n + \varphi_1 + \varphi_{\text{beat}}\right), \tag{66}$$

$$\frac{\delta s_{\text{dynamic}}(t_n, \boldsymbol{\theta})}{\delta v} = A_1 \, \omega_1 \, t_n \cos\left(\omega_1 \, t_n \, v + \omega_1 \, t_n + \varphi_1\right) \tag{67}$$

$$+ A_2 \, \omega_2 \, t_n \cos\left(\omega_{\text{beat}} \, t_n \, v + \omega_2 \, t_n + \varphi_1 + \varphi_{\text{beat}}\right), \tag{68}$$

$$\frac{\delta s_{\text{dynamic}}(t_n, \boldsymbol{\theta})}{\delta A_1} = \sin\left(\omega_1 \, t_n \, v + \omega_1 \, t_n + \varphi_1\right), \tag{69}$$

$$\frac{\delta s_{\text{dynamic}}(t_n, \boldsymbol{\theta})}{\delta A_2} = \sin\left(\omega_{\text{beat}} \, t_n \, v + \omega_2 \, t_n + \varphi_1 + \varphi_{\text{beat}}\right). \tag{70}$$

For the sake of simplicity, we give the sum over the different sine tones a name since they are no longer zero. We get

$$\psi_1 = \cos\left(2\,\omega_1\, t_n\, v + 2\,\omega_1\, t_n + 2\,\varphi_1\right), \tag{71}$$

$$\psi_2 = \cos\left(\omega_1\, t_n\, v + \omega_{\text{beat}}\, t_n\, v + \omega_1\, t_n + \omega_2\, t_n + 2\,\varphi_1 + \varphi_{\text{beat}}\right), \tag{72}$$

$$\psi_3 = \cos\left(\omega_1\, t_n\, v - \omega_{\text{beat}}\, t_n\, v + \omega_1\, t_n - \omega_2\, t_n - \varphi_{\text{beat}}\right), \tag{73}$$

$$\psi_4 = \cos\left(2\,\omega_{\text{beat}}\, t_n\, v + 2\,\omega_2\, t_n + 2\,\varphi_1 + 2\,\varphi_{\text{beat}}\right), \tag{74}$$

$$\psi_5 = \cos^2\left(\omega_2\, t_n + \omega_{\text{beat}}\, t_n\, v + \varphi_1 + \varphi_{\text{beat}}\right), \tag{75}$$

$$\psi_6 = \cos^2\left(\omega_1\, t_n\, v + \omega_1\, t_n + \varphi_1\right), \tag{76}$$

$$\psi_7 = \sin\left(2\,\omega_1\, t_n\, v + 2\,\omega_1\, t_n + 2\,\varphi_1\right), \tag{77}$$

$$\psi_8 = \sin\left(\omega_1\, t_n\, v + \omega_{\text{beat}}\, t_n\, v + \omega_1\, t_n + \omega_2\, t_n + 2\,\varphi_1 + \varphi_{\text{beat}}\right), \tag{78}$$

$$\psi_9 = \sin\left(\omega_1\, t_n\, v - \omega_{\text{beat}}\, t_n\, v + \omega_1\, t_n - \omega_2\, t_n - \varphi_{\text{beat}}\right), \tag{79}$$

$$\psi_{10} = \sin\left(2\,\omega_{\text{beat}}\, t_n\, v + 2\,\omega_2\, t_n + 2\varphi_1 + 2\varphi_{\text{beat}}\right), \tag{80}$$

$$\psi_{11} = \sin^2\left(\omega_1\, t_n\, v + \omega_1\, t_n + \varphi_1\right), \tag{81}$$

$$\psi_{12} = \sin^2\left(\omega_2\, t_n + \omega_{\text{beat}}\, t_n\, v + \varphi_1 + \varphi_{\text{beat}}\right). \tag{82}$$

Therefore we obtain the coefficients

$$\begin{aligned} \boldsymbol{J}_{\text{dynamic}_{11}} = & \frac{1}{\sigma^2} \sum_{n=0}^{N-1} \frac{1}{2}\, A_1^2 \cos\left(2\,\omega_1\, t_n\, v + 2\,\omega_1\, t_n + 2\,\varphi_1\right) + \frac{1}{2}\, A_1^2 \\ & + A_1\, A_2 \cos\left(\omega_1\, t_n\, v + \omega_{\text{beat}}\, t_n\, v + \omega_1\, t_n + \omega_2\, t_n + 2\,\varphi_1 + \varphi_{\text{beat}}\right) \\ & + A_1\, A_2 \cos\left(\omega_1\, t_n\, v - \omega_{\text{beat}}\, t_n\, v + \omega_1\, t_n - \omega_2\, t_n - \varphi_{\text{beat}}\right) \\ & + \frac{1}{2}\, A_2^2 \cos\left(2\,\omega_{\text{beat}}\, t_n\, v + 2\,\omega_2\, t_n + 2\,\varphi_1 + 2\,\varphi_{\text{beat}}\right) + \frac{1}{2}\, A_2^2 \end{aligned} \tag{83}$$

$$= \sum_{n=0}^{N-1} \frac{1}{2\sigma^2} \left(A_1^2 \psi_1 + A_1^2\, t_n + A_2^2 \psi_4 + A_2^2\, t_n\right) \tag{84}$$

$$+ \frac{1}{\sigma^2} \left(A_1\, A_2 \psi_2 + A_1\, A_2 \psi_3\right), \tag{85}$$

$$\begin{aligned} \boldsymbol{J}_{\text{dynamic}_{12}} = & \frac{1}{\sigma^2} \sum_{n=0}^{N-1} \frac{1}{2}\, A_1\, A_2 \cos\left(\omega_1\, t_n\, v + \omega_{\text{beat}}\, t_n\, v + \omega_1\, t_n + \omega_2\, t_n + 2\,\varphi_1 + \varphi_{\text{beat}}\right) \\ & + \frac{1}{2}\, A_1\, A_2 \cos\left(\omega_1\, t_n\, v - \omega_{\text{beat}}\, t_n\, v + \omega_1\, t_n - \omega_2\, t_n - \varphi_{\text{beat}}\right) \\ & + \frac{1}{2}\, A_2^2 \cos\left(2\,\omega_{\text{beat}}\, t_n\, v + 2\,\omega_2\, t_n + 2\,\varphi_1 + 2\,\varphi_{\text{beat}}\right) + \frac{1}{2}\, A_2^2 \end{aligned} \tag{86}$$

$$= \sum_{n=0}^{N-1} \frac{1}{2\sigma^2} \left(A_1\, A_2 \psi_2 + A_1\, A_2 \psi_3 + A_2^2 \psi_4 + A_2^2\, t_n\right), \tag{87}$$

$$
\begin{aligned}
\boldsymbol{J}_{\mathrm{dynamic}_{13}} = & \frac{1}{2}\, A_1^2\, \omega_1\, t_n \cos\left(2\,\omega_1\, t_n\, v + 2\,\omega_1\, t_n + 2\,\varphi_1\right) \\
& + \frac{1}{2}\, A_1^2\, \omega_1\, t_n \\
& + \frac{1}{2}\, A_1\, A_2\, \omega_1\, t_n \cos\left(\omega_1\, t_n\, v + \omega_{\mathrm{beat}}\, t_n\, v + \omega_1\, t_n + \omega_2\, t_n + 2\,\varphi_1 + \varphi_{\mathrm{beat}}\right) \\
& + \frac{1}{2}\, A_1\, A_2\, \omega_1\, t_n \cos\left(\omega_1\, t_n\, v - \omega_{\mathrm{beat}}\, t_n\, v + \omega_1\, t_n - \omega_2\, t_n - \varphi_{\mathrm{beat}}\right) \\
& + \frac{1}{2}\, A_1\, A_2\, \omega_{\mathrm{beat}}\, t_n \cos\left(\omega_1\, t_n\, v + \omega_{\mathrm{beat}}\, t_n\, v + \omega_1\, t_n + \omega_2\, t_n + 2\,\varphi_1 + \varphi_{\mathrm{beat}}\right) \\
& + \frac{1}{2}\, A_1\, A_2\, \omega_{\mathrm{beat}}\, t_n \cos\left(\omega_1\, t_n\, v - \omega_{\mathrm{beat}}\, t_n\, v + \omega_1\, t_n - \omega_2\, t_n - \varphi_{\mathrm{beat}}\right) + \\
& \frac{1}{2}\, A_2^2\, \omega_{\mathrm{beat}}\, t_n \cos\left(2\,\omega_{\mathrm{beat}}\, t_n\, v + 2\,\omega_2\, t_n + 2\,\varphi_1 + 2\,\varphi_{\mathrm{beat}}\right) + \frac{1}{2}\, A_2^2\, \omega_{\mathrm{beat}}\, t_n
\end{aligned}
\tag{88}
$$

$$
\begin{aligned}
= & \sum_{n=0}^{N-1} \frac{1}{\sigma^2} \sum_{n=0}^{N-1} A_1^2\, \omega_1\, t_n \psi_1 + A_1^2\, \omega_1\, t_n + A_1\, A_2\, \omega_1\, t_n\, \psi_2 + A_1\, A_2\, \omega_1\, t_n\, \psi_3 \\
& + A_1\, A_2\, \omega_{\mathrm{beat}}\, t_n\, \psi_2 + A_1\, A_2\, \omega_{\mathrm{beat}}\, t_n\, \psi_3 + A_2^2\, \omega_{\mathrm{beat}}\, t_n\, \psi_1 + A_2^2\, \omega_{\mathrm{beat}}\, t_n,
\end{aligned}
\tag{89}
$$

$$
\begin{aligned}
\boldsymbol{J}_{\mathrm{dynamic}_{14}} = & \frac{1}{\sigma^2} \sum_{n=0}^{N-1} \frac{1}{2}\, A_1 \sin\left(2\,\omega_1\, t_n\, v + 2\,\omega_1\, t_n + 2\,\varphi_1\right) \\
& + \frac{1}{2}\, A_2 \sin\left(\omega_1\, t_n\, v + \omega_{\mathrm{beat}}\, t_n\, v + \omega_1\, t_n + \omega_2\, t_n + 2\,\varphi_1 + \varphi_{\mathrm{beat}}\right) \\
& + \frac{1}{2}\, A_2 \sin\left(\omega_1\, t_n\, v - \omega_{\mathrm{beat}}\, t_n\, v + \omega_1\, t_n - \omega_2\, t_n - \varphi_{\mathrm{beat}}\right)
\end{aligned}
\tag{90}
$$

$$
= \sum_{n=0}^{N-1} \frac{1}{\sigma^2} \left(\frac{1}{2}\, A_1 \psi_7 + \frac{1}{2}\, A_2 \psi_8 + \frac{1}{2}\, A_2 \psi_9\right),
\tag{91}
$$

$$
\begin{aligned}
\boldsymbol{J}_{\mathrm{dynamic}_{15}} = & \frac{1}{\sigma^2} \sum_{n=0}^{N-1} \frac{1}{2}\, A_1 \sin\left(\omega_1\, t_n\, v + \omega_{\mathrm{beat}}\, t_n\, v + \omega_1\, t_n + \omega_2\, t_n + 2\,\varphi_1 + \varphi_{\mathrm{beat}}\right) \\
& - \frac{1}{2}\, A_1 \sin\left(\omega_1\, t_n\, v - \omega_{\mathrm{beat}}\, t_n\, v + \omega_1\, t_n - \omega_2\, t_n - \varphi_{\mathrm{beat}}\right) \\
& + \frac{1}{2}\, A_2 \sin\left(2\,\omega_{\mathrm{beat}}\, t_n\, v + 2\,\omega_2\, t_n + 2\,\varphi_1 + 2\,\varphi_{\mathrm{beat}}\right)
\end{aligned}
\tag{92}
$$

$$
= \sum_{n=0}^{N-1} \frac{1}{\sigma^2} \left(\frac{1}{2}\, A_1 \psi_8 - \frac{1}{2}\, A_1 \psi_9 + \frac{1}{2}\, A_2 \psi_{10}\right),
\tag{93}
$$

$$
\boldsymbol{J}_{\mathrm{dynamic}_{22}} = \frac{1}{\sigma^2} \sum_{n=0}^{N-1} A_2^2 \cos^2\left(\omega_2\, t_n + \omega_{\mathrm{beat}}\, t_n\, v + \varphi_1 + \varphi_{\mathrm{beat}}\right)
\tag{94}
$$

$$
= \sum_{n=0}^{N-1} \frac{A_2^2}{\sigma^2}\, \psi_5,
\tag{95}
$$

$$\begin{aligned}\boldsymbol{J}_{\mathrm{dynamic}_{23}} =&\frac{1}{\sigma^2}\sum_{n=0}^{N-1}\frac{1}{2}\,A_1\,A_2\,\omega_1\,t_n\cos\left(\omega_1\,t_n\,v+\omega_{\mathrm{beat}}\,t_n\,v+\omega_1\,t_n+\omega_2\,t_n+2\,\varphi_1+\varphi_{\mathrm{beat}}\right)\\ &+\frac{1}{2}\,A_1\,A_2\,\omega_1\,t_n\cos\left(\omega_1\,t_n\,v-\omega_{\mathrm{beat}}\,t_n\,v+\omega_1\,t_n-\omega_2\,t_n-\varphi_{\mathrm{beat}}\right)\\ &+\frac{1}{2}\,A_2^2\,\omega_{\mathrm{beat}}\,t_n\cos\left(2\,\omega_{\mathrm{beat}}\,t_n\,v+2\,\omega_2\,t_n+2\,\varphi_1+2\,\varphi_{\mathrm{beat}}\right)\\ &+\frac{1}{2}\,A_2^2\,\omega_{\mathrm{beat}}\,t_n\end{aligned}\tag{96}$$

$$=\sum_{n=0}^{N-1}\frac{t_n}{2\sigma^2}\left(A_1\,A_2\,\omega_1\psi_2+A_1\,A_2\,\omega_1\psi_3+A_2^2\,\omega_{\mathrm{beat}}\psi_4+A_2^2\,\omega_{\mathrm{beat}}\right),\tag{97}$$

$$\begin{aligned}\boldsymbol{J}_{\mathrm{dynamic}_{24}} =&\frac{1}{\sigma^2}\sum_{n=0}^{N-1}\frac{1}{2}\,A_2\sin\left(\omega_1\,t_n\,v+\omega_{\mathrm{beat}}\,t_n\,v+\omega_1\,t_n+\omega_2\,t_n+2\,\varphi_1+\varphi_{\mathrm{beat}}\right)\\ &+\frac{1}{2}\,A_2\sin\left(\omega_1\,t_n\,v-\omega_{\mathrm{beat}}\,t_n\,v+\omega_1\,t_n-\omega_2\,t_n-\varphi_{\mathrm{beat}}\right)\end{aligned}\tag{98}$$

$$=\sum_{n=0}^{N-1}\frac{1}{\sigma^2}\left(\frac{1}{2}\,A_2\psi_8+\frac{1}{2}\,A_2\psi_9\right),\tag{99}$$

$$\begin{aligned}\boldsymbol{J}_{\mathrm{dynamic}_{25}} =&\frac{1}{\sigma^2}\sum_{n=0}^{N-1}A_2A_2\sin\left(\omega_{\mathrm{beat}}\,t_n\,v+\omega_2\,t_n+\varphi_1+\varphi_{\mathrm{beat}}\right)\\ &\cos\left(\omega_{\mathrm{beat}}\,t_n\,v+\omega_2\,t_n+\varphi_1+\varphi_{\mathrm{beat}}\right)\end{aligned}\tag{100}$$

$$\begin{aligned}&=\frac{A_2A_2}{2\sigma^2}\sum_{n=0}^{N-1}\sin\left(2\,\omega_{\mathrm{beat}}\,t_n\,v+2\,\omega_2\,t_n+2\varphi_1+2\varphi_{\mathrm{beat}}\right)\\ &=\sum_{n=0}^{N-1}\frac{A_2A_2}{2\sigma^2}\,\psi_{10},\end{aligned}\tag{101}$$

$$\boldsymbol{J}_{\mathrm{dynamic}_{33}} =\frac{1}{\sigma^2}\sum_{n=0}^{N-1}\frac{1}{2}\,A_1^2\,t_n^2\,\omega_1^2\cos\left(2\,\omega_1\,t_n\,v+2\,\omega_1\,t_n+2\,\varphi_1\right)+\frac{1}{2}\,A_1^2\,t_n^2\,\omega_1^2\tag{102}$$

$$\begin{aligned}&+A_1\,A_2\,t_n^2\,\omega_1\,\omega_{\mathrm{beat}}\cos\left(\omega_1\,t_n\,v+\omega_{\mathrm{beat}}\,t_n\,v+\omega_1\,t_n+\omega_2\,t_n+2\,\varphi_1+\varphi_{\mathrm{beat}}\right)\\ &+A_1\,A_2\,t_n^2\,\omega_1\,\omega_{\mathrm{beat}}\cos\left(\omega_1\,t_n\,v-\omega_{\mathrm{beat}}\,t_n\,v+\omega_1\,t_n-\omega_2\,t_n-\varphi_{\mathrm{beat}}\right)\\ &+\frac{1}{2}\,A_2^2\,t_n^2\,\omega_{\mathrm{beat}}^2\cos\left(2\,\omega_{\mathrm{beat}}\,t_n\,v+2\,\omega_2\,t_n+2\,\varphi_1+2\,\varphi_{\mathrm{beat}}\right)+\frac{1}{2}\,A_2^2\,t_n^2\,\omega_{\mathrm{beat}}^2\\ &=\sum_{n=0}^{N-1}\frac{t_n^2}{2\sigma^2}\left(\omega_1^2A_1^2\psi_1+\omega_{\mathrm{beat}}^2A_2^2\psi_4+\omega_1^2A_1^2+,\omega_{\mathrm{beat}}^2A_2^2\right)\\ &+\frac{t_n^2\,\omega_1\,\omega_{\mathrm{beat}}}{\sigma^2}\left(A_1\,A_2\psi_2+A_1\,A_2\psi_3\right),\end{aligned}\tag{103}$$

$$\begin{aligned}\boldsymbol{J}_{\text{dynamic}_{34}} = &\frac{1}{\sigma^2}\sum_{n=0}^{N-1}\frac{1}{2}A_1\,\omega_1\,t_n\sin\left(2\,\omega_1\,t_n\,v + 2\,\omega_1\,t_n + 2\,\varphi_1\right)\\ &+\frac{1}{2}A_2\,\omega_{\text{beat}}\,t_n\sin\left(\omega_1\,t_n\,v + \omega_{\text{beat}}\,t_n\,v + \omega_1\,t_n + \omega_2\,t_n + 2\,\varphi_1 + \varphi_{\text{beat}}\right)\\ &+\frac{1}{2}A_2\,\omega_{\text{beat}}\,t_n\sin\left(\omega_1\,t_n\,v - \omega_{\text{beat}}\,t_n\,v + \omega_1\,t_n - \omega_2\,t_n - \varphi_{\text{beat}}\right)\end{aligned}\tag{104}$$

$$= \sum_{n=0}^{N-1}\frac{t_n}{\sigma^2}\left(\frac{\omega_1}{2}A_1\psi_7 + \frac{\omega_{\text{beat}}}{2}A_2\psi_8 + \frac{\omega_{\text{beat}}}{2}A_2\psi_9\right),\tag{105}$$

$$\begin{aligned}\boldsymbol{J}_{\text{dynamic}_{35}} = &\frac{1}{\sigma^2}\sum_{n=0}^{N-1}\frac{1}{2}A_1\,\omega_1\,t_n\sin\left(\omega_1\,t_n\,v + \omega_{\text{beat}}\,t_n\,v + \omega_1\,t_n + \omega_2\,t_n + 2\,\varphi_1 + \varphi_{\text{beat}}\right)\\ &-\frac{1}{2}A_1\,\omega_1\,t_n\sin\left(\omega_1\,t_n\,v - \omega_{\text{beat}}\,t_n\,v + \omega_1\,t_n - \omega_2\,t_n - \varphi_{\text{beat}}\right)\\ &+\frac{1}{2}A_2\,\omega_{\text{beat}}\,t_n\sin\left(2\,\omega_{\text{beat}}\,t_n\,v + 2\,\omega_2\,t_n + 2\,\varphi_1 + 2\,\varphi_{\text{beat}}\right)\end{aligned}\tag{106}$$

$$= \sum_{n=0}^{N-1}\frac{t_n}{\sigma^2}\left(\frac{\omega_1}{2}A_1\psi_8 - \frac{\omega_1}{2}A_1\psi_9 + \frac{\omega_{\text{beat}}}{2}A_2\psi_{10}\right),$$

$$\boldsymbol{J}_{\text{dynamic}_{44}} = \frac{1}{\sigma^2}\sum_{n=0}^{N-1}\sin^2\left(\omega_1\,t_n\,v + \omega_1\,t_n + \varphi_1\right)\tag{107}$$

$$= \sum_{n=0}^{N-1}\frac{1}{\sigma^2}\psi_{11},\tag{108}$$

$$\begin{aligned}\boldsymbol{J}_{\text{dynamic}_{45}} = &\frac{1}{\sigma^2}\sum_{n=0}^{N-1}-\frac{1}{2}\cos\left(\omega_1\,t_n\,v + \omega_{\text{beat}}\,t_n\,v + \omega_1\,t_n + \omega_2\,t_n + 2\,\varphi_1 + \varphi_{\text{beat}}\right)\\ &+\frac{1}{2}\cos\left(\omega_1\,t_n\,v - \omega_{\text{beat}}\,t_n\,v + \omega_1\,t_n - \omega_2\,t_n - \varphi_{\text{beat}}\right)\end{aligned}\tag{109}$$

$$= \sum_{n=0}^{N-1}\frac{1}{\sigma^2}\left(-\frac{1}{2}\psi_8 + \frac{1}{2}\psi_3\right),\tag{110}$$

$$\boldsymbol{J}_{\text{dynamic}_{55}} = \frac{1}{\sigma^2}\sum_{n=0}^{N-1}\sin^2\left(\omega_2\,t_n + \omega_{\text{beat}}\,t_n\,v + \varphi_1 + \varphi_{\text{beat}}\right)\tag{111}$$

$$= \sum_{n=0}^{N-1}\frac{1}{\sigma^2}\psi_{12}.\tag{112}$$

In the special case that v is an integer value, we can assume the sum as zero again

$$\boldsymbol{J}_{\text{dynamic}_{11}} = \frac{A_1^2 + A_2^2}{2\sigma^2}N,\tag{113}$$

$$\boldsymbol{J}_{\text{dynamic}_{12}} = \frac{1}{2\sigma^2} A_2^2 N, \tag{114}$$

$$\boldsymbol{J}_{\text{dynamic}_{13}} = \frac{\Delta t}{2\sigma^2} \left(A_1^2 \omega_1 + A_2^2 \omega_{\text{beat}}\right) \frac{N(N-1)}{2}, \tag{115}$$

$$\boldsymbol{J}_{\text{dynamic}_{14}} = 0, \tag{116}$$

$$\boldsymbol{J}_{\text{dynamic}_{15}} = 0, \tag{117}$$

$$\boldsymbol{J}_{\text{dynamic}_{22}} = \frac{1}{2\sigma^2} A_2^2 N, \tag{118}$$

$$\boldsymbol{J}_{\text{dynamic}_{23}} = \frac{\Delta t}{2\sigma^2} A_2^2 \omega_{\text{beat}} \frac{N(N-1)}{2}, \tag{119}$$

$$\boldsymbol{J}_{\text{dynamic}_{24}} = 0, \tag{120}$$

$$\boldsymbol{J}_{\text{dynamic}_{25}} = 0, \tag{121}$$

$$\boldsymbol{J}_{\text{dynamic}_{33}} = \frac{\Delta t^2}{2\sigma^2} \left(A_1^2 \omega_1^2 + A_2^2 \omega_{\text{beat}}^2\right) \frac{N(N-1)(2N-1)}{6}, \tag{122}$$

$$\boldsymbol{J}_{\text{dynamic}_{34}} = 0, \tag{123}$$

$$\boldsymbol{J}_{\text{dynamic}_{35}} = 0, \tag{124}$$

$$\boldsymbol{J}_{\text{dynamic}_{44}} = \frac{N}{2\sigma^2}, \tag{125}$$

$$\boldsymbol{J}_{\text{dynamic}_{45}} = 0, \tag{126}$$

$$\boldsymbol{J}_{\text{dynamic}_{55}} = \frac{N}{2\sigma^2}. \tag{127}$$

For this special case, we get the FIM

$$\boldsymbol{J}_{\text{dynamic}} = \frac{N}{2\sigma^2}\begin{bmatrix} A_1^2 + A_2^2 & A_2^2 & \frac{(N-1)\left(A_1^2\,\omega_1 + A_2^2\,\omega_{\text{beat}}\right)\Delta t}{2} & 0 & 0 \\ A_2^2 & A_2^2 & \frac{A_2^2\,\omega_{\text{beat}}\,(N-1)\,\Delta t}{2} & 0 & 0 \\ \frac{(N-1)\left(A_1^2\,\omega_1 + A_2^2\,\omega_{\text{beat}}\right)\Delta t}{2} & \frac{A_2^2\,\omega_{\text{beat}}\,(N-1)\,\Delta t}{2} & \frac{(N-1)\,(2\,N-1)\left(A_1^2\,\omega_1 + A_2^2\,\omega_{\text{beat}}\right)\Delta t^2}{6} & 0 & 0 \\ 0 & 0 & 0 & 1 & 0 \\ 0 & 0 & 0 & 0 & 1 \end{bmatrix}, \tag{128}$$

and consequently the inverse FIM

$$\boldsymbol{J}^{-1}_{\text{dynamic}} = \begin{bmatrix} \boldsymbol{J}^{-1}_{\text{dynamic}_{11}} & \boldsymbol{J}^{-1}_{\text{dynamic}_{12}} & \boldsymbol{J}^{-1}_{\text{dynamic}_{13}} & 0 & 0 \\ \boldsymbol{J}^{-1}_{\text{dynamic}_{12}} & \boldsymbol{J}^{-1}_{\text{dynamic}_{22}} & \boldsymbol{J}^{-1}_{\text{dynamic}_{23}} & 0 & 0 \\ ]\ \boldsymbol{J}^{-1}_{\text{dynamic}_{13}} & \boldsymbol{J}^{-1}_{\text{dynamic}_{23}} & \boldsymbol{J}^{-1}_{\text{dynamic}_{33}} & 0 & 0 \\ 0 & 0 & 0 & 1 & 0 \\ 0 & 0 & 0 & 0 & 1 \end{bmatrix}, \tag{129}$$

with the entries

$$\boldsymbol{J}^{-1}_{\text{dynamic}_{11}} = \frac{A_1^2(2-4N)\omega_1 + A_2^2\omega_{\text{beat}}(N(\omega_{\text{beat}}-4) - \omega_{\text{beat}} + 2)}{A_1^4\omega_1(N(\omega_1-4) - \omega_1 + 2) + A_1^2A_2^2\omega_{\text{beat}}(N(\omega_{\text{beat}}-4) - \omega_{\text{beat}} + 2)}, \tag{130}$$

$$\boldsymbol{J}^{-1}_{\text{dynamic}_{12}} = -\frac{(N(\omega_{\text{beat}}-4) - \omega_{\text{beat}} + 2)\left(A_1^2\omega_1 + A_2^2\omega_{\text{beat}}\right)}{A_1^4\omega_1(N(\omega_1-4) - \omega_1 + 2) + A_1^2A_2^2\omega_{\text{beat}}(N(\omega_{\text{beat}}-4) - \omega_{\text{beat}} + 2)}, \tag{131}$$

$$\boldsymbol{J}^{-1}_{\text{dynamic}_{13}} = \frac{2\omega_1}{\Delta t\left(A_1^2\omega_1(N(\omega_1-4) - \omega_1 + 2) + A_2^2\omega_{\text{beat}}(N(\omega_{\text{beat}}-4) - \omega_{\text{beat}} + 2)\right)}, \tag{132}$$

$$\boldsymbol{J}^{-1}_{\text{dynamic}_{22}} = \frac{\left(A_1^2\omega_1 + A_2^2\omega_{\text{beat}}\right)\left(A_1^2(N(\omega_1-4) - \omega_1 + 2) + A_2^2(N(\omega_{\text{beat}}-4) - \omega_{\text{beat}} + 2)\right)}{A_1^4A_2^2\omega_1(N(\omega_1-4) - \omega_1 + 2) + A_1^2A_2^4\omega_{\text{beat}}(N(\omega_{\text{beat}}-4) - \omega_{\text{beat}} + 2)}, \tag{133}$$

$$\boldsymbol{J}^{-1}_{\text{dynamic}_{23}} = \frac{2\omega_{\text{beat}} - 2\omega_1}{\Delta t\left(A_1^2\omega_1(N(\omega_1-4) - \omega_1 + 2) + A_2^2\omega_{\text{beat}}(N(\omega_{\text{beat}}-4) - \omega_{\text{beat}} + 2)\right)}, \tag{134}$$

$$\boldsymbol{J}^{-1}_{\text{dynamic}_{33}} = -\frac{4}{\Delta t^2(N-1)\left(A_1^2\omega_1(N(\omega_1-4) - \omega_1 + 2) + A_2^2\omega_{\text{beat}}(N(\omega_{\text{beat}}-4) - \omega_{\text{beat}} + 2)\right)}. \tag{135}$$

A.4 CRAMER RAÓ BOUND FOR COMPLETE R-MODE SIGNAL

From real measurement, we observe a different behaviour when we add the MSK signal. So, we need to extend the signal model with an MSK signal. In time domain an MSK modulated bit sequence $b_\tau(n)$ can be written as

$$s_{\text{signal}}(t_n) = \sin(\omega_c t_n + b_\tau(n)\frac{\pi t_n}{2T_{\text{bit}}} + \bar{\varphi}_\tau[n]), \tag{136}$$

where T_{bit} is the bit duration. We include the modulated MSK signal in our existing signal model, which leads to

$$\begin{aligned} s_{\text{signal}}(t_n,\boldsymbol{\theta}) =& A_1 \sin(\omega_1 t_n + \varphi_1) \\ &+ A_{\text{MSK}} \sin(\omega_c t_n + b_\tau(n)\frac{\pi t_n}{2T_{\text{bit}}} + \varphi_1 + \bar{\varphi}_\tau[n]) \\ &+ A_2 \sin(\omega_2 t_n + \varphi_1 + \varphi_{\text{beat}}), \end{aligned} \tag{137}$$

The parameter vector is extended to

$$s_{\text{signal}}(t_n,\boldsymbol{\theta}) \text{ with } \boldsymbol{\theta} = [\varphi_1, \bar{\varphi}_\tau[n], \varphi_{\text{beat}}, b_\tau(n), A_1, A_{\text{MSK}}, A_2]. \tag{138}$$

We get the derivates

$$\begin{aligned} \frac{\delta s_{\text{signal}}(t_n,\boldsymbol{\theta})}{\delta\varphi_1} =& A_1 \cos(\omega_1 t_n + \varphi_1) + A_{\text{MSK}} \cos(\omega_{\text{c}} t_n + b_\tau(n)\frac{\pi t_n}{2T_{\text{bit}}} + \varphi_1 + \bar{\varphi}_\tau[n]) \\ &+ A_2 \cos(\omega_2 t_n + \varphi_1 + \varphi_{\text{beat}}) \end{aligned} \tag{139}$$

$$\frac{\delta s_{\text{signal}}(t_n,\boldsymbol{\theta})}{\delta\bar{\varphi}_\tau[n]} = A_{\text{MSK}} \cos(\omega_{\text{c}} t_n + b_\tau(n)\frac{\pi t_n}{2T_{\text{bit}}} + \varphi_1 + \bar{\varphi}_\tau[n]) \tag{140}$$

$$\frac{\delta s_{\text{signal}}(t_n,\boldsymbol{\theta})}{\delta\varphi_{\text{beat}}} = A_2 \cos(\omega_2 t_n + \varphi_1 + \varphi_{\text{beat}}) \tag{141}$$

$$\frac{\delta s_{\text{signal}}(t_n,\boldsymbol{\theta})}{\delta b_\tau(n)} = A_{\text{MSK}}\frac{\pi t_n}{2T_{\text{bit}}} \cos(\omega_{\text{c}} t_n + b_\tau(n)\frac{\pi t_n}{2T_{\text{bit}}} + \varphi_1 + \bar{\varphi}_\tau[n]) \tag{142}$$

$$\frac{\delta s_{\text{signal}}(t_n,\boldsymbol{\theta})}{\delta A_1} = \sin(\omega_1 t_n + \varphi_1) \tag{143}$$

$$\frac{\delta s_{\text{signal}}(t_n,\boldsymbol{\theta})}{\delta A_{\text{MSK}}} = \sin(\omega_{\text{c}} t_n + b_\tau(n)\frac{\pi t_n}{2T_{\text{bit}}} + \varphi_1 + \bar{\varphi}_\tau[n]) \tag{144}$$

$$\frac{\delta s_{\text{signal}}(t_n,\boldsymbol{\theta})}{\delta A_2} = \sin(\omega_2 t_n + \varphi_1 + \varphi_{\text{beat}}), \tag{145}$$

$$\begin{aligned}
\boldsymbol{J}_{\mathrm{signal}_{11}} =& \frac{1}{\sigma^2}\sum_{n=0}^{N-1} A_1^2 \cos(\omega_1\, t_n + \varphi_1)^2 \\
&+ 2\, A_1\, A_2 \cos(\omega_1\, t_n + \varphi_1) \cos(\omega_2\, t_n + \varphi_1 + \varphi_{\mathrm{beat}}) \\
&+ 2\, A_1\, A_{\mathrm{MSK}} \cos(\omega_1\, t_n + \varphi_1) \cos\!\left(\omega_{\mathrm{c}}\, t_n + b_\tau(n) \frac{\pi\, t_n}{2\, T_{\mathrm{bit}}} + \varphi_1 + \bar{\varphi}_\tau[n]\right) \\
&+ A_2^2 \cos(\omega_2\, t_n + \varphi_1 + \varphi_{\mathrm{beat}})^2 \\
&+ 2\, A_2\, A_{\mathrm{MSK}} \cos(\omega_2\, t_n + \varphi_1 + \varphi_{\mathrm{beat}}) \cos\!\left(\omega_c t_n + b_\tau(n) \frac{\pi\, t_n}{2\, T_{\mathrm{bit}}} + \varphi_1 + \bar{\varphi}_\tau[n]\right) \\
&+ A_{\mathrm{MSK}}^2 \cos\!\left(\omega_c t_n + b_\tau(n) \frac{\pi\, t_n}{2\, T_{\mathrm{bit}}} + \varphi_1 + \bar{\varphi}_\tau[n]\right)^2
\end{aligned} \tag{146}$$

$$\begin{aligned}
=& \frac{1}{\sigma^2}\sum_{n=0}^{N-1} \frac{1}{2} A_1^2 (1 + \cos(2\,\omega_1\, t_n + 2\,\varphi_1)) \\
&+ 2\, A_1\, A_2 \cos(\omega_1\, t_n + \varphi_1) \cos(\omega_2\, t_n + \varphi_1 + \varphi_{\mathrm{beat}}) \\
&+ 2\, A_1\, A_{\mathrm{MSK}} \cos(\omega_1\, t_n + \varphi_1) \cos\!\left(\omega_{\mathrm{c}}\, t_n + b_\tau(n) \frac{\pi\, t_n}{2\, T_{\mathrm{bit}}} + \varphi_1 + \bar{\varphi}_\tau[n]\right) \\
&+ \frac{1}{2} A_2^2 (1 + \cos(2\,\omega_2\, t_n + 2\,\varphi_1 + 2\,\varphi_{\mathrm{beat}})) \\
&+ 2\, A_2\, A_{\mathrm{MSK}} \cos(\omega_2\, t_n + \varphi_1 + \varphi_{\mathrm{beat}}) \cos\!\left(\omega_c t_n + b_\tau(n) \frac{\pi\, t_n}{2\, T_{\mathrm{bit}}} + \varphi_1 + \bar{\varphi}_\tau[n]\right) \\
&+ \frac{1}{2}\, A_{\mathrm{MSK}}^2 \cos\!\left(2\,\omega_c t_n + 2\, b_\tau(n) \frac{\pi\, t_n}{2\, T_{\mathrm{bit}}} + 2\,\varphi_1 + 2\,\bar{\varphi}_\tau[n]\right)
\end{aligned} \tag{147}$$

$$= \frac{N(A_1^2 + A_{\mathrm{MSK}}^2 + A_2^2)}{2\sigma^2}, \tag{148}$$

$$\begin{aligned}
\boldsymbol{J}_{\mathrm{signal}_{12}} =& \frac{1}{\sigma^2}\sum_{n=0}^{N-1} A_{\mathrm{MSK}}^2 \cos\!\left(\omega_c t_n + b_\tau(n) \frac{\pi\, t_n}{2\, T_{\mathrm{bit}}} + \varphi_1 + \bar{\varphi}_\tau[n]\right)^2 \\
&+ A_1\, A_{\mathrm{MSK}} \cos(\omega_1\, t_n + \varphi_1) \cos\!\left(\omega_{\mathrm{c}}\, t_n + b_\tau(n) \frac{\pi\, t_n}{2\, T_{\mathrm{bit}}} + \varphi_1 + \bar{\varphi}_\tau[n]\right) \\
&+ A_2\, A_{\mathrm{MSK}} \cos(\omega_2\, t_n + \varphi_1 + \varphi_{\mathrm{beat}}) \cos\!\left(\omega_c t_n + b_\tau(n) \frac{\pi\, t_n}{2\, T_{\mathrm{bit}}} + \varphi_1 + \bar{\varphi}_\tau[n]\right)
\end{aligned} \tag{149}$$

$$\begin{aligned}
=& \frac{1}{\sigma^2}\sum_{n=0}^{N-1} \frac{1}{2}\, A_{\mathrm{MSK}}^2 \left(1 + \cos\!\left(2\,\omega_c t_n + 2\, b_\tau(n) \frac{\pi\, t_n}{2\, T_{\mathrm{bit}}} + 2\,\varphi_1 + 2\,\bar{\varphi}_\tau[n]\right)\right) \\
&+ A_1\, A_{\mathrm{MSK}} \cos(\omega_1\, t_n + \varphi_1) \cos\!\left(\omega_{\mathrm{c}}\, t_n + b_\tau(n) \frac{\pi\, t_n}{2\, T_{\mathrm{bit}}} + \varphi_1 + \bar{\varphi}_\tau[n]\right) \\
&+ A_2\, A_{\mathrm{MSK}} \cos(\omega_2\, t_n + \varphi_1 + \varphi_{\mathrm{beat}}) \cos\!\left(\omega_c t_n + b_\tau(n) \frac{\pi\, t_n}{2\, T_{\mathrm{bit}}} + \varphi_1 + \bar{\varphi}_\tau[n]\right)
\end{aligned} \tag{150}$$

$$= \frac{N\, A_{\mathrm{MSK}}^2}{2\sigma^2}, \tag{151}$$

$$\begin{aligned} \boldsymbol{J}_{\text{signal}_{13}} =& \frac{1}{\sigma^2}\sum_{n=0}^{N-1} A_2^2 \cos(\omega_2\, t_n + \varphi_1 + \varphi_{\text{beat}})^2 \\ &+, A_1\, A_2 \cos(\omega_1\, t_n + \varphi_1) \cos(\omega_2\, t_n + \varphi_1 + \varphi_{\text{beat}}) \\ &+ A_2\, A_{\text{MSK}} \cos(\omega_2\, t_n + \varphi_1 + \varphi_{\text{beat}}) \cos(\omega_c t_n + b_\tau(n)\frac{\pi t_n}{2T_{\text{bit}}} + \varphi_1 + \bar{\varphi}_\tau[n]) \end{aligned} \tag{152}$$

$$\begin{aligned} =& \frac{1}{\sigma^2}\sum_{n=0}^{N-1} \frac{1}{2} A_2^2 (1 + \cos(\omega_2\, t_n + \varphi_1 + \varphi_{\text{beat}})) \\ &+, A_1\, A_2 \cos(\omega_1\, t_n + \varphi_1) \cos(\omega_2\, t_n + \varphi_1 + \varphi_{\text{beat}}) \\ &+ A_2\, A_{\text{MSK}} \cos(\omega_2\, t_n + \varphi_1 + \varphi_{\text{beat}}) \cos(\omega_c t_n + b_\tau(n)\frac{\pi t_n}{2T_{\text{bit}}} + \varphi_1 + \bar{\varphi}_\tau[n]) \end{aligned} \tag{153}$$

$$= \frac{N A_2^2}{2\sigma^2}, \tag{154}$$

$$\begin{aligned} \boldsymbol{J}_{\text{signal}_{14}} =& \frac{1}{\sigma^2}\sum_{n=0}^{N-1} A_{\text{MSK}}^2 \frac{\pi t_n}{2T_{\text{bit}}} \cos(2\omega_c t_n + 2\, b_\tau(n)\frac{\pi t_n}{2T_{\text{bit}}} + 2\varphi_1 + 2\bar{\varphi}_\tau[n])^2 \\ &+ A_1\, A_{\text{MSK}} \frac{\pi t_n}{2T_{\text{bit}}} \cos(\omega_1\, t_n + \varphi_1) \cos(\omega_{\text{c}}\, t_n + b_\tau(n)\frac{\pi t_n}{2T_{\text{bit}}} + \varphi_1 + \bar{\varphi}_\tau[n]) \\ &+ A_2\, A_{\text{MSK}} \frac{\pi t_n}{2T_{\text{bit}}} \cos(\omega_2\, t_n + \varphi_1 + \varphi_{\text{beat}}) \cos(\omega_c t_n + b_\tau(n)\frac{\pi t_n}{2T_{\text{bit}}} + \varphi_1 + \bar{\varphi}_\tau[n]) \end{aligned} \tag{155}$$

$$\begin{aligned} =& \frac{1}{\sigma^2}\sum_{n=0}^{N-1} A_{\text{MSK}}^2 \frac{\pi t_n}{4T_{\text{bit}}} (1 + \cos(2\omega_c t_n + 2\, b_\tau(n)\frac{\pi t_n}{2T_{\text{bit}}} + 2\varphi_1 + 2\bar{\varphi}_\tau[n])) \\ &+ A_1\, A_{\text{MSK}} \frac{\pi t_n}{2T_{\text{bit}}} \cos(\omega_1\, t_n + \varphi_1) \cos(\omega_{\text{c}}\, t_n + b_\tau(n)\frac{\pi t_n}{2T_{\text{bit}}} + \varphi_1 + \bar{\varphi}_\tau[n]) \\ &+ A_2\, A_{\text{MSK}} \frac{\pi t_n}{2T_{\text{bit}}} \cos(\omega_2\, t_n + \varphi_1 + \varphi_{\text{beat}}) \cos(\omega_c t_n + b_\tau(n)\frac{\pi t_n}{2T_{\text{bit}}} + \varphi_1 + \bar{\varphi}_\tau[n]) \end{aligned} \tag{156}$$

$$\begin{aligned} =& \frac{\pi A_{\text{MSK}}^2}{4T_{\text{bit}}\sigma^2} \sum_{n=0}^{N-1} n \\ =& \frac{\pi A_{\text{MSK}}^2}{4T_{\text{bit}}\sigma^2} \frac{N(N-1)}{2}, \end{aligned} \tag{157}$$

$$\begin{aligned} \boldsymbol{J}_{\text{signal}_{15}} =& \frac{1}{2\sigma^2}\sum_{n=0}^{N-1} A_1 \sin(2\omega_1\, t_n + 2\varphi_1) + A_2 \sin(\omega_1\, t_n + \omega_2\, t_n + 2\varphi_1 + \varphi_{\text{beat}}) \\ &- A_2 \sin(\omega_2\, t_n - \omega_1\, t_n + \varphi_{\text{beat}}) \\ &+ A_{\text{MSK}} \sin(\omega_1\, t_n + \omega_{\text{c}}\, t_n + b_\tau(n)\frac{\pi t_n}{2T_{\text{bit}}} + 2\varphi_1 + \bar{\varphi}_\tau[n]) \\ &- A_{\text{MSK}} \sin(+\omega_{\text{c}}\, t_n - \omega_1\, t_n + b_\tau(n)\frac{\pi t_n}{2T_{\text{bit}}} + \bar{\varphi}_\tau[n]) \end{aligned} \tag{158}$$

$$= 0, \tag{159}$$

$$\begin{aligned}
\boldsymbol{J}_{\text{signal}_{16}} = & \frac{1}{\sigma^2}\sum_{n=0}^{N-1}\frac{1}{2}A_1\sin\left(b_\tau(n)\frac{\pi t_n}{2T_{\text{bit}}}+2\varphi_1+\bar{\varphi}_\tau[n]+\omega_1 t_n+\omega_{\text{c}} t_n\right)\\
& +\frac{1}{2}A_1\sin\left(b_\tau(n)\frac{\pi t_n}{2T_{\text{bit}}}+\bar{\varphi}_\tau[n]-\omega_1 t_n+\omega_{\text{c}} t_n\right) \qquad (160)\\
& +\frac{1}{2}A_2\sin\left(b_\tau(n)\frac{\pi t_n}{2T_{\text{bit}}}+2\varphi_1+\varphi_{\text{beat}}+\bar{\varphi}_\tau[n]+\omega_2 t_n+\omega_{\text{c}} t_n\right)\\
& +\frac{1}{2}A_2\sin\left(b_\tau(n)\frac{\pi t_n}{2T_{\text{bit}}}-\varphi_{\text{beat}}+\bar{\varphi}_\tau[n]-\omega_2 t_n+\omega_{\text{c}} t_n\right)\\
& +\frac{1}{2}A_{\text{MSK}}\sin\left(b_\tau(n)\frac{\pi t_n}{T_{\text{bit}}}+2\varphi_1+2\bar{\varphi}_\tau[n]+2\omega_{\text{c}} t_n\right)\\
& =0, \qquad (161)
\end{aligned}$$

$$\begin{aligned}
\boldsymbol{J}_{\text{signal}_{17}} = & \frac{1}{\sigma^2}\sum_{n=0}^{N-1}\frac{1}{2}A_1\sin\left(2\varphi_1+\varphi_{\text{beat}}+\omega_1 t_n+\omega_2 t_n\right)\\
& +\frac{1}{2}A_1\sin\left(\varphi_{\text{beat}}-\omega_1 t_n+\boldsymbol{\theta}_2\right)\\
& +\frac{1}{2}A_2\sin\left(2\varphi_1+2\varphi_{\text{beat}}+2\omega_2 t_n\right) \qquad (162)\\
& +\frac{1}{2}A_{\text{MSK}}\sin\left(b_\tau(n)\frac{\pi t_n}{2T_{\text{bit}}}+2\varphi_1+\varphi_{\text{beat}}+\bar{\varphi}_\tau[n]+\omega_2 n+\omega_{\text{c}} t_n\right)\\
& -\frac{1}{2}A_{\text{MSK}}\sin\left(b_\tau(n)\frac{\pi t_n}{2T_{\text{bit}}}-\varphi_{\text{beat}}+\bar{\varphi}_\tau[n]-\omega_2 t_n+\omega_{\text{c}} t_n\right)\\
= & 0, \qquad (163)
\end{aligned}$$

$$\begin{aligned}
\boldsymbol{J}_{\text{signal}_{22}} & =\frac{1}{\sigma^2}\sum_{n=0}^{N-1}A_{\text{MSK}}^2\cos\left(b_\tau(n)\frac{\pi t_n}{2T_{\text{bit}}}+\varphi_1+\bar{\varphi}_\tau[n]+\omega_{\text{c}} t_n\right)^2 \qquad (164)\\
& =\frac{1}{\sigma^2}\sum_{n=0}^{N-1}\frac{1}{2}A_{\text{MSK}}^2\left(1+\cos\left(2\,b_\tau(n)\frac{\pi t_n}{2T_{\text{bit}}}+2\,\varphi_1+2\,\bar{\varphi}_\tau[n]+2\,\omega_{\text{c}} t_n\right)\right) \qquad (165)\\
& =\frac{A_{\text{MSK}}^2 N}{2\sigma^2}, \qquad (166)
\end{aligned}$$

$$\begin{aligned}
\boldsymbol{J}_{\text{signal}_{23}} = & \frac{1}{\sigma^2}\sum_{n=0}^{N-1}\frac{1}{2}A_2\,A_{\text{MSK}}\cos\left(b_\tau(n)\frac{\pi t_n}{2T_{\text{bit}}}+2\varphi_1+\varphi_{\text{beat}}+\bar{\varphi}_\tau[n]+\omega_2 t_n+\omega_{\text{c}} t_n\right) \qquad (167)\\
& +\frac{1}{2}A_2\,A_{\text{MSK}}\cos\left(b_\tau(n)\frac{\pi t_n}{2T_{\text{bit}}}-\varphi_{\text{beat}}+\bar{\varphi}_\tau[n]-\omega_2 t_n+\omega_{\text{c}} t_n\right)\\
= & 0, \qquad (168)
\end{aligned}$$

$$\begin{align}
\boldsymbol{J}_{\mathrm{signal}_{24}} &= \frac{1}{\sigma^2}\sum_{n=0}^{N-1} A_{\mathrm{MSK}}^2 \frac{\pi t_n}{2T_{\mathrm{bit}}} \cos\left(b_\tau(n)\frac{\pi t_n}{2T_{\mathrm{bit}}} + \varphi_1 + \bar{\varphi}_\tau[n] + \omega_{\mathrm{c}}\, t_n\right)^2 \tag{169}\\
&= \frac{1}{\sigma^2}\sum_{n=0}^{N-1} \frac{1}{2} A_{\mathrm{MSK}}^2 \frac{\pi t_n}{2T_{\mathrm{bit}}} \left(1+\cos\left(b_\tau(n)\frac{\pi t_n}{T_{\mathrm{bit}}} + 2\varphi_1 + 2\bar{\varphi}_\tau[n] + 2\omega_{\mathrm{c}}\, t_n\right)\right) \tag{170}\\
&= \frac{A_{\mathrm{MSK}}^2 \pi}{4T_{\mathrm{bit}}\sigma^2}\sum_{n=0}^{N-1} t_n \tag{171}\\
&= \frac{A_{\mathrm{MSK}}^2 \pi}{4T_{\mathrm{bit}}\sigma^2}\frac{N(N-1)}{2}, \tag{172}
\end{align}$$

$$\begin{align}
\boldsymbol{J}_{\mathrm{signal}_{25}} &= \frac{1}{\sigma^2}\sum_{n=0}^{N-1} \frac{1}{2} A_{\mathrm{MSK}} \sin\left(b_\tau(n)\frac{\pi t_n}{2T_{\mathrm{bit}}} + 2\varphi_1 + \bar{\varphi}_\tau[n] + \omega_1\, t_n + \omega_{\mathrm{c}}\, t_n\right) \tag{173}\\
&\quad - \frac{1}{2} A_{\mathrm{MSK}} \sin\left(b_\tau(n)\frac{\pi t_n}{2T_{\mathrm{bit}}} + \bar{\varphi}_\tau[n] - \omega_1\, t_n + \omega_{\mathrm{c}}\, t_n\right) \notag\\
&= 0, \tag{174}
\end{align}$$

$$\begin{align}
\boldsymbol{J}_{\mathrm{signal}_{26}} &= \frac{1}{\sigma^2}\sum_{n=0}^{N-1} A_{\mathrm{MSK}} \sin\left(b_\tau(n)\frac{\pi t_n}{2T_{\mathrm{bit}}} + \varphi_1 + \bar{\varphi}_\tau[n] + \omega_{\mathrm{c}}\, t_n\right) \tag{175}\\
&\quad \cos\left(b_\tau(n)\frac{\pi t_n}{2T_{\mathrm{bit}}} + \varphi_1 + \bar{\varphi}_\tau[n] + \omega_{\mathrm{c}}\, t_n\right) \notag\\
&= \frac{1}{\sigma^2}\sum_{n=0}^{N-1} \frac{1}{2} A_{\mathrm{MSK}} \left(\sin(0) + \sin\left(b_\tau(n)\frac{2\pi t_n}{T_{\mathrm{bit}}} + 2\varphi_1 + 2\bar{\varphi}_\tau[n] + 2\omega_{\mathrm{c}}\, t_n\right)\right) \tag{176}\\
&= 0, \tag{177}
\end{align}$$

$$\begin{align}
\boldsymbol{J}_{\mathrm{signal}_{27}} &= \frac{1}{\sigma^2}\sum_{n=0}^{N-1} \frac{1}{2} A_{\mathrm{MSK}} \sin\left(b_\tau(n)\frac{\pi t_n}{2T_{\mathrm{bit}}} + 2\varphi_1 + \varphi_{\mathrm{beat}} + \bar{\varphi}_\tau[n] + \omega_2\, t_n + \omega_{\mathrm{c}}\, t_n\right) \tag{178}\\
&\quad - \frac{1}{2} A_{\mathrm{MSK}} \sin\left(b_\tau(n)\frac{\pi t_n}{2T_{\mathrm{bit}}} - \varphi_{\mathrm{beat}} + \bar{\varphi}_\tau[n] - \omega_2\, t_n + \omega_{\mathrm{c}}\, t_n\right) \notag\\
&= 0, \tag{179}
\end{align}$$

$$\begin{align}
\boldsymbol{J}_{\mathrm{signal}_{33}} &= \frac{1}{\sigma^2}\sum_{n=0}^{N-1} A_2^2 \cos\left(\varphi_1 + \varphi_{\mathrm{beat}} + \omega_2\, t_n\right)^2 \tag{180}\\
&= \frac{1}{\sigma^2}\sum_{n=0}^{N-1} \frac{1}{2} A_2^2 \left(1 + \cos\left(\varphi_1 + \varphi_{\mathrm{beat}} + \omega_2\, t_n\right)\right) \tag{181}\\
&= \frac{A_2^2 N}{2\sigma^2}, \tag{182}
\end{align}$$

$$
\begin{aligned}
\boldsymbol{J}_{\mathrm{signal}_{34}} =& \frac{1}{\sigma^2} \sum_{n=0}^{N-1} \frac{1}{2} A_2 \, A_{\mathrm{MSK}} \, \frac{\pi \, t_n}{2 \, T_{\mathrm{bit}}} \qquad (183) \\
& \cos\left(b_\tau(n) \frac{\pi \, t_n}{2 \, T_{\mathrm{bit}}} + 2\varphi_1 + \varphi_{\mathrm{beat}} + \bar{\varphi}_\tau[n] + \omega_2 \, t_n + \omega_{\mathrm{c}} \, t_n \right) \\
& + \frac{1}{2} A_2 \, A_{\mathrm{MSK}} \, \frac{\pi \, t_n}{2 \, T_{\mathrm{bit}}} \cos\left(b_\tau(n) \frac{\pi \, t_n}{2 \, T_{\mathrm{bit}}} - \varphi_{\mathrm{beat}} + \bar{\varphi}_\tau[n] - \omega_2 \, t_n + \omega_{\mathrm{c}} \, t_n \right) \\
=& 0, \qquad (184)
\end{aligned}
$$

$$
\begin{aligned}
\boldsymbol{J}_{\mathrm{signal}_{35}} =& \frac{1}{\sigma^2} \sum_{n=0}^{N-1} \frac{1}{2} A_2 \sin\left(2\varphi_1 + \varphi_{\mathrm{beat}} + \omega_1 \, t_n + \omega_2 \, t_n \right) \qquad (185) \\
& - \frac{1}{2} A_2 \sin\left(\varphi_{\mathrm{beat}} - \omega_1 \, t_n + \omega_2 \, t_n \right) \\
=& 0, \qquad (186)
\end{aligned}
$$

$$
\begin{aligned}
\boldsymbol{J}_{\mathrm{signal}_{36}} =& \frac{1}{\sigma^2} \sum_{n=0}^{N-1} \frac{1}{2} A_2 \sin\left(b_\tau(n) \frac{\pi \, t_n}{2 \, T_{\mathrm{bit}}} + 2 \, \varphi_1 + \varphi_{\mathrm{beat}} + \bar{\varphi}_\tau[n] + \omega_2 \, t_n + \omega_{\mathrm{c}} \, t_n \right) \qquad (187) \\
& + \frac{1}{2} A_2 \sin\left(b_\tau(n) \frac{\pi \, t_n}{2 \, T_{\mathrm{bit}}} - \varphi_{\mathrm{beat}} + \bar{\varphi}_\tau[n] - \omega_2 \, t_n + \omega_{\mathrm{c}} \, t_n \right) \\
=& 0, \qquad (188)
\end{aligned}
$$

$$
\begin{aligned}
\boldsymbol{J}_{\mathrm{signal}_{37}} =& \frac{1}{\sigma^2} \sum_{n=0}^{N-1} A_2 \, \sin\left(\omega_2 \, t_n + \varphi_1 + \varphi_{\mathrm{beat}} \right) \cos\left(\omega_2 \, t_n + \varphi_1 + \varphi_{\mathrm{beat}} \right) && (189) \\
=& \frac{1}{\sigma^2} \sum_{n=0}^{N-1} \frac{1}{2} \left(\sin(0) + \sin\left(2\omega_2 \, t_n + 2\varphi_1 + 2\varphi_{\mathrm{beat}} \right) \right) && (190) \\
=& \, 0, && (191)
\end{aligned}
$$

$$
\begin{aligned}
\boldsymbol{J}_{\mathrm{signal}_{44}} =& \frac{1}{\sigma^2} \sum_{n=0}^{N-1} A_{\mathrm{MSK}}^2 \left(\frac{\pi \, t_n}{2 \, T_{\mathrm{bit}}} \right)^2 \cos\left(b_\tau(n) \frac{\pi \, t_n}{2 \, T_{\mathrm{bit}}} + \varphi_1 + \bar{\varphi}_\tau[n] + \omega_{\mathrm{c}} \, t_n \right)^2 && (192) \\
=& \frac{1}{\sigma^2} \sum_{n=0}^{N-1} A_{\mathrm{MSK}}^2 \left(\frac{\pi \, t_n}{2 \, T_{\mathrm{bit}}} \right)^2 \frac{1}{2} \left(1 + \cos\left(b_\tau(n) \frac{\pi \, t_n}{2 \, T_{\mathrm{bit}}} + \varphi_1 + \bar{\varphi}_\tau[n] + \omega_{\mathrm{c}} \, t_n \right) \right) && (193) \\
=& \frac{A_{\mathrm{MSK}}^2}{2\sigma^2} \sum_{n=0}^{N-1} \left(\frac{\pi \, t_n}{2 \, T_{\mathrm{bit}}} \right)^2 && (194) \\
=& \frac{A_{\mathrm{MSK}}^2}{2\sigma^2} \left(\frac{\pi}{2 \, T_{\mathrm{bit}}} \right)^2 \frac{(N-1)(2N-1)N}{6} && (195) \\
=& \frac{A_{\mathrm{MSK}}^2 \, \pi^2 \, (N-1)(2N-1)N}{48 \, T_{\mathrm{bit}}^2 \, \sigma^2}, && (196)
\end{aligned}
$$

$$\begin{aligned}
\boldsymbol{J}_{\mathrm{signal}_{45}} =& \frac{1}{\sigma^2}\sum_{n=0}^{N-1}\frac{1}{2}\,A_{\mathrm{MSK}}\,\frac{\pi\,t_n}{2\,T_{\mathrm{bit}}}\sin\left(b_\tau(n)\,\frac{\pi\,t_n}{2\,T_{\mathrm{bit}}}+2\,\varphi_1+\bar{\varphi}_\tau[n]+\omega_1\,t_n+\omega_{\mathrm{c}}\,t_n\right) \tag{197}\\
&-\frac{1}{2}\,A_{\mathrm{MSK}}\,\frac{\pi\,t_n}{2\,T_{\mathrm{bit}}}\sin\left(b_\tau(n)\,\frac{\pi\,t_n}{2\,T_{\mathrm{bit}}}+\bar{\varphi}_\tau[n]-\omega_1\,t_n+\omega_{\mathrm{c}}\,t_n\right)\\
=&\,0, \tag{198}
\end{aligned}$$

$$\begin{aligned}
\boldsymbol{J}_{\mathrm{signal}_{46}} =& \frac{1}{\sigma^2}\sum_{n=0}^{N-1}A_{\mathrm{MSK}}\,\frac{\pi\,t_n}{2\,T_{\mathrm{bit}}}\sin\left(b_\tau(n)\,\frac{\pi\,t_n}{2\,T_{\mathrm{bit}}}+\varphi_1+\bar{\varphi}_\tau[n]+\omega_{\mathrm{c}}\,t_n\right) \tag{199}\\
&\cos\left(b_\tau(n)\,\frac{\pi\,t_n}{2\,T_{\mathrm{bit}}}+\varphi_1+\bar{\varphi}_\tau[n]+\omega_{\mathrm{c}}\,t_n\right)\\
=&\,A_{\mathrm{MSK}}\,\frac{\pi\,t_n}{4\,T_{\mathrm{bit}}}\left(\sin(0)+\sin\left(b_\tau(n)\,\frac{\pi\,t_n}{T_{\mathrm{bit}}}+2\varphi_1+2\bar{\varphi}_\tau[n]+2\omega_{\mathrm{c}}\,t_n\right)\right) \tag{200}\\
=&\,0, \tag{201}
\end{aligned}$$

$$\begin{aligned}
\boldsymbol{J}_{\mathrm{signal}_{47}} =& \frac{1}{\sigma^2}\sum_{n=0}^{N-1}\frac{1}{2}\,A_{\mathrm{MSK}}\,\frac{\pi\,t_n}{2\,T_{\mathrm{bit}}}\sin\left((b_\tau(n)\,\frac{\pi\,t_n}{2\,T_{\mathrm{bit}}}+2\,\varphi_1+\varphi_{\mathrm{beat}}+\bar{\varphi}_\tau[n]+\omega_2\,t_n+\omega_{\mathrm{c}}\,t_n\right)\\
&-\frac{1}{2}\,A_{\mathrm{MSK}}\,\frac{\pi\,t_n}{2\,T_{\mathrm{bit}}}\sin\left((b_\tau(n)\,\frac{\pi\,t_n}{2\,T_{\mathrm{bit}}}-\varphi_{\mathrm{beat}}+\bar{\varphi}_\tau[n]-\omega_2\,t_n+\omega_{\mathrm{c}}\,t_n\right) \tag{202}\\
=&\,0, \tag{203}
\end{aligned}$$

$$\begin{aligned}
\boldsymbol{J}_{\mathrm{signal}_{55}} =& \frac{1}{\sigma^2}\sum_{n=0}^{N-1}\sin\left(\varphi_1+\omega_1\,t_n\right)^2 \tag{204}\\
=& \frac{1}{\sigma^2}\sum_{n=0}^{N-1}\frac{1}{2}\left(1-\cos(2\varphi_1+2\omega_1\,t_n)\right) \tag{205}\\
=& \frac{N}{2\,\sigma^2}, \tag{206}
\end{aligned}$$

$$\begin{aligned}
\boldsymbol{J}_{\mathrm{signal}_{56}} =& \frac{1}{\sigma^2}\sum_{n=0}^{N-1}\frac{1}{2}\cos\left(b_\tau(n)\,\frac{\pi\,t_n}{2\,T_{\mathrm{bit}}}+\bar{\varphi}_\tau[n]-\omega_1\,t_n+\omega_{\mathrm{c}}\,t_n\right) \tag{207}\\
&-\frac{1}{2}\cos\left(b_\tau(n)\,\frac{\pi\,t_n}{2\,T_{\mathrm{bit}}}+2\,\varphi_1+\bar{\varphi}_\tau[n]+\omega_1\,t_n+\omega_{\mathrm{c}}\,t_n\right)\\
=&\,0, \tag{208}
\end{aligned}$$

$$
\begin{aligned}
\boldsymbol{J}_{\text{signal}_{57}} = & \frac{1}{\sigma^2} \sum_{n=0}^{N-1} \frac{1}{2} \cos\left(\varphi_{\text{beat}} - \omega_1\, t_n + \omega_2\, t_n\right) \tag{209}\\
& - \frac{1}{2} \cos\left(2\,\varphi_1 + \varphi_{\text{beat}} + \omega_1\, t_n + \omega_2\, t_n\right)\\
= & \, 0, \tag{210}
\end{aligned}
$$

$$
\begin{aligned}
\boldsymbol{J}_{\text{signal}_{66}} = & \frac{1}{\sigma^2} \sum_{n=0}^{N-1} \sin\left(b_\tau(n) \frac{\pi\, t_n}{2\, T_{\text{bit}}} + \varphi_1 + \bar{\varphi}_\tau[n] + \omega_{\text{c}}\, t_n\right)^2 \tag{211}\\
= & \frac{1}{\sigma^2} \sum_{n=0}^{N-1} \frac{1}{2} \left(1 - \cos\left(b_\tau(n) \frac{\pi\, t_n}{T_{\text{bit}}} + 2\varphi_1 + 2\bar{\varphi}_\tau[n] + 2\omega_{\text{c}}\, t_n\right)\right) \tag{212}\\
= & \frac{N}{2\,\sigma^2}, \tag{213}
\end{aligned}
$$

$$
\begin{aligned}
\boldsymbol{J}_{\text{signal}_{67}} = & \frac{1}{\sigma^2} \sum_{n=0}^{N-1} \frac{1}{2} \cos\left(b_\tau(n) \frac{\pi\, t_n}{T_{\text{bit}}} - \varphi_{\text{beat}} + \bar{\varphi}_\tau[n] - \omega_2\, t_n + \omega_{\text{c}}\, t_n\right) \tag{214}\\
& - \frac{1}{2} \cos\left(b_\tau(n) \frac{\pi\, t_n}{T_{\text{bit}}} + 2\,\varphi_1 + \varphi_{\text{beat}} + \bar{\varphi}_\tau[n] + \omega_2\, t_n + \omega_{\text{c}}\, t_n\right) \tag{215}\\
= & \, 0, \tag{216}
\end{aligned}
$$

$$
\begin{aligned}
\boldsymbol{J}_{\text{signal}_{77}} = & \frac{1}{\sigma^2} \sum_{n=0}^{N-1} \sin\left(\varphi_1 + \varphi_{\text{beat}} + \omega_2\, t_n\right)^2 \tag{217}\\
= & \frac{1}{\sigma^2} \sum_{n=0}^{N-1} \frac{1}{2} \left(1 - \cos\left(2\varphi_1 + 2\varphi_{\text{beat}} + 2\omega_2\, t_n\right)\right) \tag{218}\\
= & \frac{N}{2\sigma^2}. \tag{219}
\end{aligned}
$$

We obtain the Fisher information matrix

$$
\boldsymbol{J}_{\text{signal}} = \frac{N}{2\,\sigma^2} \begin{pmatrix}
A_1^2 + A_{\text{MSK}}^2 + A_2^2 & A_{\text{MSK}}^2 & A_2^2 & \frac{\pi\, A_{\text{MSK}}^2 (N-1)}{4\, T_{\text{bit}}} & 0 & 0 & 0 \\
A_{\text{MSK}}^2 & A_{\text{MSK}}^2 & 0 & \frac{A_{\text{MSK}}^2 \pi (N-1)}{4\, T_{\text{bit}}} & 0 & 0 & 0 \\
A_2^2 & 0 & A_2^2 & 0 & 0 & 0 & 0 \\
\frac{\pi\, A_{\text{MSK}}^2 (N-1)}{4\, T_{\text{bit}}} & \frac{A_{\text{MSK}}^2 \pi (N-1)}{4\, T_{\text{bit}}} & 0 & \frac{A_{\text{MSK}}^2\, \pi^2\, (N-1)(2N-1)}{24\, T_{\text{bit}}^2} & 0 & 0 & 0 \\
0 & 0 & 0 & 0 & 1 & 0 & 0 \\
0 & 0 & 0 & 0 & 0 & 1 & 0 \\
0 & 0 & 0 & 0 & 0 & 0 & 1
\end{pmatrix}, \tag{220}
$$

and the inverse

$$\boldsymbol{J}_{\text{signal}}^{-1} = \frac{N}{2\sigma^2}\begin{pmatrix} \frac{1}{A_1^2} & -\frac{1}{A_1^2} & -\frac{1}{A_1^2} & 0 & 0 & 0 & 0 \\ -\frac{1}{A_1^2} & \frac{4A_1^2 N + A_{\text{MSK}}^2 N - 2A_1^2 + A_{\text{MSK}}^2}{A_1^2 A_{\text{MSK}}^2 N + A_1^2 A_{\text{MSK}}^2} & \frac{1}{A_1^2} & -\frac{12\,T_{\text{bit}}}{\pi A_{\text{MSK}}^2 N + \pi A_{\text{MSK}}^2} & 0 & 0 & 0 \\ -\frac{1}{A_1^2} & \frac{1}{A_1^2} & \frac{A_1^2 + A_2^2}{A_1^2 A_2^2} & 0 & 0 & 0 & 0 \\ 0 & -\frac{12\,T_{\text{bit}}}{\pi A_{\text{MSK}}^2 N + \pi A_{\text{MSK}}^2} & 0 & \frac{48\,T_{\text{bit}}^2}{A_{\text{MSK}}^2 N^2 \pi^2 - A_{\text{MSK}}^2 \pi^2} & 0 & 0 & 0 \\ 0 & 0 & 0 & 0 & 1 & 0 & 0 \\ 0 & 0 & 0 & 0 & 0 & 1 & 0 \\ 0 & 0 & 0 & 0 & 0 & 0 & 1 \end{pmatrix}. \tag{221}$$

A

CHARACTERIZATION OF HARDWARE COMPONENTS

B.1 FILTER

B.1.1 DISCRETE FILTER

We have developed a passband filter of discrete elements for the low-cost receiver design. The filter us a pi structure for the 8th order Bessel filter with for the band limits of 250 kHz - 375 kHz derived from the QucsStudio [89] filter synthesis tool, obtaining the structure shown in Fig. A.1. The initial values for the discrete components derived in the filter synthesis are then optimised using the simulation part and QucsStudio's optimisation function to minimise the insertion loss. In the last step, these optimised values have to be adapted to the available components so that the values in Tab. A.1 and Tab. A.2 result.

We build the filter with through-hole components soldered to a stripboard. We calibrate the circuit with a R&S ZNL VNA [95] measurement. For calibration, we use a ZN-Z235 CalKit [96]. If we compare simulation and measurement for the size of S12, as shown in Fig.A.2a, we see that our result differs from the simulation, as the resulting bandwidth is

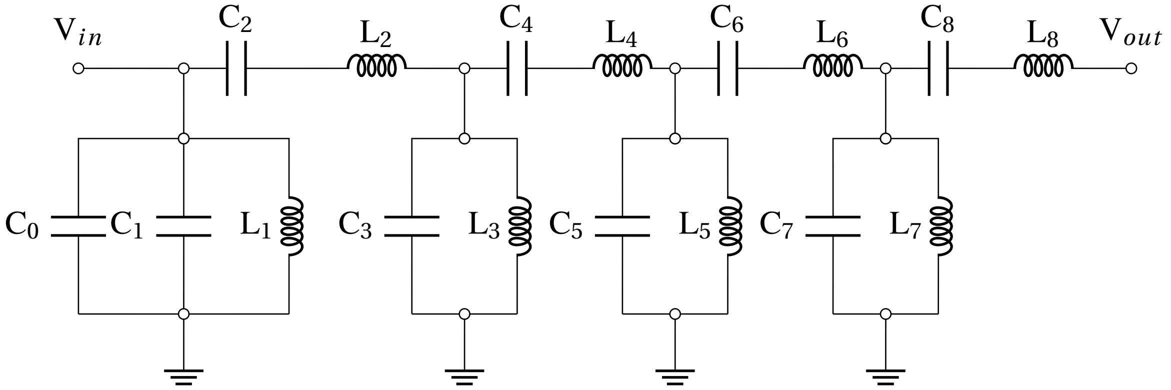

Figure A.1: Circuit diagram of bandpass filter with discrete elements

Table A.1: Capacity values for discrete bandpass filter

Capacitor	C_0	C_1	C_2	C_3	C_4	C_5	C_6	C_7	C_8
Value	1.2 nF	1.2 nF	0.015 µF	12 nF	6.8 nF	18 nF	4.8 nF	27 nF	1.8 nF

Table A.2: Inductor values for discrete bandpass filter

Inductor	L_1	L_2	L_3	L_4	L_5	L_6	L_7	L_8
Value	100 µH	18 µH	22 µH	33 µH	15 µH	54 µH	10 µH	150 µH

decreased and the loss is higher than simulated. The bandwidth limitation, on the other hand, fits the design goal of 250 kHz - 375 kHz, where the simulation became wider-band to minimise insertion loss. In addition, we note that the phase of S12, shown in Fig. A.2b, is shifted by about 17 Hz in our passband.

The difference from our simulation suggests that the techniques used to construct the filter are not optimal, as the various components are not well separated, and crosstalk is very likely. We are confident that a suitable design on a Printed Circuit Board (PCB) can improve the insertion loss so that we further increase the performance of the low-cost approach.

B.1.2 PASSIVE FILTER

We can download S-parameter files for both filters on the Mini-Circuits website. Using scikit-rf [90] to combine both data, we used them for initial component choice and comparison proposes.

Again, we measured the filter with the R&S ZNL VNA [95], calibrated with the ZN-Z235 CalKit [96]. Let us compare the result in Fig. A.3a for the magnitude and for the phase in Fig. A.3b. We find that the measurements have a wider bandwidth compared to the design files in terms of magnitude. Moreover, the Phase also behaves differently. We tested different filters from different production charges with the same result. Either our measurement setup is insufficient, or the production values have changed slightly.

B.1.3 ACTIVE FILTER

We use a Krohn-Hite FMB3002 as active filter. The filter consists of two Krohn-Hite filter modules that are tuned to form a bandpass between 285 kHz to 325 kHz. Since the distributor tuned the filter at our request, we were not involved in the overall design. To our knowledge, there is no publicly available source of design files. Nevertheless, we want to present the measured S-parameter derived from our R&S ZNL VNA [95], calibrated with the ZN-Z235 CalKit [96]. Again we present the result for amplitude and phase separately in Fig. A.4a and Fig. A.4b. As an active filter, we can also activate the internal gain. For our experiment, we set the gain to zero. The filter behaves as expected, within the specific 3 dB cut-off frequencies. However, the slopes are not as steep as the alternative passive filters. Therefore, we expect more noise from outside the band with the active filter.

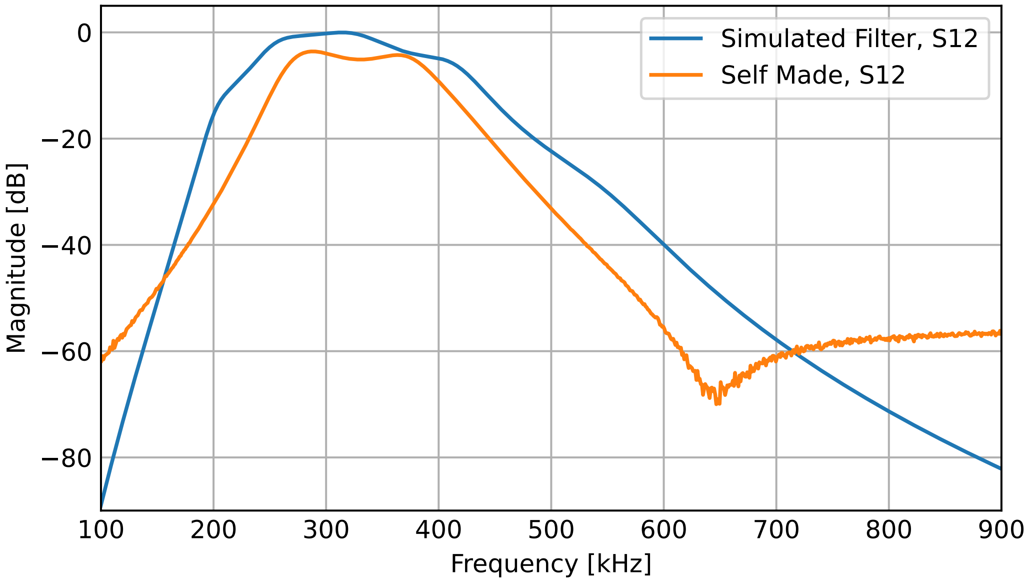

(a) Comparison magnitude of S12 between simulation and measurements.

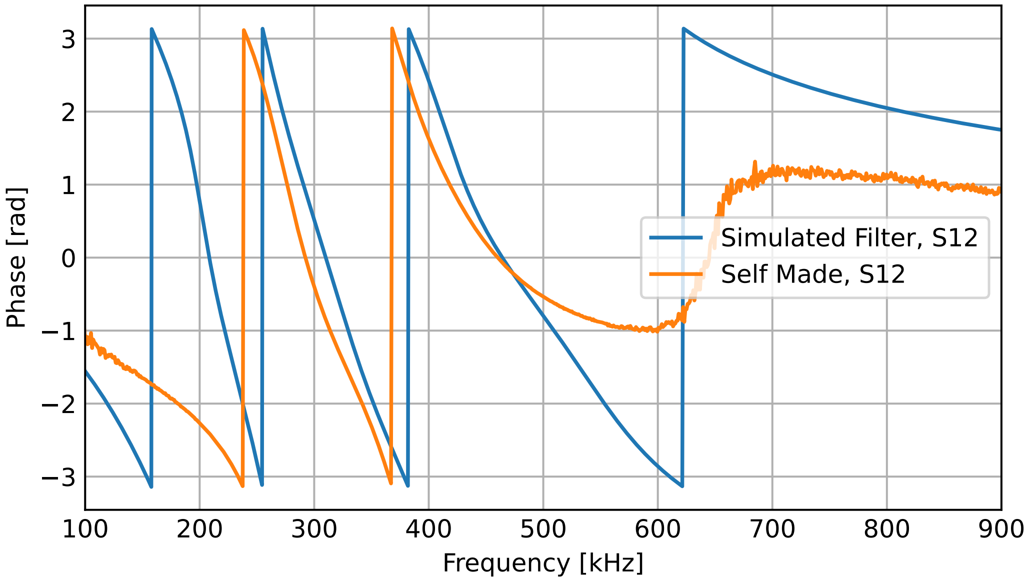

(b) Comparison phase of S12 between simulation and measurements.

Figure A.2: Comparison between simulation and measurements of the self-designed filter.

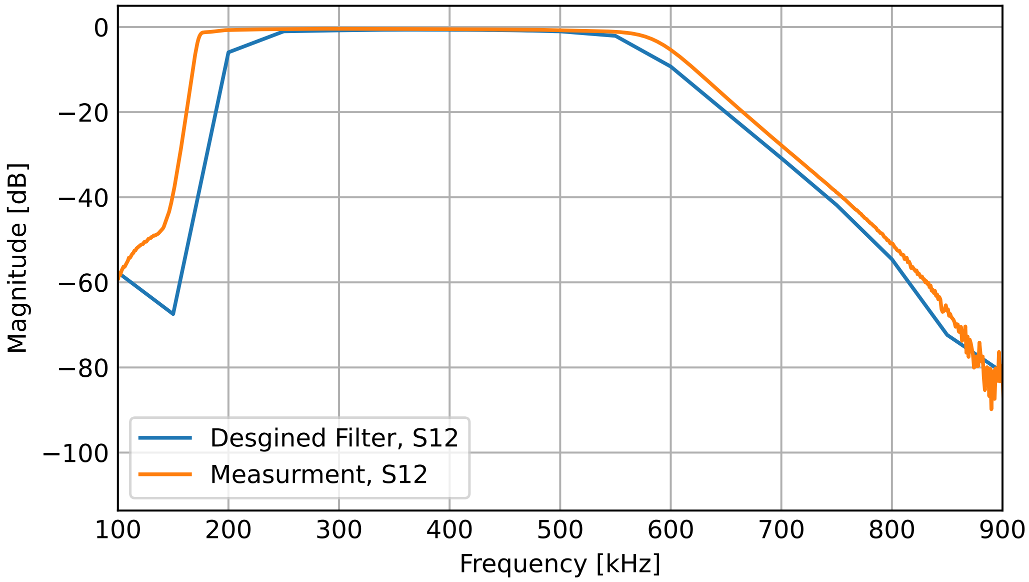

(a) Comparison magnitude of S12 between simulation and measurements.

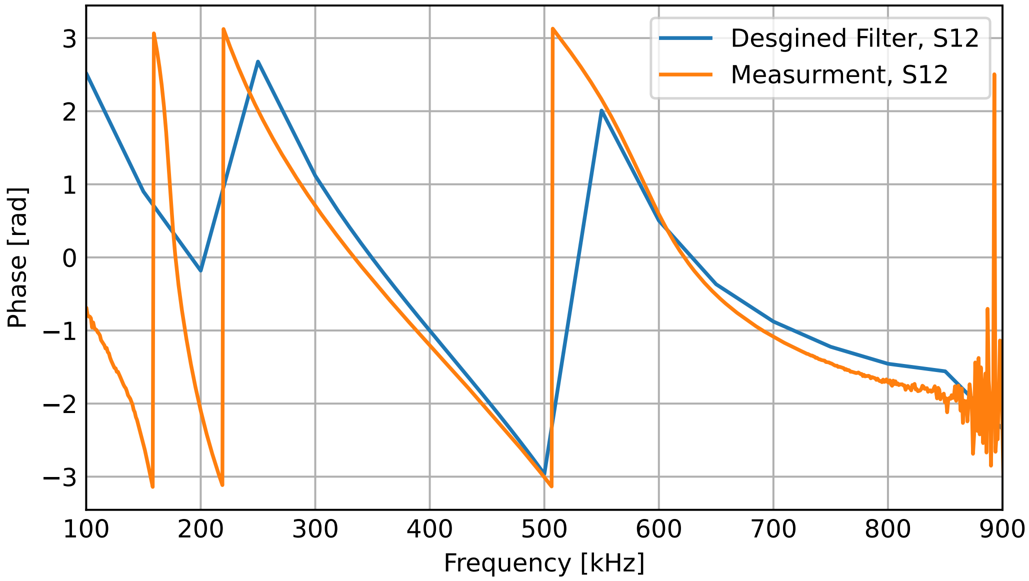

(b) Comparison phase of S12 between simulation and measurements.

Figure A.3: Comparison between design files and measurements of the Mini-Circuits filter combination.

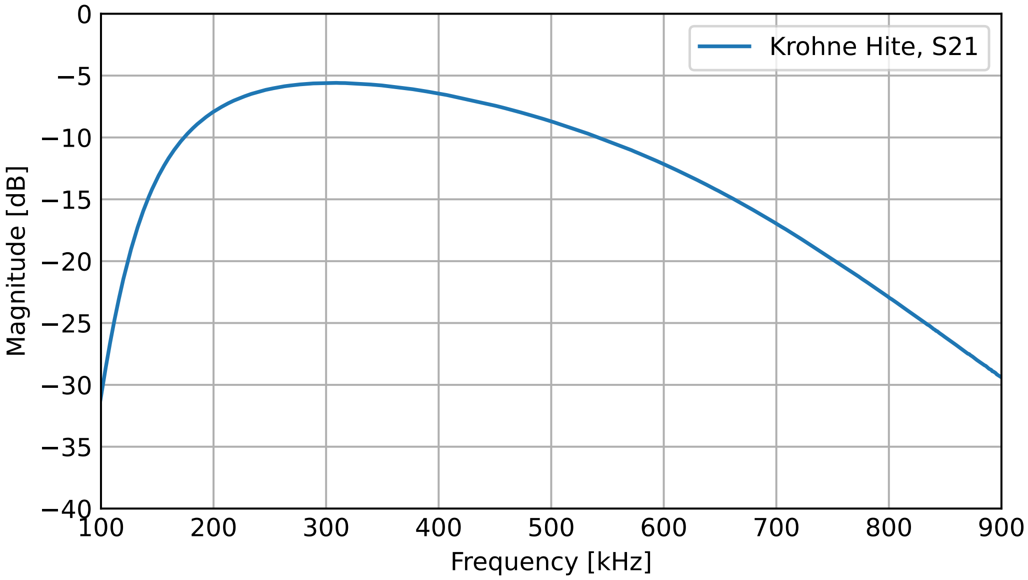

(a) Magnitude of S12.

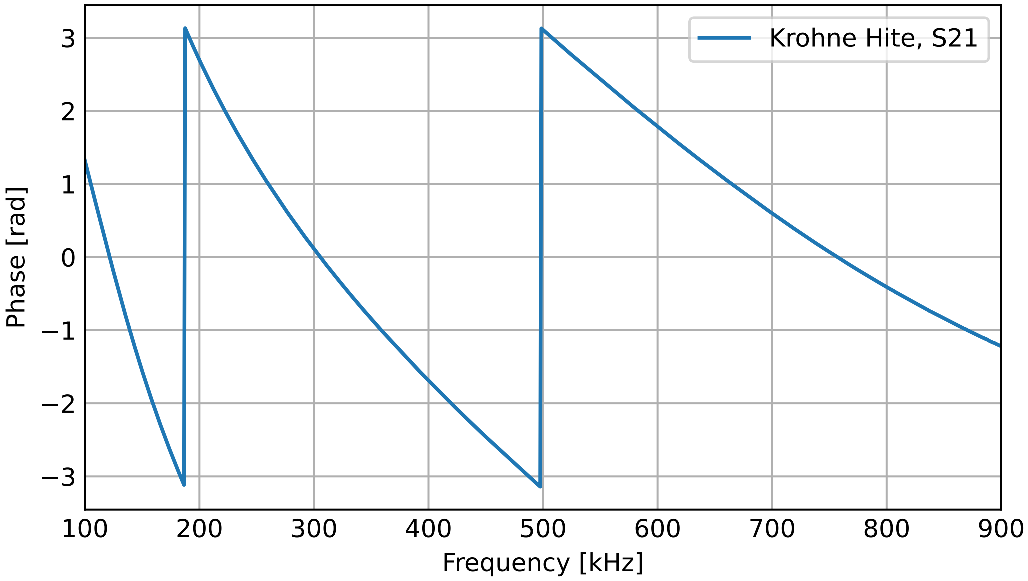

(b) Phase of S12

Figure A.4: Comparison between design files and measurements of the Krohn-Hite FMB3002 .

B.2 AMPLIFIER

In this section of the appendix, we want to provide an overview of the two amplifiers used in this work. We provide measurements and compare them to the design files provided by the manufacturer. To our knowledge, there is no information from the manufacturer available for the frequency range of interest. To present the results in a comprehensive, we choose to draw phase and magnitude in the same graph on different scales. The right axis indicates the magnitude values, while the left axis shows the phase values.

LOW NOISE AMPLIFIER

As LNA we use the ZFL-500LN+ from mini-circuit, which is a coaxial component. The manufacturer delivered the amplifier in a metal case with coax connections. Therefore we can easily use the device and place the LNA as needed. The magnitude and phase measurements presented combined in Fig. A.5. The amplifcation is about 31 dB whic his inline with the data sheet.

B.2.2 POWER AMPLIFIER

As a power amplifier, we use the MSA-0485 from Hewlett Packard. The manufacturer delivered the amplifier as MMIC. Before we can use the component, we need to solder the device onto a PCB, which provide interconnections and voltage bias. For our design, we choose a prefabricated PCB and the corresponding housing. After we assemble the part, the usage doesn't differ from the LNA. We draw the combined phase and magnitude measurements in Fig. A.6. The gain of about 10 dB is within the expected parameter from the datasheet. However, we need to consider the phase shift of the power amplifier to get the best performance in our receiver.

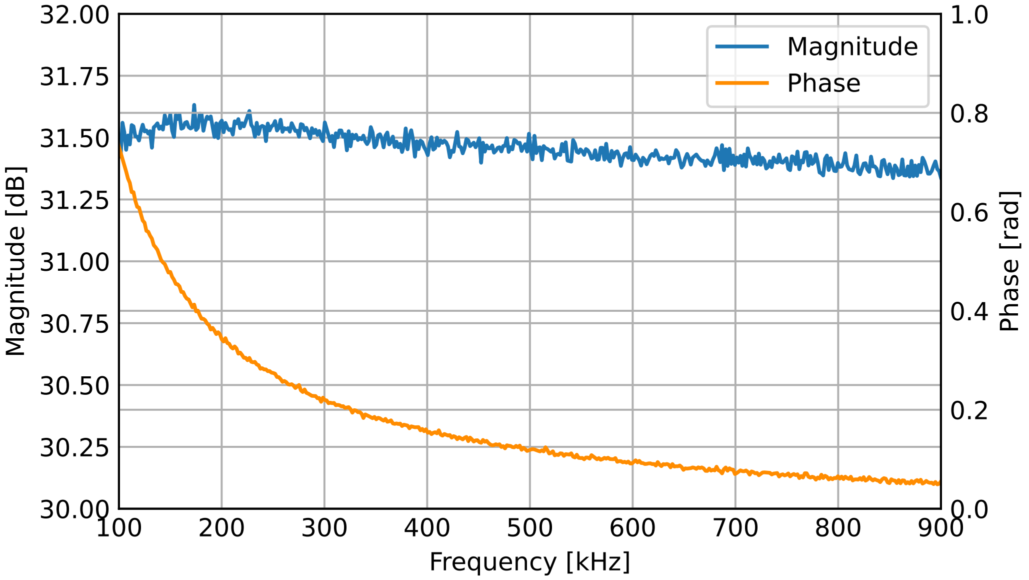

Figure A.5: Magnitude of S12 for the LNA ZFL-500LN+.

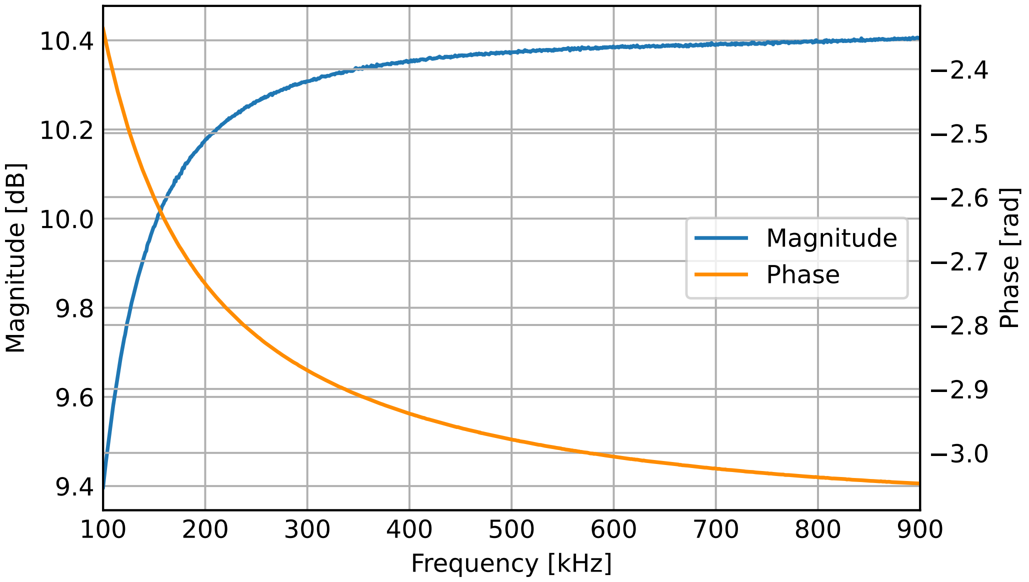

Figure A.6: Magnitude of S12 for the power amplifier MSA-0485.

B

LONG TERM EVALUATION

In this part of the appendix, we present the measurement results of the long-term observation presented in Section 6.3 for the higher frequency CW. In general, they show similar behaviour as the lower frequency signal. However, we expect a larger amplitude due to the not perfect tuning of the transmitting antenna as described in Section 2.3.3 and therefore a slightly different histogram.

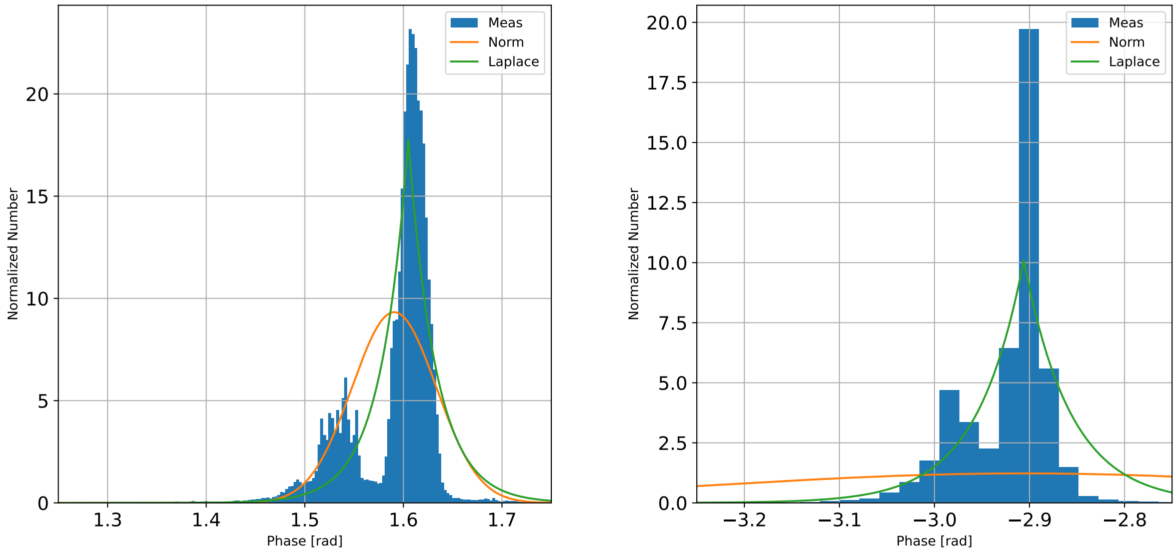

(a)

(b)

Figure B.1: Histograms of received station Zeven and distribution fit during daytime in the near field with (a) E-field antenna ,(b) H-field antenna

In Fig. B.1 we plot the results for the H-field and the E-field resulting from the normalised histogram for the signal received in the near field of the transmitter Zeven during daytime. In addition, we fit a Laplace and normal distribution to the results.

For the H-field, we get a variance of 0.0015 rad^2, and for the E-field, we obtain a variance of 0.0049 rad^2. In the plots, we see the main peak with an additional side lobe. Therefore, neither distribution describes the result adequately.

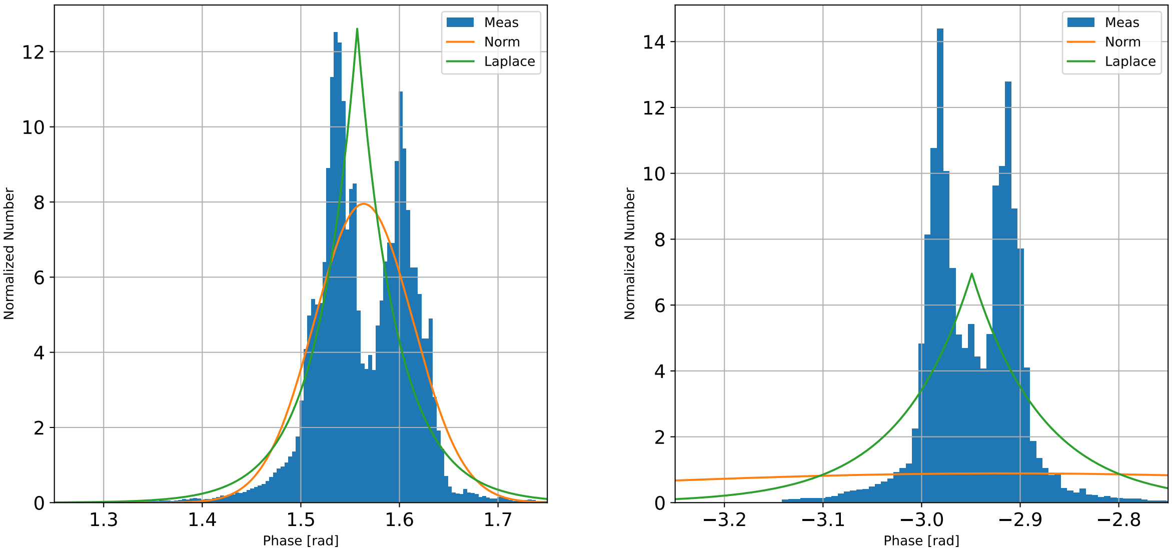

(a)

(b)

Figure B.2: Histograms of received station Zeven and distribution fit during nighttime in the near field with (a) E-field antenna ,(b) H-field antenna.

In Fig. B.2 present the corresponding results for nighttime with a variance of 0.0031 rad^2 for the E-field and a variance of 0.0103 rad^2 for the H-field. The higher variance is unexpected for the H-field antenna, as the received H-field is less prone to noise. Similar to the daytime results, we have two peaks closer in height. Again, neither distribution can follow the results. Overall, this is consistent with the result in Section 6.3.

We also received the Heligoland distant station in close proximity to the station Zeven, the daytime results obtained are shown in Fig. B.3, with a variance of 0.0630 rad^2 for Fig. B.3a, where we again see side lobes on either side of the main peak, and a variance of 0.0196 rad^2 for Fig. B.3b. For the latter plot, we see good agreement with the Laplace distribution, while for the E-field result, neither distribution describes the result.

The nighttime results of the remote station in Fig. B.4, show two side lobes for the E-field antenna result that seem to become part of the main lobe due to the skywave effect, which also increases the variance to 0.0688 rad^2. For the H-field antenna, we only observe an increased variance of 0.0688 rad^2, but compared to the E-field results, where neither fit can follow the side lobes, we see a good agreement with the Laplace fit in Fig. B.4b.

As in Section 6.3.2, we also examine how the variance of the estimate changes over time. In Fig. B.5 we plot the variance for the first 5 minutes of each hour, considering only the results from the second to the 9th of August 2020. We also consider three different preconditioning approaches, no windowing (ML) and Hann windows with $a_0 = 0.5$ and $a_0 = 0.8$. In Fig.6.16 we see increased variance every four hours, for CW2 in the near field, with two exceptions in the morning of 7th and around noon of 9th. We also note a

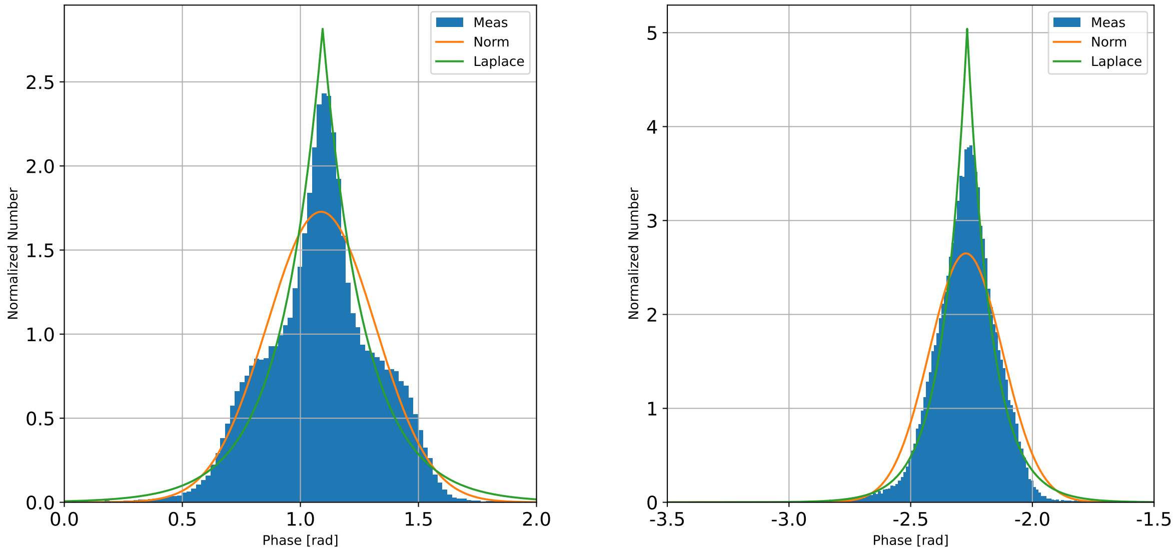

(a)

(b)

Figure B.3: Histograms of received station Heligoland and distribution fit during daytime int the far field with (a) E-field antenna, (b) H-field antenna

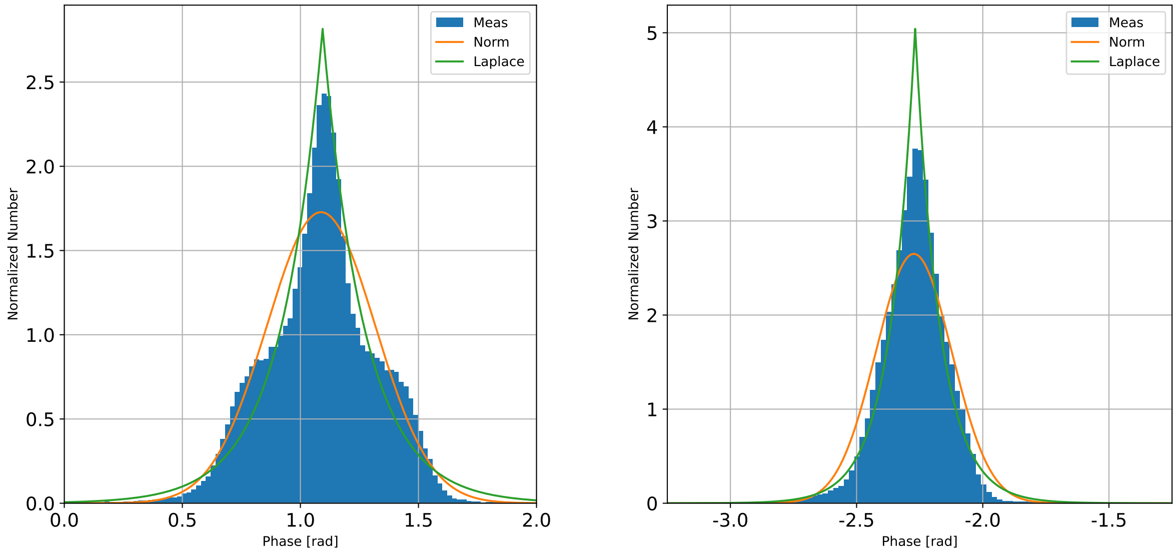

(a)

(b)

Figure B.4: Histograms of received station Heligoland and distribution fit during nighttime in the far-field with (a) E-field antenna, (b) H-field antenna.

larger value of spurious values of about 1.35 rad^2 in the first two days, which then drops to 0.25 rad^2. In addition, an outlier occurs in our pattern on the morning of 9^{th}.

Due to the scaling of Fig. B.5, apart from a single outlier, we cannot detect any difference between the different approaches, which is also reflected in the mean values calculated to 0.1782 rad^2 for ML, 0.1789 rad^2 for $a_0 = 0.5$ and 0.1782 rad^2 for $a_0 = 0.8$.

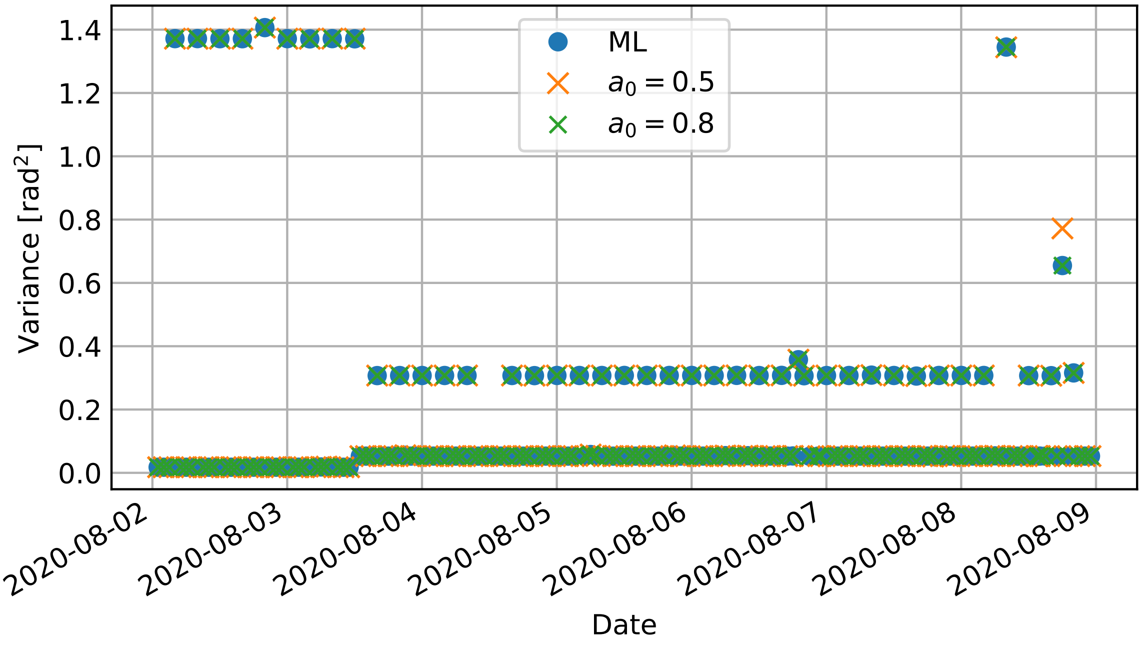

Figure B.5: Variance for CW2 from transmitter Zeven the first 5min of each hour for different window functions

The time series of far-field reception in Zeven is shown in Fig. B.6, in this result the outliers are not on a regular four-hour grid and are not as stable as before. As expected, we have a general higher variance in the estimated phase. Windowing reduces the variance, with the largest gain for the window with $a_0 = 0.5$. The benefit is most evident in the first two days, where the overall variance is higher than in the rest of the analysed period. In general, the observations are following our result from Section 6.3.2.

For the sake of completeness, we also present here the result of daytime and nighttime phase estimation in Groß Königsförde for the Helgoland transmitter in Fig. B.7, for Zeven in Fig. B.8 and Groß Mohrdorf in Fig. B.9.

For the resulting histogram of the signal received from Heligoland during daytime, shown in Fig. B.7a, we again see two peaks and a tail to the lower phase values, with a variance of 0.0024 rad^2. We cannot describe the result by any of the tested distributions. However, for nighttime, in Fig. B.7b, we observe good agreement with the Laplace fit, with a variance of 0.0407 rad^2.

The graphs in Fig. B.8 describe the estimated phase of the CW2 signal from Zeven. As we can see in Fig. B.8a two peaks and a tail, with a variance of 0.0028 rad^2. As before, none of the statistics used can describe the histogram. In agreement with the other results, we observe a suitable fit for the Laplace distribution for nighttime in Fig. B.8b. Here we obtain a variance of 0.0787 rad^2.

The third station to be evaluated is the estimated phase of Groß Mohrdorf. Fig. B.9a show the results for daytime. We cannot detect a second peak. However, the overall distribution does not fit with any of the functions we tested. During nighttime, however, as shown in Fig. B.9b, there is again only a small divergence between the Laplace fit and the

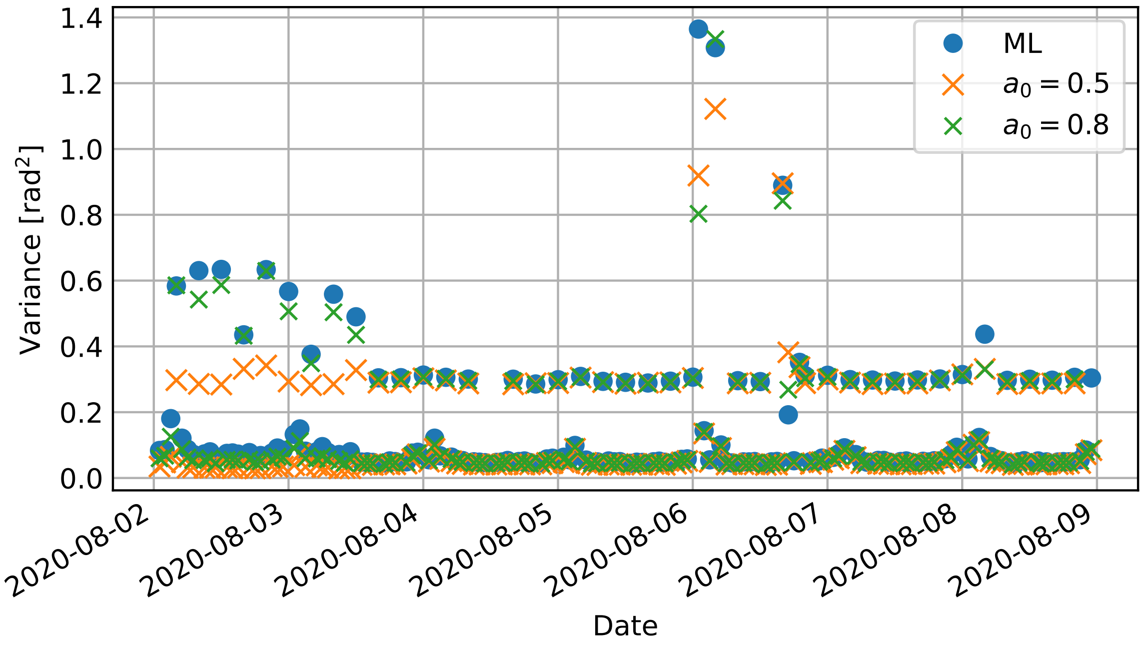

Figure B.6: Variance for CW2 from transmitter Heligoland the first 5min of each hour for different window functions

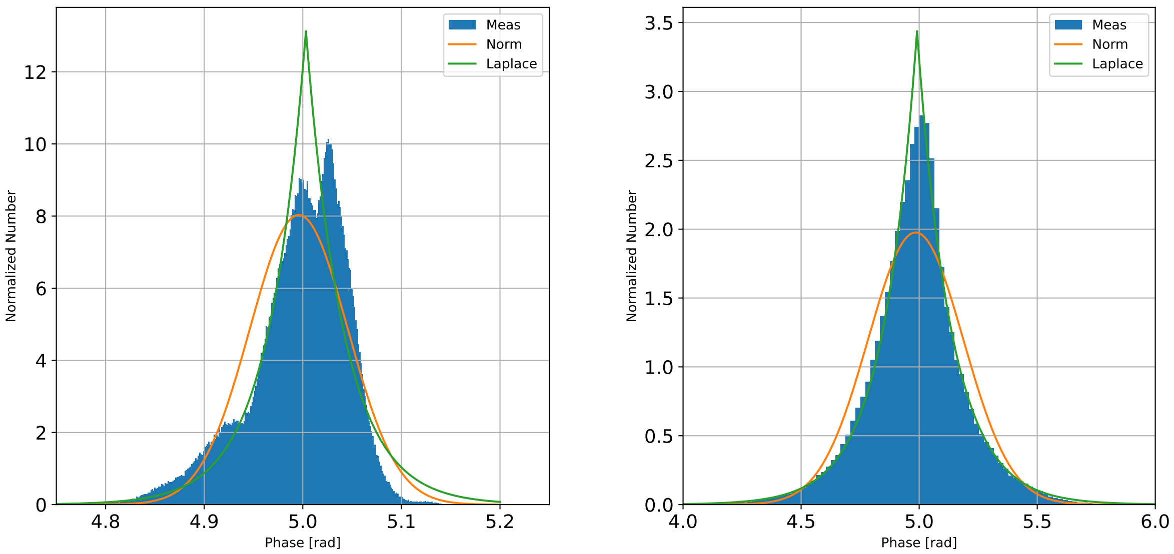

(a)

(b)

Figure B.7: Histograms of received station Heligoland with distribution fit during (a) daytime, (b) nighttime.

resulting histogram, with a variance of 0.3048 rad^2. Therefore, the result for the second CWs agrees with the description in Section 6.3.2.

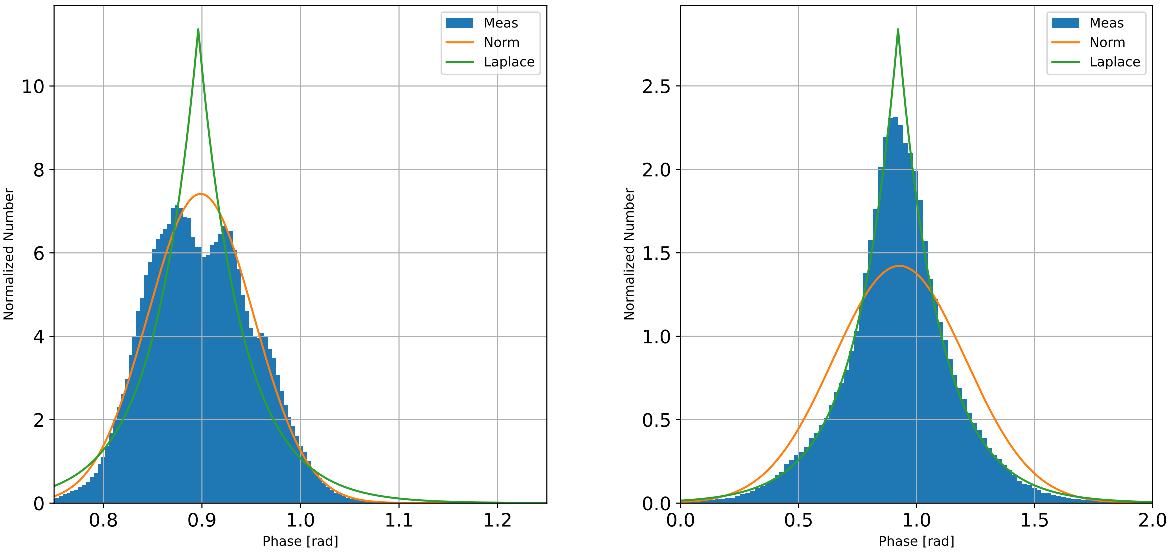

(a)

(b)

Figure B.8: Histograms of received station Zeven with distribution fit during (a) daytime, (b) nighttime.

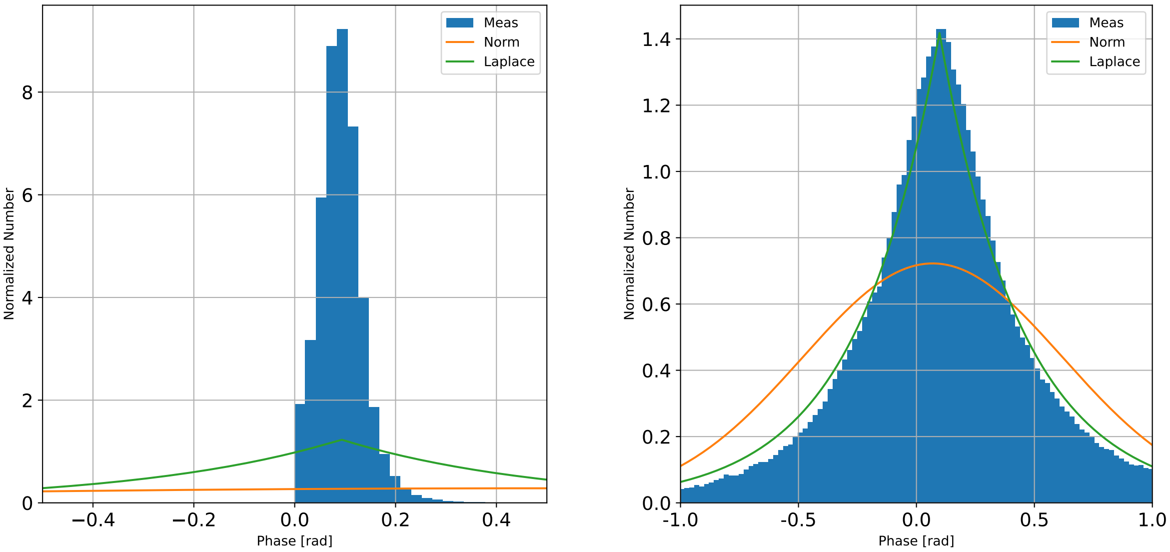

(a)

(b) t

Figure B.9: Histograms of received station Groß Mohrdorf with distribution fit at (a) daytime, (b) nighttime.

ACRONYMS

ADC Analog Digital Converter

AIS Automatic Identification System

ATU antenna tuning unit

AWGN Additive White Gaussian Noise

BDS BeiDou Navigation Satellite System

BSH Federal Maritime and Hydrographic Agency of Germany

CDMA Code Division Multiplexing Access

CISA Cybersecurity & Infrastructure Security Agency

CN$_0$ Carrier-to-Noise Ratio

CPM Continuous Phase Modulation

CPU Central Processing Unit

CRB Cramer-Raó Bound

CSV Comma Separated Values

CW Continuous Wave

CW1 lower frequency Continuous Wave

CW2 higher frequency Continuous Wave

DFT Discrete Fourier Transform

DGNSS Differential Global Navigation Satellite System

DLR German Aerospace Center

DSP Digital Signal Processing

DUT Device Under Test

E-field electric field

ESPRIT Estimation of Signal Parameters via Rotational Invariance Techniques

FDMA frequency division multiplexing access

FFT	Fast Fourier Transform
FIM	Fisher Information Matrix
GIRO	Global Ionospheric Radio Observatory
GLA	General Lighthouse Authority
GLONASS	Global Navigation Satellite System
GMSK	Gaussian Minimum Shift Keying
GNSS	Global Navigation Satellite System
GPS	Global Positioning System
GSM	Global System for Mobile Communications
H-field	magnetic field
HDD	Hard Disk Drive
IALA	International Association of Lighthouse Authorities
IMD	Intermodulation Distortion
IMO	International Maritime Organisation
ITU	International Telecommunication Union
LF	Loop Filter
LNA	Low Noise Amplifier
LS	Least Square
MF	Medium Frequency
ML	Maximum Likelihood
MSK	Minimum Shift Keyed
MUSIC	MUltiple SIgnal Classification
NavCen	United States Coast Guard Navigation Center
NavIC	Navigation Indian Constellation
NCO	Numerically Controlled Oscillator
PC	Personal Computer
PCB	Printed Circuit Board
PD	Phase Detector

PDM Pulse Density Modulation

PI Proportional Plus Integrator

PLL Phase Lock Loop

PNT Position Navigation and Timing

PPS Pulse Per Second

PSD Power Spectrum Density

PWM Pulse Width Modulation

QZSS Quasi-Zenith Satellite System

R-Mode Ranging-Mode

R&S Rohde & Schwarz

RAM Random-Access Memory

RTCM Radio Technical Commission for Maritime Services

RTK Real Time Kinematic

SA Selective Availability

SALSA Split Augmented Lagrangian Shrinkage Algorithm

SDR Software Defined Radio

SMA Swedish Maritime Administration

SNR Signal-to-Noise Ratio

SSD Solid State Disk

Std Standard Deviations

TCP Transmission Control Protocol

TCXO Temperature Compensated Oscillator

TDMA Time Division Multiplexing Access

USA United States of America

VDES VHF Data Exchange System

VHF Very High Frequency

VNA Vector Network Analyser

WSV Federal Water and Shipping Administration

REFERENCES

[1] L. Grundhöfer, M. Wirsing, S. Gewies, and G. D. Galdo, “Phase estimation of single tones next to modulated signals in the medium frequency R-Mode system,” *IEEE Access*, pp. 1–1, 2022.

[2] L. Grundhöfer, F. G. Rizzi, S. Gewies, M. Hoppe, J. Bäckstedt, M. Dziewicki, and G. D. Galdo, “Positioning with medium frequency R-Mode,” *ION Navigation*, vol. 68, pp. 829–841, 2021.

[3] L. Grundhöfer, S. Gewies, and G. D. Galdo, “Estimation bounds of beat signal in the R-Mode localization system,” *IEEE Access*, vol. 9, pp. 69 278–69 286, 2021.

[4] L. Grundhöfer and S. Gewies, “R-Mode receiver development for medium frequency signals,” *Scientific Journals of the Maritime University of Szczecin*, no. 56, pp. 57–62, 2018.

[5] L. Grundhöfer, F. G. Rizzi, S. Gewies, and G. Del Galdo, “Improving medium frequency R-Mode ranging with GMSK modulation.” in *Proceedings of the 34th International Technical Meeting of the Satellite Division of the Institute of Navigation ION GNSS + 2021 : Sept. 20-24, 2021, St. Louis Union Station Hotel, St. Louis, Missouri*. Manassas, VA: the Institute of Navigation, 2021.

[6] F. G. Rizzi, L. Grundhöfer, and S. Gewies, “Medium frequency R-Mode range estimation with phase locked loop approach,” in *Navigation 2021*, 2021. [Online]. Available: https://elib.dlr.de/146221/

[7] L. Grundhöfer and S. Gewies, “Equivalent circuit for phase delay in a medium frequency antenna,” in *2020 European Navigation Conference (ENC)*, 2020, pp. 1–6.

[8] L. Grundhöfer, S. Gewies, N. Hehenkamp, and G. Del Galdo, “Redesigned waveforms in the maritime medium frequency bands,” in *2020 IEEE/ION Position, Location and Navigation Symposium (PLANS)*, 2020, pp. 827–831.

[9] L. Grundhöfer, S. Gewies, N. Hehenkamp, M. Hoppe, and M. Walterfang, “Characterization of a transmitter in a medium frequency maritime terrestrial navigation system,” in *2019 IEEE Intelligent Transportation Systems Conference (ITSC)*, 2019, pp. 3828–3832.

[10] L. Grundhöfer, N. Meinert, F. G. Rizzi, S. Gewies, and R. Ziebold, “Calculating lower bounds within the PyTorch framework,” in *Proceedings of the 35th International Technical Meeting of the Satellite Division of the Institute of Navigation ION GNSS + 2022 : Sept. 19-23, 2022, Denver, Colorado*. Manassas, VA: the Institute of Navigation, Sep. 2022.

[11] S. Meister, L. Grundhöfer, J. Stüve, and R. M. Groves, “Imaging sensor data modelling and evaluation based on optical composite characteristics,” *The International Journal of Advanced Manufacturing Technology*, vol. 116, no. 11-12, pp. 3965–3990, Jul. 2021.

[12] D. Medina, L. Grundhofer, and N. Hehenkamp, “Evaluation of estimators for hybrid GNSS-terrestrial localization in collaborative networks,” in *2020 IEEE 23rd International Conference on Intelligent Transportation Systems (ITSC)*. IEEE, Sep. 2020.

[13] C. Rieck, S. Gewies, L. Grundhöfer, and M. Hoppe, “Synchronization of R-Mode base stations,” in *2020 Joint Conference of the IEEE International Frequency Control Symposium and International Symposium on Applications of Ferroelectrics (IFCS-ISAF)*. Keystone, CO, USA: IEEE, 2020, pp. 1–5.

[14] S. Gewies, L. Grundhöfer, and N. Hehenkamp, “Availability of maritime radio beacon signals for R-Mode in the southern baltic sea,” *TransNav : International Journal on Marine Navigation and Safety of Sea Transportation*, vol. 14, no. 1, pp. 173–178, Mar. 2020. [Online]. Available: https://elib.dlr.de/132191/

[15] S. Gewies, L. Grundhöfer, M. Wirsing, R. Raulefs, K. Bronk, P. Koncicki, N. Rafał, M. Hoppe, J. Bäckstedt, and C. Rieck, “R-Mode in the baltic sea region,” Sep. 2019. [Online]. Available: https://elib.dlr.de/132190/

[16] L. Grundhofer, N. Hehenkamp, and F. Heymann, “Concept for selectable composite radar screens,” in *2019 20th International Radar Symposium (IRS)*. IEEE, Jun. 2019.

[17] “GPS online representation,” Feb. 2022. [Online]. Available: https://www.gps.gov

[18] “Galileo online representation,” Feb. 2022. [Online]. Available: https://www.gsc-europa.eu/

[19] “BeiDou online representation,” Feb. 2022. [Online]. Available: http://en.beidou.gov.cn/

[20] “NacIC online representation,” Feb. 2022. [Online]. Available: https://www.isro.gov.in/irnss-programme

[21] “QZSS online representation,” Feb. 2022. [Online]. Available: https://qzss.go.jp/en/

[22] Cybersecurity & Infrastructure Security Agency, “Understanding Vulnerabilities of Positioning, Navigation and Timing,” 2020.

[23] M. L. Psiaki and T. E. Humphreys, “GNSS spoofing and detection,” *Proceedings of the IEEE*, vol. 104, no. 6, pp. 1258–1270, 2016.

[24] J. Guasch, *Impact study of unintentional interference on GNSS receivers*. Luxembourg: Publications Office, 2010.

[25] J. Bhatti and T. E. Humphreys, “Hostile control of ships via false GPS signals: Demonstration and detection,” *NAVIGATION*, vol. 64, no. 1, pp. 51–66, Mar. 2017.

[26] A. J. Kerns, D. P. Shepard, J. A. Bhatti, and T. E. Humphreys, “Unmanned aircraft capture and control via GPS spoofing,” *Journal of Field Robotics*, vol. 31, no. 4, pp. 617–636, Apr. 2014.

[27] GPS World Staff, “Massive GPS jamming attack by North Korea,” Jan. 2012. [Online]. Available: https://www.gpsworld.com/massive-gps-jamming-attack-by-north-korea/

[28] BBC, “North Korea ’jamming GPS signals’ near South border,” Apr. 2016. [Online]. Available: https://www.bbc.com/news/world-asia-35940542

[29] United States Coast Guard Navigation Center, “NavCen online representation,” Sep. 2022. [Online]. Available: https://navcen.uscg.gov/gps-problem-report-status

[30] “Executiv order 13905,” Feb. 2020. [Online]. Available: https://www.federalregister.gov/documents/2020/02/18/2020-03337/strengthening-national-resilience-through-responsible-use-of-positioning-navigation-and-timing

[31] W. F. Blanchard, “Air navigation systems chapter 4. hyperbolic airborne radio navigation aids – a navigator’s view of their history and development,” *Journal of Navigation*, vol. 44, no. 3, p. 285–315, 1991.

[32] G. Hefley, *The development of Loran-C navigation and timing*. U.S. Dept. of the Commerce, National Bureau of Standards, 1972.

[33] Resilient Navigation and Timing Foundation, “Loran off air in most of europe – move to commercial possible,” Jan. 2016. [Online]. Available: https://rntfnd.org/2016/01/04/loran-off-air-in-most-of-europe-move-to-commercial-possible/

[34] Nautical Institute, “Focus on pilots,” *The navigator*, Oct. 2021.

[35] H. C, W. P, and B. M, “ASF quality assurance for eLoran,” in *Proceedings of the 2012 IEEE/ION Position, Location and Navigation Symposium*, 2012, pp. 1169–1174.

[36] P.-W. Son, S. G. Park, Y. Han, and K. Seo, “eLoran: Resilient positioning, navigation, and timing infrastructure in maritime areas,” *IEEE Access*, vol. 8, pp. 193 708–193 716, 2020.

[37] A. Grant, P. Williams, N. Ward, and S. Basker, “GPS jamming and the impact on maritime navigation,” *Journal of Navigation*, vol. 62, no. 2, p. 173–187, 2009.

[38] J.-H. Oltmann and M. Hoppe, “Contribution to the IALA world wide radio navigation plan (IALAWWRNP) / recapitalization of MF DGNSS systems. input document to IALA ENAV4.” International Association of Lighthouse Authorities, 2008.

[39] G. Johnson and P. Swaszek, “Feasibility study of R-Mode using MF DGPS transmissions,” ACCSEAS, Tech. Rep., 2014.

[40] ——, “Feasibility study of R-Mode using AIS transmissions,” ACCSEAS, Tech. Rep., 2014.

[41] ——, “Feasibility study of R-Mode combining MF DGNSS, AIS, and eLoran transmissions,” ACCSEAS, Tech. Rep., 2014.

[42] M. Wirsing, A. Dammann, and R. Raulefs, “Investigating R-Mode Signals for the VDE System,” in *OCEANS 2019 Seattle*. IEEE, Oct. 2019. [Online]. Available: https://elib.dlr.de/129283/

[43] M. Wirsing, A. Dammann, and R. Raulefs, “Designing a ranging signal for use with VDE R-Mode,” in *2020 IEEE/ION Position, Location and Navigation Symposium (PLANS)*, 2020, pp. 822–826.

[44] IALA, “R0129 GNSS Vulnerability and Mitigation Measures,” International Association of Lighthouse Authorities, Saint Germain en Laye; Franc, Tech. Rep., Dec. 2012.

[45] IMO, “Resolution A.915(22) Revised Maritime Policy and Requirements for a Future GNSS,” International Maritime Organization, Tech. Rep., Jan. 2002.

[46] ——, “Resolution A.1046(27) Worldwide Radionavigation System,” International Maritime Organization, Tech. Rep., Nov. 2011.

[47] P. Enge, R. Kalafus, and M. Ruane, “Differential operation of the global positioning system,” *IEEE Communications Magazine*, vol. 26, no. 7, pp. 48–60, 1988.

[48] National Coordination Office for Space-Based Positioning, Navigation, and Timing., “Selective availability,” 2000. [Online]. Available: https://www.gps.gov/systems/gps/modernization/sa/

[49] RTCM Special Committee No. 104, *RTCM 10402.3 Recommended Standards for Differential Navstar GPS Service*, Radio Technical Commission for Maritime Services, 2200 Wilson Blvd Suite 102-109, Arlington VA 22201 US, May 2010.

[50] “Final acts of the regional administrative conference for the planning of the maritime radionavigation service (radiobeacons) in the european maritime area,” *Regional Administrative Conference for the Planning of the Maritime Radionavigation Service (Radiobeacons) in the European Maritime Area*, p. 41 p., 1986. [Online]. Available: http://digitallibrary.un.org/record/1120

[51] S. Gewies, “R-Mode Baltic Project Website,” Online, Feb. 2022. [Online]. Available: https://www.r-mode-baltic.eu/about-r-mode-baltic/

[52] P. Swaszek, “Analysis of MF-DGNSS modifications for improved ranging,” in *European Navigation Conference (ENC)*, 2014.

[53] G. Johnson, K. Dykstra, S. Ordell, and P. Swaszek, “R-Mode positioning system demonstration,” in *Proceedings ION GNSS+ 2020*. ION, Sep. 2020.

[54] G. Johnson, P. Swaszek, M. Hoppe, A. Grant, and J. Safar, “Initial results of MF-DGNSS R-Mode as an alternative position navigation and timing service,” in *Proceedings of the 2017 International Technical Meeting of The Institute of Navigation*, 2017.

[55] M. Hoppe, A. Grant, C. Hargreaves, and P. Williams, “R-Mode: The story so far,” in *IALA Conference*, 2018.

[56] International Telecommunication Union, “ITU-R M.823-2 technical characteristics of differential transmissions for global navigation satellite systems from maritimeradio beacons in the frequency band 283.5-315 kHz in region 1 and 285-325 kHz in regions 2 and 3,” 2006.

[57] S. Pasupathy, “Minimum shift keying: A spectrally efficient modulation,” *IEEE Communications Magazine*, vol. 17, no. 4, pp. 14–22, Jul. 1979.

[58] G. Van Rossum and F. L. Drake, *Python 3 Reference Manual*. Scotts Valley, CA: CreateSpace, 2009.

[59] E. Voges, *Hochfrequenztechnik Band 2*. Heidelberg: Hüthig, 1987.

[60] J. R. Wait, “The ancient and modern history of EM ground-wave propagation,” *IEEE Antennas and Propagation Magazine*, vol. 40, no. 5, pp. 7–24, 1998.

[61] G. Millington, “Ground-wave propagation over an inhomogeneous smooth earth,” *Journal of the Institution of Electrical Engineers*, vol. 96, pp. 53–64, 1949.

[62] B. W. Reinisch and I. A. Galkin, “Global ionospheric radio observatory (GIRO),” *Earth, Planets and Space*, vol. 63, no. 4, pp. 377–381, Apr. 2011. [Online]. Available: https://doi.org/10.5047/eps.2011.03.001

[63] J. Yu, M. T. Tan, S. M. Cox, and W. L. Goh, “Time-domain analysis of intermodulation distortion of closed-loop Class-D amplifiers,” *IEEE Transactions on Power Electronics*, vol. 27, no. 5, pp. 2453–2461, 2012.

[64] S. Kovačević, T. Pešić-Brđanin, and J. Galić, “Intermodulation distortion of class D audio amplifier using pulse density modulation,” in *2016 Zooming Innovation in Consumer Electronics International Conference (ZINC)*, 2016, pp. 46–49.

[65] H. Schmidt-Walter and R. Kories, *Electrical Engineering: A Pocket Reference*. Artech House, 2007.

[66] C. A. Balanis, *Antenna Theory : Analysis and Design*. John Wiley & Sons, Incorporated, 2016.

[67] M. Hoppe, “New MF beacon antenna,” German Federal Waterways and Shipping Administration, Tech. Rep., Dec. 2002.

[68] D. C. Rife and R. Boorstyn, “Single tone parameter estimation from discrete-time observations,” *IEEE Transactions on Information Theory*, vol. 20, no. 5, pp. 591–598, Sep 1974.

[69] D. C. Rife and R. R. Boorstyn, “Multiple tone parameter estimation from discrete-time observations,” *The Bell System Technical Journal*, vol. 55, no. 9, pp. 1389–1410, Nov 1976.

[70] S. M. Kay, *Fundamentals of Statistical Signal Processing: Estimation Theory*. USA: Prentice-Hall, Inc., 1993.

[71] D. Nion and N. D. Sidiropoulos, "Tensor algebra and multidimensional harmonic retrieval in signal processing for MIMO radar," *IEEE Transactions on Signal Processing*, vol. 58, no. 11, pp. 5693–5705, Nov. 2010.

[72] H. Cox, "Fundamentals of bistatic active sonar," in *NATO Advanced Study Institute on Underwater Acoustic Data Processing*, E. N. Y. T.Chan, Ed. Kluwer, 1989.

[73] M. Haardt, R. S. Thoma, and A. Richter, "Multidimensional highresolution parameter estimation with applications to channel sounding," in *High-resolution and robust signal processing*, Y. Hua, A. Gershman, and Q. Chen, Eds. New York: CRC Press, 2004, ch. 5, pp. 255–338.

[74] M. Pesavento, C. F. Mecklenbräuker, and J. F. Böhme, "Multidimensional rank reduction estimator for parametric MIMO channel models," *EURASIP Journal on Advances in Signal Processing*, vol. 2004, no. 9, Aug. 2004.

[75] M. L. Pay and H. Ahmed, "Parameter estimation of harmonics-polluted single-phase grid voltage signal," *Electrical Engineering*, vol. 102, no. 3, pp. 1351–1359, Feb. 2020.

[76] J. Steinwandt, F. Roemer, M. Haardt, and G. D. Galdo, "Performance analysis of multi-dimensional ESPRIT-type algorithms for arbitrary and strictly non-circular sources with spatial smoothing," *IEEE Transactions on Signal Processing*, vol. 65, no. 9, pp. 2262–2276, May 2017.

[77] X. Hu, T. Lyu, M. Zhang, H. Zhang, and T. A. Gulliver, "MUSIC and improved MUSIC algorithms for parameter estimation using a polarization sensitive array," in *2021 IEEE 21st International Conference on Communication Technology (ICCT)*. IEEE, Oct 2021.

[78] S. Schuster, S. Scheiblhofer, and A. Stelzer, "The Influence of Windowing on Bias and Variance of DFT-Based Frequency and Phase Estimation," *IEEE Transactions on Instrumentation and Measurement*, vol. 58, no. 6, pp. 1975–1990, 2009.

[79] D. W. Kammler, *A First Course in Fourier Analysis*. Cambridge New York: Cambridge University Press, 2008.

[80] F. J. Harris, "On the use of windows for harmonic analysis with the discrete Fourier transform," *Proceedings of the IEEE*, vol. 66, no. 1, pp. 51–83, 1978.

[81] J. Proakis, *Digital Communications*, ser. Electrical engineering series. McGraw-Hill, 2001. [Online]. Available: https://books.google.co.in/books?id=sbr8QwAACAAJ

[82] D. Borio, "Loop analysis of adaptive notch filters," vol. 10, pp. 659–669, 2016.

[83] W. Qin, F. Dovis, M. T. Gamba, and E. Falletti, “A comparison of optimized mitigation techniques for swept-frequency jammers.”

[84] C. Jekeli, *Geometric Reference Systems in Geodesy*. Division of Geodetic Science School of Earth Sciences: Ohio State University, 2016.

[85] P. D. Groves, *Principles of GNSS, Inertial and Multisensor Integrated Navigation Systems*. Artech House, 2008.

[86] T. Vincenty, “Direct and inverse solutions of the geodesics on the ellipsoid with application of nested equations,” *Survey Review*, vol. 23, no. 176, pp. 88–93, Apr 1975.

[87] S. J. Subirana, J. J. Zornoza, and M. Hernández-Pajares, *GNSS Data Processing, Vol. I: Fundamentals and Algorithms*. ESTEC, PO Box 299, 2200 AG Noordwijk, the Netherlands: ESA Communications, 2013.

[88] RTCM Special Commitee 127, “Minimum performance standards for marine eLoran receiving equipment,” Radio Technical Commission for Maritime Services, 1611 N. Kent St., Suite 605 Alexandria, Virginia 22209 U.S.A, Tech. Rep., Jan 2016.

[89] M. Margraf, “Qucs studio,” Feb 2022. [Online]. Available: http://qucsstudio.de/de/start/

[90] A. Arsenovic, J. Hillairet, J. Anderson, H. Forstén, V. Rieß, M. Eller, N. Sauber, R. Weikle, W. Barnhart, and F. Forstmayr, “scikit-rf: An open source python package for microwave network creation, analysis, and calibration [speaker’s corner],” *IEEE Microwave Magazine*, vol. 23, no. 1, pp. 98–105, 2022.

[91] E. Ramsden, *Hall-effect sensors : theory and applications*. Amsterdam Boston: Elsevier/Newnes, 2006.

[92] NTi Rudolf Ille Nachrichtentechnik, *Active Loop Antenna Amplifier9kHz - max. 180MHz & FM Trap Operating ManualVersion V2.1*, Dinkelbergstr. 10D-79540 Lörrach.

[93] D. Walter, *Boni-Whip-Manual*, Gerichtsweg 3 – 29320 Hermannsburg, 2014. [Online]. Available: https://hamradioshop.net/media/pdf/b7/11/97/Manual_de_en.pdf

[94] Rohde & Schwarz, *R&SFPC Spectrum Analyzer Data Sheet*, 06th ed., 2021.

[95] ——, *R&S ZNL Vector Network and Analyzer and Specifications Datasheet*, 06th ed., Aug. 2021.

[96] ——, *R&S ZN-Z2xx | ZV-Z2xx Calibration Kits Specification*, 06th ed., Jun. 2021.

[97] Mini Circuit, *Low Noise Amplifier ZFL-500LN+- Datasheet*, rev. F ed., Mini-Circuit, P.O. Box 350166, Brooklyn, NY.

[98] H. Packard, *Cascadable Silicon Bipolar MMIC Amplifiers MSA-0335 Technical Data*, 5965th ed., 5965.

[99] Krohn-Hite Corporation, *FMB3002 V1-1 Manual*, 15 Jonathan Drive, Brockton, MA 02301-5566, 2011.

[100] Mini Circuits, *Surface Mount Low Pass Filter LPF-B0R35+ Datasheet*, rev.b. ed., P.O. Box 350166, Brooklyn, NY 11235-0003, 2008.

[101] ——, *Coaxial High Pass and Filter ZFHP-0R23-S+ 50■ 0.23 to 1000 MHz Datasheet*, rev.b ed., P.O. Box 350166, Brooklyn, NY 11235-0003, 2005.

[102] Ettus Research, *N200 and N310 N Series Datasheet*, Sep. 2019.

[103] ——, " X300 and X310 X Series datasheet," Sep. 2019.

[104] J. Malsbury and M. Ettus, "Simplifying FPGA design with a novel network-on-chip architecture," in *Proceedings of the second workshop on Software radio implementation forum - SRIF '13*. ACM Press, 2013.

[105] W. Feng, J.-M. Friedt, G. Cherniak, and M. Sato, "Passive bistatic radar using digital video broadcasting–terrestrial receivers as general-purpose software-defined radio receivers," *Review of Scientific Instruments*, vol. 89, no. 10, p. 104701, Oct. 2018.

[106] Siglent Technologies, *SDS1000X-E Series Super Phosphor Oscilloscope Datasheet*, Blog No.4 & No.5, Antongda Industrial Zone,3rd Liuxian Road, Bao'an District,Shenzhen, 518101, China., Sep. 2017.

[107] B. Uengtrakul and D. Bunnjaweht, "A cost efficient software defined radio receiver for demonstrating concepts in communication and signal processing using python and RTL-SDR," in *2014 Fourth International Conference on Digital Information and Communication Technology and its Applications (DICTAP)*. IEEE, 2014, pp. 394–399.

[108] Realtek Semiconductor Corp., "Realtek RTL2832U," Feb. 2022. [Online]. Available: https://www.realtek.com/en/products/communications-network-ics/item/rtl2832u

[109] C. Laufer, *RTL-SDR Blog V3 Datasheet*, 2020.

[110] M. Laakso, R. Rajamäki, R. Wichman, and V. Koivunen, "Phase-coherent multichannel SDR-sparse array beamforming," in *2020 28th European Signal Processing Conference (EUSIPCO)*. IEEE, 2021, pp. 1856–1860.

[111] J. Kaderka and T. Urbanec, "Time and sample rate synchronization of RTL-SDR using a GPS receiver," in *2020 30th International Conference Radioelektronika (RADIOELEKTRONIKA)*, 2020, pp. 1–4.

[112] Tektronix Inc, *Arbitrary Function Generators AFG31000 Series Datasheet*, Oct. 2020.

[113] M. Sústrik, “The architecture of open source applications (volume 2): ZeroMQ,” 2020. [Online]. Available: http://www.aosabook.org/en/zeromq.html

[114] O. Holland, H. Bogucka, and A. Medeisis, *Opportunistic Spectrum Sharing and White Space Access: The Practical Reality*. WILEY, May 2015. [Online]. Available: https://www.ebook.de/de/product/22771210/oliver_holland_hanna_bogucka_arturas_medeisis_opportunistic_spectrum_sharing_and_white_space_access_the_practical_reality.html

[115] Saab Transponder Tech, *R5 SUPREME NAV MkII Datasheet*, Låsblecksgatan 3SE-589 41 Linköping,Sweden, Sep. 2020.

[116] J. B. Anderson, T. Aulin, and C.-E. Sundberg, *Digital Phase Modulation*, 1st ed. Plenum Press, New York, 1986.

[117] T. Muller, H. Rohling, and H. E. Speckter, “Reduction of interference from DGPS transmissions in the MF band using a GMSK modulation scheme,” *IEEE Transactions on Aerospace and Electronic Systems*, vol. 30, no. 4, pp. 1104–1108, 1994.

[118] K. Murota and K. Hirade, “GMSK modulation for digital mobile radio telephony,” *IEEE Transactions on Communications*, vol. 29, no. 7, pp. 1044–1050, 1981.

[119] S. G. Mallat and Z. Zhang, “Matching pursuits with time-frequency dictionaries,” *IEEE Transaction on Signal Processing*, vol. 41, no. 12, 1993.

[120] W. Lei and B. Chen, “Low complexity sparse noise reduction method for Loran-C skywave delay estimation,” *Electronics Letters*, vol. 49, no. 24, pp. 1572–1574, Nov. 2013.

LIST OF FIGURES

LIST OF TABLES